



**HAL**  
open science

# Novel multi-spectral imaging technique for the spatial quantification of optical properties

Verónica Sorgato Casares

► **To cite this version:**

Verónica Sorgato Casares. Novel multi-spectral imaging technique for the spatial quantification of optical properties. Optics [physics.optics]. Université Pierre et Marie Curie - Paris VI, 2016. English. NNT : 2016PA066284 . tel-01449392

**HAL Id: tel-01449392**

**<https://theses.hal.science/tel-01449392>**

Submitted on 30 Jan 2017

**HAL** is a multi-disciplinary open access archive for the deposit and dissemination of scientific research documents, whether they are published or not. The documents may come from teaching and research institutions in France or abroad, or from public or private research centers.

L'archive ouverte pluridisciplinaire **HAL**, est destinée au dépôt et à la diffusion de documents scientifiques de niveau recherche, publiés ou non, émanant des établissements d'enseignement et de recherche français ou étrangers, des laboratoires publics ou privés.



**PHD THESIS OF THE  
UNIVERSITY PIERRE AND MARIE CURIE**

Speciality **Physics**

Doctoral School of The Particle Physics in Condensed Matter (Paris)

Presented by

**Verónica SORGATO CASARES**

To achieve the degree of

**DOCTOR of the UNIVERSITY PIERRE AND MARIE  
CURIE**

Title of the Thesis :

**Novel Multispectral Imaging Technique for the  
Spatial Quantification of Optical Properties**

Supervised by :

Dr. Anne PLANAT-CHRÉTIEN	Supervisor
Dr. Geneviève BOURG-HECKLY	Director
M. Michel BERGER	Co-Supervisor
Dr. Christine VEVER-BIZET	Co-Supervisor

defended on 18 October 2016, in front of the jury composed by :

Mme. Anabela DA SILVA	Reporter
M. Bruno MONTCEL	Reporter
M. Jacques LAFAIT	Examiner
Mme. Anne PLANAT-CHRÉTIEN	Examiner
M. Walter BLONDEL	Examiner
Mme. Geneviève BOURG-HECKLY	Invited guest
M. Michel BERGER	Invited guest
Mme. Christine VEVER-BIZET	Invited guest





**THÈSE DE DOCTORAT DE  
L'UNIVERSITÉ PIERRE ET MARIE CURIE**

Spécialité **Physique**

École Doctorale Physique de la Particule à la Matière Condensée (Paris)

Présentée par

**Verónica SORGATO CASARES**

Pour obtenir le grade de

**DOCTEUR de l'UNIVERSITÉ PIERRE ET MARIE CURIE**

Sujet de la thèse :

**Détermination et Mise en Œuvre d'une Technique  
d'Imagerie Multi-Spectrale pour la Quantification  
Spatiale des Propriétés Optiques**

encadrée par :

Dr. Anne PLANAT-CHRÉTIEN	Encadrante
Dr. Geneviève BOURG-HECKLY	Directeur de thèse
M. Michel BERGER	Co-Encadrant
Dr. Christine VEVER-BIZET	Co-Encadrante

soutenue le 18 Octobre 2016, devant le jury composé de :

Mme. Anabela DA SILVA	Rapporteur
M. Bruno MONTCEL	Rapporteur
M. Jacques LAFAIT	Examinateur
Mme. Anne PLANAT-CHRÉTIEN	Examinateur
M. Walter BLONDEL	Examinateur
Mme. Geneviève BOURG-HECKLY	Invitée
M. Michel BERGER	Invité
Mme. Christine VEVER-BIZET	Invitée



## INSTITUTE CONTACTS

Laboratoire Jean Perrin  
F-75005 Paris — France  
École Doctorale de Physique ED389  
P2MC La Physique de la Particule à la Matière Condensée  
Université Pierre et Marie Curie  
33100 Paris — France  
<http://www.ed389.upmc.fr/fr/index.php>

Laboratoire LISA, CEA  
CEA/LETI/STD/DTBS/LISA  
17 Rue des Martyrs  
38054 Grenoble — France  
<http://www-leti.cea.fr/>

AUTHOR'S CONTACTS  
[veronica.sorgato88@gmail.com](mailto:veronica.sorgato88@gmail.com)



*'A river cuts through rock,  
not because of its power,  
but because of its persistence'.*

Jim Watkins

*'Where there is love,  
there is life'.*

Mahatma Gandhi



# Acknowledgements

I would like to express my sincere gratitude to the people that have provided me the opportunity to embark on this PhD in CEA and UPMC, a project that was born between Patricia Le Coupanec, Jean-Marc Dinten, and Geneviève Bourg-Heckly.

In the CEA team, I would like to especially thank Anne Planat-Chrétien, my supervisor, who constantly guided me with her enthusiasm, caring, and rigorous scientific devotion in this research work. I also thank Michel Berger who has been a great teacher for me in the world of optics. Both Anne and Michel, together with Charlotte Emain have accompanied me all along the instrumental development of this work teaching me their expertise and having always a smile and funny anecdotes to share. It was a privilege for me to closely work with them and enjoy their support, that sometimes persevered until late hours in the afternoon. I am also grateful to Jean-Marc Dinten for his serviceability, dedication, and understanding.

I would also like to acknowledge Véronique Josserand that provided and helped us in the manipulation of the rats for the most important experiments of this work.

In the UPMC team, it is a pleasure to express my gratitude to Geneviève Bourg-Heckly, my thesis director, not only for her support in all aspects but also for her extremely kind hospitality. Also, I acknowledge Christine Vever-Bizet for her advice, good humour, and support in administrative tasks.

Without them, this work would not have been possible.

It is my privilege to acknowledge the members of the jury. I thank Anabela Da Silva and Bruno Montcel, the reporters of this PhD, for the analysis and reading time dedicated to this work. I thank Jacques Lafait, Walter Blondel, and Anne Planat-Chrétien for their interest in our work and their role as examiners. I am also grateful to the invited members Sylvain Gioux, Geneviève Bourg- Heckly, Michel Berger, and Christine Vever-Bizet for their participation and stimulation.

I acknowledge many other colleagues in our *LISA* laboratory for their advice and friendship. Sophie Morel and Judy Zouaoui who were comrades in the research adventure and quickly became precious moral foundations for me. They offered me a very nice and long-living friendship. Blandine Roig, Charlotte Emain, and Agathe Puszka for their kindness, empathy, and scientific advice. Véronique Duvocelle and Laurence Chassouant for their adorable smile and incredibly efficient assistance in administrative tasks. Anne

Koenig, my office neighbour, who was always available to answer my questions and with whom I shared day-to-day experiences. Romaric Vincent, Damien Decq, and Audrey Dot for the interesting conversations, their joyfulness, and sincere altruism. Lionel Hervé for his immense trust and valuable theoretical explanations. Jérôme Boutet, Nils Petitdidier, Poon Woei Jye, and Anthony Berdeau for their mathematical contributions. I also thank other members of the lab for their warm reception.

I am fully indebted to my family and friends for the great moral support that they have given me all along these three years. It is mostly thanks to them that I have completed this work.

I express the immense gratitude I have to my close family that were able to give me their most positive energy from the other part of the Atlantic Ocean. I especially thank my wonderful mom, Paulina Casares Zurita, for her dedication and limitless love.

I would like to thank Elvira Rodriguez Alonso who has become a ‘ñaña’ to me and has always been there to encourage me in the hard times as well as to celebrate the innumerable good moments.

Florent Berthier supported me not only with his high performing computer but especially with his caring and inestimable friendship. I thank him wholeheartedly.

Friederike Neumann, my best house-mate and friend I have had in these years. I thank her for her music, laugh, positive energy, and great moments spent together.

I thank Encarna Micó Amigo for the eternal friendship that we conserve and which once again we have proved to be stronger than distance and time.

I am grateful to Eloise Van Caloen for the long friendship that I luckily enjoyed in the same city after so many years. Florent Duval, Ana Luisa, and Maxime Damery for their cheerfulness and invaluable support in the first year of PhD. Tommaso Dreossi for his mathematical advice, music, and love during the first year and a half of PhD. Lauren Thevin, Laurence Tordjman, Pierre Gouvernel, and Guillaume Sturni for the memorable moments and genuine friendship that we built since I arrived to Grenoble. Etzael Espino and Giovanni Orazio Lepore for their new caring friendship. Olivier Ray and Marie Spitoni for their constant encouragements in the last months of this PhD. Susana Bonnetier and Robert Baptist for their professional advice and vast kindness.

I thank all these people for having turned these three years into an unforgettable and precious experience of my life.





# Abstract

The Novel *Dual-Step* Multispectral Imaging Technique that has been developed intends to contribute to the clinical diagnosis of superficial lesions by providing non-invasively quantitative spatial wide field maps of absorption and scattering endogenous optical properties. The approach relies on the combination of a Non-Contact Spatially-resolved Diffuse Reflectance Spectroscopy (DRSsr) technique with a Multispectral Imaging (MSI) technique. Absolute quantification is based on the scattering estimation with Non-Contact DRSsr which is subsequently used by MSI to estimate wide field absorption. The instrumental setups of each technique are built and thoroughly characterized in this work. The optimal quantification of optical properties relies on a newly established calibration algorithm (*ACA-Pro*) that achieves minimal estimation errors inferior to 3.3% for scattering and 5.5% for absorption. The developed *Dual-Step* technique has been validated not only with an extensive intralipid phantom study but also with *ex-vivo* biological human skin samples and *in-vivo* inflammation skin models on rats. The results show the potential of the *Dual-Step* technique as a valid quantitative, wide-field, and non-invasive clinical diagnosis approach.



# Résumé

La nouvelle technique '*Dual-Step*' d'Imagerie Multispectrale qui a été développée a comme objectif de contribuer au diagnostic clinique des lésions superficielles, en procurant des cartes grand champ quantitatives des propriétés optiques endogènes telles que l'absorption et la diffusion. L'approche repose sur la combinaison d'une technique sans-contact de Spectroscopie de Réflectance Diffuse spatialement résolue (DRSsr) pour estimer la diffusion utilisée ensuite par une autre technique d'Imagerie Multispectrale (MSI) pour estimer l'absorption. Les bancs d'essai de chaque technique ont été construits et caractérisés dans le cadre de ce travail. La quantification optimale des propriétés optiques s'appuie sur un nouvel algorithme de calibration (*ACA-Pro*) qui atteint des erreurs d'estimation minimales et inférieures à 3.3% pour la diffusion et 5.5% pour l'absorption. La technique '*Dual-Step*' a été validée sur des fantômes d'intralipide mais aussi sur des échantillons *ex-vivo* de peau humaine et des modèles *in-vivo* d'inflammation de peau de rats. Les résultats montrent la faisabilité de la technique '*Dual-Step*' et son potentiel en diagnostic clinique grâce à son approche quantitative, grand champ et non-invasive.







# Contents

<b>1</b>	<b>Introduction</b>	<b>3</b>
<b>2</b>	<b>Context</b>	<b>7</b>
2.1	Light propagation in a biological medium . . . . .	8
2.1.1	Reflection and Refraction . . . . .	9
2.1.2	Scattering . . . . .	10
2.1.3	Absorption . . . . .	13
2.2	Biological Application . . . . .	16
2.2.1	Function of skin . . . . .	16
2.2.2	Histological structure . . . . .	17
2.2.3	Optical Properties . . . . .	18
2.3	Intralipid phantoms . . . . .	19
2.3.1	Manufacturing Protocol . . . . .	19
2.3.2	Selected Optical Properties . . . . .	20
2.4	Solutions of the Radiative Transfer Equation according to the photon transport regime . . . . .	21
2.5	Spectral Imaging Methods . . . . .	22
2.5.1	Chosen Spectral Range . . . . .	22
2.5.2	Spectral Imaging Instrumentation . . . . .	23
2.5.3	Quantification Problematic . . . . .	24
2.5.4	State of the Art according to the Quantification Problematic . . . . .	26
2.6	Proposition . . . . .	33
<b>3</b>	<b>Spatially Resolved Diffuse Reflectance Spectroscopy</b>	<b>35</b>
3.1	Spatial Resolution of DRS for optical properties quantification . . . . .	36
3.2	Existing <i>Contact DRSSr</i> system . . . . .	38
3.2.1	Instrumental Setup . . . . .	38
3.2.2	Measurement Procedure . . . . .	40
3.2.3	Signal Processing . . . . .	42
3.2.4	Method for the Derivation of Optical Properties . . . . .	43
3.2.5	Results . . . . .	49
3.2.6	Limitations of current method . . . . .	49
3.3	Non-contact probe-based DRSSr . . . . .	52
3.3.1	Instrumental Setup . . . . .	53
3.3.2	Geometrical alteration induced by the optical path . . . . .	54
3.3.3	Spectral effect of components on signals . . . . .	58

3.3.4	Measurement Procedure . . . . .	60
3.3.5	Signal Processing . . . . .	60
3.4	Non-Contact CCD-based DRSsr . . . . .	62
3.4.1	Instrumental Setup . . . . .	63
3.4.2	Geometrical alterations induced by the optical path . . . . .	65
3.4.3	Spectral effect of components on signals . . . . .	68
3.4.4	Measurement Procedure . . . . .	70
3.4.5	Image Processing . . . . .	71
3.4.6	Signal Processing . . . . .	71
3.5	Challenges encountered with Non-Contact DRSsr . . . . .	73
3.5.1	Quantification Method Challenges . . . . .	73
3.5.2	Instrumental Challenges . . . . .	75
3.6	Conclusion . . . . .	80
<b>4</b>	<b>ACA-Pro algorithm</b> . . . . .	<b>81</b>
4.1	Non-modelled illumination profile effect . . . . .	81
4.2	State of the Art . . . . .	82
4.3	Proposition: ACA-Pro algorithm . . . . .	85
4.4	Principle of ACA-Pro . . . . .	85
4.4.1	Reference CFs . . . . .	85
4.4.2	Interpolation . . . . .	86
4.4.3	Correction of Instrumental Variations . . . . .	86
4.5	Results on phantoms . . . . .	89
4.5.1	CF reference base . . . . .	89
4.5.2	Optical Properties estimation with the $CF$ reference base for all setups . . . . .	92
4.5.3	Absorption difference with probe-based setups. . . . .	95
4.5.4	Optical Properties estimation with Monte Carlo simulation considering Non-Contact conditions . . . . .	97
4.5.5	Interpolation . . . . .	100
4.5.6	Correction of Instrumental Variations . . . . .	102
4.6	First probe measurements on biological samples . . . . .	108
4.6.1	Heterogeneous Ham sample . . . . .	108
4.6.2	Measurement procedure . . . . .	108
4.6.3	Method . . . . .	108
4.6.4	Results and Discussion . . . . .	109
4.7	Conclusion . . . . .	110
<b>5</b>	<b>Large Field of View Multispectral Imaging</b> . . . . .	<b>113</b>
5.1	Instrumental Setup . . . . .	114
5.2	Measurement Procedure . . . . .	116
5.2.1	Focusing . . . . .	116
5.2.2	Flat Field . . . . .	116
5.3	Image Processing . . . . .	116
5.3.1	Flat Field Correction . . . . .	116
5.3.2	Averaged intensity . . . . .	117
5.3.3	Correction of Illumination fluctuations . . . . .	118

5.4	Method for the derivation of Optical Properties . . . . .	119
5.4.1	Diffusion Model with homogeneous illumination . . . . .	119
5.4.2	Instrumental Calibration . . . . .	120
5.4.3	Non-Uniqueness Problem . . . . .	120
5.5	Absorption Quantification . . . . .	122
5.6	Wide-field Absorption Optimization with ACA-Pro . . . . .	127
5.6.1	CF Reference base . . . . .	128
5.6.2	CF Interpolation . . . . .	131
5.6.3	Intensity variation correction . . . . .	132
5.7	Spatial distribution optimization . . . . .	133
5.8	Depth of Field . . . . .	135
5.9	Measurement of a heterogeneous medium . . . . .	136
5.9.1	Image acquisition . . . . .	137
5.9.2	Wide-field absorption quantification . . . . .	138
5.10	Conclusion . . . . .	142
<b>6</b>	<b>Optical properties quantification of biological tissue with Dual-step technique</b>	<b>143</b>
6.1	Instrumental Setup . . . . .	144
6.2	Samples . . . . .	145
6.2.1	<i>Ex-vivo</i> Human abdominal skin . . . . .	145
6.2.2	<i>In-vivo</i> rat models . . . . .	146
6.2.3	Reference samples . . . . .	147
6.3	Measurement Procedure . . . . .	148
6.4	Signal and Image Processing . . . . .	150
6.4.1	Filtering of Specular Reflections . . . . .	150
6.4.2	Position Correspondence . . . . .	150
6.5	Quantification of optical properties . . . . .	152
6.5.1	DRSsr . . . . .	152
6.5.2	<i>Dual-Step</i> technique . . . . .	153
6.5.3	Wide field quantification of $\mu_a$ . . . . .	157
6.6	Validation of <i>Dual-Step</i> technique using <i>ex-vivo</i> human skin samples . . . . .	158
6.6.1	Heterogeneous skin model, Phototype 2 . . . . .	158
6.6.2	Homogeneous skin model, Phototype 5 . . . . .	163
6.7	Validation of <i>Dual-Step</i> technique using <i>in-vivo</i> rat skin models . . . . .	168
6.7.1	Bi-coloured model . . . . .	168
6.7.2	Inflammation model Type 1 . . . . .	174
6.7.3	Inflammation model Type 2 . . . . .	181
6.8	Discussion and Conclusion . . . . .	187
<b>7</b>	<b>Conclusions and Perspectives</b>	<b>189</b>
7.1	Conclusions . . . . .	189
7.2	Perspectives . . . . .	193
7.2.1	Non-Contact DRSsr perspectives . . . . .	193
7.2.2	LFOV MSI Perspectives . . . . .	196
7.2.3	<i>Dual-Step</i> technique Perspectives . . . . .	198

<b>A</b>	<b>Appendix</b>	<b>203</b>
A.1	Contributions to the current DRSSr procedure . . . . .	203
A.1.1	Reduction of numerical noise . . . . .	203
A.2	Detectors' specifications . . . . .	204
A.2.1	PixelFly VGA CCD . . . . .	204
A.2.2	<i>JETI</i> Spectrometer . . . . .	206
A.3	Transmission of Filters . . . . .	207
A.4	Relationship of Spectral Imaging and Spectroscopy . . . . .	208
A.4.1	Experimental setup . . . . .	208
A.4.2	Measurement procedure . . . . .	209
A.4.3	Signal Processing . . . . .	210
A.4.4	Optical analysis for unit agreement . . . . .	210
A.4.5	Spectroscopy: Radiance conversion . . . . .	211
A.4.6	Imaging: Intensity conversion . . . . .	212
A.4.7	Results and Discussion . . . . .	212
A.4.8	Conclusion . . . . .	213
A.5	Improved CCD-based Non-Contact DRSSr setup . . . . .	214
A.6	Validation of ACA-Pro with folded Non-Contact DRSSr measurements . . . . .	216
<b>B</b>	<b>Scientific Communications</b>	<b>217</b>
B.1	Patents . . . . .	217
B.2	Communications . . . . .	217
B.3	Journal Articles . . . . .	217
	<b>Bibliography</b>	<b>219</b>





# Glossary

$A$  Absorbance.

$B$  Constant.

$C$  Concentration.

$D$  Distances of different detection fibre rings of the DRSSr probe.

$E$  Excitation source signal.

$E_{PF}$  Photon Flux.

$E_{photon}$  Quantum energy of a single photon.

$E_{total}$  Total energy.

$F$  Fibre rings.

$G$  Magnification.

$I$  Intensity.

$Im$  Image.

$K$  Correction constant.

$L$  Optical pathlength.

$N_p$  Number of photons.

$QE$  Quantum Efficiency.

$R^{LUT}$  Simulated Reflectance saved in the Look-up table.

$R_m$  Radiance.

$R_{CF}$  Calibrated measured Reflectance.

$S$  Measured signal.

$S_N$  Measured signal normalized by the illumination source signal.

$S_c$  Measured signal corrected from offset and scaled according to  $t$ .

$S_F$  Final signal corrected from parasite reflections and offset, and scaled according to  $t$ .

- $S_{offset}$  Measured offset or background signal.
- $S_{parasite}$  Measured signal of parasite reflections.
- $S_{sample}$  Measured signal at the surface of the sample.
- $Spec$  Spectralon.
- $T$  Transmission.
- $\Delta$  Difference.
- $\Phi$  Surface area.
- $\beta$  Scattering component.
- $\delta_{eff}$  Effective penetration depth.
- $\gamma$  Reflection factor of sample surface.
- $l'_s$  Reduced mean free path.
- $l_s$  Mean free path.
- $l_{tr}$  Transport length.
- $\lambda$  Wavelength.
- $\mu'_s$  Reduced scattering coefficient.
- $\mu_a$  Absorption coefficient.
- $\mu_s$  Scattering coefficient.
- $\mu_{eff}$  Effective attenuation coefficient.
- $\mu_t$  Total attenuation coefficient.
- $\rho(\theta)$  Phase Function.
- $\varepsilon$  Extinction coefficient.
- arb.unit* Arbitrary unit.
- $c$  Speed of light.
- det* Detection.
- $f$  Focal length.
- $f\#$  F-number.
- $g$  Anisotropy factor.
- $gv$  Grey value.

*h* Planck constant.

*ill* Illumination.

*n* Refraction index.

*p* Scatterer particle size.

*p<sub>i</sub>* Image plane pixel size.

*p<sub>o</sub>* Object plane pixel size.

*pixel* Picture Element.

*q* Quantization step.

*ref* Reference.

*t* Acquisition time.

*theo* Theoretical.

*var* Variation.

*z* Depth.

**ACA-Pro** Adaptive Calibration Algorithm and Protocol.

**BS** Beamsplitter.

**BVF** Blood Volume Fraction.

**CCD** Charge Coupled Device.

**CF** Correction Factor.

**DOF** Depth of Field.

**DPF** Differential Pathlength Factor.

**DRS** Diffuse Reflectance Spectroscopy.

**DRSsr** Spatially-resolved Diffuse Reflectance Spectroscopy.

**FF** Flat Field.

**FOV** Field of View.

**FWHM** Full Width Half Maximum.

**H<sub>2</sub>O** Water.

**Hb** Deoxy-haemoglobin.

**HbO<sub>2</sub>** Oxy-haemoglobin.

**HSI** Hyperspectral Imaging.

**IL** Intralipid.

**IP** Intralipid Phantom.

**IR** Infrared.

**IRF** Instrument Response Function.

**LFOV** Large Field of View.

**LOD** Limit of Detection.

**LPS** Lipopolysaccharide.

**LUT** Look-up table.

**M** Measurement set.

**MC** Monte-Carlo.

**MSI** Multispectral Imaging.

**NA** Numerical Aperture.

**NBI** Narrow Band Imaging.

**NC** Non-Contact.

**NIR** Near-Infrared.

**OD** Optical Density.

**PR** Parasite Reflections.

**RGB** Red-green-blue.

**RTE** Radiative Transfer Equation.

**SD** Source-Detector distance.

**SFDI** Spatial Frequency Domain Imaging.

**SNR** Signal to Noise Ratio.

**SR** Specular Reflections.

**T-H** Tungsten Halogen.

**TF** Transfer Function.

**UV** Ultra-violet.

**vis** Visible.



# Résumé

L'objectif général de ce travail est de contribuer à l'amélioration du diagnostic des lésions superficielles avec le développement d'une nouvelle technique quantitative d'imagerie multispectrale. L'utilisation de cette technique en imagerie médicale vise une quantification grand champ des propriétés optiques avec des mesures non-invasives dans le spectre 450-880 *nm*.

L'aspect non-invasif de la technique est assuré par la mesure d'un contraste endogène, c'est à dire sans produit de contraste, tel que par exemple des fluorophores ou des colorants, et par la modalité sans-contact de la mesure. Cette dernière est une nécessité pour la mesure d'échantillons sensibles comme des lésions qui requièrent une manipulation complètement stérile.

La quantification absolue des propriétés optiques doit permettre un diagnostic robuste. En effet, les propriétés d'absorption et de diffusion tissulaires sont reliées aux caractéristiques biochimiques et histologiques et fournissent des informations sur le métabolisme et la structure du tissu pour la détection précoce et le diagnostic précis des maladies.

Par ailleurs, la quantification d'un grand champ à travers l'imagerie apporte beaucoup d'avantages en termes de pratique clinique, de temps et de coût.

La technique '*Dual-Step*' que nous proposons dans le cadre de cette thèse s'appuie sur la combinaison d'une modalité sans-contact de Spectroscopie de Réflectance Diffuse spatialement résolue (DRSsr) et d'Imagerie Multispectrale couvrant un large champ (LFOV MSI).

La DRSsr repose sur la mesure de la réflectance diffuse sur une large gamme spectrale, qui dépend des propriétés optiques du milieu traversé, à des distances spécifiques de la source ponctuelle (voir Figure 1). L'ouverture confinée de la source d'illumination et de la détection, permet de déterminer le chemin optique. Ce dernier, avec les différentes distances de détection, permet de dissocier les effets d'absorption et de diffusion. Ainsi, la DRSsr atteint une quantification absolue et robuste des propriétés optiques d'absorption et de diffusion.

Du fait de sa modalité ponctuelle, la DRSsr scrute une petite zone et n'est donc appropriée que pour un nombre restreint d'applications cliniques. Par conséquent, l'élargissement des mesures quantitatives vers un champ plus large favorise le diagnostic de la majorité des applications cliniques ayant besoin d'une analyse plus large et plus rapide. Nous proposons pour cela une combinaison de la DRSsr, méthode quantitative et ponctuelle, avec la MSI couvrant un grand champ.

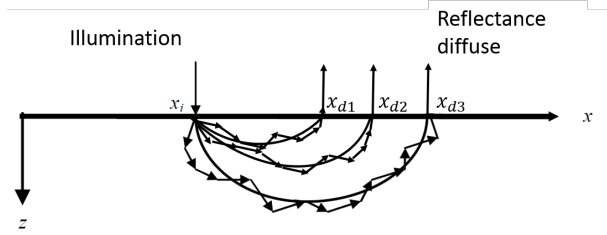


Figure 1: DRSsr: L'ouverture confinée de la source à  $x_i$  et des détecteurs à  $x_d$  permettent la détermination du chemin optique pour dissocier les propriétés optiques d'absorption et de diffusion [Zonios et al., 2006].

La technique LFOV MSI utilise une illumination homogène et une détection de la réflectance diffuse résultante sur un large champ (voir Figure 2) et sur un spectre discret, selon les filtres employés. L'absence d'une ouverture confinée des signaux ne permet pas de dissocier les paramètres d'absorption et de diffusion de la lumière. Cependant, si un paramètre est connu, l'autre peut être calculé; par exemple à partir d'une diffusion connue, l'absorption peut être déduite.

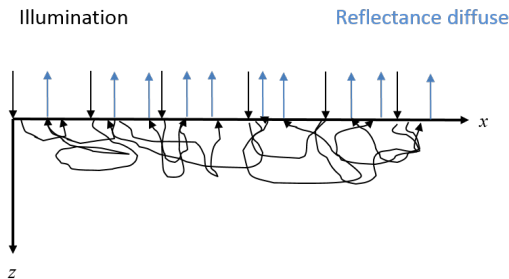


Figure 2: LFOV MSI: Réflectance diffuse résultant d'une illumination homogène qui ne permet pas la détermination du chemin optique pour dissocier les propriétés optiques d'absorption et de diffusion.

Le principe de la technique '*Dual-Step*' que nous proposons permet de quantifier l'absorption avec la LFOV MSI en s'appuyant sur la diffusion estimée par la DRSsr sans-contact.

Ce travail de recherche décrit la construction et la mise en œuvre des montages instrumentaux ainsi que la méthodologie de quantification associée à chacune des techniques composantes (DRS sans-contact et LFOV MSI). La validation des techniques est réalisée sur des fantômes bien caractérisés et sur des échantillons biologiques pertinents de peau humaine *ex-vivo* et de peau de rongeur *in-vivo*. Les résultats obtenus constituent une première étape de validation de la technique '*Dual-Step*' et montrent son potentiel pour le diagnostic clinique.





# 1

---

## Introduction

The general aim of this work is to contribute to the improvement of diagnosis of superficial lesions with the development of a novel quantitative Multispectral Imaging Technique. The use of this technique in medical imaging aspires for the non-invasive quantification of optical properties in a wide field of view. The non-invasive approach of the technique is considered with the use of endogenous contrast for which no external agent is needed (eg. fluorophore or chromophore injection) and a Non-Contact measurement modality. The latter addresses a big advantage for the measurement of sensitive samples such as injured tissue which requires a no-touch and sterile manipulation. The quantification aspect aims to improve the accuracy of diagnosis. Indeed, the correlation of chromophore absorption and scattering properties with biochemical and histological characteristics provides a wealth of information regarding metabolism and tissue composition that can be used to study its physiology and morphology for the early detection and diagnosis of disease. Moreover, fast quantification of a wide field of view through imaging brings many advantages in terms of clinical practice, speed, and cost.

The technique we propose in this work is based on the combination of punctual Non-Contact spatially-resolved Diffuse Reflectance Spectroscopy (DRSsr) and Large Field of View Multispectral Imaging (LFOV MSI).

DRSsr is based on the measurement of diffuse reflectance throughout a spectrum at specific distances from a punctual source (see Figure 1.1) which depends on the optical properties of the medium it traverses. The confined aperture of the punctual illumination and detection signals at different distances allows the derivation of the optical pathlength from which absorption and scattering effects, contributing to the measured diffuse reflectance, can be separately deduced. Thereby, DRSsr can achieve a robust absolute quantification of both absorption and scattering optical properties.

Being a punctual measurement modality, DRSsr inspects a small area which is appropriate to a restricted number of specific clinical applications. Hence, the extension of quantitative measurements to a larger field of view allows the accurate diagnosis in many clinical applications requiring a larger and faster analysis. For this purpose, we propose a combination of punctual quantitative DRSsr with a MSI technique covering a large field of view.

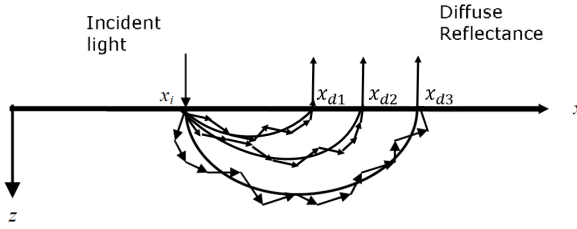


Figure 1.1: DRSr: the confined aperture of the source at  $x_i$  and detectors at  $x_d$  enables the determination of optical pathlength [Zonios et al., 2006].

The LFOV MSI technique uses a homogeneous illumination and detection of the resulting diffuse reflectance on a wide field (see Figure 1.2) throughout a discrete spectrum which depends on the filters used. The lack of confined aperture of the signals does not allow the derivation of the optical pathlength to separate absorption from scattering parameters. However, if one parameter is known, the other can be derived, i.e. absolute absorption quantification is possible if the scattering property is known.

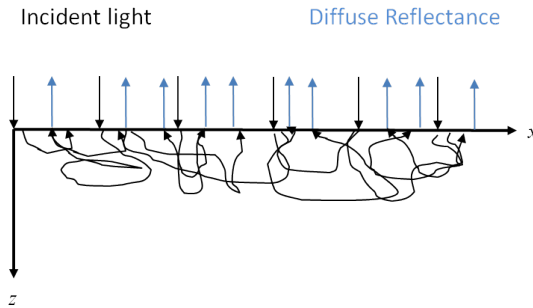


Figure 1.2: LFOV MSI: Diffuse reflectance resulting from homogeneous illumination which makes the determination of optical pathlength untenable.

The principle of the *Dual-Step* technique that we propose achieves absorption quantification from LFOV MSI images based on the scattering quantification provided by Non-Contact DRSr.

This research work presents the development of the instrumental setups and quantification methodology of the combination of Non-Contact DRSr and LFOV MSI. The validation process is performed not only on well-characterized phantoms but also on pertinent biological human *ex-vivo* and animal *in-vivo* skin models. The results obtained establish a first validation stage of the *Dual-Step* and show its potential for clinical diagnosis.

The present work is constructed in different chapters covering the principles, scientific challenges, instrumental and quantification method developments for the validation of the *Dual-Step* technique.

Chapter 2 presents the context of this research work. Theoretical principles are explained together with the state of the art and the targeted biological application. A detailed description of the general scientific challenge is given as well as a clear explanation of the proposition which poses the structural basis upon which the developed technique is built.

Chapter 3 describes the Spatially-resolved Diffuse Reflectance Spectroscopy (DRSsr) technique, which is able to provide quantification of scattering and absorption optical properties throughout the considered spectrum (470-880 nm). Based on the geometry and quantification method of an existing probe-based *Contact DRSsr* technique, two Non-Contact DRSsr setups are built. The probe-based *initial Non-Contact DRSsr* system is integrated into the developed *Dual-Step* technique to perform scattering estimations in a valid 1.2 mm depth of field. A *CCD-based DRSsr* system is also explored because of the advantages it would offer in a perspective integration of the *Dual-Step* technique.

To obtain optimal optical property quantification, the deviation that exists between Non-Contact DRSsr reflectance measurements and modelled reflectance has to be corrected. For this, we developed the Adaptive Calibration Algorithm *ACA-Pro*, described in Chapter 4. *ACA-Pro* is a calibration procedure which is based on the interpolation of correction factors determined with the measurement of a few reference phantoms having known optical properties. Moreover, *ACA-Pro* also allows to correct from instrumental variations, common between different experiments, to increase the robustness of the DRSsr quantification method. The performance of this algorithm is validated for all Non-Contact DRSsr setups on homogeneous phantoms covering a pertinent range of optical properties. Scattering and absorption estimation errors of the *initial Non-Contact DRSsr* system are inferior to 3.3% and 7.6%, respectively, for all phantoms placed at the focal plane. Quantification of optical properties has also been validated on heterogeneous biological tissue samples.

Chapter 5 focuses on the description of the LFOV MSI instrumental setup and the developed method for wide-field absorption quantification based on DRSsr estimations of scattering properties. The absorption quantification is optimized with a correction procedure of the illumination intensity fluctuations and the *ACA-Pro* calibration approach. The validation on homogeneous phantoms achieves absorption errors inferior to 5.3 % within the whole field, optical property range, and for all the wavelengths considered (500, 550, 600, and 700 nm). An intermediate stage between homogeneous phantoms and biological samples, corroborates the wide-field absorption quantification and derived dye concentration maps of a heterogeneous gelatine phantom with different scattering and absorbing inclusions of different shapes.

The combination of the *initial Non-Contact DRSsr* and the LFOV MSI setups is the frame upon which the validation system of the developed *Dual-Step* technique, described in Chapter 6, is built. The setups are connected with a motorized translation

stage on which pertinent samples are measured. Three *ex-vivo* human skin samples are considered: two homogeneous samples of different Phototypes (2 and 5) and a heterogeneous sample with stretch marks. Also, three *in-vivo* rat skin models are examined: a bi-coloured and two different inflammation types showing different absorption and scattering contrasts. Wide-field quantification of optical properties of these samples is validated with the reference *Contact DRSSr* technique.

The general conclusions and further developments to be achieved for the evolution of the developed *Dual-Step* technique towards a valid clinical diagnostic tool are detailed in Chapter 7.

Additional relevant information is given in Appendix A and the Scientific communications that resulted from this work are recapitulated in Appendix B.

# 2

---

## Context

In this work, we focus on an imaging technique based on non-fluorescent endogenous contrast. The latter originates from the internal chromophores that absorb light and autogenous structural arrangement of tissue that scatters light. The methodology analyses both features through the quantification of absorption and scattering optical properties, correspondingly, for which a theoretical explanation is given in the first Section 2.1.

Section 2.2 specifies the biological application of this work and outlines the characteristics of skin tissue, being the chosen biological model. The range of optical properties in skin defines the characteristics of the intralipid phantoms (Section 2.3) that are manufactured for the calibration and validation of the systems developed along this work and explained in the next Chapters.

The nature of photon propagation in a turbid medium, such as that occurring in biological tissue and intralipid phantoms, is described in Section 2.4.

Section 2.5 proceeds by giving details on the existing Spectral Imaging Methods according to the different spectral range, instrumental setups and quantification capacities that enable the understanding of the proposition of this work described in the last Section 2.6.

## 2.1 Light propagation in a biological medium

Biological tissues are complex heterogeneous media with numerous absorbing and scattering structures with different densities, sizes and shapes. Because of its optical inhomogeneity, biological tissue is defined as a turbid medium.

When light photons encounter a turbid medium, they undergo physical interactions of reflection, scattering, and absorption as shown in Figure 2.1.

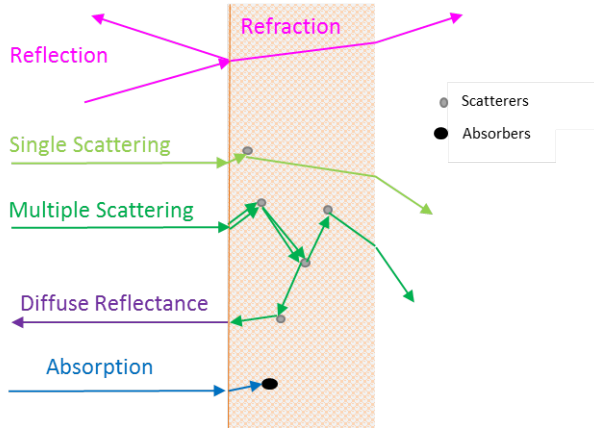


Figure 2.1: Processes of light interaction on a medium: reflection, refraction, absorption, scattering, and diffuse reflectance.

Further details on these processes are given in the following Sections.

### 2.1.1 Reflection and Refraction

Reflection of photons occurs due to a change of refractive index  $n$  between two media which vary in function of temperature and wavelength  $\lambda$ . The difference in  $n$  also leads to refraction by which photons are transmitted in the medium with a change in forward speed and direction. The fractions of reflected and refracted photons are determined by the medium's reflectivity and transmittance, respectively, through the Fresnel equations.

The direction that the reflected or refracted photons take after the collision is described by the Snell-Descartes Law according to their incident angle  $\theta_i$  and the refractive index ratio of the incident medium  $n_i$  and refractive medium  $n_r$  (see Figure 2.2).

Depending on the quality of the interface, Reflection of light is either essentially specular or diffuse. On a very smooth flat surface the organization of the incident ray is retained by the reflected ray, resulting in specular reflection. On an irregular surface, the orientation of the normal lines are no longer parallel resulting in non-parallel diffuse reflected rays.

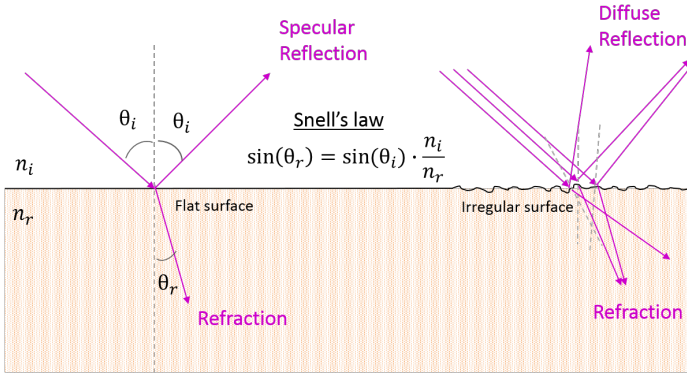


Figure 2.2: Reflection and Refraction of light between two media with  $n_r > n_i$ .

Whilst some incident photons are directly reflected at the surface, other photons, neither absorbed nor scattered, are able to travel through the medium. These are called ballistic photons and can be detected as transmitted light (Transmittance) at the opposite side (see pink arrow of Figure 2.1 traversing the medium).

### 2.1.2 Scattering

Scattering is a process of reflection that occurs when photons encounter a particle (scatterer) with a refractive index  $n$  different to that of the medium producing a deviation of the photon's incident direction. Photons that collide with only one or multiple scatterers undergo simple or multiple scattering, respectively (see green paths of Figure 2.1). Scattered photons that travel through the medium to the opposite side are considered to be quasi-ballistic. Contrarily, some of the photons that experience multiple scattering through the tissue come back to the surface at many different angles and contribute to the Diffuse Reflectance (see purple arrow of Figure 2.1).

Approximately, only 1 photon in a million loses its energy (changes frequency) through inelastic scattering, referred to as Raman scattering. Most of the scattered photons are elastically scattered with no energy loss. Two types of elastic scattering are distinguished depending on the size of the scatterer particle  $p$  with respect to the wavelength  $\lambda$  of the incident wave:

- Rayleigh scattering occurs when  $p < \frac{1}{15}\lambda$  and is strongly  $\lambda$ -dependent.
- Mie scattering occurs when  $p \approx \lambda$  or  $p > \lambda$  and is less strongly  $\lambda$ -dependent.

Figure 2.3 illustrates the scattering patterns under the Rayleigh and Mie regime.

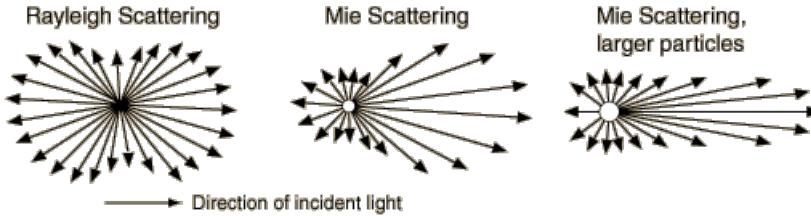


Figure 2.3: Rayleigh and Mie scattering patterns [Nave, 2012].

Scattering can be quantified through four parameters that are strongly dependent on the  $\lambda$  of the incident ray and on the shape, density, and size of the scatterers it encounters.

The first two main parameters are:

1. The scattering coefficient  $\mu_s$  ( $cm^{-1}$ ) is defined as the inverse of the mean free path  $l_s = 1/\mu_s$  (in  $cm$ ), related to the average distance that a photon covers between two scattering events (see Figure 2.5).
2. The phase function  $\rho(\theta)$  is the probability that a photon's direction is deviated by an angle  $\theta$  after a scattering event. It is most commonly approximated by the Henyey-Greenstein function. Depending on the regime (Rayleigh or Mie) and polarization of light,  $\rho(\theta)$  is calculated according to different theories, explained by [Hulst et al., 1957].

From these two principal parameters we can derive other that are particularly useful to quantify multiple scattering events that occur in turbid media:

3. The anisotropy factor  $g$  is defined as the mean value of  $\cos(\theta)$ :  $g = \langle \cos(\theta) \rangle$  and can be derived from the  $\rho(\theta)$ . Depending on the  $g$  value, the scattering is isotropic ( $g = 0$ ) or anisotropic ( $g > 0$ ). Figure 2.4 shows the different most probable volumes through which photons are propagated after a scattering event for different  $g$  values.

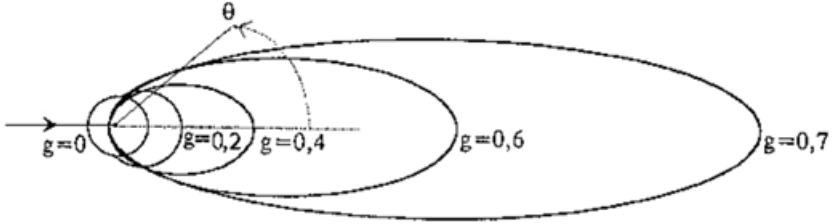


Figure 2.4: Different shapes of the Henyey-Greenstein function for different values of the anisotropy factor  $g$  [Bourg-Heckly et al., 2013].

4. To fully encompass the scattering effects, the reduced scattering coefficient  $\mu'_s$  ( $cm^{-1}$ ) is commonly used.  $\mu'_s$  combines  $\mu_s$  and  $g$  in the form  $\mu'_s = \mu_s(1 - g)$ . It can be said that  $\mu'_s$  describes scattering of photons in terms of bigger isotropic steps of length  $l'_s = 1/\mu'_s$  that consist of small  $l_s$  steps with partial deviation angle  $\theta$ . An example of this relationship is illustrated in Figure 2.5 for  $g = 0.9$ .

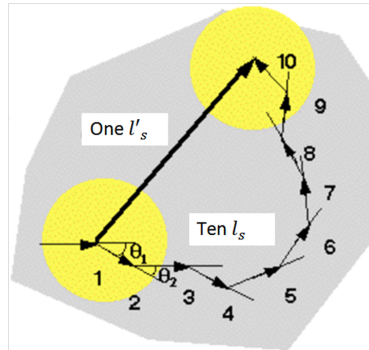


Figure 2.5: Example of the equivalence of 10 anisotropic  $l_s$  steps with a single isotropic  $l'_s$  step for  $g=0.9$  [Jacques et al., 1998].

The reduced mean free path  $l'_s$  is the scattering step length (in  $cm$ ) for which the initial direction of the incident photon has been ‘forgotten’. Thereby, it can be said that there is no effect of individual scattering events on the direction change, which allows scattering to be considered isotropic. This interpretation is particularly useful in the case of the diffusion regime for which  $\mu'_s \gg \mu_a$ , meaning that many more scattering than absorption events occur [Jacques et al., 1998] (refer to Section 2.4).

The diffusion regime commonly dominates light interactions in biological tissues in the visible red and near infrared spectrum [Jacques et al., 1998]. Biological scatterers include intracellular components, such as cell organelles (Golgi apparatus, nucleus, mitochondria, lysosomes...), and extracellular matrix components, such as the collagen and elastin network [Jacques et al., 1998]. The mean size of scatterers is around  $20\text{ nm} - 1\text{ }\mu\text{m}$ , which is close to the wavelength range of the visible-near infrared light ( $0.4 - 0.9\text{ }\mu\text{m}$ ), and therefore defines the prevalence of Mie scattering over Rayleigh scattering processes at this spectral range. The contribution of each type of scattering process depends on the tissue. Some generic spectra of  $\mu'_s$  with different contributions of Mie and Rayleigh scattering have been determined by [Jacques, 2013] and are shown in Figure 2.6.

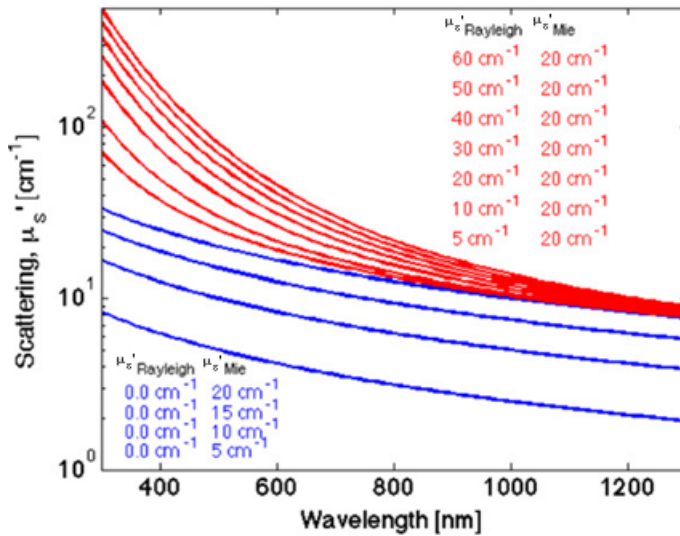


Figure 2.6: Generic  $\mu'_s$  of tissue with different contributions of Mie and Rayleigh scattering. The generic range of Mie scattering alone is illustrated with blue lines and the combination of constant Mie and different levels of Rayleigh is illustrated with red lines [Jacques, 2013].

### 2.1.3 Absorption

From a macroscopic perspective, absorption is explained as the fraction of light intensity loss  $dI$  of ballistic photons having intensity  $I$  and travelling a homogeneous medium of thickness  $dz$ , according to Equation 2.1 and Figure 2.7.

$$dI = I(z_1 + dz) - I(z_1) \quad (2.1)$$

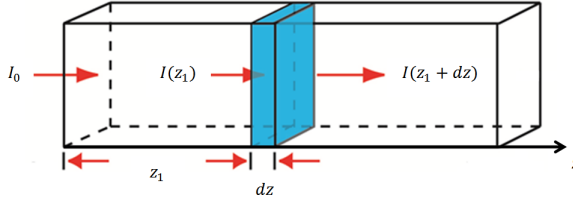


Figure 2.7: Illustration of the intensity absorption  $dI$  by a small layer  $dz$ .

According to Equation 2.1,  $dI$  is also expressed as

$$dI = -\varepsilon \cdot C \cdot I(z) dz \quad (2.2)$$

where  $\varepsilon$  ( $L \text{ mol}^{-1} \text{ cm}^{-1}$ ) is the molar extinction coefficient and  $C$  ( $\text{mol L}^{-1}$ ) is the molar concentration of the molecule present in the medium.

The general Beer Lambert Law, defining the proportion of light transmitted  $I(z)$  is given by Equation 2.3 and illustrated in Figure 2.8.

$$I(z) = I_0 \cdot 10^{-\varepsilon C z} = I_0 \cdot e^{-\mu_a z} \quad (2.3)$$

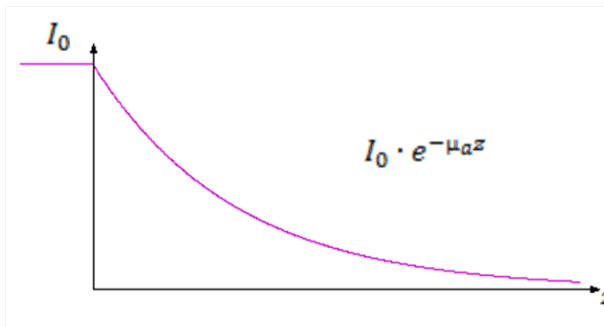


Figure 2.8:  $I(z)$  according to the Beer Lambert Law [Bourg-Heckly et al., 2013].

The absorption of an incident wave at a given  $\lambda$  by a given molecule is quantified through the absorption coefficient  $\mu_a$  ( $\text{cm}^{-1}$ ) that, according to Equation 2.3, is given by Equation 2.4.

$$\mu_a = \ln 10 \cdot \varepsilon \cdot C \quad (2.4)$$

The Beer-Lambert Equation 2.3 can also be defined in terms of absorbance  $A$  (also called optical density  $OD$ ) according to Equation 2.5.

$$A = OD = \log_{10} \frac{I_0}{I} = \varepsilon \cdot C \cdot z \quad (2.5)$$

Combining Equations 2.4 and 2.5 it can be said that

$$\mu_a(\lambda) = \ln 10 \cdot A(\lambda) \quad (2.6)$$

The absorption coefficient  $\mu_a$  is also defined as the inverse of the mean absorption length  $l_a = 1/\mu_a$  being the average distance travelled (in  $cm$ ) by a photon before being absorbed.

Absorption in biological tissue is composed of the individual extinction coefficient at a determined  $\lambda$  of its chromophores, their concentration, chemical composition, temperature and molecular configuration. Common chromophores in biological tissue absorb in the infrared (IR), visible (vis) and ultraviolet (UV) spectral range ([Scott, 1998], [Tuan, 2003]).

In the near infrared (NIR) - IR range, tissue absorption is dominated by that of water, which makes up for 60-80 % of biological tissue. Other biochromes include porphyrins, such as heme that is present in haemoglobin, and pigments, such as melanin present in melanocytes of the epidermis. Absorption of water, haemoglobin and melanin is minimal between 700 - 1200  $nm$ , opening a ‘spectral biological window’ for the detection of melanin-less, water-less and haemoglobin-less baseline absorption of skin [Jacques, 1998] (see Figure 2.9).

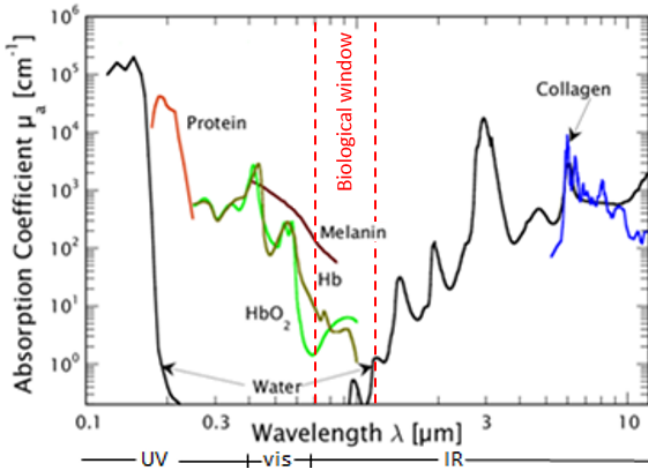


Figure 2.9: Absorption spectra for different biological chromophores of skin in the UV-vis-IR spectral range [Vogel et al., 2003].

In the UV-visible spectrum (400 - 700 nm), oxy-haemoglobin ( $HbO_2$ ), deoxy-haemoglobin ( $Hb$ ) and melanin are the most absorbing chromophores in skin, as illustrated by Figure 2.10.

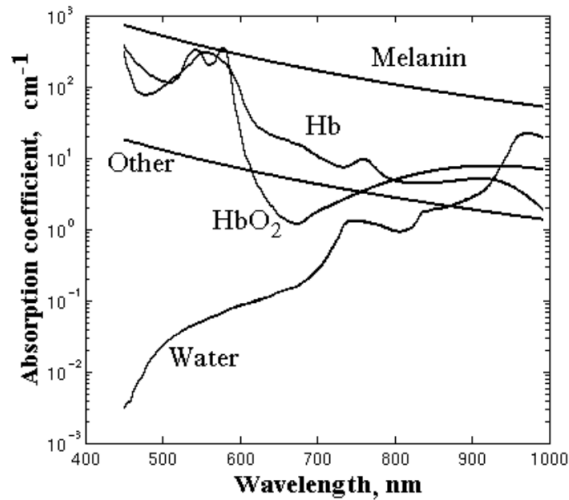


Figure 2.10: Absorption spectra for most predominant biological chromophores of skin in the UV-vis-NIR spectral range. The baseline absorption, proper of the fibrous material, is defined as ‘Other’ [Meglinski et al., 2002].

Therefore, to allow the detection of  $HbO_2$ ,  $Hb$ , and melanin with minimal water absorption, we use the spectral range 470 - 880 nm that has been used in previous techniques developed in our *LISA* laboratory.

These chromophores are present in skin, the chosen biological model, outlined in the next Section 2.2.

## 2.2 Biological Application

The biological application to which we aspire in this work is the wide field quantification of superficial tissue lesions, such as skin lesions and oral cancer.

Our motivation for this application lies in the need for more accurate, fast and non-invasive optical diagnosis techniques capable of differentiating, at an early stage, injured lesions from healthy tissue. For this, it is necessary to accurately detect the main optical differences between healthy and injured tissue including a change in scattering and absorption properties due to necrotic tissue, scarring and vessel oxygen saturation.

As a first proof of concept, we propose to use some skin inflammation models.

To better understand the biological structure of the chosen tissue samples, the following Sections 2.2.1 and 2.2.2 describes the function and histology of skin.

Characteristic optical properties of skin are presented in Section 2.2.3.

### 2.2.1 Function of skin

The skin is the most extensive multifunctional organ, covering the external surface of the body. Its average mean surface area ranges between 1.5 and 2  $m^2$  [Bouslimani et al., 2015] and its thickness depends on the area of the body varying between 1.5  $mm$  (scalp) and 4  $mm$  (back) [Ross et al., 2003].

The main functions of the skin include:

- Protection barrier from mechanical impacts, temperature variations, micro-organisms and chemical.
- Regulation of body temperature via sweat glands, hair and blood circulation.
- Reservoir of Vitamin D
- Sensation of environmental changes through nerve cell receptors for temperature, touch and pain.

### 2.2.2 Histological structure

Skin is made up of three basic layers: hypodermis, dermis, and epidermis (see Figure 2.11).

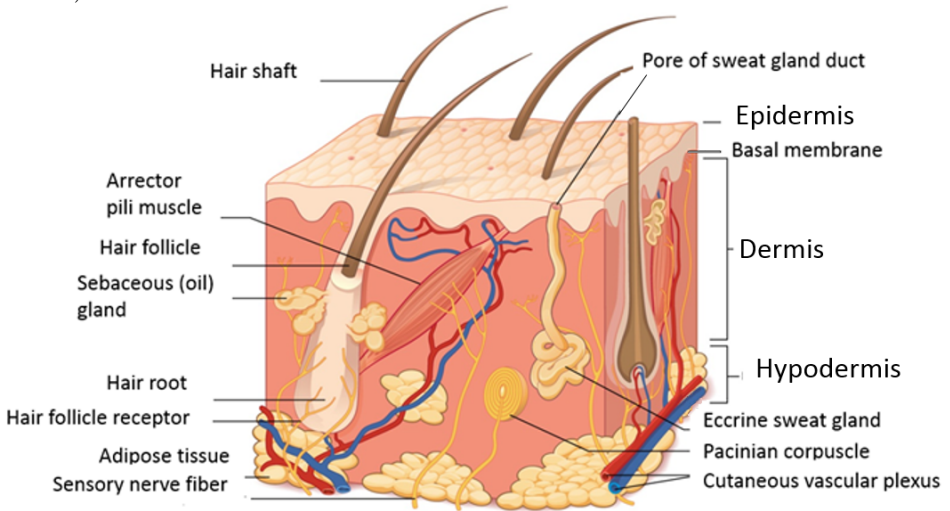


Figure 2.11: Structure of the human skin composed of epidermis, dermis and hypodermis layers [Schatz, 2012].

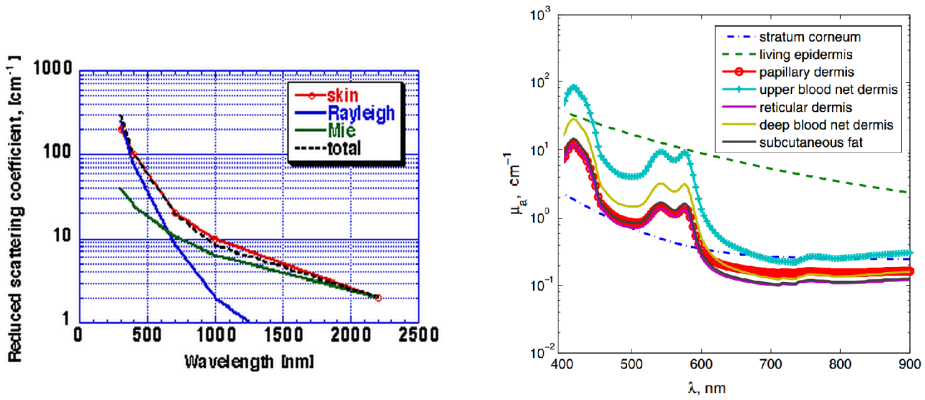
The hypodermis layer (1-6 *mm* thick [Bashkatov et al., 2005]) is basically subcutaneous fat that insulates the body from cold temperatures and provides shock absorption.

The dermis, roughly 1-4 *mm* thick [Bashkatov et al., 2005], consists of a papillary and a reticular layer which serves to provide structure and flexibility to skin. This fibrous network is composed of structural proteins (collagen and elastin), blood and lymph vessels, mast cells and fibroblast cells. The whole structure is surrounded by the ground substance that plays a critical role in the hydration of the skin.

The epidermis is basically made of stratified squamous (flattened) epithelial cells (50-100  $\mu\text{m}$  ([Bashkatov et al., 2005], [Schwarz et al., 2008a]) arranged in layers on top of the basal membrane. The most superficial layer of the epidermis, called the stratum corneum, is composed of extremely flat and dehydrated cells without many of the cellular organelles and filled with keratin. Keratin is a fibrous protein that protects the epithelium and is characterized by high scattering light properties. The skin epithelium is also made up of melanocytes that synthesize the pigment melanin which absorbs light in the UV-visible spectrum. Melanin granules accumulate in the nucleus of cells and screen from harmful UV-A and UV-B radiation from the sun. The amount of melanin produced, gives rise to the different visible skin color tones or phototypes.

### 2.2.3 Optical Properties

General optical properties of absorption and scattering of skin are shown in Figure 2.12.



(a) Reduced scattering coefficient [Jacques, 1998].

(b) Absorption spectrum of different skin layers [Kim et al., 2012].

Figure 2.12: Skin optical properties.

The differences in scattering coefficient between dermis and epidermis are too small to be detected by current spectroscopy techniques [Jacques, 1998]. Therefore, a general scattering coefficient for both epidermis and dermis layers is commonly considered and shown in red in Figure 2.12a. Notice the combined contribution of Rayleigh scattering (in blue) at lower wavelengths by small-scale structures, and Mie scattering (in green) at higher wavelengths by large cylindrical dermal collagen fibres [Jacques, 1998].

Contrarily, absorption properties are significantly diverse at different layers of the skin. Figure 2.12b shows the characteristic absorption spectra of each layer simulated by [Kim et al., 2012]. The high epidermis absorption (dotted green) is due to the melanin chromophore which varies according to the skin phototype. The illustrated upper blood dermis (cyan) regards a 30% of blood volume fraction which is slightly higher than the typical value of 20% according to [Jacques, 1998].

The average refractive index value  $n = 1.37$  is usually used for skin ([Igarashi et al., 2007], [Ding et al., 2006]).

These optical properties define the optical properties range of the intralipid phantoms we used, which are clearly detailed in the next Section 2.3.

## 2.3 Intralipid phantoms

Phantoms with similar optical properties to those of skin (refer to Section 2.2.3) are used to calibrate optical instruments and validate their ability in optical properties quantification. The homogeneous liquid phantoms we used consist of an aqueous solution of distilled water with different concentrations of the following ingredients: fat emulsion scatterer Intralipid 200mg/ml (IL) (Figure 2.13a) to control scattering and black *Rotring* ink (Figure 2.13b) or blue *GUBRA* pigment (Figure 2.13c) to control absorption and model the spectral signature of melanin and haemoglobin, respectively (see Figure 2.14).



(a) Intralipid fat emulsifier. (b) Black *Rotring* ink. (c) Blue *GUBRA* pigment.

Figure 2.13: Main components of intralipid phantoms.

### 2.3.1 Manufacturing Protocol

The first step in the manufacturing of intralipid phantoms consists in mixing distilled water with a determined concentration of black ink or blue pigment. Conventional absorption measurement of the aqueous solution is taken in the spectral range with the Spectrophotometer *Cary 300* [Cary-300, 2015]. The measured absorbance  $A(\lambda)$  is then converted to  $\mu_a(\lambda)$  according to Equation 2.6.

In a second step, after having characterized the absorption, the aqueous-ink solution is mixed with a given concentration of intralipid to control the scattering properties. The average size of particles in the intralipid fat emulsifier is around 250 nm [Whateley et al., 1984], which lies in the range of the visible  $\lambda$ s. Consequently for the chosen spectral range (470-880 nm), the predominating type of scattering of the phantoms is Mie. Remark that, except for the shortest wavelengths, this Mie delineation correlates to the scattering behaviour of skin (see Figure 2.12a). Expected  $\mu_s(\lambda)$  is determined according to [Van Staveren et al., 1991] who used the Mie theory to relate it to the percentage of Intralip  $IL(\%)$  and anisotropy coefficient  $g(\lambda)$ , according to Equation 2.7, where the wavelength  $\lambda$  is expressed in nm.

$$\mu_s(\lambda) = \frac{2.54 \cdot 10^9 \cdot \lambda^{-2.4}}{10} \cdot IL(\%)$$

$$g(\lambda) = 1.1 - (0.58 \cdot 10^{-3} \cdot \lambda)$$

$$\mu'_s(\lambda) = \mu_s(\lambda) \cdot (1 - g(\lambda))$$
(2.7)

For notation simplification purposes, along this report, we will refer to  $IL(\%)$  to describe scattering properties of phantoms and the absorption coefficient  $\mu_a$  will be given at  $600\text{ nm}$  unless stated otherwise. Moreover, the  $\mu_a(\lambda)$  measured with the Spectrophotometer *Cary 300* and the  $\mu'_s(\lambda)$  modelled with the Mie theory are used as the theoretical gold standard:  $\mu_{a,theo}$  and  $\mu'_{s,theo}$ , respectively. These values are used to evaluate the optical properties estimation accuracy of the techniques developed.

### 2.3.2 Selected Optical Properties

Intralipid phantoms covering a large range of  $\mu'_s$  and  $\mu_a$  are manufactured according to the general values of optical properties values of skin shown previously in Figure 2.12.

The chosen reduced scattering coefficient  $\mu'_s$  range lies between  $6.8$  and  $40.6\text{ cm}^{-1}$  at  $600\text{ nm}$ , as illustrated in Figure 2.14a. These values are obtained with  $IL = 0.5 - 3\%$ .

The minimal  $\mu_a$  value of phantoms chosen is  $0.2\text{ cm}^{-1}$  at  $600\text{ nm}$ . Higher absorptions are covered until  $\mu_a = 10\text{ cm}^{-1}$  at  $600\text{ nm}$ . The absorptions of diluted black ink (black curves) modelling the melanin signature for different concentrations and blue pigment (blue curve) modelling the haemoglobin signature, throughout the working spectral range  $480\text{-}870\text{ nm}$ , are illustrated in Figure 2.14b.

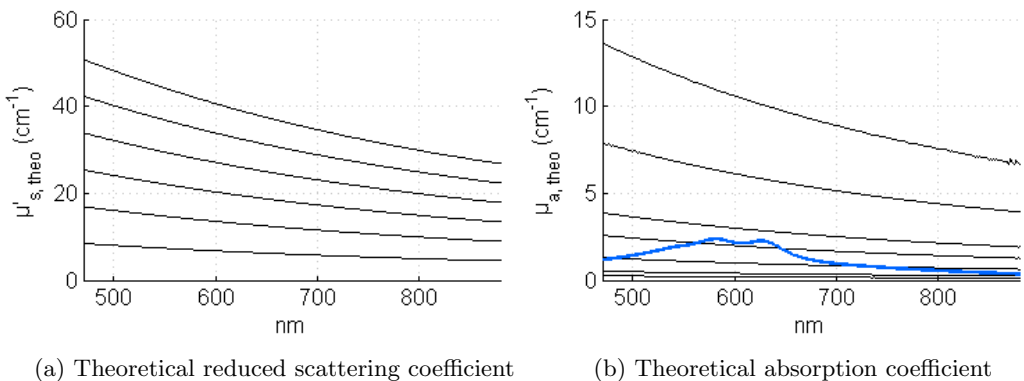


Figure 2.14: Optical properties of all intralipid phantoms with black ink or blue pigment.

In intralipid phantoms and biological tissue, photons undergo multiple scattering and absorption events. Depending on the optical parameters of the medium, the photon propagation regime differs and so does the corresponding solution for the photon transport model, as explained in the next Section 2.4.

## 2.4 Solutions of the Radiative Transfer Equation according to the photon transport regime

Photon transport in turbid medium (eg. biological tissue or intralipid phantom) is modelled by the Radiative Transfer Equation (RTE) that expresses the energy conservation of a collimated beam of radiance ( $Wsr^{-1}m^{-2}$ ) travelling through an absorbing, scattering and emitting medium. Depending on the diffusive propagation of photons three main regimes are defined: the ballistic, the diffusion, and the transition regime.

In the ballistic regime, photons retain their initial direction, according to the laws of geometrical optics, and their decay is governed by absorption, since photons that experience more than a single scattering are no longer ballistic. This decay can be expressed in terms of depth  $z$  by the law:

$$I(z) = I_0 \cdot e^{-(\mu_a + \mu_s)z} = I_0 \cdot e^{-\mu_t \cdot z} \quad (2.8)$$

where  $I_0$  is the initial intensity at depth  $z = 0$ ,  $I_0 = I(z = 0)$ ;  $\mu_t = (\mu_a + \mu_s)$  is the total attenuation coefficient; and its inverse  $l_t = 1/\mu_t$  the transport mean free path. The exponential attenuation poses the major difficulty of optical imaging techniques that detect ballistic photons in the depth of tissues [Bourg-Heckly et al., 2013].

In the diffusion regime, the radiance is considered isotropic when two assumptions are made:

1. Multiple scattering events predominate in the medium ( $\mu'_s \gg \mu_a$ ), as it is the case between 600 and 1100 nm for low biological tissues.
2. The distance travelled by the photons is greater than the reduced mean free path  $l'_s = 1/\mu'_s$ , meaning that the observation point is sufficiently far from sources or boundaries [Wang et al., 2012].

These two assumptions are made by the Diffusion Theory to analytically approximate the RTE.

The decay of photons with depth in the diffusion regime is governed by the effective attenuation coefficient  $\mu_{eff} = [3\mu_a(\mu_a + \mu'_s)]^{1/2}$ , which determines the penetration depth  $\delta_{eff} = 1/\mu_{eff}$  of light in the medium. The fluence rate  $\Phi$  ( $Wm^{-2}$ ), being the radiance coming from all directions on a point, is hence given in terms of depth  $z$  by Equation 2.9.

$$\Phi(z) = B \cdot e^{-\mu_{eff} \cdot z} \quad (2.9)$$

where  $B$  is a constant different from  $I_0$  [Bourg-Heckly et al., 2013].

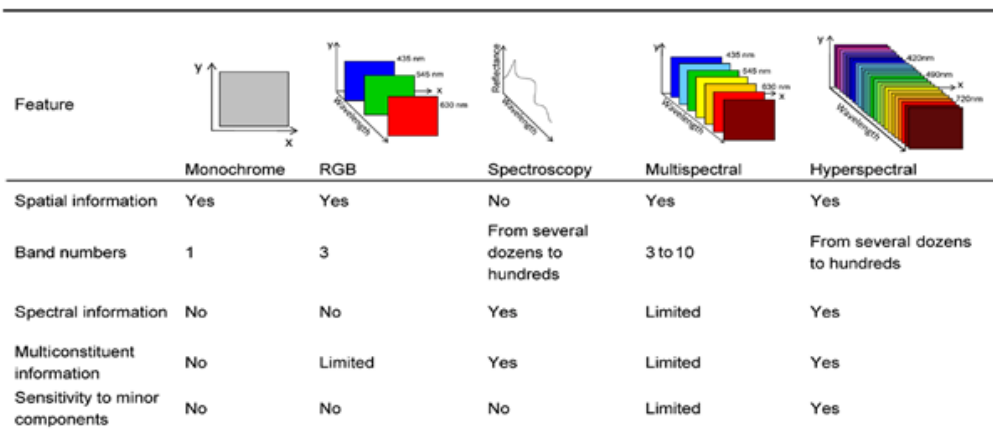
The transition regime, between ballistic and diffusive propagation has an approximate width of several mean free paths and holds valuable information on the nature of scattering [Yaroshevsky et al., 2011]. A numerical solution of the RTE in this regime is achieved through Monte Carlo simulation which, contrarily to the diffusion approximation, makes no assumptions of directional broadening of photons or detection distance. In other words, Monte Carlo simulations are accurate for highly absorbing media and at very close distances from the source ( $< l'_s$ ).

In the first part of this work, we use a Monte Carlo simulation for multi-layered media (MCML) which has been developed in our *LISA* laboratory [Rakotomanga et al., 2015].

These theoretical physical concepts pose the basis upon which quantitative optical technologies are developed. The quantification of spectral imaging techniques, which are the focus of this work, are described in the next Section 2.5.

## 2.5 Spectral Imaging Methods

Spectral Imaging technology has arisen in the biomedical field as a powerful analytical tool because of its capability in providing spectral information in a large field of view, which considerably improves the accuracy and speed of clinical diagnosis. It integrates imaging and spectroscopy to obtain simultaneously 2D spatial and spectral information that are saved in the so called ‘3D-data cube’. This information goes beyond some of the limits of conventional monochrome, RGB imaging or spectroscopy methods, as summarized in Figure 2.15 [Li et al., 2013].



Feature	Monochrome	RGB	Spectroscopy	Multispectral	Hyperspectral
Spatial information	Yes	Yes	No	Yes	Yes
Band numbers	1	3	From several dozens to hundreds	3 to 10	From several dozens to hundreds
Spectral information	No	No	Yes	Limited	Yes
Multiconstituent information	No	Limited	Yes	Limited	Yes
Sensitivity to minor components	No	No	No	Limited	Yes

Figure 2.15: Type of information and resolution provided by the different imaging and spectroscopy techniques [Li et al., 2013].

Depending on the spectral resolution, Spectral Imaging can be categorized into Multispectral or Hyperspectral Imaging. Multispectral Imaging (MSI) uses less spectral band numbers and thereby needs a shorter measurement time than Hyperspectral Imaging (HSI). Thus, we focused on Multispectral Imaging technique.

### 2.5.1 Chosen Spectral Range

The possible spectrum for optical imaging lies in the UV-vis-IR. In this work, we have chosen to work in the vis-NIR spectral range (470-880 *nm*) because it enables the detection of haemoglobin peaks at 545 and 575 *nm* to deduce oxygenation parameters. Moreover, it encompasses a fragment of the ‘spectral biological window’ in which melanin,

haemoglobin and water absorptions are low and the detection of the baseline absorption of skin, proper of the fibrous material, is possible (see Figure 2.10).

### 2.5.2 Spectral Imaging Instrumentation

In the past decades, four different Spectral Imaging modalities, clearly described by [Li et al., 2013] and illustrated in Figure 2.16, have been developed. They are bound to different speeds of spatial or spectral scanning.

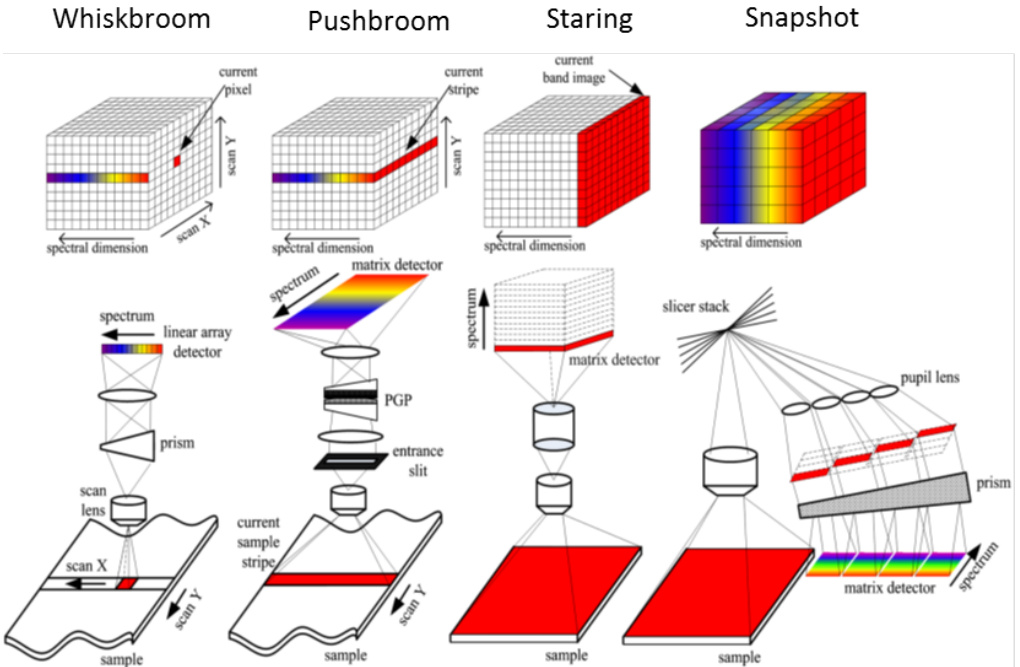


Figure 2.16: Different Spectral Imaging techniques [Li et al., 2013].

The Whiskbroom is the slowest technique since it makes use of punctual spectral measurements that are scanned spatially through the sample. The Pushbroom is an extended and faster version of the Whiskbroom in which a slit (and not a point) with its corresponding spectral information, is spatially scanned through the sample. Spatial scanning of the latter techniques should be well controlled and synchronized to obtain a smooth image. This can be very difficult to achieve in an in-vivo measurement due to motion artifacts. This is why these techniques are mostly used for ex-vivo microscopy.

The Staring is the most straightforward Multispectral Imaging modality in which a monochrome large field of view image is acquired per illumination spectral band. Several bands, which are selected and adapted to the application, are then used to build up the '3D-data' cube. In this case, patient movement can be corrected with a spatial reference present in each monochrome image. Moreover, the integration time is adapted to preserve a good dynamic range. Overall, this modality is the least complex.

The Snapshot is the fastest imaging modality that acquires 3D data cubes in a single exposure with no need of spatial or spectral scanning, unlike the previous modalities. 2D-Images under white (or other combination of wavelengths) illumination are spectrally decomposed to derive each pixel's spectrum through a scanning mirror, an array of lenses, and prisms that have to be well-aligned throughout a complicated manufacturing procedure. Spatial and spectral information are recorded on individual CCD pixels, meaning that the total number of voxels cannot exceed the number of CCD pixels. Therefore, the overall possible spatial and spectral resolutions are smaller than those of other modalities.

To achieve fast diagnosis of a large field of view, this work focuses on the staring MSI technique that provides fast and good resolution of spatial and spectral information of single pixels.

### 2.5.3 Quantification Problematic

To improve the accuracy of clinical diagnosis, the absolute quantification of optical parameters containing information of the biochemical and structural properties is desired.

A simple analysis of the spectral Reflectance provided by the multispectral images can be achieved through the modified Law of Beer-Lambert (Equation 2.10) for which the optical density  $OD$  is expressed not only as a function of absorption, (recall Equation 2.5) but also of scattering of the medium it traverses.

$$OD(\lambda) = \log_{10} \frac{I_0(\lambda)}{I(\lambda)} = \varepsilon(\lambda) \cdot C \cdot L - \beta(\lambda) \quad (2.10)$$

where:

- $I_0(\lambda)$  is the incident light
- $I(\lambda)$  is the detected light as Diffuse Reflectance
- $\varepsilon(\lambda)$  is the  $\lambda$ -dependent extinction coefficient of the absorbing molecule in the medium
- $C$  is the concentration of the absorbing molecule in the medium
- $L$  is the average optical pathlength from the point where photons enter the medium and come out at the surface. It may be thought of as a 'banana -shaped' pathlength between the source and detection points.  $L$  can be expressed in terms of the source-detector distance  $SD$  and the Differential Pathlength Factor  $DPF$  through Equation 2.11.

$$L = SD \cdot DPF \quad (2.11)$$

$DPF$  indicates how many times the distance  $SD$  has been travelled by the detected photons [Scholkmann et al., 2013]. According to the Diffusion Theory, it can be demonstrated that the  $DPF$  depends on the absorption coefficient  $\mu_a$  and the reduced scattering coefficient  $\mu'_s$ .

- $\beta(\lambda)$  is the scattering component that provokes light dispersion due to scattering.

Staring MSI (refer to Section 2.5.2) cannot provide with absolute quantification of optical properties due to the use of non-punctual illumination with no spatial confinement necessary for the determination of  $L$ . Hence, the effects of absorption and scattering properties cannot be separated from the detected diffuse reflectance. This is the origin of the so-called ‘non-uniqueness’ problem which states that for a given reflectance value, an infinite number of possible  $\mu_a$ - $\mu'_s$  couples exists [Arridge et al., 1998]. Therefore, only relative differences of a given optical property between different media can be derived by making suppositions on the other optical property. For example, to obtain relative absorption (or  $OD$ ) contrast, two possible assumptions on the scattering property can be made.

The first assumes the scattering coefficient  $\mu'_s$  (and related  $\beta$ ) to be the same in both media, which allows to express their optical density difference  $\Delta OD$  according to Equation 2.12. Hence, it can then be said that  $\Delta OD$  is proportional to the concentration difference  $\Delta C$  of the molecule of interest (eg. haemoglobin).

$$\Delta OD = \varepsilon \cdot \Delta C \cdot L \quad (2.12)$$

The second fixes the value of  $\mu'_s$  scattering properties to derive a relative quantification of  $\mu_a$  absorption properties. Consequently, the absorption quantification error depends on the accuracy of the fixed  $\mu'_s$ .

Therefore, the scientific challenge of this work lies in the accurate quantification of both optical properties on an image obtained with wide field MSI of a heterogeneous medium (such as tissue) to improve the accuracy of clinical diagnosis.

## 2.5.4 State of the Art according to the Quantification Problematic

Various Multispectral Imaging (MSI) techniques have been developed to improve clinical diagnosis in the last years. We here describe the most relevant works that have helped us to develop the new technique. Table 2.1 at the end of this Section provides an organized summary of the advantages and disadvantages of the different techniques.

Narrow band imaging (NBI) is a form of MSI, first described by [Gono et al., 2004] as an ‘electronic chromo-endoscopy’ technique. Indeed, NBI makes no use of pigments but bases its principle on the invalidation of the red light waves and narrowing of the blue and green spectral bands. The latter are strongly absorbed by haemoglobin which enhances the detailed visualization of patterns in the surface of mucosa and capillary structures (see Figure 2.17). This technique is widely used in cystoscopy [Herr et al., 2011] and gastro-intestinal endoscopy of the colon [East et al., 2008], esophagus [Yoshida et al., 2004] or oral mucosa ([Gono et al., 2003], [Yang et al., 2015]). Even though, this technique improves visual perception of pathological tissue with respect to white-light endoscopy, it achieves no quantification of optical properties. The diagnosis is therefore still subjective as it mainly depends on the experience of the user.



Figure 2.17: Left: Absorption spectrum of haemoglobin. Right: Typical (a) white and (b) narrow band endoscope images of squamous hyperplasia [Yang et al., 2015].

Remarkable work has been done by [Bedard et al., 2013] who developed a non-contact MSI technique under clinical conditions. The established instrument is a Snapshot Spectral Imager that acquires fast images of Reflectance and Autofluorescence between 471-667 nm of a 3-5 cm<sup>2</sup> Field of View (FOV) of the oral cavity. The results obtained (see Figure 2.18) are limited to spectral intensity ratios and fluorescence spectra which are not corrected from absorption distortions. In other words, the lack of absolute quantification of optical properties limits the accuracy of the diagnosis.

Near-infrared (NIR) spectroscopy has been widely used to determine oxygenation-dependent changes in melanin-free tissues. Quantification of these blood concentrations has been achieved through the determination of the optical pathlength of water, being the most significant absorber (apart from haemoglobin) in the NIR range (see Figure 2.10). This methodology is used by [Gussakovsky et al., 2010] in NIR MSI to determine the optical pathlength  $L$  which allows the derivation of myoglobin concentration maps through the first derivative of the modified Beer-Lambert law (see Equation 2.10).

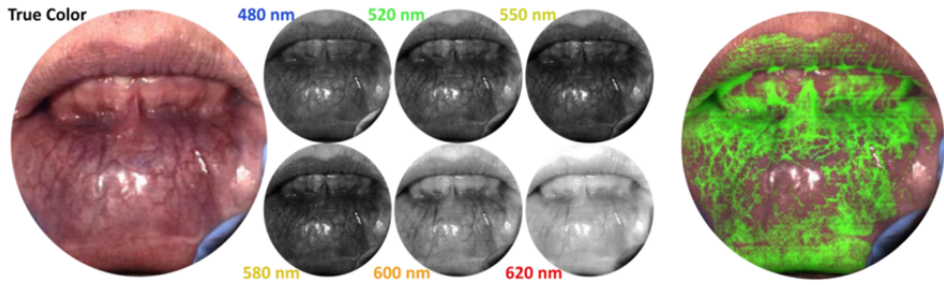


Figure 2.18: Spectral Imaging from the lower lip used to visualize vasculature of different sizes and depths [Bedard et al., 2013].

This is then used to derive an additional oxygenation quantitative map as shown in Figure 2.19. Nonetheless, this technique is restricted to the NIR range since the absorption or optical pathlength for water is negligible in the visible spectral range. Moreover, the technique is not valid for skin since it is limited to melanin-less tissues.

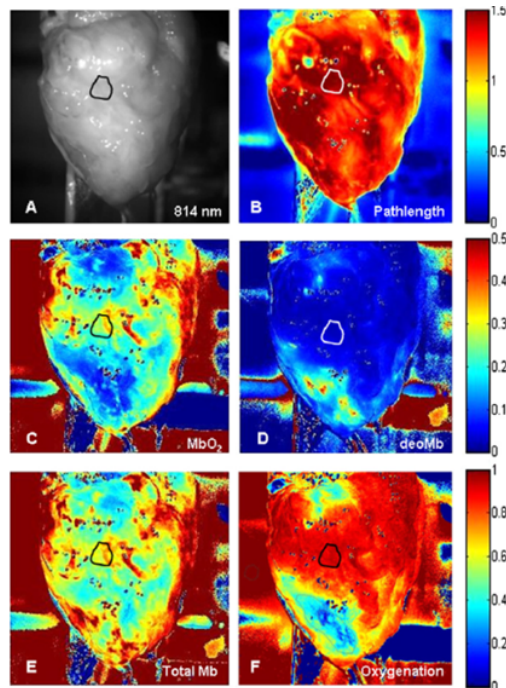


Figure 2.19: (A) Monochrome image of the heart sample; (B) Quantitative maps of (water) optical pathlength; (C) Oxygenated and (D) Deoxygenated myoglobin concentrations (0-0.5mM); (E) Total myoglobin concentration (0-0.5mM); and (F) Oxygen saturation range (0-1). [Gussakovsky et al., 2010].

The principal limitation of homogeneous illumination (as mentioned in Section 2.5.3) is that optical properties cannot be discriminated from a single reflectance measurement. Some groups, such as [Bjorgan et al., 2014], [Basiri et al., 2010], [Vogel et al., 2007] and [Zuzak et al., 2002] have therefore supposed a unique a-priori homogeneous scattering property to obtain relative absorption wide field maps. A similar use of optical scattering specification to quantify absorption changes is done by [Jacques et al., 2010] through the supposition of tissue water content and scattering-dependent variables. However, these techniques are limited by the accuracy of the scattering model and to homogeneous samples. As soon as some scattering heterogeneities exist, absolute absorption estimation error undoubtedly increases. Moreover, the structural information difference given by these scattering heterogeneities that carry valuable diagnosis information is overlooked.

Several Whiskbroom Spectral Imaging setups, have been developed for in-vivo imaging by [Bish et al., 2014] and [Yu et al., 2008] with a compromise between spatial resolution and acquisition time. The techniques spatially scan punctual illumination all throughout the sample. At each point, the diffuse reflectance at a single distance from the source is measured through concentric fibres (see Figure 2.20).

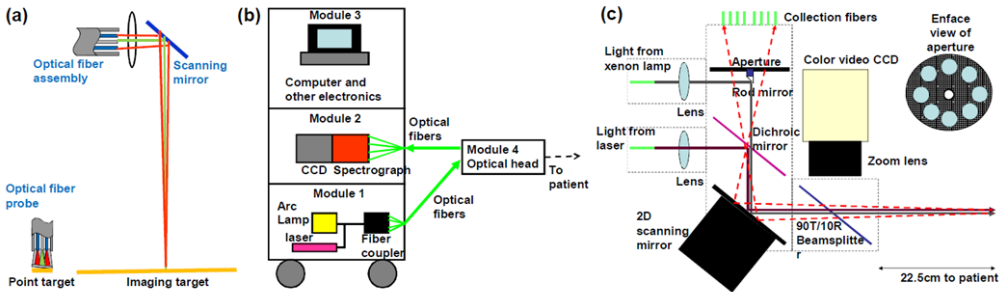


Figure 2.20: (a) Principle of Quantitative spectroscopic imaging. Green beams are illumination and red are collection. (b) Instrument scheme. (c) Schematic of the optical head of the fibre probe [Yu et al., 2008].

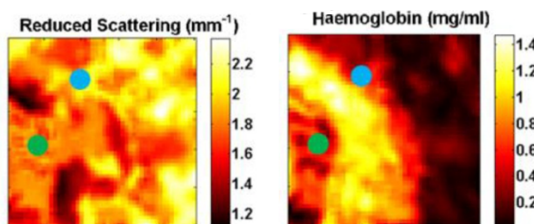


Figure 2.21: Reduced scattering and haemoglobin maps of a Basal Cell Carcinoma. Green and blue points illustrate the position of selected and analysed pixels having different spectral responses [Bish et al., 2014].

This is equivalent to a scanning Diffuse Reflectance Spectroscopy (DRS) technique. DRS technique is based on the spatial confinement of punctual illumination and diffuse

reflectance detection that allows the estimation of the optical pathlength (see Figure 1.1). Hence, the optical properties can be separated and spatially quantified as 2D maps (see Figure 2.21). However, to obtain a smooth ‘3D-data’ cube, this modality requires complex control of the spatial scan and a considerable amount of time which is impractical for clinical applications.

A Multiplexing optical fibre-based tool has been developed by [Nichols et al., 2015] under contact modality for ex-vivo samples (see Figure 2.22). This technique corresponds to a parallel whiskbroom scan that achieves optical properties quantification maps (see Figure 2.23) in a single go, largely reducing acquisition time. However, the system is affected by contact modality limitations such as pressure-dependent coupling.

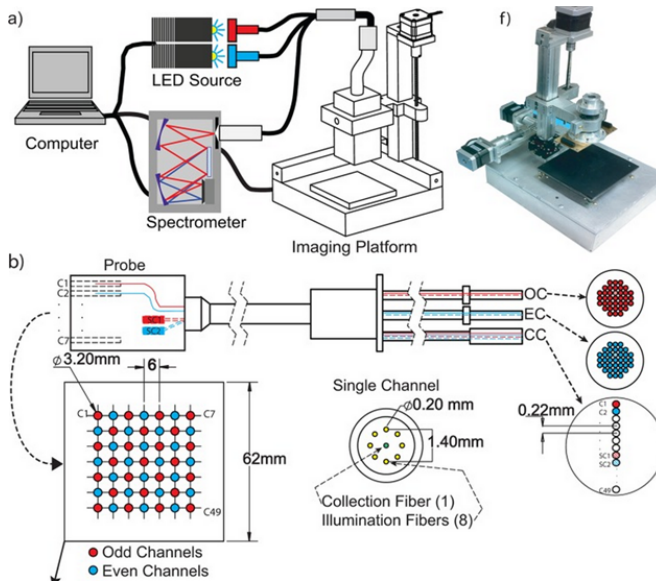


Figure 2.22: Diagram of the Integrated System including a 7x7 grid of fiber optic channels, each of which is comprised of 8 illumination channels and a single central detection. The 49 detection fibres are ordered in a linear array and imaged onto the CCD and spectrograph [Nichols et al., 2015].

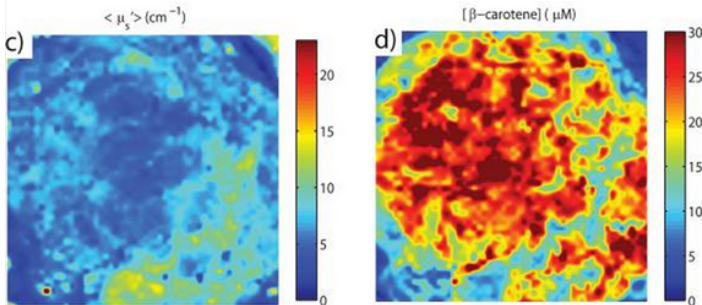


Figure 2.23: Absolute quantitative maps of reduced scattering coefficient and -carotene concentration [Nichols et al., 2015].

A completely new approach of wide field quantification, established in the spatial frequency domain and designated as spatial frequency domain imaging (SFDI), has been developed by [Cuccia et al., 2009]. Figure 2.24 depicts the basic Modulated Imaging platform that is used, including the digital projector that modulates the different illumination spatial frequencies.

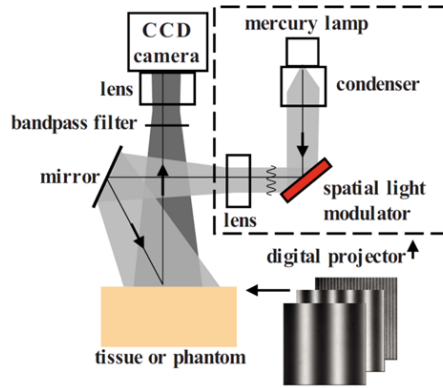


Figure 2.24: Modulated Imaging Instrument platform [Cuccia et al., 2009].

The Fourier transformation of the Diffusion Model derives an expression of diffuse reflectance in terms of illumination spatial frequency. This model is compared to the measurements of diffuse reflectance resulting from the different illumination spatial frequencies to allow the discrimination and wide-field quantification of optical properties. Hence, maps of physiological properties in turbid media can be obtained (see Figure 2.25).

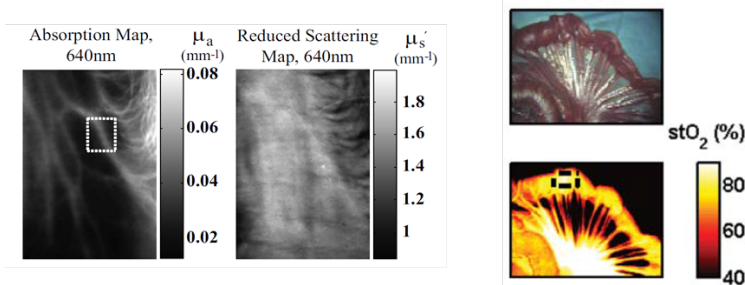


Figure 2.25: Optical property maps and derivation of oxygen saturation in in-vivo samples ([Gioux et al., 2011], [Cuccia et al., 2009]).

The advantages of this technique are many: quantitative scattering and absorption coefficients, inspection of a large field of view, and fast measurement and signal processing, facilitating its use under clinical conditions.

The spatial resolution of optical properties estimated with SFDI has been analyzed by [Laughney et al., 2013] using phantoms with different sizes of inclusions. It was shown that quantification of optical properties depended on the inclusion size. Inclusions

had to present a scattering contrast of at least 28 % to achieve a resolution 1.25 *mm*. Likewise, the absorption contrast had to be of at least 29%, to detect inclusions of 5 *mm* size. This gives an idea of the spatial resolution limit of *SFDI*.

The technique has also been investigated towards a depth resolution of quantified optical properties ([Saager et al., 2011][Laughney et al., 2013][Burmeister et al., 2015]). However, absolute quantitative estimation of optical properties at different depths has not yet been achieved.

Table 2.1: Summary of relevant Spectral Imaging Methods developed to improve clinical diagnosis.

Method	Author	Spectrum	Remarks	Advantages	Disadvantages
NBI	[Gono et al., 2004]	vis	Mainly used in endoscopy	Improves contrast	No absolute quantification
Snapshot MSI	[Bedard et al., 2013]	UV-vis	FOV: 3-5cm	-Fast acquisition -Reflectance and Autofluorescence	No absolute quantification
NIR MSI	[Gussakovsky et al., 2010]	NIR	-Derives $L$ with water absorption in NIR -Used to quantify oxygentation	-Fast acquisition -Absolute quantification	Cannot be used in UV-vis
Relative MSI/HSI	[Bjorgan et al., 2014], [Basiri et al., 2010], [Vogel et al., 2007], [Zuzak et al., 2002], [Jacques et al., 2010]	UV-vis	Fix a general inaccurate scattering coefficient	Fast acquisition	Relative absorption quantification due to inaccurate scattering estimation
<b>Snapshot MSI + Non-Contact DRSSr</b>	<b>This work</b>	UV-vis	Quantify scattering with DRS according to scattering-based segmentation	-Potential for fast acquisition -Absolute quantification	Not optimized instrument
Whiskbroom MSI	[Bish et al., 2014], [Yu et al., 2008]	UV-vis	DRS scan	Absolute quantification	-Not fast -Compromise between spatial resolution and acquisition time -Sensitive to motion artefacts
Parallel Whiskbroom Contact MSI	[Nichols et al., 2015]	UV-vis	- Parallel Contact DRS -Ex-vivo sample	-Fast acquisition -Absolute quantification	Affected by contact pressure-dependent coupling
SFDI	[Gioux et al., 2011], [Cuccia et al., 2009]	UV-vis	Use of structural illumination	-Fast acquisition -Absolute quantification -In-depth inspection	Limitations in terms of spatial distribution and quantification in depth

In summary, the main challenges for optical techniques in the clinical domain include:

- The quantification of optical properties to improve the accuracy of the diagnosis.
- The consideration of a wide spatial field to optimally reduce the measurement time of the region of interest.
- The non-invasive modality of the measurement.

Spectroscopy techniques are capable of quantifying optical properties but are limited to a small region due to their punctual measurement modality. Conversely, Imaging techniques cover a large field of view, reducing acquisition time but provide with a non-quantitative analysis.

## 2.6 Proposition

To deal with the quantification problematic of Spectral Imaging described in Section 2.5.3, this thesis proposes to combine the quantification capacity of Diffuse Reflectance Spectroscopy (DRS) with the spatial wide field of view offered by the staring Multispectral Imaging (MSI) system, to obtain wide field maps of quantitative scattering and absorption optical properties, in the *Dual-Step* technique.

On the one hand, we promote the use of a Non-Contact DRS instrumental setup to perform quantitative and non-invasive measurements convenient for clinical application. On the other hand, we choose the staring modality for the new developed MSI technique because of the various advantages in speed and low complexity it gives for a simple proof of concept.

Similar instrumental combinations have been already developed by [Zeng et al., 2008] and [Kan, 2012] who built endoscopic techniques with wide field imaging and punctual Diffuse, Raman and Fluorescence Spectroscopy to improve the sensitivity and specificity of cancer diagnosis. The punctual DRS measurement is used to measure spectral reflectance differences of individual sites in the imaged field of view. However, no optical property quantification maps are considered.

The principle of the *Dual-Step* technique that we propose goes a stage further with the wide field MSI absorption quantification. The latter is based on estimations of common scattering properties, in specific zones of the imaged sample, with punctual DRS measurements. These DRS estimated scattering coefficients are used to quantify absorption over the whole image. Contrarily to the techniques that suppose a single modelled scattering coefficient and hinder the absolute quantification of absorption coefficient ([Bjorgan et al., 2014], [Basiri et al., 2010], [Vogel et al., 2007],[Zuzak et al., 2002]), our system intends to quantitatively estimate both absolute optical properties over a wide field of view.

We describe the quantitative DRS technique in the next Chapter 3 and the MSI technique in Chapter 5. The coupling of both into the proposed *Dual-Step* technique is clearly outlined in Chapter 6.



---

# Spatially Resolved Diffuse Reflectance Spectroscopy

The Dual-Step technique that we develop in this work aims to provide wide-field quantitative maps of scattering and absorption properties through non-contact measurements. This allows to address speed (covering of a wide field), accuracy (absolute quantification of optical parameters), and non-invasiveness (non-contact measurement of endogenous contrast) which are remarkable benefits for clinical diagnosis.

Considering the quantification ability of Diffuse Reflectance Spectroscopy (DRSsr) and the wide field covered by Multispectral Imaging (MSI), we propose a Dual-Step technique coupling both approaches. The basic principle of the proposed technique implicates the initial estimation of scattering with DRS, which consequently allows absolute wide field quantification of absorption with MSI.

This Chapter focuses on the development of a non-contact modality of DRS to be coupled with MSI (refer to Chapter 5) in the Dual-Step technique (Chapter 6).

Section 3.1 introduces the theoretical principles of DRS and the more accurate spatially-resolved Diffuse Reflectance Spectroscopy (DRSsr) technique.

A pre-existing Contact DRSsr instrument, explained in Section 3.2, poses the reference instrumental geometry and the quantification method we use. The new Non-Contact DRSsr setups which are developed are directly compared to this reference Contact DRSsr system for validation and rigorous quantitative performance evaluation. The new developed DRSsr setups include the *initial Non-Contact probe-based DRSsr* and the *CCD-based Non-Contact DRSsr*.

The *initial probe-based Non-Contact DRSsr* setup, used for the coupling in the Dual-Step technique developed in this thesis, is fully described in Section 3.3.

The *CCD-based Non-Contact DRSsr* setup (described in Section 3.4) is developed for the advantages it would offer in a perspective Dual-Step instrument integration. To allow its use, the separation of illumination and detection paths is first tested with a preliminary *folded Non-Contact DRSsr* setup.

The chain of optical components of the developed Non-Contact DRSsr setups pose new methodological and instrumental challenges that have to be considered to allow

quantification of optical properties (Section 3.5).

Methodological challenges arise because the optical components of the Non-Contact setups spectrally alter signals and spatially extend the projection of rays. The latter poses the biggest challenge for the quantification of optical properties (Section 3.5.1), which is thoroughly examined and overcome through an Adaptive Calibration Algorithm *ACA-Pro* described in Chapter 4.

The main instrumental distinction is the sensitivity of Non-Contact DRSsr to the focal plane, which is quantified through optical properties estimation errors and corresponding depth of field (DOF) (Section 3.5.2). As a matter of fact, the quantification of scattering defines a convenient DOF of the *initial Non-Contact DRSsr* setup used in the Dual-Step technique.

Section 3.6 summarizes the characteristics and challenges posed by the developed Non-Contact DRSsr setups.

## 3.1 Spatial Resolution of DRS for optical properties quantification

### Diffuse Reflectance Spectroscopy

Diffuse reflectance consists of photons that propagate into the tissue without being absorbed and that reach the surface after having experienced multiple scattering (see Section 2.1.2). Diffuse Reflectance Spectroscopy (DRS) measures throughout the spectrum this diffuse reflectance that depends on the tissue's optical parameters of absorption  $\mu_a(\lambda)$  and reduced scattering  $\mu'_s(\lambda)$ .

Some authors claim it is possible to decouple optical properties with the detection of diffuse reflectance at a single distance. This is done with an extensive calibration of the model proposed by [Zonios et al., 2006] or an iterative estimation process used by [Palmer et al., 2006] (see Figure 3.1a).

The methodology proposed by [Zonios et al., 2011] develops a Diffusion model based on experimental correction factors obtained through an extensive study of calibration phantoms. Although straightforward, the model is constrained to the optical properties range used in the empirical study of phantoms. Moreover, the model is limited to haemoglobin as being the only absorber that contributes to the estimated wavelength-dependent absorption coefficient. Other research groups [Yu et al., 2008] and [Bish et al., 2014] rely on this model to obtain quantitative estimations.

[Palmer et al., 2006] introduces an iterative methodology that adjusts an initial prediction of optical parameters. These input parameters are used to generate the modelled reflectance to which the measured reflectance is compared. The free parameters are iteratively updated until the error between model-measurement is minimized. The convergence to a global minimum is ensured through the repetition of the process for several randomly chosen starting optical parameters.

### Diffuse Reflectance Spectroscopy with spatial resolution

Alternatively, Spatially Resolved DRS (DRSsr) improves the estimation accuracy

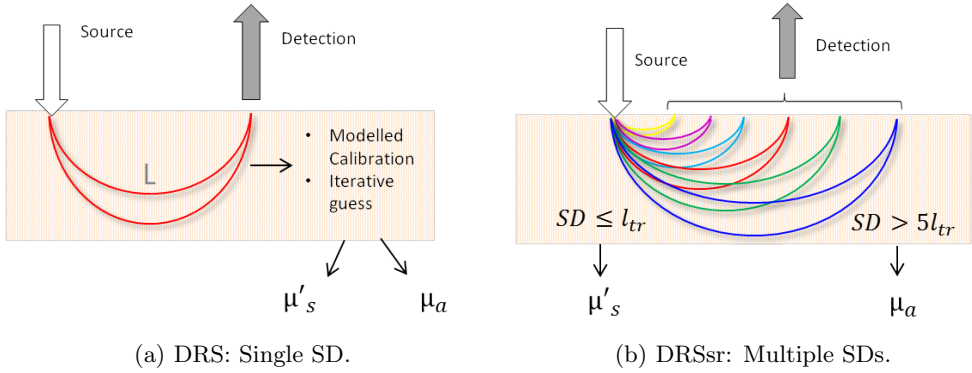


Figure 3.1: DRS with single or multiple SDs for diffuse reflectance.

and dynamic range by detecting diffuse reflectance at numerous distances and using those for which the optical parameters are most sensitive [Kim et al., 2010] (see Figure 3.1b). This allows the use of a single phantom to calibrate the measured reflectance and requires no extensive iterative procedure. Indeed, it is known that diffuse reflectance signals close and far from the light source have different sensitivities to the medium's optical properties. For instance, at distances smaller than one transport length  $l_{tr} = 1/(\mu_a + \mu'_s)$ , reflectance strongly depends on the scattering properties, phase function, and anisotropy factor but is weakly conditioned by absorption ([Venugopalan et al., 1998], [Bevilacqua, 1998],[Bays et al., 1996]). On the contrary, larger distances ( $> 5l_{tr}$ ) measure a reflectance that has a high dependence on absorption and minimal dependence on scattering interactions [Venugopalan et al., 1998].

The use of the different detection distances allow a precise separation of absorption and scattering contributions to the measured reflectance and thus, absolute quantification of optical properties.

These principles build the foundation of DRSsr, for which measurements of diffuse reflectance are taken at various identified distances from the source and calibrated from the instrumental effect to separate and quantitatively determine absolute optical properties.

This thesis is therefore based on the DRSsr technique to optimally quantify optical properties.

## 3.2 Existing *Contact DRSSr* system

A well-established *Contact DRSSr* system has been developed in the last years at the Laboratory of Imaging and Acquisition Systems (LISA) of the CEA-LETI. This instrument is capable of determining optical properties of absorption and scattering of a small volume through contact punctual measurements in the spectral range 470-880  $nm$ .

The applications it has been used for, cover a large range of topics: analysis of skin irritation induced by the tuberculosis test [Koenig et al., 2013], measurement of haemoglobin to aid the diagnosis of anemia, deduction of skin ageing [Roig et al., 2013], and skin complexion [Planat-Chrétien et al., 2016] for cosmetology. Figure 3.2 shows an example of the instrumental setup for comfortable in-vivo measurement of skin inflammation to aid the diagnosis of tuberculosis.

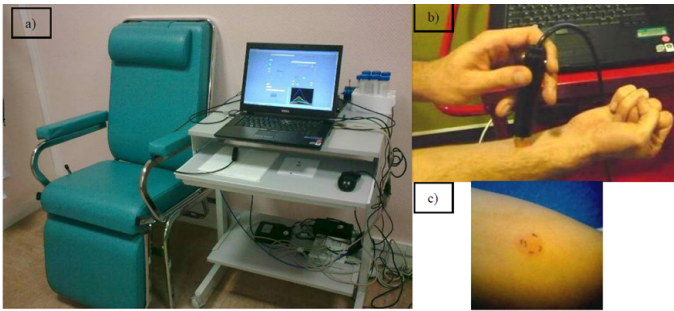


Figure 3.2: Optical Setup installed at the hospital for in-vivo skin measurements [Koenig et al., 2013].

The existing DRSSr technique operating under contact conditions, is the foundation of the DRSSr systems developed in the context of this thesis. This Section describes in detail the *Contact DRSSr* instrument and related analysis method that fix the framework of geometrical instrumental dimensions (Section 3.2.1) and methodology procedure (Section 3.2.4) for the developed Non-Contact DRSSr systems described in the next Sections 3.3 and 3.4.

### 3.2.1 Instrumental Setup

Figure 3.3 schematically illustrates the contact measurement setup and the distal end of the *Contact DRSSr* probe. A Tungsten Halogen (T-H) Lamp *HL2000 Ocean Optics* is used as the illumination source. The spectrometer detector used is the *QE65000* from *Ocean Optics* which is cooled down to  $-15^{\circ}C$  to reduce dark noise.

Light from the source follows two paths. The first enables a direct measurement of the illumination spectrum. The second conducts light to the sample through the central illumination / excitation fibre of the probe. Resulting diffuse reflectance is measured by the same probe featuring concentric detection fibres at 6 different distances  $D$  from the central excitation fibre (source-detector distances SD), ranging from 300- 2488  $\mu m$  centre-to-centre (see Figure 3.4). These detection fibre rings are referred to as  $F6 - F1$ , with  $F6$  and  $F1$  being the closest ( $D6$ ) and furthest ( $D1$ ) ring, respectively, from the



central Excitation fibre  $E$ . Correspondingly, the general reflectance signal  $S$  measured by the fibres are referred to as  $S_6 - S_1$  and  $S_{source}$  is the source signal injected by the fibre  $E$ .

The diameters (with no fibre coating) of the excitation fibre  $E$  and detection fibres  $F1 - F6$  are  $500 \mu\text{m}$  and  $100 \mu\text{m}$ , respectively (see Figure 3.4). The seven detection fibres of each concentric ring are grouped into a single fibre bundle at the proximal end of the probe (see Figure 3.3). The six fibre bundles, appertaining to individual concentric ring groups  $F1 - F6$ , are arranged in a line together with the fibre directly connected to the source through the first path. Figure 3.5 shows the arrangement of the fibres at the proximal end to allow a step-wise measurement of each  $SD$  signal by the spectrometer.

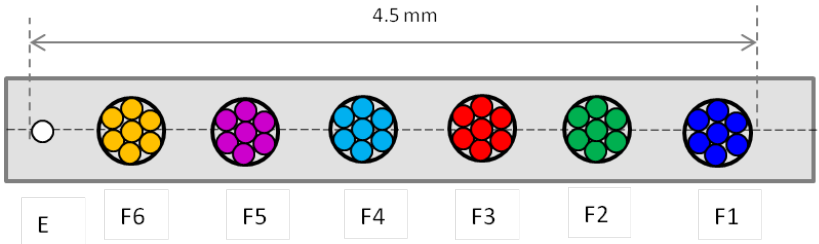


Figure 3.5: Arrangement of fibres at the proximal end of the probe.

The motorized translation table positions the individual fibre bundles ( $SDs$ ) in front of a slit (see zoom of Figure 3.3). For each position, the signal is transmitted to the spectrometer through the slit. In this way, the spectrometer measures the diffuse reflectance at all  $SD$  distances individually and sequentially (see Figure 3.7a).

### 3.2.2 Measurement Procedure

Before taking measurements, a geometrical alignment process is performed. This consists in finding the positions of the motor for which the center of each fibre bundle (see Figure 3.5) is aligned in front of the slit. To do so, a lambertian reflecting white material is placed around the probe, as shown in Figure 3.6a. Light from the source  $E$  is consequently reflected onto fibres  $F6 - F1$  with similar intensity. The intensity is constantly measured by the spectrometer whilst the slit-motor sweeps all distances of the proximal end of the probe. The maximal detected signal determines the centre position of each fibre bundle that are saved into a position file and fixed all throughout the experiment.

After fixing the motor positions that align the center of the fibre bundles with the slit, DRSr measurements are acquired by placing the probe in contact with the sample/phantom. The container of the phantom (see Figure 3.6b) is large enough to ensure that no parasite reflections from its walls pollute the measurements at its centre. No significant difference is noticed in the measurements when the probe, inside the phantom, is inclined or moved slightly around the centre of the container. We supposed that the intralipid phantoms are overall homogeneous. As studied by [Foschum et al., 2015], this supposition is only valid if the fresh phantoms are uniformly shaken to avoid the formation of superficial cream layer having different optical properties. Therefore, in our

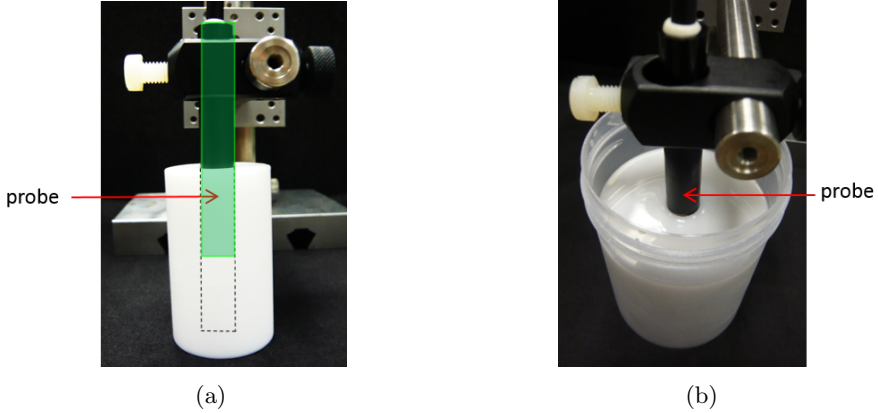


Figure 3.6: (a) Lambertian material surrounding the probe for geometrical calibration (b) Intralipid phantom in container of 5 cm in diameter and 8 cm in height.

measurement protocol, a manual positioning of the probe inside the shaken phantom is enough. Yet, special attention is required to ensure that no air bubbles are present between the probe and the phantom that alter the coupling (through the refractive index  $n$ ) and deteriorate measurements.

Integration time  $t$  of each signal  $S_1 - S_6$  is adapted to the dynamic range of the spectrometer. Figure 3.7a shows an example of the signals  $S_1 - S_6$  measured by  $F_6 - F_1$  bundles and the first illumination path arranged at the proximal end of the probe. Measurements are taken on a phantom having  $\mu_{a,theo} = 0.4 \text{ cm}^{-1}$  at 600 nm and  $IL_{theo} = 1\%$  ( $\mu'_{s,theo} = 13.5 \text{ cm}^{-1}$  at 600 nm according to Equation 2.7).

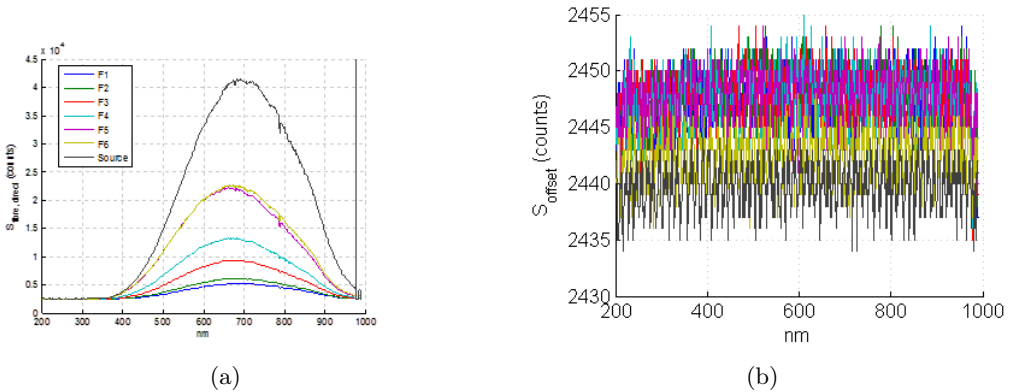


Figure 3.7: (a) Raw signals  $S$  appertaining to fibre bundles  $F_1 - F_6$  and  $S_{source}$ . For  $S_1 - S_5$   $t = 1200 \text{ ms}$ , for  $S_6$   $t = 400 \text{ ms}$ , and for  $S_{source}$   $t = 10 \text{ ms}$ . The measured phantom has  $\mu_{a,theo} = 0.4 \text{ cm}^{-1}$  at 600 nm and  $IL_{theo} = 1\%$ . (b) Instrumental offset  $S_{offset}$ .

Constant ambient darkness conditions are kept all throughout the procedure. Offset measurements for each fibre ring ( $F1 - F6$ ) are taken with no source signal at the same  $t$  and denominated  $S_{offset}$  (see Figure 3.7b).

### 3.2.3 Signal Processing

Signal processing is performed in two steps. First, the raw reflectance signal  $S$  is corrected from the additive offset signal  $S_{offset}$  and scaled according to the integration time  $t$  (see Equation 3.1). Figure 3.8a shows an example of the resulting corrected signals  $S_c$  and  $S_{c,source}$  on the working spectral range 470-880 nm.

$$S_c = \frac{S - S_{offset}}{t}, \quad S_{c,source} = \frac{S_{source} - S_{offset}}{t} \quad (3.1)$$

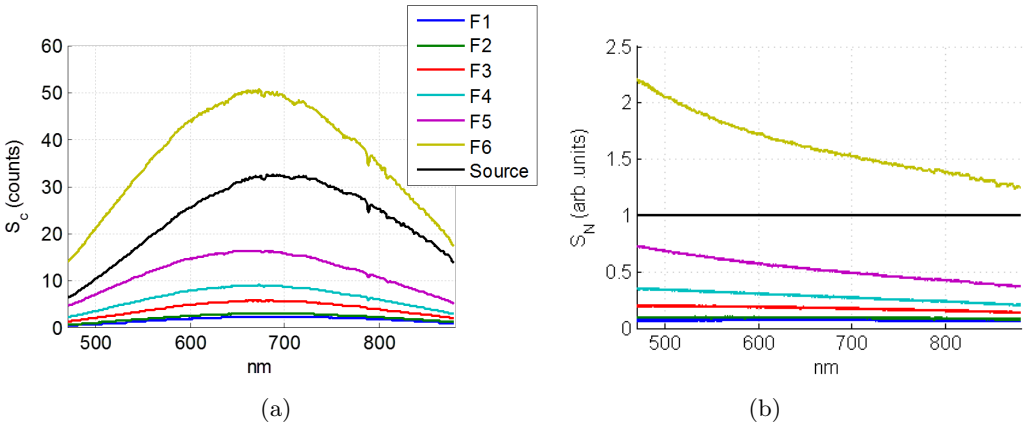


Figure 3.8: (a)  $S_c$  and  $S_{c,source}$  signals resulting from offset subtraction and  $t$  scaling. (b)  $S_N$  signals obtained by normalizing  $S_c$  with  $S_{c,source}$ .

Subsequently, the spectral temporal variations of the source and the constant spectrometer detector response are corrected. To do so,  $S_c$  from  $F1 - F6$  are normalized from the source excitation measurement  $S_{c,source}$  deriving the normalized signal  $S_N$  (see Equation 3.2).  $S_N$  is illustrated in Figure 3.8b.

$$S_N = \frac{S_c}{S_{c,source}} \quad (3.2)$$

Note that the measured fluctuations of the source (see Figure 3.9), corrected through Equation 3.2, remain small. Average relative errors are lower than 1.5% for periods of about 7 hours.

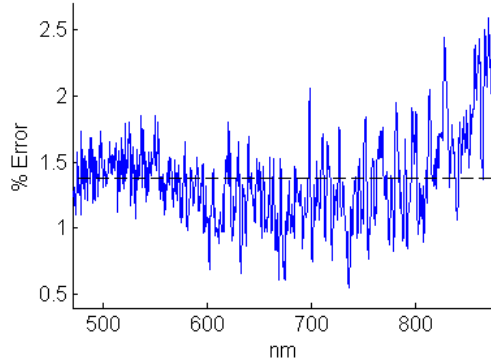


Figure 3.9: Maximum relative error calculated with several measurements of source intensity during 7 hours.

### 3.2.4 Method for the Derivation of Optical Properties

Optical properties are derived from a comparison between a modelled reflectance from a medium, with a wide range of known optical properties, and the calibrated measured reflectance (see Figure 3.10). The modelled reflectance is determined with the forward model through the solution of the radiative transport equation RTE (refer to Section 2.4). The inverse model is in charge of fitting the reflectance measurements to the reflectance model, i.e., finding the modelled reflectance value which better corresponds to the measured reflectance. Thereby, the optical properties of the chosen modelled reflectance value are the estimated optical properties  $\hat{\mu}_a$  and  $\hat{\mu}'_s$  of the measured sample.

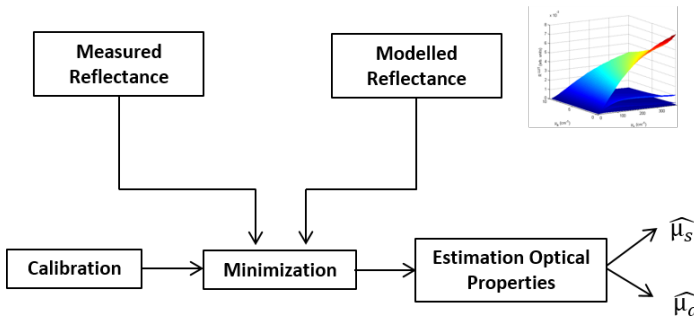


Figure 3.10: General stages for the determination of optical properties.

In the following Paragraphs, we explain in detail the forward model, the instrumental calibration procedure of measurements, and the inverse model that we have used for fitting to estimate optical properties.

### Forward model: Monte Carlo Simulation

A Monte Carlo simulation is used as a solution of the radiative transfer equation (RTE) (see Section 2.4) because it is valid for the highly absorbing samples we use and at the very close SD distances ( $D6$ ,  $D5$ , and  $D4$ ), which are smaller than the typical value of  $l'_s = 1 \text{ mm}$  in biological tissue.

The Monte Carlo simulation we use models photons reaching the medium's surface with no inclination angle, travelling through the semi-infinite medium and measured back at the surface as reflectance, under contact conditions. The geometrical features of the simulation correspond to the *Contact DRSSr* probe according to Figure 3.4 and the numerical aperture 0.22 of the illumination and detection fibres. The range of optical properties considered in the simulated medium is  $\mu_a \in [0.05, 25] \text{ cm}^{-1}$  and  $\mu_s \in [10, 400] \text{ cm}^{-1}$  covering that proper to all evaluated phantoms and skin measurements. The original step size of the LUT is reduced to  $0.2 \text{ cm}^{-1}$  for  $\mu_s$  and  $0.01 \text{ cm}^{-1}$  for  $\mu_a$ , to reduce the numerical error due to sampling and improve the estimation precision (refer to Appendix A.1.1).

A constant anisotropy factor  $g = 0.8$  throughout the spectrum is used and its wavelength dependence is considered in a further scaling procedure, as described further. The refraction index of the refraction medium  $n_r$  is set to 1.37, proper of skin (see Section 2.2.3). The refraction index of the incident medium  $n_i$  is set to that of silica (material of the probe) and equal to 1.45.

The resulting simulated reflectance  $R^{LUT}$  is saved under a look up table (LUT) which is used for comparison and data fitting with the measured normalized signal  $S_N$ . Figure 3.11 summarizes the forward model for which the Monte Carlo simulation calculates  $R^{LUT}$  according to the considered parameters:  $\mu_a$ ,  $\mu_s$ , and  $SD$  distance ( $D1 - D6$ ).

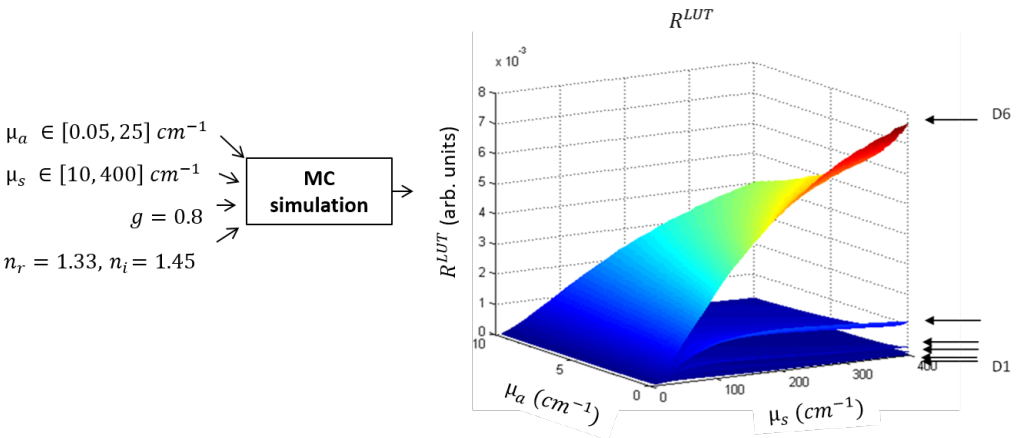


Figure 3.11:  $R^{LUT}$  built from Monte Carlo simulated reflectance for a given range of  $\mu_a$  and  $\mu_s$ .

Before fitting measured reflectance to  $R^{LUT}$ , it has to be calibrated from the instrumental effect as explained in the next Paragraph.

### Instrumental calibration

The multiplicative instrumental effect on the detected signals includes the response functions of individual components, such as fibres or spectrometer detector response, and the emission spectrum of the source. The existing method corrects the normalized signal measurements  $S_N$  from the constant instrumental multiplicative effect through a calibration signal  $S_{N,ref}$ , measured on a reference phantom for which optical properties are known. This method is valid only if the measured reflectance signal  $S$  and  $S_{ref}$  of unknown and reference phantoms, respectively, are taken under the same instrumental conditions, meaning that the instrumental effect remains constant between the two measurements.

To derive the correction factor  $CF$  for instrumental calibration, the simulated reflectance corresponding to the reference phantom  $R_{ref}^{LUT}$  is needed.  $R_{ref}^{LUT}$  is derived from  $R^{LUT}$  with the reference optical properties  $\mu_{a,ref}$  and  $\mu_{s,ref}$  which are the theoretical properties  $\mu_{a,theo}$  and  $\mu_{s,theo}$ , respectively, of the reference phantoms (refer to Section 2.3) at a given wavelength  $\lambda$ . Figure 3.12 depicts the determination of  $R_{ref}^{LUT}$ .

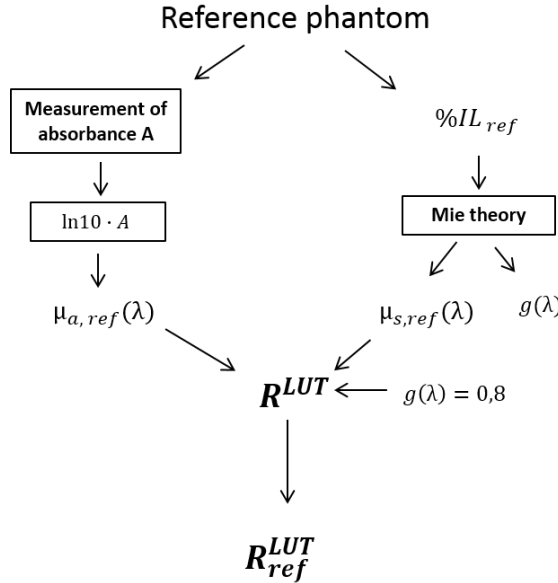


Figure 3.12: Derivation of  $R_{ref}^{LUT}$  from the Monte Carlo simulation.

Knowing  $R_{ref}^{LUT}$ , the correction factor  $CF$  is derived according to Equation 3.3.

$$CF = \frac{R_{ref}^{LUT}}{S_{N,ref}} \quad (3.3)$$

$CF$  is calculated for each wavelength  $\lambda$  and source detector distance of rings  $F6-F1$ .  $CF$  considers the discrepancy between measured and modelled reflectance, including not only the model approximation but also the multiplicative instrumental effect like the spectral response function of fibres and the inequality in simulated and experimental

source power. Figure 3.13 depicts an example of a  $CF$  calculated with a reference phantom having reference optical properties  $\mu_{a,ref} = 0.4 \text{ cm}^{-1}$  at  $600 \text{ nm}$  and  $IL_{ref} = 1\%$ .

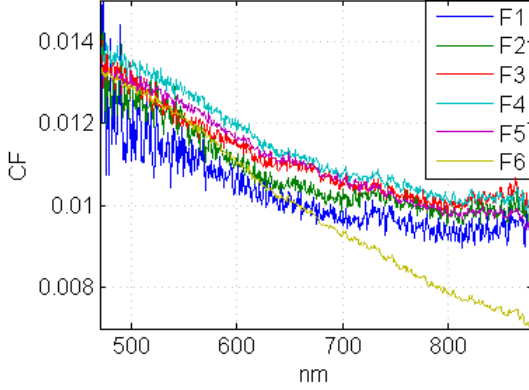


Figure 3.13: Correction Factor  $CF$  used for the instrumental calibration.

Notice that the  $CF$  of the closest fibre F6, being the most sensitive to the scattering effect, is the most different. This is most probably related to the scattering Mie theory approximation error at larger wavelengths, discussed further in Section 3.2.6.

To calibrate  $S_N$  from the instrumental setup, the product with  $CF$  is computed according to Equation 3.4 which results in the corrected measured reflectance  $R_{CF}$ .

$$R_{CF} = S_N \cdot CF \quad (3.4)$$

### Fitting procedure with inverse model

The calibrated measured reflectance  $R_{CF}$  is fitted to  $R^{LUT}$  to estimate the unknown optical properties at each wavelength  $\lambda$ . For this purpose, the difference  $\Delta$  is calculated between  $R_{CF}$  (at each  $\lambda$ ) and all  $R^{LUT}$  for different distances  $D$  according to Equation 3.5.

$$\Delta(\mu_a, \mu_s) = R^{LUT}(\mu_a, \mu_s) - R_{CF} \quad (3.5)$$

The Euclidian Norm of  $\Delta$ ,  $\Delta_{Norm}$ , is then obtained according to Equation 3.6.

$$\Delta_{Norm}(\mu_a, \mu_s) = \sqrt{\sum_{S_i} \left[ \Delta(\mu_a, \mu_s) \right]^2} \quad (3.6)$$

where  $S_i \in S3 - S6$  for  $\mu_s$  estimation and  $S_i \in S1 - S5$  for  $\mu_a$  estimation. These signals  $S$  are chosen according to the sensitivity degree to  $\mu_a$  and  $\mu_s$  of the different SD distances  $D$  (see Section 3.1 and Figure 3.14).

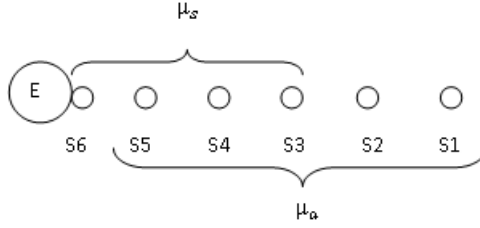


Figure 3.14: Use of S1 – S5 for the estimation of  $\mu_a$  and S3 – S6 for the estimation of  $\mu_s$ .

The inverse model finds the minimum Euclidian distance  $\Delta_{Norm}$  value to initially estimate  $\mu_s$ . A further minimization of  $\Delta_{Norm}$  is then performed for the established  $\mu_s$  to estimate  $\mu_a$ .

### Scaling procedure: Derivation of $\mu'_s$

As mentioned in Section 2.3.1, the anisotropy factor  $g$  depends on the wavelength  $\lambda$  and is estimated according to [Van Staveren et al., 1991] as  $g = 1.1 - (0.58 \cdot 10^{-3}) \lambda$  for intralipid - based phantoms. To consider this wavelength dependence, the reference  $\mu_{s,ref}$  and estimated  $\widehat{\mu}_s$  scattering coefficients, of reference and tested phantoms, respectively, are corrected from the constant  $g = 0.8$  considered in the Monte Carlo simulation, as shown in Equations 3.7 and 3.8.

$$\mu_{s,MC} = \frac{\mu'_{s,ref}}{(1 - 0.8)} \quad (3.7)$$

$$\widehat{\mu}'_s = \mu_{s,MC} \cdot (1 - 0.8) \quad (3.8)$$

This correction strategy allows to derive simulated values with varying  $g$  using the single Monte Carlo simulation with a fixed  $g = 0.8$ .

Figure 3.15 shows a flowchart that summarizes the whole method of optical properties estimations from *Contact DRSr* measurements of unknown and reference phantoms. Keep in mind that we use unknown phantoms with theoretical optical properties ( $\mu'_{s,theo}, \mu_{a,theo}$ ) to demonstrate the performance of the technique.

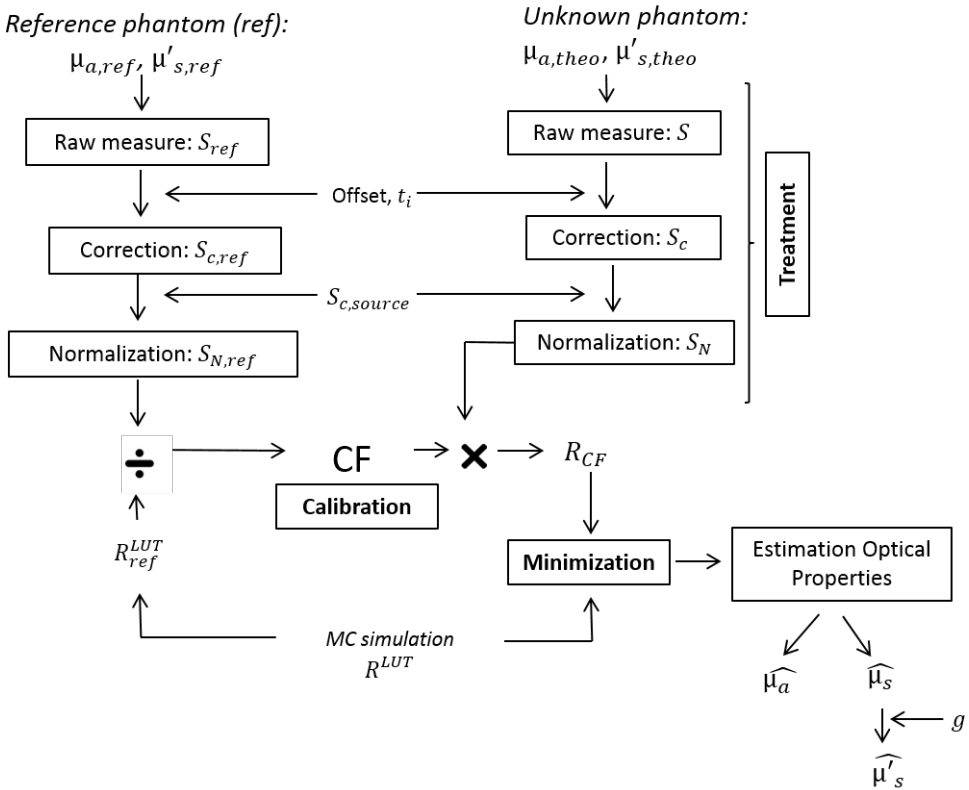


Figure 3.15: Existing DRSsr methodology for the estimation of optical properties at each wavelength  $\lambda$ .

### 3.2.5 Results

Figure 3.16 shows an example of estimation of an unknown phantom with  $\mu_{a,theo} = 0.4 \text{ cm}^{-1}$  at  $580 \text{ nm}$  and  $IL_{theo} = 1.5\%$  with a reference phantom having  $\mu_{a,ref} = 0.2 \text{ cm}^{-1}$  at  $580 \text{ nm}$  and  $IL_{ref} = 1.5\%$ . For this example, the approximate relative error is 1.1% and 5.6% for  $\hat{\mu}'_s$  and  $\hat{\mu}_a$  estimations, respectively. These define the reference range of estimation errors for the developed Non-Contact DRSSr setups explained further in Sections 3.3 and 3.4.

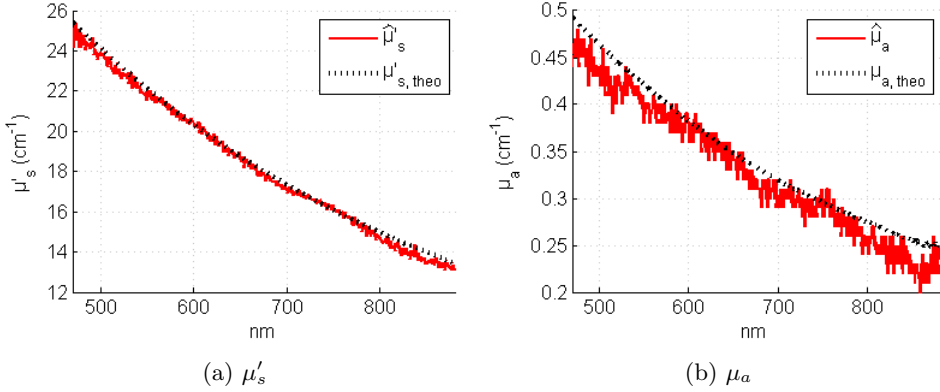


Figure 3.16: Optical properties estimation of a tested phantom with  $\mu_{a,theo} = 0.4 \text{ cm}^{-1}$  at  $580 \text{ nm}$  and  $IL_{theo} = 1.5\%$  with a reference calibration having  $\mu_{a,ref} = 0.2 \text{ cm}^{-1}$  at  $580 \text{ nm}$  and  $IL_{ref} = 1.5\%$ .

### 3.2.6 Limitations of current method

This reference-based methodology obtains good optical properties estimations when the unknown and reference optical properties are close. However, the more the unknown optical properties differ from the reference's, the more is the estimation degraded. This is directly related to the non-constant deviation between real measurements  $S_{N,ref}$  and the model  $R_{ref}^{LUT}$  which is not corrected by the CF. Several reasons may explain this deviation, such as: the limitations of the intralipid scattering model, the cross-talk between optical properties, and the inaccurate definition of the refraction index value.

#### Intralipid scattering model

The used scattering-intralipid model of [Van Staveren et al., 1991] (see Equation 2.7), which follows the Mie theory, approximates the real scattering properties of intralipid suspensions. This approximation like other (eg. [Mourant et al., 1997]) have accuracy limitations. In other words, there exists a model-related error in the establishment of the reference scattering properties  $\mu'_{s,ref}$  and thus on the correction factor  $CF$ . This error is then carried on towards the scattering estimation  $\hat{\mu}'_s$  of unknown phantoms. Thereby, the larger the scattering difference between reference and unknown phantoms, the higher

the estimation error is. Moreover, the scattering estimation error is transmitted to the absorption estimation through cross-talk, as explained in the next Paragraph.

### *Cross-talk*

Due to the scattering model approximation error, the degradation of both optical properties is higher when the scattering difference between the reference and the unknown phantoms is too large. An example is shown in Figure 3.17 with unknown phantoms having different  $IL_{theo} = 0.5, 1, 2, 3\%$  and common  $\mu_{a,theo} = 1 \text{ cm}^{-1}$  at  $600 \text{ nm}$  calibrated with a reference phantom having  $IL_{ref} = 1\%$  and  $\mu_{a,ref} = 0.4 \text{ cm}^{-1}$  at  $600 \text{ nm}$ . It is seen that the further the difference between reference and unknown, the higher the degradation of  $\mu'_s$  and thereby of  $\mu_a$  estimation (eg.  $IL_{theo} = 3\%$ ) is. It is clear that a bad estimation of  $\mu'_s$  induces a cross-talk error on the estimation of  $\mu_a$ .

Notice that the  $\mu_a$  estimation of the least scattering phantom ( $IL0.5\%$ ) is highly deviated because of the accuracy degradation of the forward model at these low scattering values.

Overall, it is clear that with no scattering difference, the method achieves the best estimation in both optical properties (eg.  $IL_{theo} = 1\%$ ).

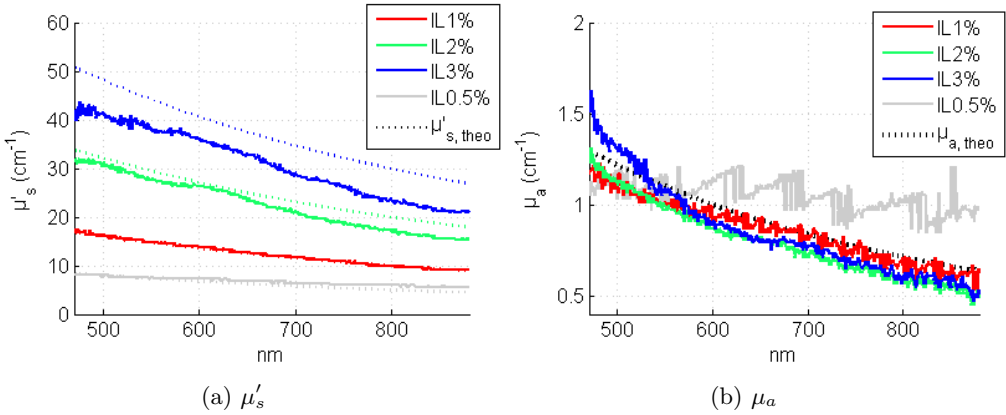


Figure 3.17: Estimation of (a)  $\widehat{\mu}'_s$  of phantoms having different  $\mu'_{s,theo}$  proper of  $IL_{theo} = 0.5, 1, 2, 3 \%$  (dotted lines) and (b)  $\widehat{\mu}_a$  of the same phantoms having common  $\mu_{a,theo} = 1 \text{ cm}^{-1}$  at  $600 \text{ nm}$  (dotted line). The reference phantom used for instrumental calibration has  $IL_{ref} = 1\%$  and  $\mu_{a,ref} = 0.4 \text{ cm}^{-1}$  at  $600 \text{ nm}$ .

### Refraction index

An additional source of error originates from the Monte Carlo simulated medium's refractive index  $n$ . Not only is it fixed for all  $\lambda$ , but it is also considered to be 1.37 proper of tissue instead of 1.33, proper of water-based intralipid phantoms.

The influence of  $n$  on the estimation of optical properties has been studied by [Foschum et al., 2011] and is presented in Figure 3.18.

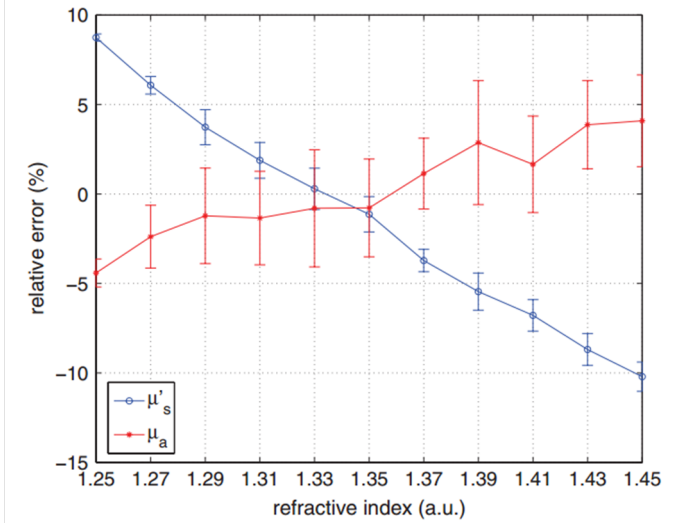


Figure 3.18: Relative error of optical properties estimation assuming a wrong refractive index [Foschum et al., 2011].

The study showed that if  $n$  is assumed higher than what it should be (in our case  $n=1.37$  instead of 1.33 and stable throughout the spectrum),  $\mu_a$  is overestimated and subject to a relative error smaller than 2%. Recall from Section 2.1.2 that  $\mu'_s$  depends on  $n$ . Therefore it is more affected by the wrong assumption of  $n$  causing an absolute relative error of 5%, in this case. In our method, and as mentioned in the previous paragraphs, the estimation errors of both optical properties increase with the scattering difference between reference and unknown phantoms.

Overall, it is seen that all the described sources of error between the measured and modelled reflectance are overcome with the use of a reference phantom having close scattering properties to the unknown phantom (see Figure 3.17). This is the foundation upon which we propose a scattering-based Adaptive Calibration Algorithm (*ACA-Pro*) which is further explained in Chapter 4.

### 3.3 Non-contact probe-based DRSSr

The *Dual-Step* technique that we develop in this work, couples Multispectral Imaging (MSI) with a non-contact modality of the DRSSr technique. This Section focuses on the development of the Non-Contact DRSSr system.

We adopt the non-contact measurement modality of the DRSSr technique because it provides many advantages in the clinical environment with respect to the contact modality:

- Measurements of sensitive samples such as injured or infected tissues are complicated and sometimes not even possible with a contact probe. Adversely, non-contact measurements are completely non-invasive and therefore sterile, allowing measurements of these vulnerable samples.
- Coupling variations due to probe positioning that determine different pressures on the sample have an effect in contact modality measurements that directly influence the estimation of optical properties [Nichols et al., 2015]. Repeatability of the measurement procedure is subject to the user handling of the probe. This is completely avoided by the non-contact modality in which no pressure dependence exists in the measurements.
- The use of optics in a non-contact setup provides higher flexibility in the choice of geometrical dimensions of the projected illumination beam and thereby the volumes that the detected reflectance inspects.

However, in non-contact systems other challenges, non-existent in the contact modality of DRSSr, arise.

For instance, the dramatic widening of the illumination projected beam originated by the optical components of the Non-Contact DRSSr setup, challenges the estimation of optical properties. Moreover, the spectral effects of the components, such as parasite reflections and the multiplicative instrument response function, should be considered. These effects are further analysed in Section 3.5.1.

Besides, Non-Contact DRSSr systems are sensitive to the focus procedure. Samples should be at the focus plane to acquire robust measurements. In Section 3.5.2 we characterize the non-contact system's focusing sensitivity according to the error in optical properties estimations with which a depth of field is defined.

To develop the Non-Contact DRSSr instrumental setups, the reference geometrical dimensions of the well-established *Contact DRSSr*, described in the previous Section 3.2.1, are considered. This is done to ensure that the same sample volume is inspected and signals are analysed with the same Monte Carlo *LUT*. This facilitates direct comparison to allow the accurate validation of the new Non-Contact setup.

In this Section, we focus on the *initial Non-contact probe-based DRSSr*, which is integrated in the *Dual-Step* technique that we develop. Section 3.3.1 introduces the instrumental setup built according to the geometrical design of *Contact DRSSr*. Sections 3.3.2 and 3.3.3 describe the geometrical and spectral effects, respectively, that the optical component chain has on the signals. According to the new constraints of the *initial Non-Contact DRSSr* system, the measurement procedure, described in Section

3.3.4 is followed, and the corresponding signal processing, described in Section 3.3.5, is employed.

### 3.3.1 Instrumental Setup

As mentioned before, the various Non-Contact DRSSr setups that have been built intend to preserve the geometrical dimensions of the *Contact DRSSr* instrument, described in the previous Section 3.2.1. This important geometrical constrain was abided to directly relate non-contact measurements to the same Monte Carlo simulation  $R^{LUT}$  that considers the geometrical dimensions of the real *Contact DRSSr* setup. Furthermore, it ensures that the same volume of the measured sample is inspected with both systems, which facilitates direct comparison of signals and validation of the developed Non-Contact DRSSr.

According to this, we have verified that the Non-Contact DRSSr system ensures a magnification of the detection and illumination paths equal to 1 (data not shown). Moreover, no inclination angle of projections is considered to approach the perpendicular injection and detection of photons with respect to the surface of the sample considered by the Monte Carlo simulation.

The initial Non-Contact DRSSr setup that was built is shown in Figure 3.19. The system consists of the same *Contact DRSSr* setup described in Section 3.2 with an additional achromatic doublet pair placed between the probe and the sample.

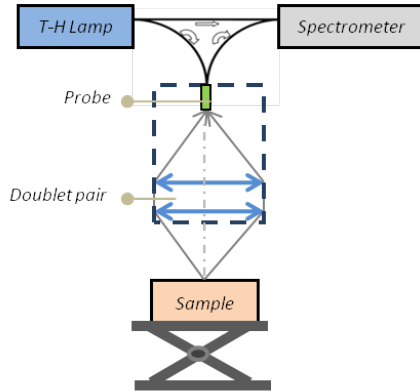


Figure 3.19: Initial Non-contact probe DRSSr setup

The focal distance of the doublets is chosen to be the same to guarantee magnification equal to 1 at a convenient focal distance of 100 mm from the sample. To fix the probe at the focal distance from the doublet pair, a framework with black Delrin (polyoxymethylene) has been manufactured to hold fast both components (see Figure 3.20).

The framework is positioned parallel to the sample to promote the perpendicular projection between the sample surface and the probe.

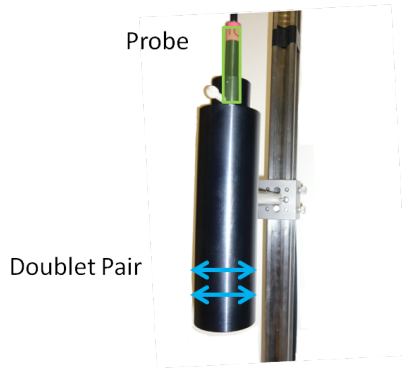


Figure 3.20: Framework to fix the probe and the doublet pair

### 3.3.2 Geometrical alteration induced by the optical path

To ensure that the size of the illumination and detection beams projected through the non-contact system are the same to that of the contact probe, the geometrical deviation with respect to the Monte Carlo model should be negligible. The latter is defined as geometrical alteration or change in the rest of this document. This geometrical alteration mainly originates from the doublet pair effect.

The following Paragraphs explain how we measured geometrical changes both on the detection and the illumination paths.

#### *Detection path*

To measure the geometrical alteration on the detection path, all detection fibres are illuminated with an extra lamp. A CCD camera (with pixel size=9.9  $\mu\text{m}$ ) is centered at the object plane as shown in Figure 3.21 to visualize the projection of the illuminated fibres. The acquired image is shown in Figure 3.22.

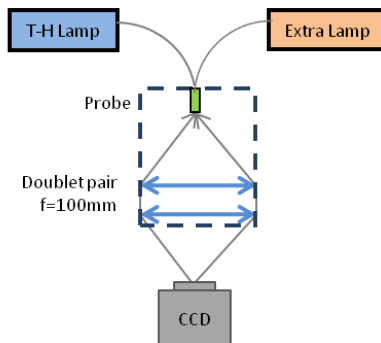


Figure 3.21: Setup used to measure the geometrical alteration effect of the doublet pair in the detection path of the initial Non-Contact DRSr setup.

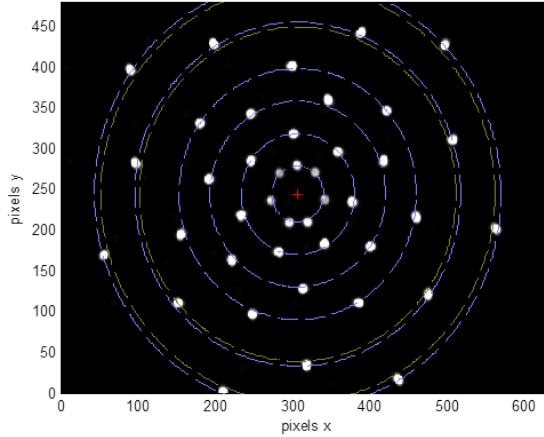


Figure 3.22: Measurement of the geometrical alteration effect caused by the doublet pair, with the setup shown in Figure 3.21.

In Figure 3.22, the probe's measured dimensions (related to the contact measurements) are shown in dark yellow, whilst the blue circles follow the center of the fibres appertaining to each ring in the non-contact projected image, affected by the doublet's geometrical aberration. The maximal geometrical change is present at the last fibre ring  $F1$  (last blue circle) and is measured to be no more than  $80 \mu m$ . This means that non-contact  $S1$  is measured  $80 \mu m$  further from the source than  $S1$  acquired with the contact modality.  $F2$  is also affected by a geometrical alteration of  $60 \mu m$ .

These alterations are considered imperceptible since they have a negligible effect on the quantification of optical properties. Therefore, their correction has not been considered.

### Illumination path

The projected illumination beam at the object plane is spatially spread by the doublet pair. To determine this elongation, the projected spatial illumination profile is measured with the setup shown in Figure 3.23.

The illumination projected point is placed at a side of the image as shown in Figure 3.24 to maximize the measurement distance along the horizontal profile (green line). By taking images with several increasing integration time  $t$  values, all distances from the central point of the horizontal profile can be measured inside the dynamic range of the 12-bit CCD (see Figure 3.25). We verified that blooming at nearby pixels did not occur and that detectable signals increased linearly with time despite pixel saturation at close distances.

Hence, through the selection of the detectable signal at each integration time  $t$ , the entire illumination profile at all distances can be recovered. This strategy is also used by other groups such as [Jacques et al., 1993], [Bolt et al., 1993] and [Foschum et al., 2011].

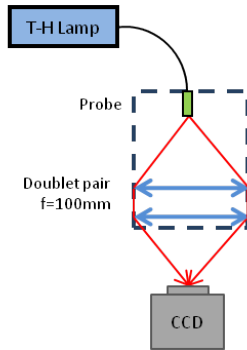


Figure 3.23: Setup used to measure the spatial profile of the projected illumination beam at the object plane of the initial Non-Contact DRSsr setup.

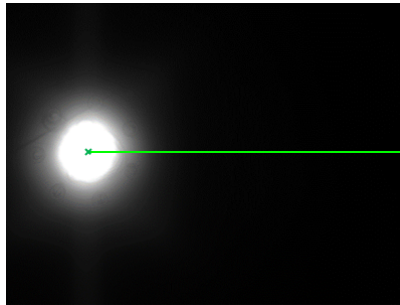


Figure 3.24: Image of the projected illumination beam at the object plane, obtained with the setup of Figure 3.23. The considered horizontal profile is illustrated with the green line.

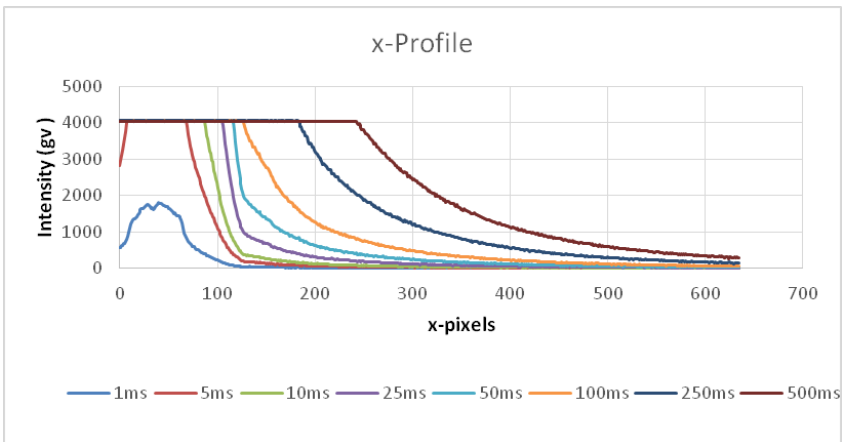


Figure 3.25: Horizontal x-profile of the image shown in Figure 3.24 taken with different integration times  $t$ . Signals have been previously corrected from the instrumental offset.

For this, only non-saturated average intensities with a signal higher than the limit of detection  $LOD$  (see Equation 3.9) are selected.

$$LOD = 3 \cdot \sigma_{offset} \quad (3.9)$$

where  $\sigma_{offset}$  is the standard deviation of the offset signal at the corresponding integration time  $t$ .

Selected intensities are then scaled according to  $t$  and combined to reconstruct the illumination beam profile up to 2.8 mm. The normalized horizontal profile of the *initial Non-Contact DRSSr* system is shown in Figure 3.26.

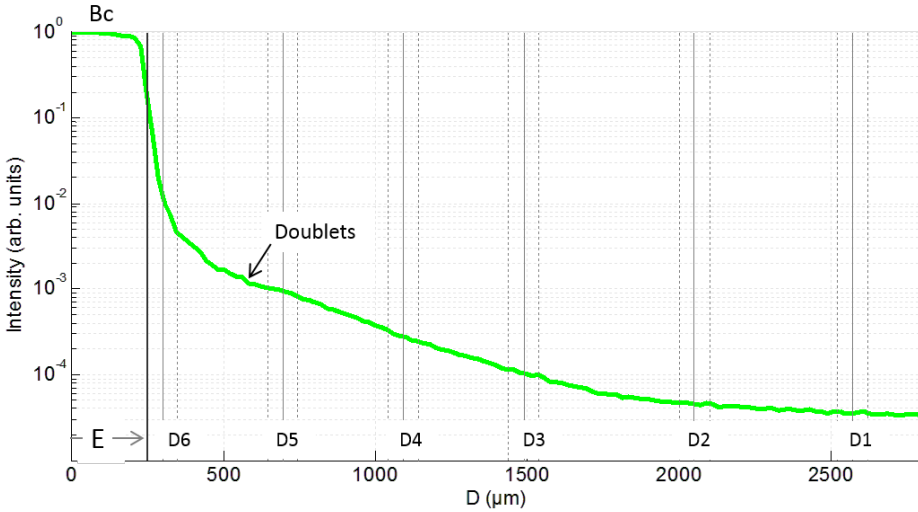


Figure 3.26: Horizontal illumination profile of the *initial Non-Contact DRSSr* setup. The theoretical radius of the excitation fibre  $E$  and  $D1 - D6$  distances used in the *Contact DRSSr* Monte Carlo simulation are defined.

It is clear that the projected beam of the Non-Contact DRSSr setup does not have an accurate radius of  $250 \mu\text{m}$ , as that of the Monte Carlo excitation fibre, and extends far beyond  $D6$ . Indeed, the illumination signal reaching  $D6$  is comparable to that of the center of the illumination beam (denominated  $Bc$  at the origin), being  $\sim 10^{-2}Bc$ . The intensity at  $D5$  is  $\sim 10^{-3}Bc$  and lower at  $D4 - D1$ .

This illumination profile extension poses the most important challenge for the estimation of optical properties with the Monte Carlo simulation used which considers the *Contact DRSSr* illumination profile. A more detailed explanation of this effect is given in Section 3.5.1.

### 3.3.3 Spectral effect of components on signals

The additional doublet pair also has a spectral effect on the signals. These effects include the additive parasite reflections of the doublet pair and the constant multiplicative instrument response function which are briefly explained in the following Paragraphs.

#### Parasite Reflections

In the *initial Non-Contact DRSSr setup*, the achromatic doublet pair is part of both illumination and detection paths. Therefore, direct parasite reflections from the illumination pollute the detected signal. The doublet pair that is used has an anti-reflection coating ensuring optimal transmission between 400-700 nm. Parasite reflections consequently arise after 700 nm. To measure them, no object is placed at the object plane and a black absorbing cloth is disposed far from the focal plane to fully absorb the illumination signal that goes through the system and ensure no reflection back (see Figure 3.27). This allows only parasite reflections from the doublet pair to be detected.

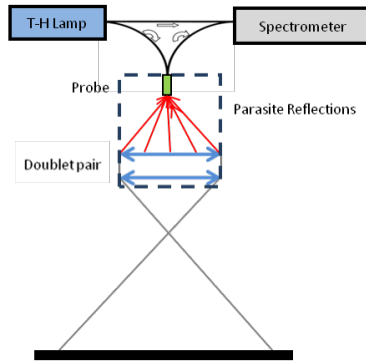


Figure 3.27: Setup used to measure parasite reflections originated at the doublet pair.

An example of the measured parasite reflection signal is shown in Figure 3.28.

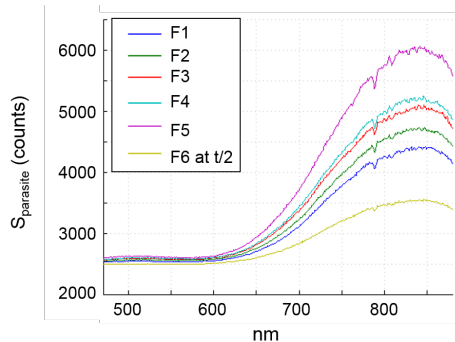


Figure 3.28: Parasite Reflection of the doublet pair  $S_{parasite}$  measured by all fibre rings at an integration time  $t = 3$  s for  $F1 - F5$  and  $t = 1.5$  s for  $F6$ .

Reflectance measurements are then corrected from these parasite reflections as explained further in Section 3.3.5.

### *Constant Multiplicative Effect: Instrument Response Function*

The constant multiplicative modification of the reflectance signal by the different components is described by its instrument response function (IRF). The spectral IRF is calculated from the ratio between the measurement of a signal before and after going through the components.

During the IRF measurements, we realized that the entrance angle of the beam on the spectrometer fibre had an effect on the spectral measurement. This is most probably due to the wavelength dependence of the fiber numerical aperture as studied by [Kersten et al., 1982]. To cancel this angle dependence, we placed a lambertian diffusor at the entrance of the spectrometer fibre. Figure 3.29 illustrates the setups used to derive the IRF of the doublet pair, shown in Figure 3.30.

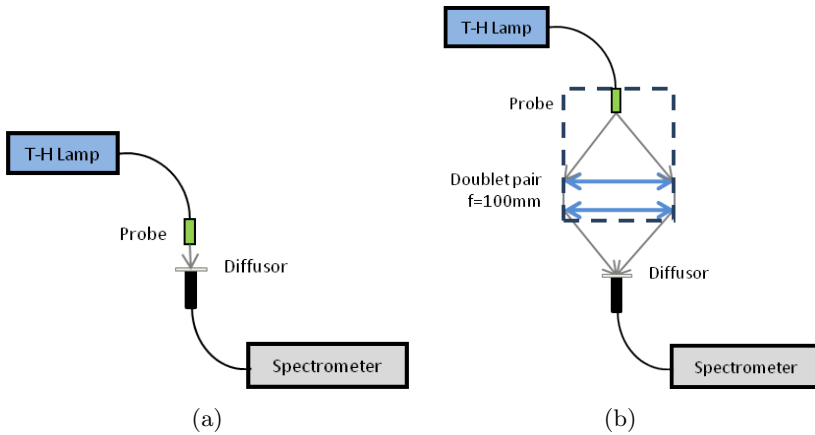


Figure 3.29: Setup describing the measurement of the illumination beam (a) before and (b) after being transmitted through the doublet pair.

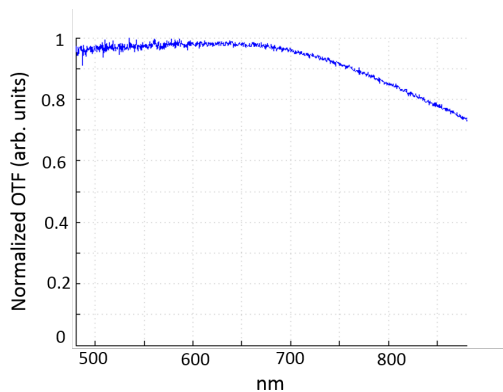


Figure 3.30: Normalized measured IRF of the doublet pair transmission.

Measured signals are corrected from this multiplicative IRF as explained further in Section 3.3.5.

### 3.3.4 Measurement Procedure

Before measurement acquisition of any sample, the focal plane of the sample's surface is found according to the focusing protocol described further in Section 3.5.2.

Once the sample is focused,  $S$ ,  $S_{source}$ ,  $S_{parasite}$ , and  $S_{offset}$  are acquired under the same ambient darkness conditions and with constant integration time  $t$ . For each concentric fibre measurement,  $t$  is adjusted to the signal intensity and dynamic range of the spectrometer. Generally,  $S1 - S5$  are taken at the same  $t$ , whilst  $S6$  is taken at a lower  $t$  to avoid saturation.

### 3.3.5 Signal Processing

Raw signals  $S1 - S6$  are corrected from the offset and scaled with the integration time  $t$  according to Equation 3.10 to obtain  $S_c$  and  $S_{c,source}$ . Temporal source variations are also considered by using  $S_N$  derived from Equation 3.11.

$$S_c = \frac{S - S_{offset}}{t}, \quad S_{c,source} = \frac{S_{source} - S_{offset}}{t} \quad (3.10)$$

$$S_N = \frac{S_c}{S_{c,source}} \quad (3.11)$$

Moreover, the correction of the doublet pair's parasite reflections and multiplicative instrument response function has to be considered. The following Paragraphs explain each of these corrections.

#### Additive effect: Parasite Reflections

Normalized signals have to be corrected from the additive parasite reflections of the achromatic doublet pair. These are measured as described previously, corrected from the instrumental offset, scaled with the integration time  $t$  and corrected from source variations to obtain  $S_{N,parasite}$  (see Equation 3.12).

$$S_{N,parasite} = \frac{(S_{parasite} - S_{offset})/t}{S_{c,source}} \quad (3.12)$$

The final signal  $S_F$ , corrected from the doublet pair parasite reflection, is obtained through a simple subtraction of  $S_{N,parasite}$  from  $S_N$ , according to Equation 3.13.

$$S_F = S_N - S_{N,parasite} \quad (3.13)$$

#### Multiplicative effect: IRF

To recover the spectral signal reaching the sample and diffusing back to its surface, the illumination and detection paths' IRFs ( $IRF_{ill}$  and  $IRF_{det}$ ) are considered separately. Figure 3.31 illustrates the effect of the doublet pair IRF ( $IRF_{pair}$ ) on the illumination signal, when reaching the surface of the sample, and on the resulting reflectance, when reaching the detection fibres.

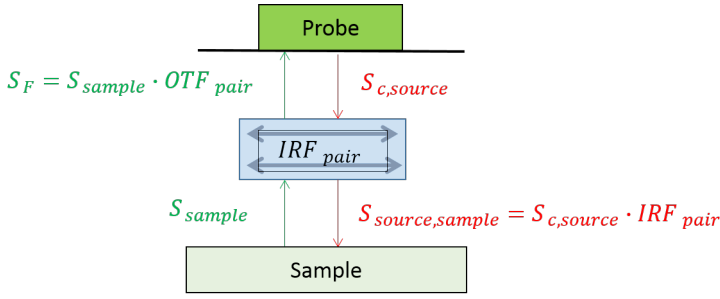


Figure 3.31: Multiplicative effect of the doublet pair IRF on the signals going through the *initial Non-Contact DRSSr setup*.

To derive the illumination signal reaching the sample,  $S_{source,sample}$ , the measured source signal  $S_{c,source}$  is multiplied by  $IRF_{pair} = IRF_{ill}$ , according to Equation 3.14.

$$S_{source,sample} = S_{c,source} \cdot IRF_{ill} \quad (3.14)$$

Analogously, to recover the reflectance signal resulting at the sample's surface before it goes through the doublet pair,  $S_{sample}$ , the measured  $S_F$  is divided by the  $IRF_{pair} = IRF_{det}$  according to Equation 3.15.

$$S_{sample} = \frac{S_F}{IRF_{det}} \quad (3.15)$$

$S_{sample}$  corresponds to the reflectance of the sample derived after correction of the parasite reflections, source variations and IRF of the doublet pair. This is the signal to be calibrated and fitted to  $R^{LUT}$  to recover the optical parameters of the unknown sample, as explained in the next Section 3.5.1.

## 3.4 Non-Contact CCD-based DRSSr

As a validation stage, the *Dual-Step* technique that we develop in this work makes use of a probe-based Non-Contact DRSSr setup (described in the previous Section 3.3). Yet, we explored the use of a more advanced CCD-based Non-Contact DRSSr setup. A perspective improved stage of the *Dual-Step* technique, would consider the use of this *CCD-based DRSSr* setup for the various advantages it offers with respect to probe-based DRSSr setups.

Firstly, the use of a CCD detector allows the online visualization of the sample surface, which is not possible with a fibered probe. This valuable information not only facilitates focusing of the illumination beam on the sample, but also aids the analysis of the surface heterogeneities in biological samples. For instance, skin corrugations which alter the diffuse reflectance measurements are clearly seen on the images acquired with the CCD.

Secondly, the higher spatial resolution of the CCD detector compared to that of the probe, brings several advantages, such as the large flexibility range of possible magnification in the detection path, only limited by the CCD pixel size. Moreover, the higher spatial resolution directly increases the depth resolution of the measurements. Various groups such as [Kienle et al., 1998], [Doornbos et al., 1999], [Cen et al., 2009] have already investigated the use of the spatially resolved reflectance offered by DRSSr instruments to derive optical properties at different layers. The depth selectivity can enhance the detection of optical changes associated with superficial early stage cancer, as demonstrated by [Schwarz et al., 2008b]. This depth resolution investigation will be further discussed in Section 7.2.3.

For all these advantages, the *CCD-based DRSSr* setup is a valuable alternative to probe-based DRSSr setups. Therefore, it will be considered for integration in a more advanced perspective version of the *Dual-Step* technique.

This Section focuses on the *CCD-based DRSSr* system that we developed, based on the measurement linearity of imaging with respect to conventional point Spectroscopy (see Appendix A.4).

Recall from Section 3.3 that to inspect the same sample volume and allow the use of the same contact Monte Carlo simulation in a non-contact configuration, the magnification of the detection path is set to 1. The corresponding *CCD-based DRSSr* instrumental setup, with a preliminary probe-based DRSSr stage, is described in Section 3.4.1. As a matter of fact, the optical components in the systems provoke spatial elongation (Section 3.4.2) and spectral effects (Section 3.4.3) on the projected beams that are corrected, as explained further in Section 3.5.1, to allow the quantification of optical properties. Section 3.4.4 describes the measurement procedure of the different setups to obtain images or signals that are treated as explained in Sections 3.4.5 and 3.4.6.

### 3.4.1 Instrumental Setup

The use of a CCD requires the separation of the illumination and detection paths. Therefore, as a translational stage with respect to the *initial Non-Contact DRSSr* (refer to Section 3.3), we built the *folded Non-Contact DRSSr* setup with separate illumination and detection paths, described in the next Paragraph.

#### Folded Non-Contact DRSSr setup

As shown in Figure 3.32, the *folded Non-Contact DRSSr* setup projects the illumination beam in a folded manner whilst keeping the original vertical detection path of the *initial Non-Contact DRSSr* setup. The additional components used include two achromatic doublets and a 50:50 plate beamsplitter. Using an illumination fibre of  $100\ \mu\text{m}$  in diameter, the focal distance of the doublets is chosen to be  $30\ \text{mm}$  and  $100\ \text{mm}$  to obtain a projected beam of  $500\ \mu\text{m}$  in diameter at the object plane, according to the beam dimensions of the *Contact DRSSr* instrument (see Figure 3.4). The use of the 50:50 plate beamsplitter allows the separation and perpendicular projection of the illumination and detection signals.

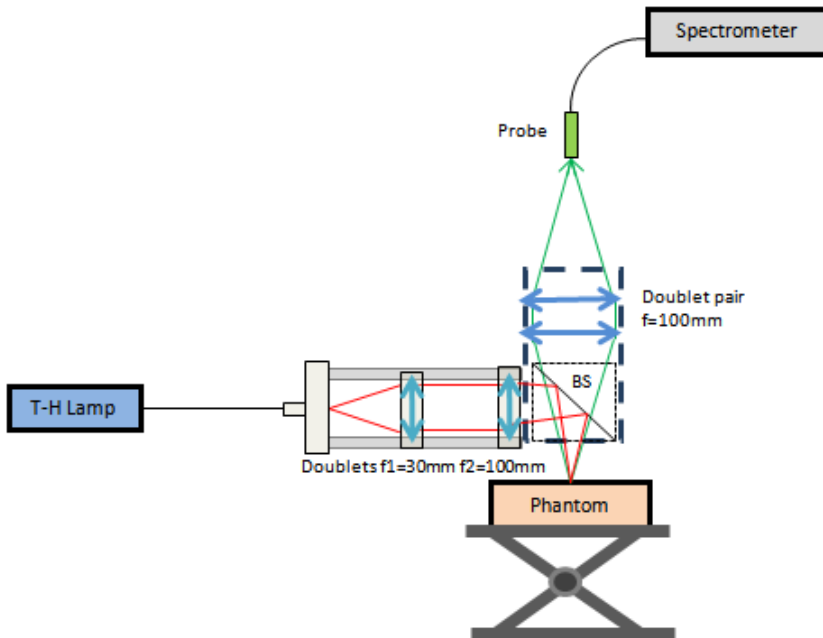


Figure 3.32: Folded Non-Contact probe DRSSr setup

### CCD-based Non-Contact DRSSr setup

To build the *CCD-based DRSSr* system, we replace the probe of the *folded Non-Contact DRSSr* setup (see Figure 3.32) with a 12-bit monochrome *PixelFly VGA CCD* [PixelFly, 2015] (refer to Appendix A.2.1 for instrument specifications) and include a collimator filter support just after the lamp source, as shown in Figure 3.33.

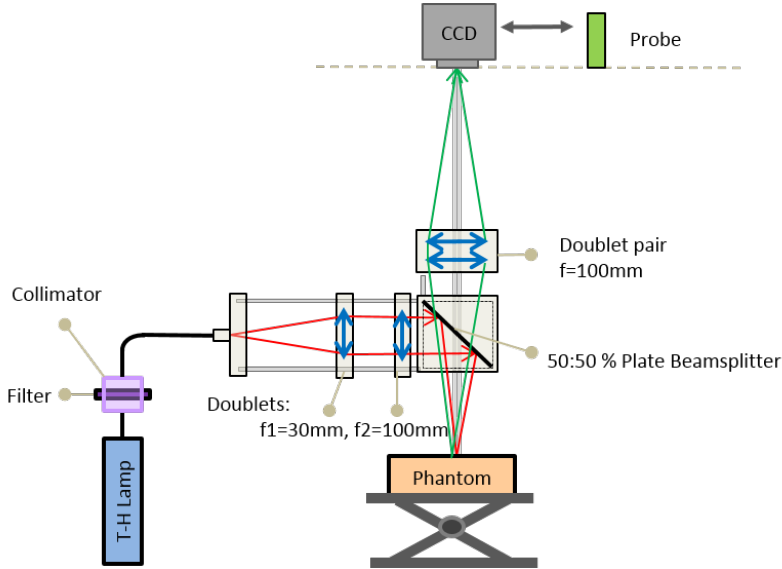


Figure 3.33: *Non-Contact CCD-based DRSSr* setup with separated illumination and detection paths and a CCD detector.

Since this work aims for a proof of concept, spectral resolution is not a priority so we make use of four different conventional filters only, to cover the working spectral range: 450, 550, 650 and 750  $nm$ . The filters have a  $FWHM = 10\text{ nm}$  and further specifications are given in Appendix A.3.

The effect of the optical components of these setups is explained in the next Sections 3.4.2 and 3.4.3, respectively.

### 3.4.2 Geometrical alterations induced by the optical path

The various optical components involved in the *folded* and *CCD-based Non-Contact DRSsr* setups have an effect on the geometrical disposition of the illumination and detection signals projected on the sample or on the detector, respectively. The following Paragraphs describe the effect on each of these paths individually.

#### Detection path

The geometrical alteration of signals on the detection path is measured with the setup shown in Figure 3.34. The effect on the projection of the illuminated detection fibres is comparable to that obtained with the *initial Non-Contact DRSsr* setup described in Section 3.3.2. Therefore, the geometrical alteration on the detection signals originated from the plate beamsplitter is considered negligible.

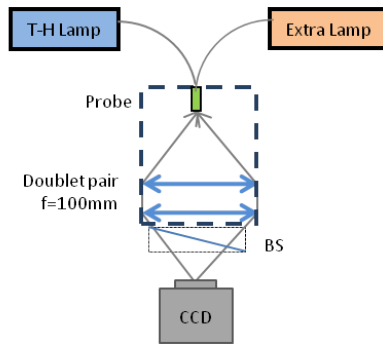


Figure 3.34: Setup used to measure the geometrical effect of the detection path in both Non-Contact setups featuring a doublet pair and plate beamsplitter BS.

#### Illumination path

The projected illumination beam of the *folded* and *CCD-based Non-Contact DRSsr* setups on the object plane is measured with the setups shown in Figure 3.35 and according to the procedure described in Section 3.3.2.

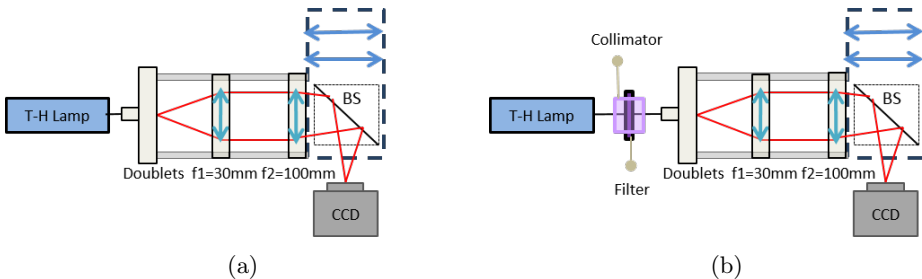


Figure 3.35: Setups used to measure the profile of the illumination beam at the object plane of the (a) *folded Non-Contact DRSsr* setup (b) *CCD-based DRSsr* setup, equivalent to the folded setup with an additional filter and collimator.

Images acquired with both setups are similar and an example is shown in Figure 3.36.

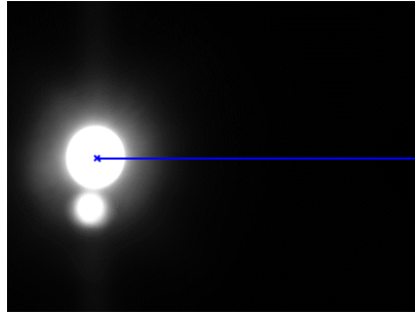


Figure 3.36: Projected illumination beam on the object plane of the setup shown in Figure 3.35a. The considered horizontal profile is illustrated with the blue line.

When comparing the illumination beam images obtained with the *initial Non-Contact DRSSr* setup (see Figure 3.26) and the *folded Non-Contact DRSSr* setup (see Figure 3.36), the effect of the 50:50 plate beamsplitter is made clear with a parasite halo and a punctual parasite reflection adjacent to the central illumination beam. This is one of the multiple reflections that occur in any type of plate beamsplitter because the incident beam is refracted and reflected multiple times adjacent to each other. Figure 3.37 illustrates the relative reflection power of the multiple subsidiary reflections ( $R_n$ ) from the beamsplitter's front and back surfaces with reflectivity  $r_1$  and  $r_2$ , and transmittance  $t_1$  and  $t_2$ , respectively.

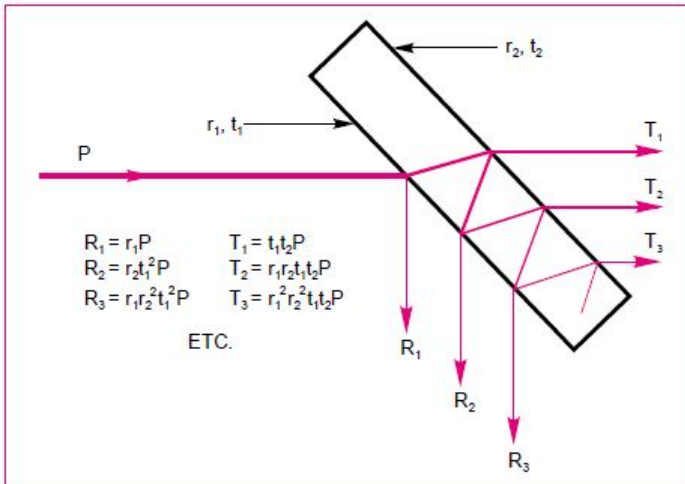


Figure 3.37: Multiple reflections from the plate plate beamsplitter at  $45^\circ$  [Optics, 2015].

To better visualize the effect of the different components on the projected illumination beam, we select a horizontal profile (along the blue line of Figure 3.36) and compare it to the previous *initial Non-Contact DRSSr* and *Contact DRSSr* setups (see Figure

3.38).

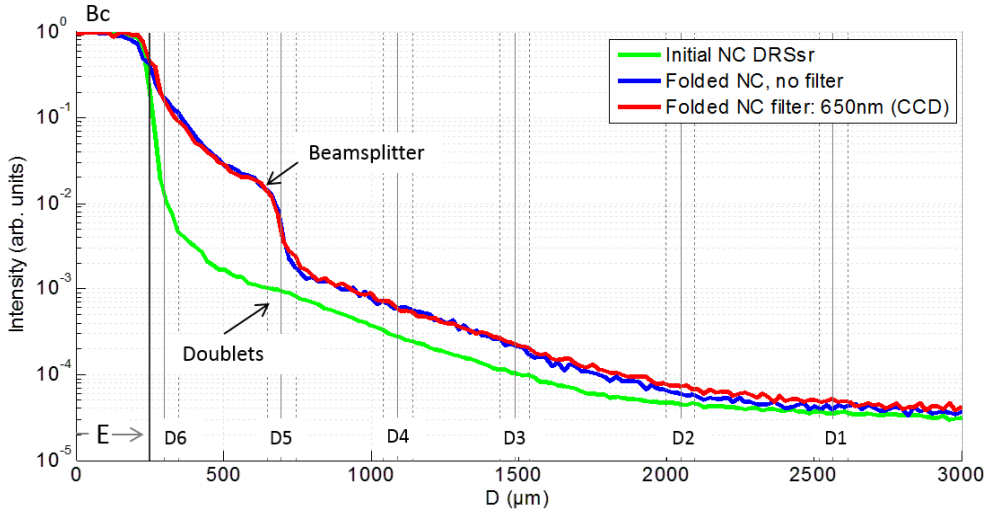


Figure 3.38: Illumination beam profiles of *folded* and *CCD-based Non-Contact* (NC) *DRSsr* setups compared to that of the initial NC setup.

Notice that the illumination profiles of the *folded* and *CCD-based* (equivalent to the folded with additional filter) *Non-Contact DRSsr* are comparable, meaning that the filter effect is negligible. Compared to the *initial Non-Contact DRSsr*, the folded illumination signal is higher due to the effect of the doublets and plate beamsplitter. The folded signal reaching  $D_6$  is half the signal of the central illumination beam ( $B_c$ ) and 10 times higher than that of the *initial Non-Contact DRSsr* setup. Remark the intensity protrusion occurring between  $D_6$  and  $D_5$  caused by the beamsplitter's parasite halo of the folded illumination path.  $D_5$  is  $\approx 2 \times 10^{-3} B_c$ , whilst that of the *initial Non-Contact DRSsr* beam is  $\approx 10^{-3} B_c$ . At  $D_4 - D_2$  the illumination is  $< 10^{-3} B_c$  for all Non-Contact signals and slightly higher for the folded setups. All signals are comparable at  $D_1$ .

The consequences of the extended Non-Contact projected illumination beams are dramatic on the resulting diffuse reflectance and they should be considered to allow the quantification of optical properties, as explained further in Section 3.5.1.

### 3.4.3 Spectral effect of components on signals

As described in the previous Section 3.3.3, the different optical components have a spectral effect on the signals. Since the illumination and detection paths are separated, the *folded DRSSr* setups are not affected by the additive parasite reflections as it is the case for the *initial Non-Contact DRSSr* setup. Yet, the multiplicative effect described by the instrument response function (IRF) of the components is present and described in the next Paragraph.

#### Constant Multiplicative Effect: Instrument Response Function

Analogously to the procedure described in Section 3.3.3, the IRF of the detection path ( $IRF_{det}$ ) and that of the illumination path ( $IRF_{ill}$ ) of the *folded Non-Contact DRSSr* setups is derived from the ratio of signals measured with the setups shown in Figures 3.39 and 3.40, respectively.

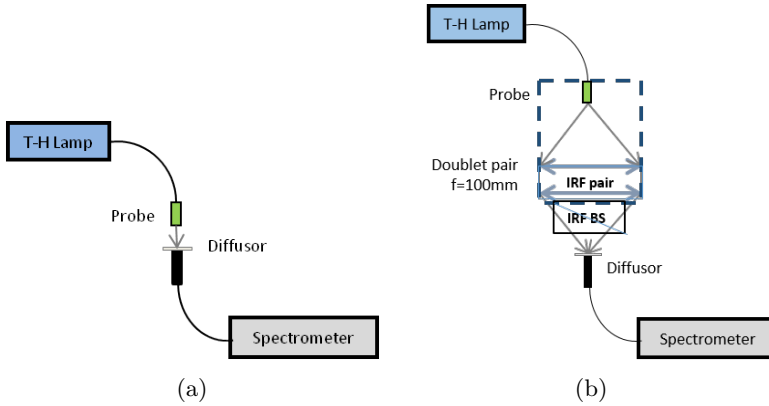


Figure 3.39: Setup describing the measurement of the detection beams (a) before and (b) after being transmitted through the beamsplitter and doublet pair of the *folded Non-Contact DRSSr* setup.

The normalized  $IRF_{det}$ , including the doublet pair and plate beamsplitter transmission, is shown in Figure 3.41a and  $IRF_{ill}$ , including the lens transmission and plate beamsplitter under reflection, is shown in Figure 3.41b.

The  $IRF_{ill}$  of the *folded Non-Contact DRSSr* setup is multiplied by the spectral transmission of the filters (given in Appendix A.3) to obtain that of the *CCD-based DRSSr* setup.

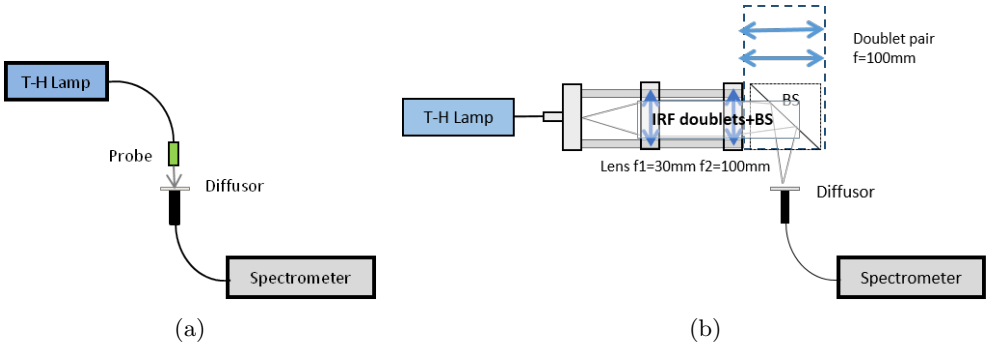


Figure 3.40: Setup describing the measurement of the illumination beam (a) before and (b) after being transmitted through the lenses and beamsplitter of the *folded Non-Contact DRSsr* setup.

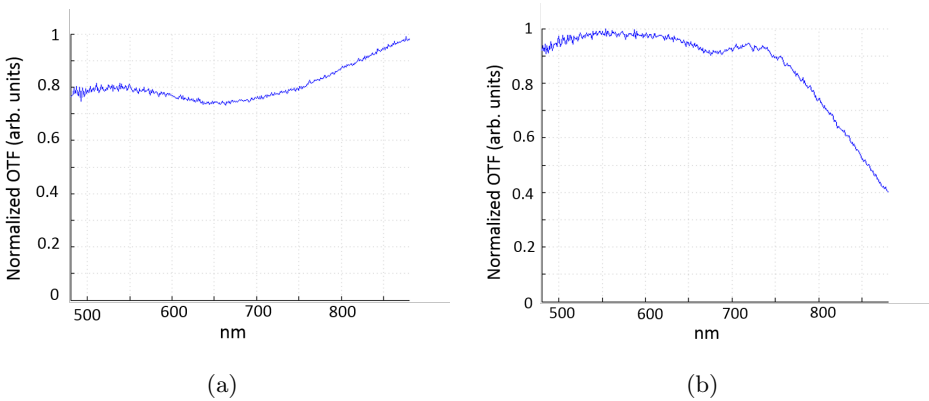


Figure 3.41: (a) Normalized  $IRF_{det}$ , including the doublet pair with the plate beam-splitter's transmission in the detection path (b) Normalized  $IRF_{ill}$ , including the lens transmission and beamsplitter reflection in the illumination path.

### 3.4.4 Measurement Procedure

The measurement procedure for the probe-based *folded Non-Contact DRSSr* setup (see Figure 3.32) is the same as that described for the *initial Non-Contact DRSSr* setup in Section 3.3.4.

In the case of the *CCD-based DRSSr* system (see Figure 3.33), a different protocol is needed to acquire diffuse reflectance images.

First of all, focusing of the illumination beam on the sample is performed through video-mode for each sample individually. The achromatic lenses of the illumination path ensure that the variation of the focal plane between the different filters is negligible (around  $100 \mu\text{m}$ ).

Diffuse reflectance images are then acquired under constant dark conditions. An example is shown in Figure 3.42. It is seen that the punctual parasite reflection due to the beamsplitter's reflection previously detected (see Figure 3.36) is duplicated by the beamsplitter's transmission on the detection path and is visible on the diffuse reflectance image at the CCD detector's plane. The measurement area that we defined in the image avoids these parasite reflections (see cyan square of Figure 3.42).

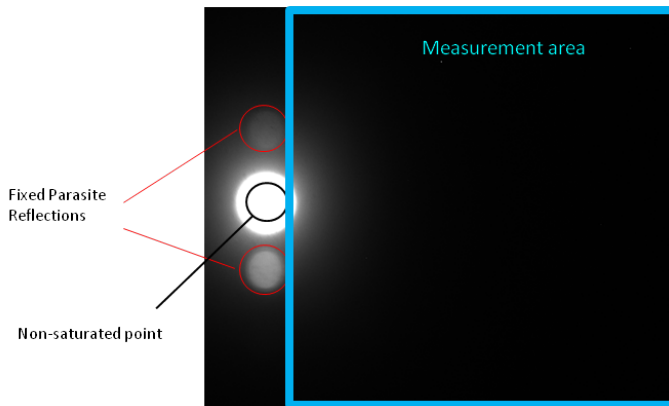


Figure 3.42: Typical image showing the projected illumination beam and two parasite reflections originating at the beamsplitter. The latter are kept out from the selected measurement area.

To measure the diffused reflectance decay along the distance from the illumination beam (SD distance) the same procedure as the one used to measure the illumination beam profile (refer to Section 3.3.2) is used. That is, various images with different acquisition times are used to overcome the limited dynamic range of the CCD. Moreover, background images  $S_{offset}$  are acquired with no light source under the same dark conditions for some acquisition times  $t$ , spanning the  $t$  range used for reflectance measurements. The next Sections 3.4.5 and 3.4.6 explain how all these images are combined to derive the spatial reflectance decay.

### 3.4.5 Image Processing

Diffuse reflectance images acquired with the *CCD-based DRSsr* setup, are corrected from the background  $S_{offset}$  signal according to the exposure time  $t$ . Because the offset is measured for a few  $ts$ , we build the linear  $S_{offset} - t$  curve with the average intensity of a common area in all background images. This curve then allows to derive the offset intensity for any integration time  $t$  through interpolation.

To determine  $S_6 - S_1$  in the images, the detection of the illumination point center, obtained through a Canny filter, is first required (see red cross of Figure 3.43). Concentric pixels of rings corresponding to  $F_6 - F_1$  (see Figure 3.4) and inside the measurement area are selected, as illustrated by the cyan curves of Figure 3.43.

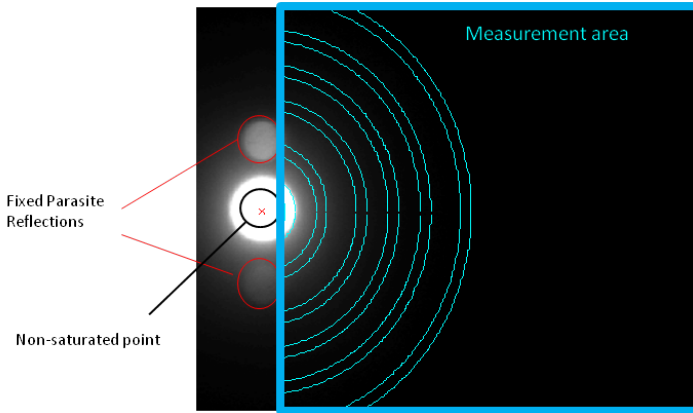


Figure 3.43: Selection of relevant areas of an image. Cyan curves delimit  $F_6 - F_1$  detection rings with a diameter of  $100 \mu\text{m}$ .

Non-saturated average signals higher than  $LOD$  (see Equation 3.9) are selected to determine  $S_6 - S_1$ .

### 3.4.6 Signal Processing

Raw signals  $S_6 - S_1$  obtained with the *folded probe-based* and *CCD-based Non-Contact DRSsr* systems, are scaled according to  $t$ , to obtain  $S_c$  through Equation 3.16.

$$S_c = \frac{S - S_{offset}}{t} \quad (3.16)$$

The variations of the separated illumination source signal is considered stable enough (1.5% variation in 7 hours, see Figure 3.9) and thereby it is measured only once and not all along the experimental process. Slight variations of  $S_{source}$  are therefore not corrected in the *folded* or *CCD-based DRSsr* setups as it is done in the *initial Non-Contact* and *Contact DRSsr* setups (see Equation 3.11) and we define  $S_N = S_c$ .

Moreover, because parasite reflections do not occur with the folded illumination setups (see Equation 3.13), we define  $S_F = S_N$ .

The multiplicative effect of the  $IRF_{ill}$  and  $IRF_{det}$  is considered in the next Paragraph.

### Multiplicative effect: IRF

The same analysis of the *IRF* effect on signals done for the *initial Non-Contact DRSSr* (see Section 3.3.5) is considered for the *folded* and *CCD-based Non-Contact DRSSr* setups. Figure 3.41 shows the various signal effects of the components on the illumination and detection path.

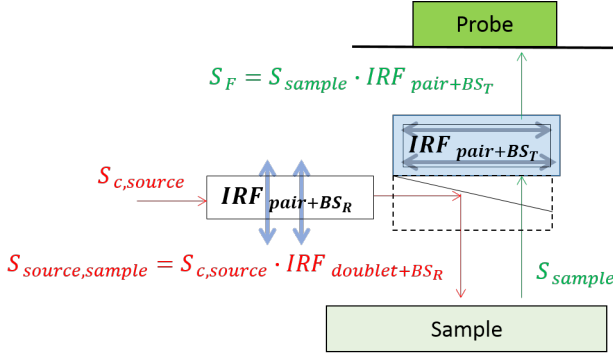


Figure 3.44: Multiplicative effect of the doublets and plate beamsplitter reflection  $IRF_{pair+BS_R} = IRF_{ill}$  on the illumination signals, and transmission of the doublet pair and beamsplitter  $IRF_{pair+BS_T} = IRF_{det}$  on the detection signals.

The illumination signal reaching the surface of the sample,  $S_{source,sample}$ , is obtained by considering  $IRF_{ill} = IRF_{pair+BS_R}$ , including the transmission of lenses and the beamsplitter reflection, on the measured  $S_{c,source}$ , as defined by Equation 3.17.

$$S_{source,sample} = S_{c,source} \cdot IRF_{ill} \quad (3.17)$$

Equivalently, the measured resulting reflectance signal  $S_F$  is to be corrected from the  $IRF_{det} = IRF_{pair+BS_T}$ , including the transmission of the doublet pair and beamsplitter, to recover  $S_{sample}$  according to Equation 3.18.

$$S_{sample} = \frac{S_F}{IRF_{det}} \quad (3.18)$$

$S_{sample}$  is the reflectance of the sample corrected from the multiplicative *IRF* effect which is considered for optical property estimation after calibration and fit to the  $R^{LUT}$ , as explained in the next Section 3.5.1.

## 3.5 Challenges encountered with Non-Contact DRSSr

The Non-Contact DRSSr setups that have been built pose new methodology and instrumental problems, which are not present on the reference Contact DRSSr setup. This Section describes the challenges and proposes solutions to overcome them.

### 3.5.1 Quantification Method Challenges

To estimate optical parameters, the quantification method proper of the Contact DRSSr setup and described in Section 3.2.4, is adopted. In other words, it was decided to use the same  $R^{LUT}$  built with the Monte Carlo simulation under contact conditions to derive optical properties from non-contact measurements taken with the developed probe-based and CCD-based DRSSr setups. This strategy avoids the simulation of individual Monte Carlo simulations, adapted to each DRSSr system, as has been done by [Foschum et al., 2011].

For this purpose, the correction of the non-simulated non-contact instrumental effects is essential. Recall that these include spectral effects (Sections 3.3.3 and 3.4.3) and spatial spread (Sections 3.3.2 and 3.4.2) originated from the various optical components. Spectral effects include the components' additive parasite reflections and/or their constant multiplicative IRF. The non-negligible effect of the illumination path is particularly influential since it causes a dramatic extension of the projected illumination profile.

The following paragraphs explain how the technique we propose considers and corrects these non-modelled effects to allow quantification of optical parameters.

#### Instrumental Calibration of constant spectral effects

The spectral non-modelled additive and constant multiplicative effects of the Non-Contact DRSSr setups are corrected as described in Section 3.3.5. The resulting corrected signal is defined as  $S_{sample}$ .

Recall from Equation 3.4 that the instrumental calibration of the current method is performed through the signal of a reference phantom  $S_{sample,ref}$  according to Equation 3.19.

$$R_{CF} = S_{sample} \cdot CF = S_{sample} \cdot \frac{R_{ref}^{LUT}}{S_{sample,ref}} \quad (3.19)$$

Consider  $IRF_{det}$  to be the IRF of the detection path of any of the developed Non-Contact setups (see Figures 3.31 and 3.44). Using Equations 3.15 (or equivalent 3.18) and 3.19 it can be said that

$$R_{CF} = \frac{S_F}{IRF_{det}} \cdot \frac{R_{ref}^{LUT}}{S_{F,ref}} = S_F \cdot \frac{R_{ref}^{LUT}}{S_{F,ref}}$$

Notice that, since  $IRF_{det}$  is constant, once the instrumental calibration is considered in the unknown measurement, it has no effect. In other words, IRF-corrected  $S_{sample}$  and

uncorrected  $S_F$  signals calculate the same  $R_{CF}$  and thereby determine the same optical properties. Therefore, the non-contact constant calibration Equation 3.19 is equivalent to the contact constant calibration Equation 3.4. This proves the method's robustness regarding constant multiplicative instrumental calibration. Thus, the measurement of any  $IRF$  is not required. This is why, the constant CCD quantum efficiency is not considered either.

### *Instrumental Calibration of the varying effect of the illumination spatial extension*

When the non-modelled effect is no longer constant, the instrumental calibration step, described in the previous paragraph, is not enough to allow optical properties quantification. This is the case with the spatial extension of the non-contact illumination profiles (see Figure 3.38), which affect the detected reflectance according to the optical parameters of the sample. In other words, the effect can be considered constant only if the reference and unknown phantoms have similar optical properties and are illuminated by the same beam profile. As soon as the optical properties between them change, the effect on the reflectance is no longer constant and remains uncorrected.

To tackle the varying repercussion of the extended illumination profile on the reflectance, we propose to use an adaptive calibration strategy. This strategy is based on the optimal choice of the closest reference optical properties to the unknown sample's, so that the illumination extension effect remains constant. For this, the adaptive calibration makes use of a base of various measured reference phantoms with different reference optical properties. This is the principle for the Adaptive Calibration Algorithm (ACA-Pro) that we have developed and that is thoroughly explained in Chapter 4.

### 3.5.2 Instrumental Challenges

To preserve the geometrical dimensions and intensities of the Non-Contact DRSsr projected images, samples should be placed at the focal plane. Thus, focusing is an essential step to acquire robust measurements with Non-Contact DRSsr, since it directly affects the estimation accuracy of optical properties. We use this optical property estimation accuracy to define a depth of field (DOF) range, which is particularly relevant for measuring uneven biological samples. The following paragraphs analyse the instrumental aspects of focusing and DOF, individually.

#### Focusing

Focusing of the sample is performed before measurement acquisition, and it is achieved in two steps. In the first step, the height of the support is accommodated to a visually-acceptable first focusing range. In the second step, we make use of  $S6$  since it is a direct measurement of the signal at the borders of the projected illumination beam that decreases at the focal plane. To visualize this, some pictures were taken with the setup shown in Figure 3.21 by placing the CCD camera at different heights. An example of focused and unfocused images is shown in Figure 3.45 with the corresponding x-profiles crossing the illumination beam,  $F6$ , and  $F5$  (red line on images). It is clear that  $F6$  is the most sensitive to the focused or unfocused central point. This is why we used  $S6$  intensity as a good indicator for focusing.

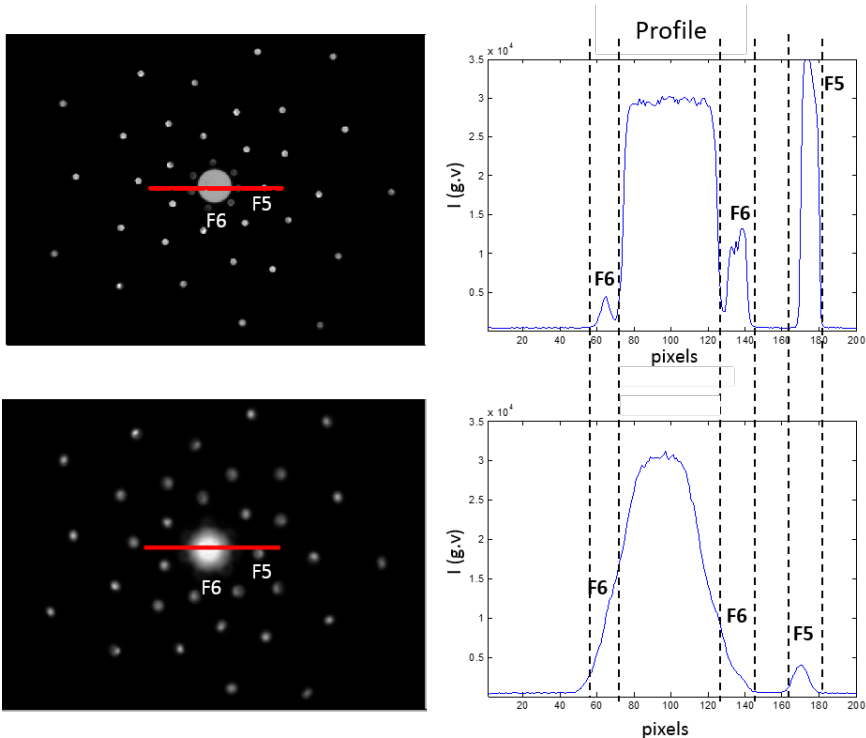


Figure 3.45: Focused and unfocused images with their corresponding profiles.

To better understand the changes of reflectance intensity in  $F5 - F6$  with focusing, we measured  $S5 - S6$  with both probe-based Non-Contact DRSSr setups on a liquid phantom at different object planes. A span of  $6.5 \text{ mm}$ , around the visually-fixed initial focal plane, is covered with  $500 \mu\text{m}$  steps. Measured  $S5 - S6$  are corrected from offset and integration time ( $S5_c$  and  $S6_c$ ) and averaged over the whole spectrum. Figure 3.46 shows  $S5_c$  and  $S6_c$  in function of the object plane height.

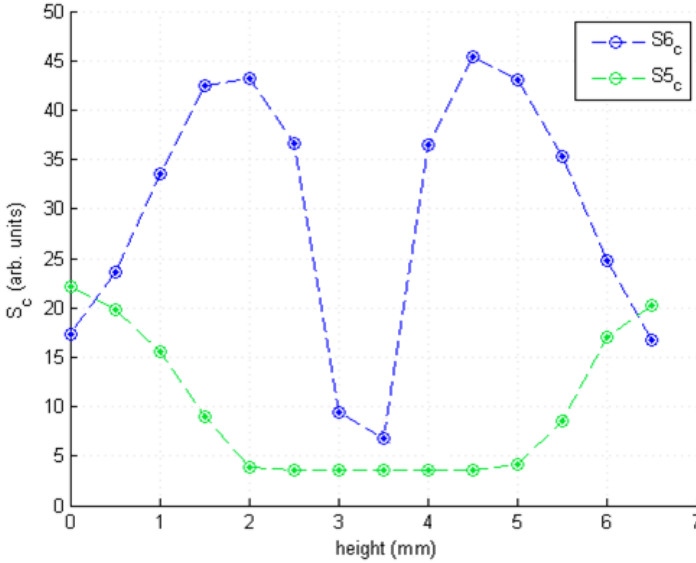


Figure 3.46: Reflectance Intensity appertaining to fibre rings  $F5$  and  $F6$  of a phantom placed at an object plane between  $-3.5 \text{ mm}$  and  $+3 \text{ mm}$  from the focal plane.

The high sensitivity of  $S6_c$  to the object plane height is confirmed. Consequently, the height obtaining minimal  $S6_c$  within the first focusing range is determined to be the methodical focal plane for all experimental procedures. Remark that the height range for which  $S6_c$  is stable is smaller than  $500 \mu\text{m}$ .

To ensure the same focal plane for measurements on different phantoms, it was decided to fix the height of the adjustable support for one phantom and preserve it for all other phantoms. For this purpose, the same container is used for all measurements and the phantom volume is kept constant by controlling its weight.

This focusing protocol is not feasible for biological samples in which surface heterogeneities are usually larger than  $500 \mu\text{m}$ . The robustness of these measurements will completely depend on the depth of field (DOF). To define the DOF range of the technique, the error of estimated optical properties of reflectance signals taken at different object planes, is calculated, as explained in the next paragraph.

### Depth of Field (DOF)

As explained and demonstrated in Section 3.5.1, the calibration of the instrumental effects is only possible if non-simulated changes remain constant. Therefore, not only measurement conditions but also all non-simulated effects (geometrical alterations and specular effects) of the Non-Contact setups should be kept constant for all measurements.

In all Non-Contact setups,  $F6$  is greatly affected by the non-simulated extension of the illumination profile (see Figure 3.38). As seen in Figure 3.46, the strong sensitivity of  $S6$ , requires a positioning repeatability of the object plane to be within a range smaller than  $500 \mu m$  so that  $S6$  signals remain constant and can be corrected by the instrumental calibration strategy. To consider a more convenient DOF (higher than  $500 \mu m$ ) for biological samples,  $S6$  cannot participate in the optical properties estimation of Non-Contact systems. Thereby,  $S5 - S1$  having a constant non-modelled effect on the object plane (placed in a range of  $3 mm$ , see Figure 3.46) of the same phantom, are considered. The optical properties estimated with  $S5 - S1$  measured at different object planes, are consequently used to define the DOF.

Figures 3.47 - 3.50 show the estimated  $\mu'_s$  and  $\mu_a$  at various object plane height ranges:  $2.5 - 5$ ,  $3 - 4.2$ , and  $3 - 3.5 mm$ . Notice from Figure 3.48a that the  $\mu'_s$  estimation error for a range of  $2.5 mm$  (between  $2.5 - 5 mm$ ), is very high, especially after  $750 nm$ . When considering a smaller range of  $1.2 mm$  (between  $3$  and  $4.2 mm$ ), the relative error is  $4.1 \%$  for  $\mu'_s$  (see Figure 3.48b) and  $27\%$  for  $\mu_a$  (see Figure 3.50a). A further reduction of the height range to  $500 \mu m$  (between  $3 - 3.5 mm$ ) achieves minimal  $\mu_a$  relative error of  $17\%$  (see Figure 3.50b). Because the latter  $\mu_a$  relative error is too high, the absorption of biological samples cannot be optimally quantified within this DOF. Only plane samples, such as intralipid liquid phantoms, for which the entire measured surface lies at the focal plane can be optimally quantified in  $\mu_a$ . This poses a major limitation for the absorption quantification of biological samples with the Non-Contact DRSSr technique. We can define a convenient DOF of  $1.2 mm$  that achieves only acceptable  $\mu'_s$  estimation with Non-Contact DRSSr measurements and corresponding error of  $4.1\%$ .

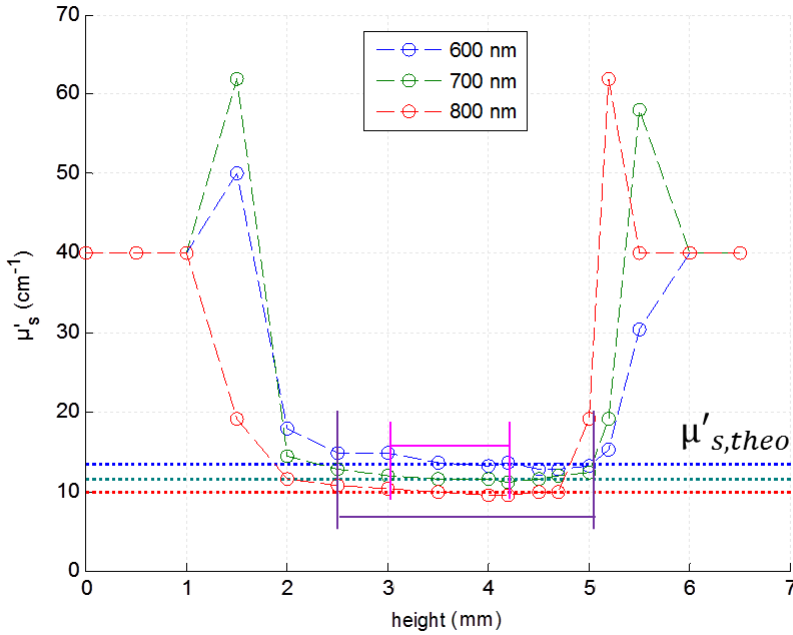


Figure 3.47:  $\mu'_s$  estimated with measurements at different heights and a fixed calibration measurement at the methodical focal plane ( $3.5\text{ mm}$ ) of a phantom with  $IL_{theo} = 1\%$  (equivalent  $\mu'_{s,theo}$ ). The color code between estimated (circles) and theoretical (dotted lines)  $\mu'_s$  applies for the different wavelengths:  $600$ ,  $700$  and  $800\text{ nm}$ .

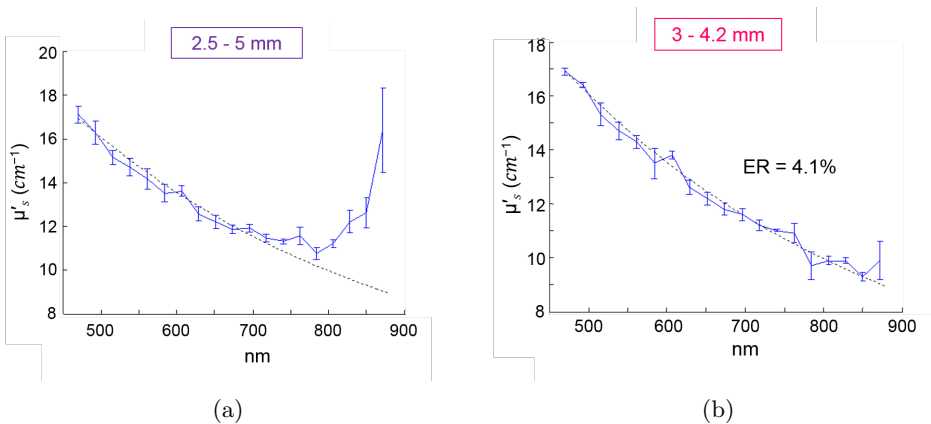


Figure 3.48:  $\mu'_s$  calculated over the entire spectrum with a fixed focused reference phantom and measurements at object plane height ranges: (a)  $2.5\text{ mm}$  and (b)  $1.2\text{ mm}$ , defined in Figure 3.47. For (a), the divergence at  $\lambda > 700\text{ nm}$  is most probably related to the faulty correction of the doublet's parasite reflections.

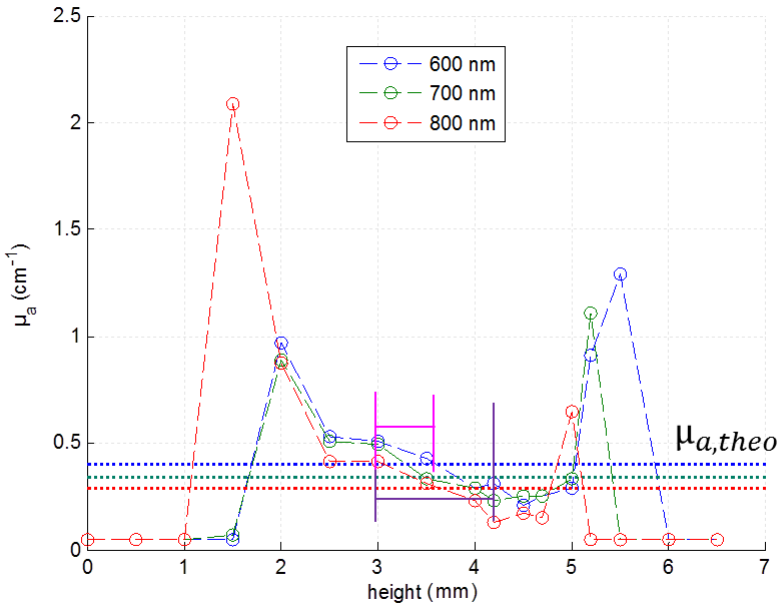


Figure 3.49:  $\mu_a$  estimated with measurements at different heights and a fixed calibration measurement at the methodical focal plane (3.5 mm) of a phantom with  $\mu_{a,theo} = 0.4 \text{ cm}^{-1}$ . The color code between estimated (circles) and theoretical (dotted lines)  $\mu_a$  applies for the different wavelengths: 600, 700 and 800 nm.

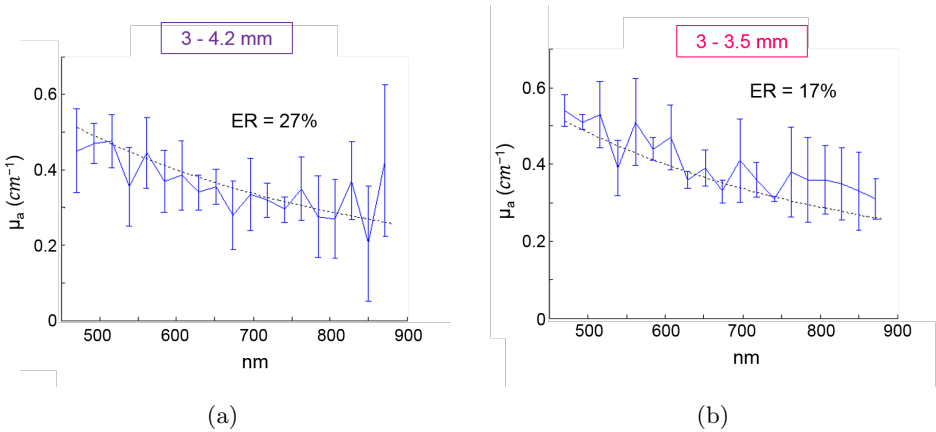


Figure 3.50:  $\mu_a$  calculated with a fixed focused reference phantom and measurements at object plane height ranges: (a) 1.2 mm, defined in Figure 3.47 for minimal  $\mu'_s$  and (b) 500  $\mu\text{m}$ , defined with both Figures 3.47 and 3.49 for minimal  $\mu'_s$  and  $\mu_a$ .

## 3.6 Conclusion

In this Chapter we have described the development of the *initial Non-Contact DRSSr*, used for the *Dual-Step* technique, and the *CCD-based Non-Contact DRSSr* setups. These were built according to the same instrumental geometry of the reference contact DRSSr setup used for the Monte Carlo simulation. Because this Monte Carlo model considers a contact measurement modality, the different effects on non-contact measurements should be corrected to allow quantification of optical properties with the corresponding Non-Contact DRSSr setups. The major non-modelled changes include the spectral effect of optical components on signals and the spatial elongation of projected beams. These are considered by an instrumental calibration approach, that corrects only constant effects of changes. To calibrate from the non-constant effect of changes, the instrumental calibration is extended towards an Adaptive Calibration Algorithm (ACA-Pro), described in the next Chapter 4.

# 4

---

## ACA-Pro algorithm

This Chapter describes the *Adaptive Calibration Algorithm and Protocol (ACA-Pro)* that has been developed to correct for the varying geometrical effect (see Section 3.5.1) of DRSsr setups. The algorithm makes use of reference signals to calibrate measurements taken with any DRSsr setup and a unique Monte Carlo simulation. *ACA-Pro* plays an essential role in the quantification of optical properties with all the optical instruments considered in this work.

The first Section 4.1 briefly explains the main alteration of the spatial illumination profile between DRSsr measurements and the Monte Carlo simulation that has to be corrected to allow absolute quantification.

Section 4.2 shows about the already existing calibration methods for DRSsr and marks out the main differences with respect to our proposition, *ACA-Pro* (Section 4.3). Section 4.4 details the principle of the algorithm and the different strategies considered.

Section 4.5 validates the performance of *ACA-Pro* with the first results on liquid phantoms with different optical properties. Section 4.5.4 is particularly interesting as it confirms the interest of *ACA-Pro* for non-contact measurements even with a more adapted Monte Carlo simulation that considers a Non-Contact DRSsr illumination profile. The validation of the entire algorithm is performed not only on intralipid phantoms but also on an ex-vivo biological tissue (Section 4.6).

Section 4.7 summarizes the main achievements of the developed algorithm ACA-Pro.

### 4.1 Non-modelled illumination profile effect

The various non-contact components: doublets, plate beamsplitter and filters (depending on the Non-Contact DRSsr setup), induce optical geometrical aberrations that broaden the projection of the illumination point on the sample (see Sections 3.3.2 and 3.4.2). To allow the estimation of optical properties with a single Monte Carlo simulation under contact conditions (see Section 3.2.4) this non-modelled illumination extension is to be corrected.

As mentioned in the previous Section 3.5.1, the non-simulated extension of the illumination profile effect on the reflectance  $S1 - S5$  can be kept constant only on phan-

toms having the same optical properties. However, changing the optical properties of the measured phantoms, changes the non-simulated reflectance on  $S5 - S1$ . In other words,  $F5 - F1$  fibre rings measure a combined diffuse reflectance signal resulting from the modelled central illumination point and the non-modelled illumination extension. Recall that in all Non-Contact setups, the influence of the non-modelled extended illumination profile is strongest for the closest fibres  $F6 - F4$  (see Figure 3.38). Moreover, as explained previously,  $\mu'_s$  and  $\mu_a$  are estimated with fibres  $F5 - F3$  and  $F5 - F1$ , respectively (see Figure 3.14). Consequently,  $\mu'_s$  estimation is the most affected optical property by this non-modelled extension of the illumination profile. It follows that, because of cross-talk, the degradation of  $\mu'_s$  estimation is forwarded to the  $\mu_a$  estimation. Thus, to achieve optimal estimation of both optical properties, it is fundamental to correct for this non-constant illumination profile extension effect which is not done in the current Instrumental Calibration method described previously in Section 3.5.1.

## 4.2 State of the Art

To derive absolute quantitative optical properties of  $\mu_a$  and  $\mu'_s$  with DRSSr techniques, several research groups have proposed different calibration approaches.

A possible correction strategy considers the non-contact projected illumination beam profile in the Monte Carlo simulations as it is done by [Foschum et al., 2011]. Not only is this process individual to each instrumental setup, but the methodology achieves only appropriate  $\mu'_s$  evaluation. Estimation errors of  $\mu_a$  reach 20% (at the focal plane) and the considered values of  $\mu_a$  do not encompass those proper to biological tissue.

Other methods rely on the instrumental calibration of DRS measurements through phantoms. This instrumental calibration may be integrated in inverse models such as diffusion analytical models ([Zonios et al., 2006], [Zonios et al., 2011], [Yu et al., 2008], [Qin et al., 2006]), Monte-Carlo simulations ([Palmer et al., 2006], [Thueller et al., 2003], [Zhong et al., 2014]) or experiment-based look-up-tables (LUT) ([Rajaram et al., 2008], [Bish et al., 2014]).

For instance, [Zonios et al., 2006] uses multiple phantoms, made of polystyrene beads and bovine blood, to deduce two unknown factors  $k_1$  and  $k_2$ . These factors are integrated in the modified diffusion equation to obtain a semi-analytical model of the diffuse reflectance. Factors  $k_1$  and  $k_2$  depend not only on the geometrical of the probe and the refractive indices of the medium but also on the optical properties of the calibration phantom. Therefore, for a wider range of optical properties, the accuracy of the solution with a single pair  $k_1$  and  $k_2$ , is deteriorated. This was verified through a comparison with Monte Carlo simulations by [Zonios et al., 2011], who proposed modelling  $k_1$  and  $k_2$  in function of the absorption and scattering coefficients. For this, an extensive phantom study and additional parameters are used. This increases the number of fixed variables that influence estimation accuracy. Moreover, the semi-analytical model is limited to samples having haemoglobin as the only present chromophore.

[Yu et al., 2008] makes use of the [Zonios et al., 2006] model and multiple calibration phantoms, made of intralipid and haemoglobin, to fit measurements and derive scattering and haemoglobin concentration parameters with a Non-Contact DRSSr system. Scattering and haemoglobin concentration parameter errors are less than 5% and 10%, respectively.

[Qin et al., 2006] makes use of the diffusion approximation at several  $SD$  distances and calibrates from the instrumental effect through the measurement of a single intralipid phantom having optical properties values in the middle of the considered range. The average estimation errors are 7% for  $\mu'_s$  and 12% for  $\mu_a$ , being higher for those far away from the calibration phantom.

With a single calibration phantom measurement at a single  $SD$ , [Palmer et al., 2006] achieves optical properties estimation errors  $<12\%$  for a large range of absorption properties. A big advantage of this work is that the Monte-Carlo is not individually simulated for the specific contact probe geometry. It is the calibration measurement that compensates all the geometrical changes of the single  $SD$  probe. The technique is based on an iterative methodology that adjusts an initial guess of optical properties estimations until the error between the measured and simulated reflectance is minimized. To ensure convergence to a global minimum, the procedure is repeated many times with randomly chosen initial guesses of optical parameters. This can be computationally expensive.

[Pham et al., 2000] calibrates hyperspectral CCD measurements with a single reference intralipid phantom and achieves errors  $<5\%$  for  $\mu'_s$  and  $<11\%$  for  $\mu_a$  but only for a low to moderate absorption range.

[Thueller et al., 2003] uses various  $SD$  separations and required multiple phantoms for calibration, performed at each wavelength and  $SD$  distance of the contact probe. Errors are lower than 10% both for  $\mu_a$  and  $\mu'_s$  in a low to moderate absorption range.

[Zhong et al., 2014] develops a two-layered Monte Carlo simulation and uses a general calibration factor to correct measurements at a single  $SD$  of a contact probe. The calibration factor is derived from measurements of 7 phantoms with different  $\mu'_s$  and  $\mu_a$  values. The estimated results show high correlation of estimated parameters of melanin and blood oxygenation with gold-standard measurements.

Other groups avoid the use of analytical diffusion models which are not valid for short source-detector distances and high absorbing media, or Monte Carlo simulations which are complex and require long computing times. They achieve this through an inverse model based on a look-up-table built with experimental measurements of phantoms in which the instrumental calibration is already integrated.

[Rajaram et al., 2008] use a matrix of 24 phantoms, made of polystyrene spheres and diluted ink with varying optical properties. Average estimation errors are lower than 5.9% for  $\mu'_s$  and 11.6% for  $\mu_a$ .

[Bish et al., 2014] used the same methodology for a non-contact probe, achieving an average error of 5.14% for  $\mu'_s$  and 8.34% for  $\mu_a$ .

The merit of this experimental inverse-model technique is that it achieves good estimation accuracy which might however be vulnerable to the accumulation of experimental noise. Moreover, it is limited by the amount of phantoms that need to be produced and the bound range of finite optical properties measured.

Table 4.1 summarizes the previously described methods including the light-transport model, the optical properties range, the geometry and type of detector used together with the measurement modality (contact/non-contact) and estimation errors achieved.

For comparison, we included the performance of the *ACA-Pro* algorithm developed in this work and further explained in the next Sections.

Table 4.1: Summary of Calibration procedures.

Author	Model	Optical Properties Range	Geometry, Modality, and Detector	Calibration	Relative Error <
[Zonios et al., 2011]	Diffusion approximation	$\mu'_s = 5 - 30 \text{ cm}^{-1}$ $\mu_a = 0.01 - 100 \text{ cm}^{-1}$	Single <i>SD</i> , contact many probe geometries	Multiple phantoms	7% for $\mu'_s$ 12% for $\mu_a$
[Yu et al., 2008]	Diffusion approximation [Zonios et al., 2011]	$\mu'_s = 13.5 - 40.6 \text{ cm}^{-1}$ $Hb = 0.5 - 1.5 \text{ mg/ml}$	Single <i>SD</i> , non-contact probe	Multiple phantoms IL+Hb, $\lambda$ -specific	5% for $\mu'_s$ 10% for Hb
[Qin et al., 2006]	Diffusion approximation	$\mu'_s = 2.2 - 23.2 \text{ cm}^{-1}$ $\mu_a = 0.4 - 0.8 \text{ cm}^{-1}$	Multiple <i>SDs</i> , non-contact hyperspectral CCD	Multiple phantoms IL+dye, $\lambda$ - <i>SD</i> -specific	5% for $\mu'_s$ 10% for $\mu_a$
[Palmer et al., 2006]	Monte Carlo	$\mu'_s = 0 - 20.1 \text{ cm}^{-1}$ $\mu_a = 0 - 13 \text{ cm}^{-1}$	Single <i>SD</i> , contact any probe geometry	Single phantom PS+blood/dye, $\lambda$ -specific	12% for $\mu'_s$ and $\mu_a$
[Thueller et al., 2003]	Monte Carlo	$\mu'_s = 10 - 20 \text{ cm}^{-1}$ $\mu_a = 0.5 - 3 \text{ cm}^{-1}$	Multiple <i>SDs</i> , contact probe	Multiple phantoms, PS+dye $\lambda$ - <i>SD</i> -specific	10% for $\mu'_s$ and $\mu_a$
[Pham et al., 2000]	Monte Carlo	$\mu'_s = 3 - 25 \text{ cm}^{-1}$ $\mu_a = 0.01 - 2 \text{ cm}^{-1}$	Multiple <i>SDs</i> , non-contact hyperspectral CCD	Single phantom IL+dye, $\lambda$ - <i>SD</i> -specific	5% for $\mu'_s$ 11% for $\mu_a$
[Zhong et al., 2014]	2-layer Monte Carlo	$\mu'_s = 5.7 - 85 \text{ cm}^{-1}$ $\mu_a = 35 - 36 \text{ cm}^{-1}$	Single <i>SD</i> , contact probe	Multiple phantoms IL+dye, $\lambda$ - <i>SD</i> -specific	good match melanin blood
<b>This work</b>	<b>Monte Carlo</b>	$\mu'_s = 6.8\text{-}40.6 \text{ cm}^{-1}$ $\mu_a = 0.2\text{-}3 \text{ cm}^{-1}$	<b>Multiple <i>SDs</i>, non-contact / contact any geometry probe or CCD</b>	<b>Multiple IL+dye phantoms, <math>\lambda</math>-<i>SD</i>-specific</b>	<b>4% for <math>\mu'_s</math> 8% for <math>\mu_a</math></b>
[Rajaram et al., 2008]	Experimental LUT	$\mu'_s = 7.2 - 49.1 \text{ cm}^{-1}$ $\mu_a = 0 - 22.9 \text{ cm}^{-1}$	Multiple <i>SDs</i> , contact probe	Multiple PS+dye phantoms, $\lambda$ - <i>SD</i> -specific	5.9% for $\mu'_s$ 11.6% for $\mu_a$
[Bish et al., 2014]	Experimental LUT	$\mu'_s = 2.8 - 19.1 \text{ cm}^{-1}$ $BVF = 2.1 - 2.6 \text{ mg/ml}$	Single <i>SD</i> , non-contact probe	Multiple PS+dye phantoms, $\lambda$ -specific	5.14% for $\mu'_s$ 8.34% for $\mu_a$

## 4.3 Proposition: ACA-Pro algorithm

Our method for optical properties estimations relies on the calculating precision of a unique Monte Carlo simulation under contact conditions and the instrumental *ACA-Pro* calibration of non-contact measurements. This establishes a new way to overcome the high deviations between reflectances measured with the contact and those measured with the developed Non-Contact DRSSr setups without the need to establish individualized Monte Carlo simulations for each measurement modality. From all the studied research groups, [Palmer et al., 2006] is the only that develops a similar calibration procedure providing flexibility for different contact probe geometries. However, non-contact measurements are not taken into account and the procedure iterates several Monte Carlo simulations, which can be computationally expensive.

The *ACA-Pro* algorithm we propose is born as a  $\mu'_s$ -based calibration approach and relies on the fact that for the same  $\mu'_s$  of reference and unknown phantoms the non-modelled effect of the illumination profile on the measured reflectance remains minimal. Consequently, we propose the use of a limited number (3 to 6) of reference phantoms, having different scattering properties, to build an experimental interpolated model of the illumination effect on the measured reflectance.

Furthermore, we include a robust additional calibration approach that compensates all instrumental intensity variations that can occur between experiments such as those originated by probe ageing or fibre alignment in front of the spectrometer fibre (see Figure 3.5 and Section 3.2.2). We achieve this through the use of a single measurement of an optically stable solid material that characterizes experimental conditions. The new and many advantages of this strategy include the exemption of phantom manufacturing for each experiment and optical stability of the solid material compared to liquid phantoms.

## 4.4 Principle of ACA-Pro

The developed adaptive algorithm has been first developed for  $\mu'_s$ , based on the fact that a  $\mu'_s$  difference between reference and unknown phantoms provokes an unacceptable error in the estimation of  $\mu_a$ . In other words, the *CF* between measurement and simulation mainly changes with the scattering coefficient difference. This is mostly recognizable in non-contact measurements since we use a Monte Carlo simulation under contact conditions.

### 4.4.1 Reference CFs

The key characteristic of the adaptive calibration algorithm (*ACA-Pro*) lies on the selection of the best *CF* for any unknown  $\mu'_s$  inside a studied range. For this purpose, several correction factors *CFs* are pre-computed with  $S_{N,ref}$  corresponding to a set of reference  $\mu'_{s,ref}$  within the studied range. These *CFs*, computed for the signals  $S1 - S5$  used for optical properties estimation (see Section 4.1) and individual wavelength  $\lambda$ , constitute the *CF* reference base set.

The characterization of an unknown phantom follows a first estimation step and, if required, a supplementary linear interpolation step. Using the *CF* reference base set

proper of several  $\mu'_{s,ref}$ , a set of possible unknown  $\widetilde{\mu}'_s$  is computed. In the first step, an error minimization between  $\widetilde{\mu}'_s$  and  $\mu'_{s,ref}$  leads to the choice of the correction factor *CFA*. If *CFA* estimates a  $\widetilde{\mu}'_s^*$  corresponding to a specific  $\mu'_{s,ref}$ ,  $\widetilde{\mu}'_s^*$  and the complementary  $\widetilde{\mu}_a^*$  are considered to be the optimal estimated unknown optical properties  $\widehat{\mu}'_s$  and  $\widehat{\mu}_a$ . This is done individually for each  $\lambda$  and  $S$  signal.

A faster implementation of *ACA-Pro* in the selection of *CFA* is achieved through an iterative method, which initially makes use of single (not the whole set) random  $\mu'_{s,ref}$  and corresponding *CF* to determine  $\widetilde{\mu}'_{s,r}$ . Through an error minimization between  $\mu'_{s,r}$  and all  $\mu'_{s,ref}$ , *CFA* estimating  $\widetilde{\mu}'_s^*$  and  $\widetilde{\mu}_a^*$  is chosen. The flowchart of Figure 4.1 and the results shown in Section 4.5 facilitate the understanding of the algorithm's performance.

#### 4.4.2 Interpolation

If *CFA* estimates  $\widetilde{\mu}'_s^*$  which lies between two neighbouring  $\mu'_{s,ref}$ , a linear interpolation step follows. Neighbouring  $\mu'_{s,ref}$  are used to define an interpolated correction factor *CFB* (corresponding to an interpolated  $\mu'_{s,ref,i}$ ) for each  $S$  and  $\lambda$ . This process is iterated until convergence occurs:  $\widetilde{\mu}'_s = \mu'_{s,ref,i}$ . Thereby, the final correction factor *CFB* obtains the optimal estimation of both optical properties  $\widehat{\mu}'_s = \widetilde{\mu}'_s = \mu'_{s,ref,i}$  and  $\widehat{\mu}_a$  (see Figure 4.1).

#### 4.4.3 Correction of Instrumental Variations

We propose to compensate intensity variations between experiments through an additional robust calibration approach of the *ACA-Pro* algorithm.

Indeed, when comparing two different experiments with the same instrumental setup, conditions may not be identical because of minimal instrumental variations that affect intensity. Change in conditions can be related to:

- The change of motor positions that will change the geometrical alignment between detection fibre bundles and the slit which drives the signal to the spectrometer (see Section 3.2.2), provoking different measured intensities.
- Fibre ageing that will directly provoke a decrease in intensity or even spectral shifts of the measurements.

For the optimal performance of *ACA-Pro* the measurement of the reference phantoms should be done under the same conditions to that of the unknown phantom/sample. In other words, measurements of reference phantoms should be proper of each experiment. Because of the evolving nature of intralipid phantoms that make optical properties mutate after some days, experiments outside this time period ( $t_0$ ) require manufacturing of new fresh phantoms. Only by using freshly fabricated phantoms are their characteristic theoretical absorption and scattering properties (see Section 2.3.1) guaranteed during the experiment. Therefore, each experiment requires a time-consuming preparation of the same fresh phantoms.

To allow a faster and less burdensome instrumental calibration between different experiments, a new approach has been explored. The latter makes use of a single measured signal of a common material  $S_k$  that is taken for each experiment and characterizes the experimental conditions. For this, it is important to guarantee homogeneous constant optical properties of the material over indefinite time periods separating experiments. An attractive alternative to liquid phantoms is the use of homogeneous solids with negligible surface variations and temporal optical stability. Moreover, solid materials do not pose the other problems of liquid phantoms including short-term conservation at low temperatures, and demanding manipulation.

Before considering the instrumental calibration,  $S_k$  is first corrected from the source variations as described in Equation 3.2 to obtain  $S_{Nk}$ . The calibration is then performed by calculating the ratio between  $S_{Nk}$  taken for one experiment or moment  $t_0$ , and that taken for a second experiment or moment  $t_1$  (see Equation 4.1).

$$K_{t_0-t_1} = \frac{S_{Nk,t_0}}{S_{Nk,t_1}} \quad (4.1)$$

Hence, the unknown phantom measurement  $S_N$  at  $t_1$  ( $S_{N,t_1}$ ) is adapted to the original instrumental conditions of the single  $CF$  reference base built with measurements at  $t_0$ . The corresponding signal at  $t_0$   $S_{N,t_0}$  is obtained through the ratio  $K_{t_0-t_1}$  and according to Equation 4.2.

$$S_{N,t_0} = K_{t_0-t_1} \cdot S_{N,t_1} \quad (4.2)$$

Figure 4.1 summarizes the method for optical properties estimation with the *ACA-Pro* calibration process that makes use of a  $CF(\mu'_{s,ref})$  reference base and includes an instrumental variation correction strategy for each  $S$  and  $\lambda$ .

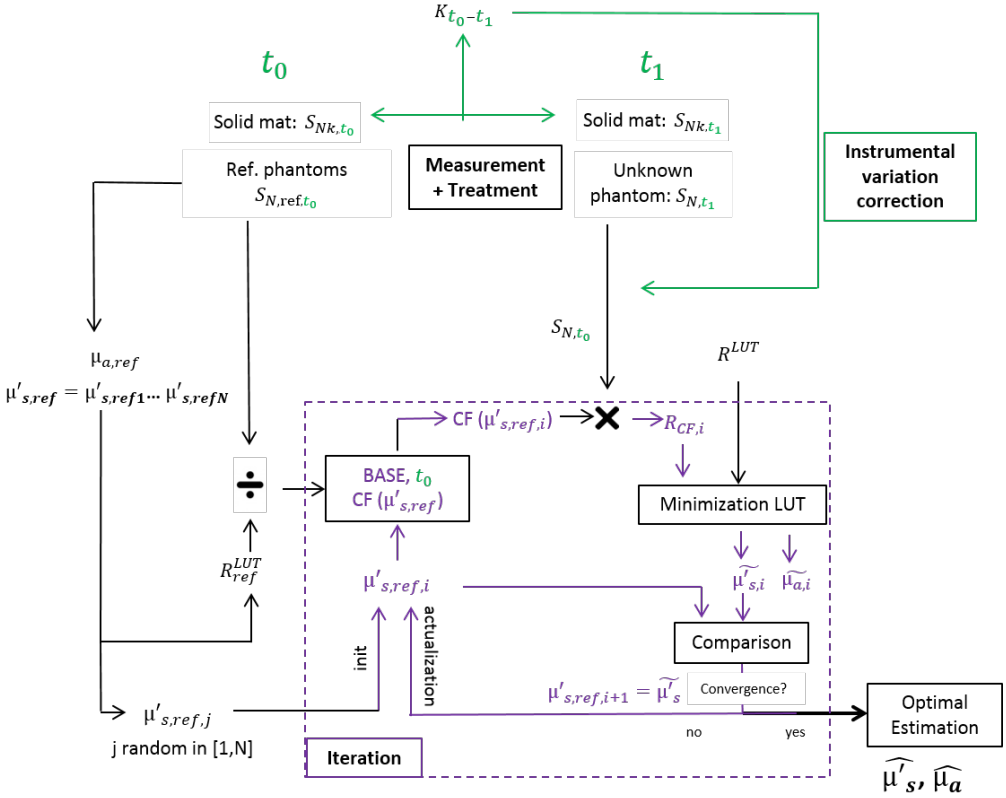


Figure 4.1: Summary of *ACA-Pro* execution with the Principle and Interpolation approach in purple and the Correction of Instrumental Variations in green. keep in mind that the process is performed for individual  $\lambda$ .

## 4.5 Results on phantoms

In the first stage of this study, we mainly validate the *ACA-Pro* algorithm with the probe-based *Contact* and the Non-Contact DRSSr setups. In a second stage, we have tested the performance of the algorithm with a single measurement taken with the *CCD-based DRSSr* setup.

### 4.5.1 CF reference base

A comprehensive *CF* 6-reference base is built with six reference phantoms having common  $\mu_{a,ref} = 0.4 \text{ cm}^{-1}$  and different  $\mu'_{s,ref}$  corresponding to  $IL_{ref} = 0.5, 1, 1.5, 2, 2.5,$  and  $3\%$ . The base is created with measurements proper of each of the three instrumental setups: *Contact*, *initial Non-Contact* and *CCD-based DRSSr*.

Figures 4.2 and 4.3 show examples of the *CF* 6-reference base, measured with the *Contact* and *initial Non-Contact* probe DRSSr systems, respectively, for *F5 – F1* and some representative wavelengths  $\lambda$ . All *CF* values have been normalized with respect to a common phantom having  $IL_{ref} = 1\%$ . Ideally, if no calibration were necessary, all normalized *CF*s should be equal to 1.

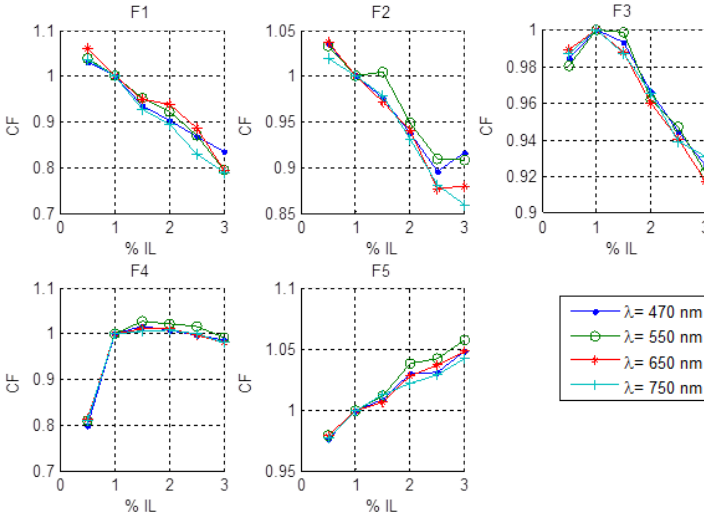


Figure 4.2: Normalized  $CF(IL_{ref})$  6-reference base proper of the *Contact probe DRSSr* setup.

The  $CF(IL - ref)$  6-reference base shows the variability of the relationship between Monte Carlo simulated and measured reflectance of phantoms having different scattering properties.

As mentioned in Section 3.2.6, we note the low accuracy of the Monte Carlo simulation at low scattering values  $IL_{ref} = 0.5\%$ .

It is clear that the relationship over all fibres and wavelengths is more uniform for the *initial Non-Contact DRSSr* setup (Figure 4.3) than that of the *Contact DRSSr* setup

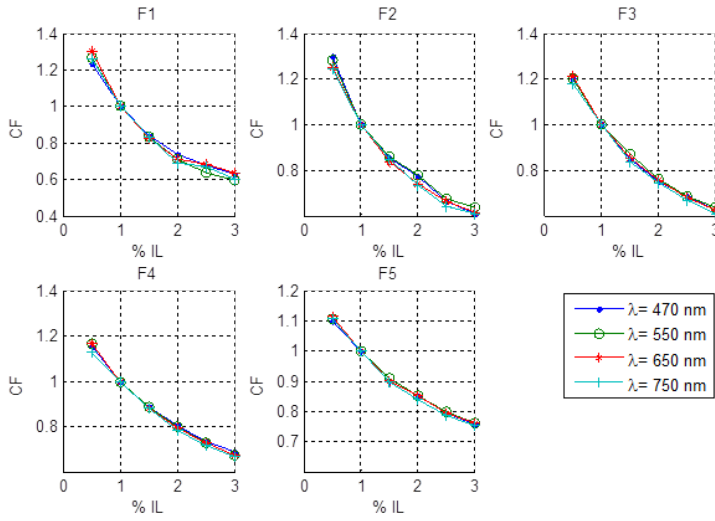


Figure 4.3: Normalized  $CF(IL_{ref})$  6-reference base proper of the *initial Non-Contact probe DRSSr* setup.

(Figure 4.2). For better comparison, we plotted their  $CF$ s on the same Figure 4.4.

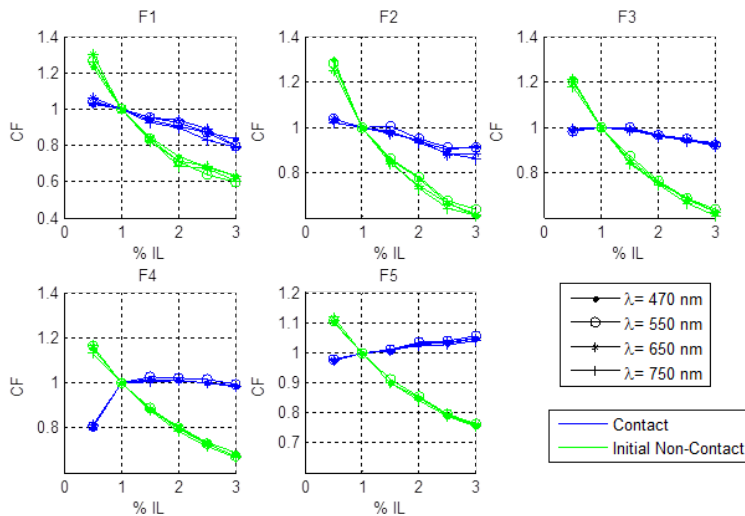


Figure 4.4: Normalized  $CF(IL_{ref})$  proper of *Contact* (Figure 4.2) and *initial Non-Contact* (Figure 4.3) probe DRSSr setups.

It is not surprising that  $CF$ s of different scattering phantoms measured with *initial Non-Contact DRSsr* tend to be generally more uniform than those measured with *Contact DRSsr*. This is because the higher deviation between simulated  $R_{calib}^{LUT}$  and non-contact measurements (due to the different illumination beam profiles) renders experimental noise negligible and results in a more predictable  $CF$  function. Contrarily, the smallest deviations between Monte Carlo and measured contact reflectances make the Contact  $CF$ s more vulnerable to experimental noise. This can be proved when comparing two different measurement sets  $M1$  and  $M2$  deriving different  $CF(IL_{ref})$ -bases (shown in Figures 4.5 and 4.6).

Notice that  $CF(IL_{ref})$ -bases of both Non-Contact measurement sets (see Figure 4.6) are much closer than that of both Contact measurement sets (see Figure 4.5). This illustrates the higher robustness of the Non-Contact  $CF(IL_{ref})$ -base.

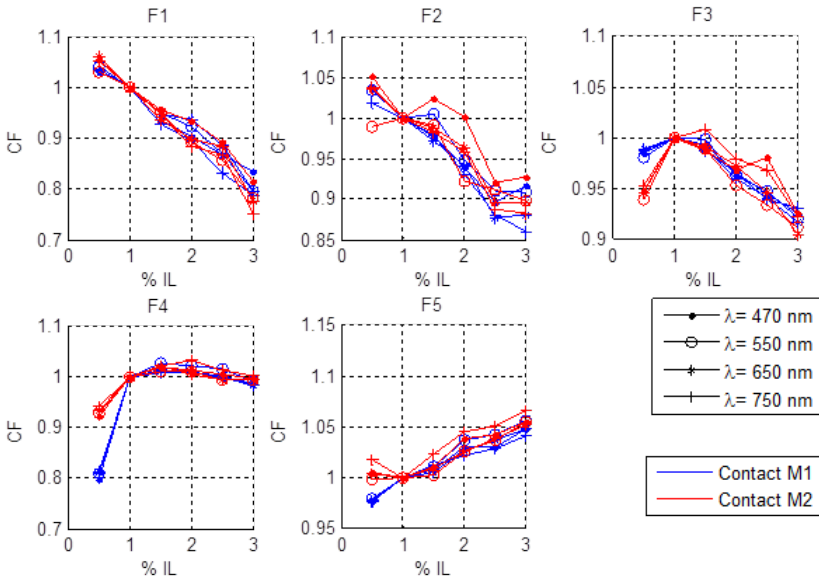


Figure 4.5:  $CF(IL_{ref})$  6-reference base proper of the *Contact probe DRSsr* setup. Measurement sets 1 (M1) and 2 (M2) are compared.

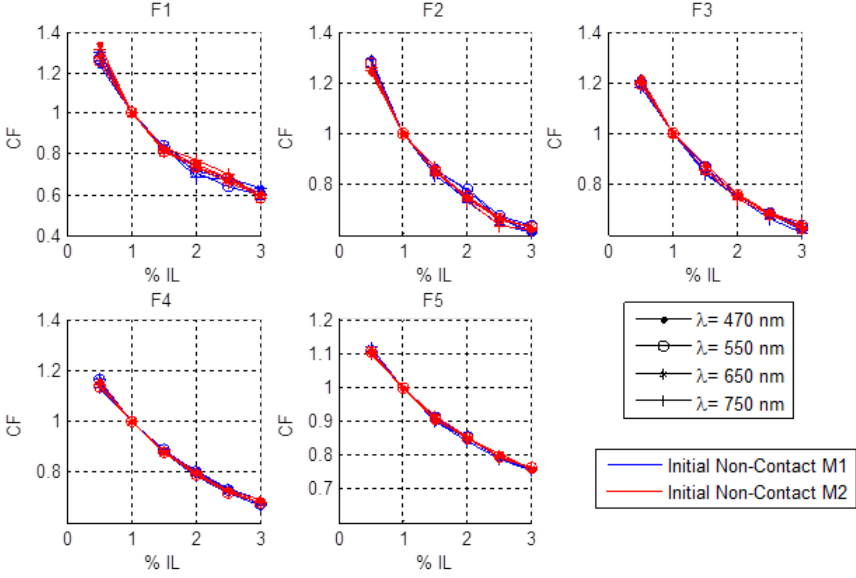


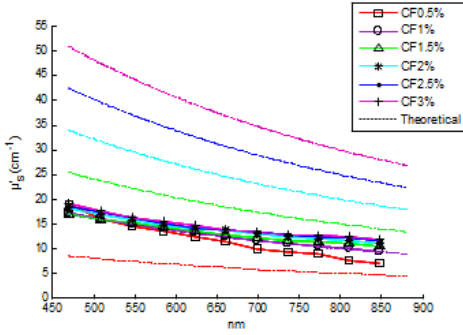
Figure 4.6:  $CF(IL_{ref})$  6-reference base proper of the *initial Non-Contact probe DRSSr* setup. Measurement sets 1 (M1) and 2 (M2) are compared.

#### 4.5.2 Optical Properties estimation with the $CF$ reference base for all setups

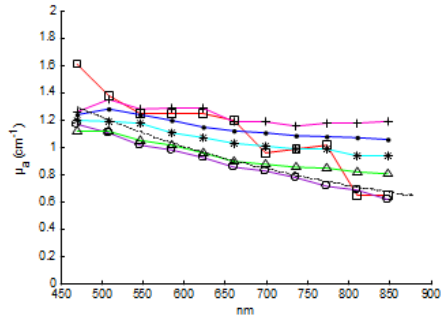
The interest of *ACA-Pro* with the  $CF(IL_{ref})$  reference base set is shown in Figure 4.7 with an unknown phantom having theoretical  $IL_{theo} = 1\%$  and  $\mu_{a,theo} = 1 \text{ cm}^{-1}$  at  $600 \text{ nm}$ . Optical properties  $\tilde{\mu}'_s$  and  $\tilde{\mu}_a$  are estimated with all  $CF$  from the different  $IL_{ref} = X\%$  ( $CFX\%$ ) of the  $CF(IL_{ref})$  6-reference base. The estimation results of the three setups are compared.

When looking at  $\tilde{\mu}'_s$  estimated with all  $CFX\%$  (see Figures 4.7a, 4.7c, and 4.7e), it is clear that most of them are closest to the  $\mu'_{s,ref}$  curve proper of  $IL_{ref} = 1\%$  (dotted violet curve) because  $IL_{theo} = 1\%$ . Not surprisingly, when comparing all  $\tilde{\mu}'_s$  separately, the  $\tilde{\mu}'_s$  estimated with  $CF1\%$  is the nearest (circle-violet curve) to  $IL_{theo}$ . The algorithm therefore chooses  $CF1\%$  as  $CFA$ .

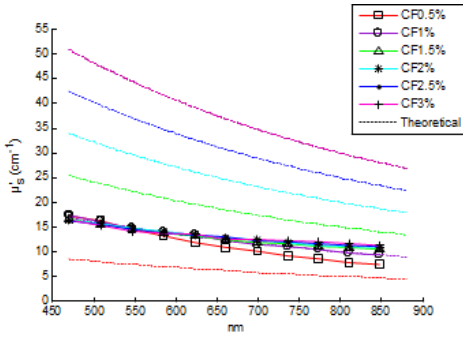
In terms of absorption (see Figures 4.7b, 4.7d, and 4.7f),  $\tilde{\mu}_a$  estimated with  $CF1\%$  (circle-violet curve) obtains the minimal error with respect to  $\mu_{a,theo}$  (dotted-black curve). This is consistent with all probe-based and CCD-based DRSSr measurements, which validates the new *ACA-Pro* algorithm. Additional results validating the use of *ACA-Pro* on measurements obtained with the *folded probe-based Non-Contact DRSSr* instrument (see Figure 3.32) are shown in Appendix A.6.



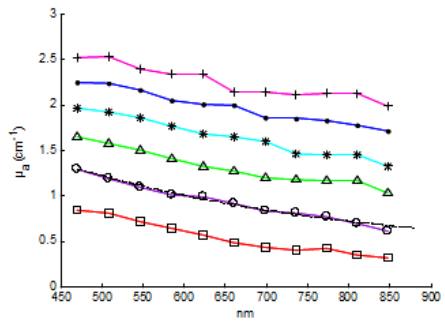
(a) Contact probe DRSSr  $\widetilde{\mu}'_s$  estimation



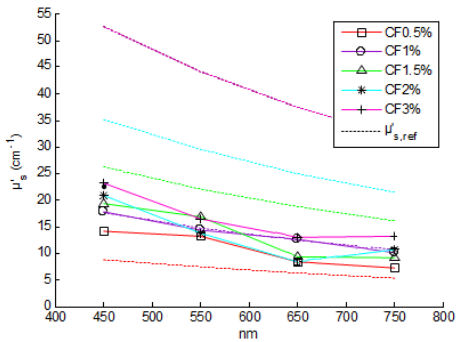
(b) Contact probe DRSSr  $\widetilde{\mu}_a$  estimation



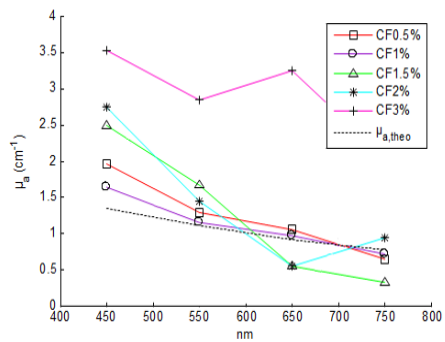
(c) Initial Non-Contact probe DRSSr  $\widetilde{\mu}'_s$  estimation



(d) Initial Non-Contact probe DRSSr  $\widetilde{\mu}_a$  estimation



(e) CCD-based DRSSr  $\widetilde{\mu}'_s$  estimation



(f) CCD-based DRSSr  $\widetilde{\mu}_a$  estimation

Figure 4.7: Estimation of  $\widetilde{\mu}'_s$  and  $\widetilde{\mu}_a$  optical properties of an unknown phantom ( $IL_{theo}=1\%$  and  $\mu_{a,theo}=1\text{ cm}^{-1}$  at  $600\text{ nm}$ ) with the CF( $IL_{ref}$ ) 6-reference base for all DRSSr setups.

Figure 4.8 summarizes the average relative error of optical properties estimations shown in Figure 4.7. Keep in mind that these errors are not impartial because only 4  $\lambda$ s are considered for the *CCD-based DRSsr* setup whilst 11  $\lambda$ s are considered for the probe-based setups, spreading further the weight of a single  $\lambda$  error. The errors give a general idea of the *ACA-Pro* performance and confirm that minimal errors are achieved with  $CF = 1\%$  with all setups.

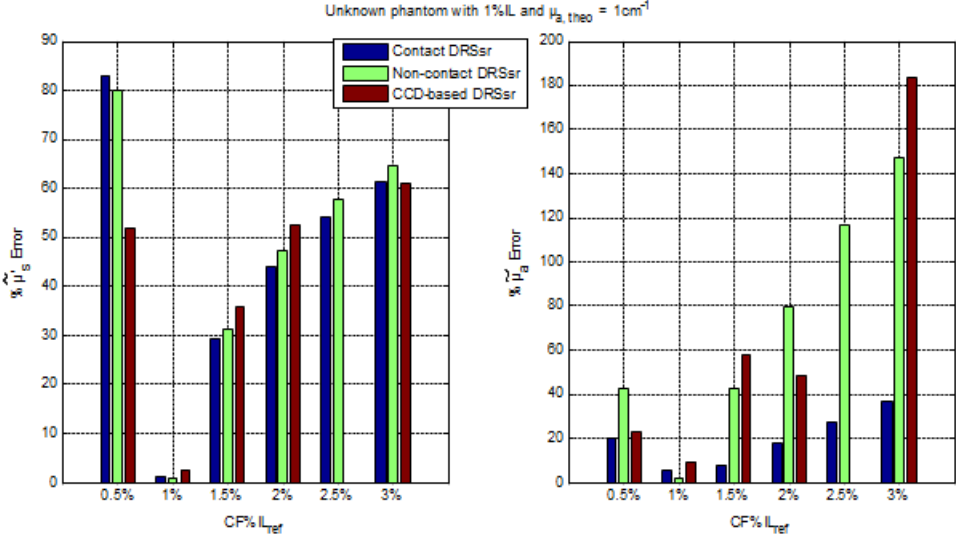


Figure 4.8: Left: Average  $\widetilde{\mu}'_s$  errors between estimation with each  $CFX\%$  and  $\mu'_{s,ref}$  of the reference phantom proper to  $CFX\%$ . Right: Average  $\widetilde{\mu}'_a$  errors between estimation with each  $CFX\%$  and  $\mu_{a,theo}$  of the unknown phantom ( $1\text{ cm}^{-1}$  at  $600\text{ nm}$ ). It is confirmed that  $CF1\%$  achieves minimal errors of both optical properties with all setups.

The average  $\mu'_s$  relative error throughout the spectrum is calculated for each  $\widetilde{\mu}'_s$  and  $\widetilde{\mu}'_a$  with corresponding  $\mu'_{s,ref}$  and  $\mu_{a,theo}$ , respectively. The minimal errors, for the three setups, achieved with  $CFA = CF1\%$ , obtaining  $\widehat{\mu}'_s$  and  $\widehat{\mu}'_a$ , are displayed in Table 4.2.

Table 4.2: Optical properties errors achieved with  $CFA$  for all DRSsr setups.

	$\widehat{\mu}'_s$ error	$\widehat{\mu}'_a$ error
<i>Contact DRSsr</i>	1.3%	5.3%
<i>Initial Non-Contact DRSsr</i>	1%	2.4%
<i>CCD-based DRSsr</i>	2.7%	9.5%

Estimation of unknown optical properties is best achieved for *initial Non-Contact DRSsr* because of its robust  $CF(IL_{ref})$  6-reference base (see Figure 4.6). Correspondingly, *Contact DRSsr* obtains slightly higher error due to the vulnerability to measurement noise of its  $CF(IL_{ref})$  6-reference base (see Figure 4.5).

With *CCD-based DRSsr* optical properties are still estimated within an acceptable range although higher than with the probe-based setups. To further improve estima-

tions, we propose a more advanced *CCD-based DRSSr* setup, with an improved illumination profile, discussed in Appendix A.5.

### 4.5.3 Absorption difference with probe-based setups.

When comparing optical properties estimation with probe-based DRSSr setups of unknown phantoms having several  $\mu_{a,theo} \geq 1 \text{ cm}^{-1}$  and same  $IL_{theo} = IL_{ref} = 1\%$ , the average relative errors, illustrated in Figure 4.9, are obtained.

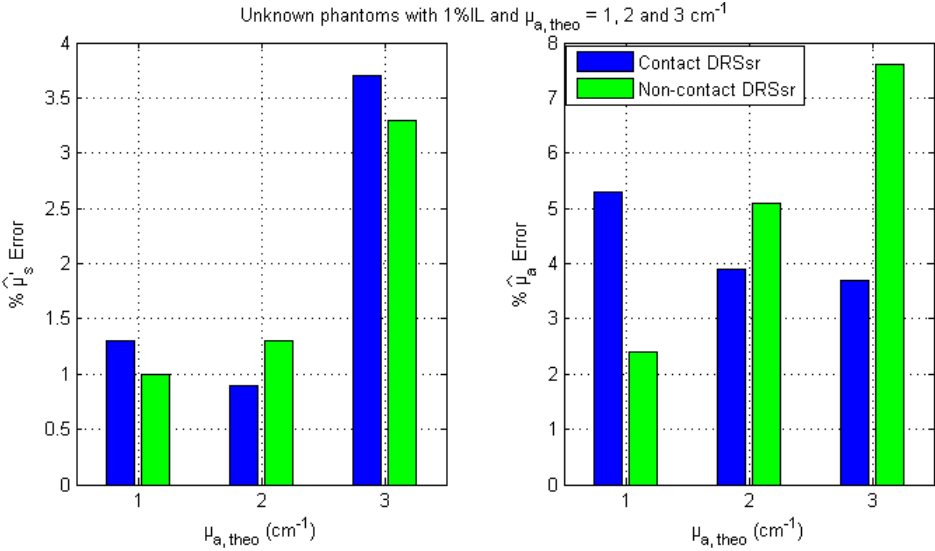


Figure 4.9: Average  $\hat{\mu}'_s$  and  $\hat{\mu}_a$  errors over the working spectrum for different unknown phantoms with  $IL_{theo} = 1\%$  and  $\mu_{a,theo} = 1, 2 \text{ and } 3 \text{ cm}^{-1}$ . *Contact DRSSr* and *Initial Non-Contact DRSSr* estimations.

All  $\hat{\mu}'_s$  errors are considered below 4% for both probe-based DRSSr as a result of the  $\mu'_s$ -based *ACA-Pro* algorithm. For what concerns the  $\hat{\mu}_a$  error, it is seen that for *Contact DRSSr* it tends to stay constant, whilst for the *initial Non-Contact DRSSr* setup it increases proportionally to the deviation from  $\mu_{a,ref}=0.4 \text{ cm}^{-1}$ . To better understand these results, we examined the *CF* obtained with different  $\mu_{a,ref}$ , analogously to what has been done for different  $IL_{ref}$ . Figure 4.10 shows the *CF* calculated from measurements of phantoms with different  $\mu_{a,ref}$  taken with the *Contact* and the *initial Non-Contact* probe-based DRSSr setups. All *CF*s are normalized according to the *CF* of  $\mu_{a,ref}=0.4 \text{ cm}^{-1}$ . Notice that the *CF*s are not constant for all  $\mu_{a,ref}$  and that the deviation from 1 is a direct explanation of the errors seen in Figure 4.9. Comparing Figure 4.4 with Figure 4.10, it can be concluded that the extension of the Non-Contact illumination profile dramatically affects  $\mu'_s$ , but also, to a minor extent,  $\mu_a$ .

Therefore, to further improve the estimation of  $\mu_a$ , the adaptive calibration *ACA-Pro* based on  $\mu_a$  is an attractive approach.

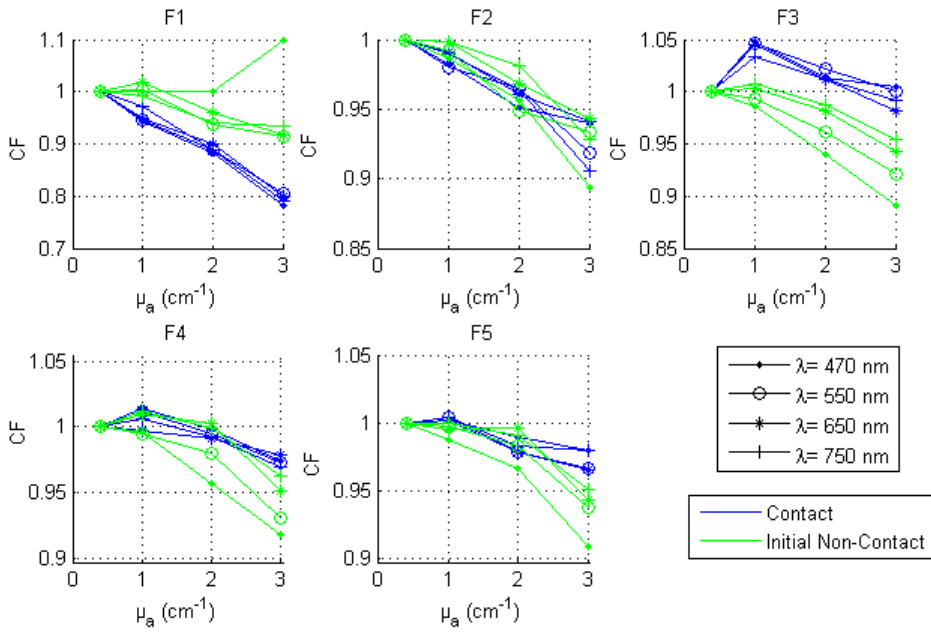


Figure 4.10: CF calculated for different  $\mu_a$  (given at  $600\text{ nm}$ ) with the *Contact* and *initial Non-Contact* DRSr setups.

#### 4.5.4 Optical Properties estimation with Monte Carlo simulation considering Non-Contact conditions

As explained in Section 4.1 and shown by the results of Section 4.5, the profile extension in Non-Contact DRSsr setups, is the main obstacle that *ACA-Pro* overcomes. Still, there are other deviations between experimental measures and the forward model (built for contact DRSsr conditions) that *ACA-Pro* is able to correct to allow for absolute quantification of Non-Contact DRSsr. To prove this, we built a Monte Carlo simulation under non-contact DRSsr conditions and used it to estimate optical properties with the *initial Non-Contact DRSsr* setup.

To build the latter, the impulse response of the simulated medium is necessary, which is obtained with a Monte Carlo simulation in which the illumination photons reach the medium at a single point, propagate in the medium and are finally detected at the surface at different distances. *SD* distances are fixed according to the probe geometry (refer to Figure 3.4) and the considered numerical aperture (0.22) is that of the fibres. This simulation, is employed to obtain  $R^{LUT}$  for a wide range of optical properties,  $\mu_a$  and  $\mu'_s$ . The convolution of this LUT with the measured illumination profile of the *initial Non-Contact DRSsr* setup (shown in Figure 3.26) is performed to obtain  $R^{LUT}$  proper of a Monte-Carlo simulation under the same Non-Contact DRSsr illumination conditions. Figure 4.11 shows the modelled reflectance obtained at *D5* for punctual and Non-Contact DRSsr illumination ( $MC_{Non-Contact}$ ).

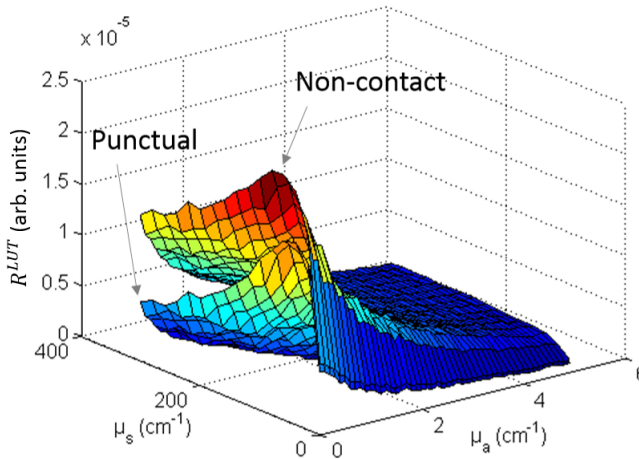


Figure 4.11: Modelled reflectance at *D5* from a Monte-Carlo simulation generated with punctual and extended (Non-Contact DRSsr) illumination.

We used this convoluted Monte Carlo simulation and the same Non-Contact measurements taken with the *initial Non-Contact DRSsr* setup (on phantoms having different scattering properties  $IL = 0.5 - 3\%$ ) to build another  $CF(IL_{ref})$  6-reference base that can be directly compared with Figure 4.4. Figure 4.12 shows the direct comparison of  $CF(IL_{ref})$  6-reference bases generated with Contact and Non-Contact DRSsr measurements comparison with Monte Carlo (MC) simulations that consider the Contact or Non-Contact illumination profiles.

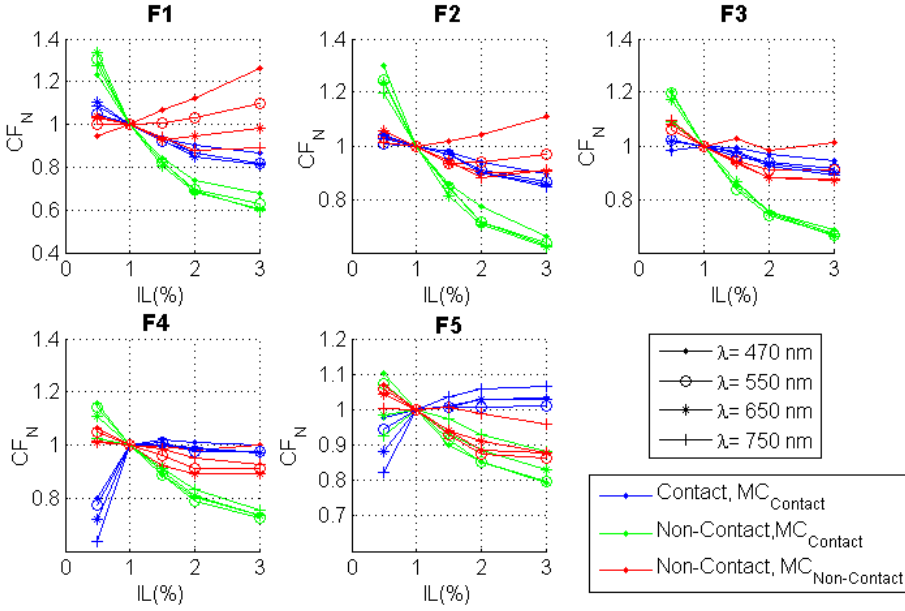


Figure 4.12:  $CF(IL_{ref})$  6-reference bases built with Contact and Non-Contact DRSsr measurements. The latter are compared with the Contact or Non-Contact Monte Carlo (MC) models.  $CF$ s are shown for  $F1 - F5$  and 4  $\lambda$ s.

Notice that, in general, Non-Contact  $CF$ s (for different  $IL_{ref}$ ) have comparable stability to Contact  $CF$ s (Contact  $MC_{Contact}$ ) and, as expected, are closer to 1 for Monte Carlo simulation considering the Non-Contact illumination (Non-Contact  $MC_{Non-Contact}$ ) rather than the Contact illumination profile (Non-Contact  $MC_{Contact}$ ). Yet, Non-Contact  $MC_{Non-Contact}$   $CF$ s are still far from being uniform which directly affect quantification. To further prove this, we estimated an unknown phantom having theoretical  $IL_{theo} = 1\%$  and  $\mu_{a,theo} = 1\text{ cm}^{-1}$  at 600 nm with the different Non-Contact  $MC_{Non-Contact}$   $CF$ s of the reference base. Estimation results and corresponding average errors are shown in Figures 4.24 and 4.14, respectively. It is observable that optimal estimation is still achieved with the  $CF$  having the closest optical properties to the unknown phantom. Therefore, it can be concluded that even with an adapted Monte Carlo simulation, *ACA-Pro* still optimizes quantitative estimation of optical properties with a few reference measurements.

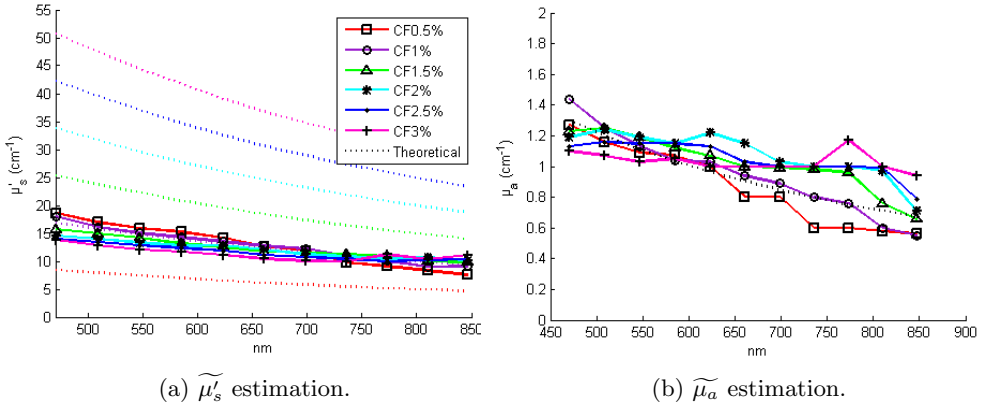


Figure 4.13: *Initial Non-Contact DRSsr* optical properties estimation with punctual Monte Carlo (MC) convoluted with Non-Contact illumination profile,  $MC_{Non-Contact}$ .

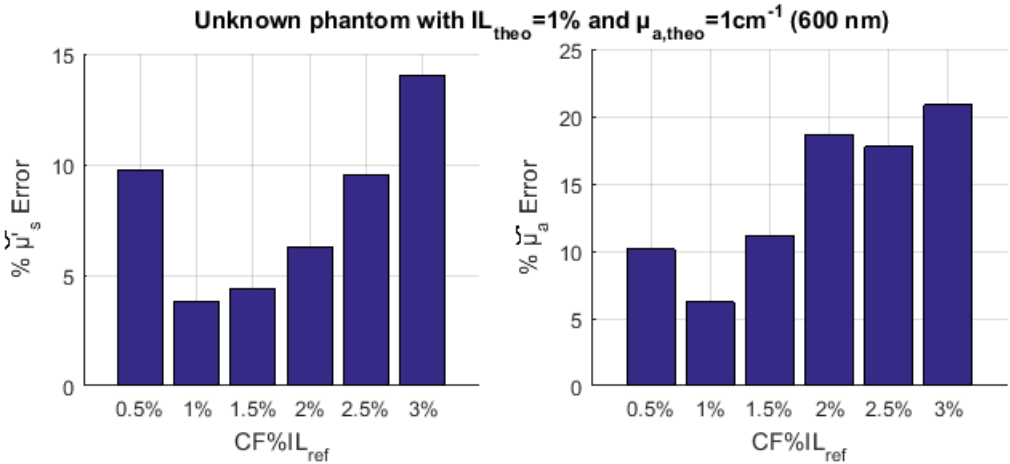


Figure 4.14: Average errors of optical properties estimations obtained with Non-Contact measurements and  $MC_{Non-Contact}$ , shown in Figure 4.24. Left: Average  $\widetilde{\mu}'_s$  errors between estimation with each  $CF\%IL_{ref}$  and  $\mu'_{s,theo}$  ( $IL_{theo} = 1\%$ ) of the unknown phantom. Right: Average  $\widetilde{\mu}_a$  errors between estimation with each  $CF\%IL_{ref}$  and  $\mu_{a,theo} = 1\text{cm}^{-1}$  of the unknown phantom. It is confirmed that CF1% achieves minimal errors of both optical properties.

### 4.5.5 Interpolation

To validate the interpolation method of ACA-Pro, we built a  $CF(IL_{ref})$  2-reference base set with 2 reference phantoms (having common  $\mu_{a,ref}=0.4 \text{ cm}^{-1}$  and  $IL_{ref}=0.5$  and  $1.5 \%$ ) and used it to estimate the optical properties of an unknown phantom with  $IL_{theo} = 1\%$  in an aqueous blue pigment solution.

Recall from Section 4.4.2 that interpolated estimations ( $\widehat{\mu}'_s, \widehat{\mu}_a$ ) are found with correction factor  $CFB$  whilst non-interpolated estimations ( $\widetilde{\mu}'_s, \widetilde{\mu}_a$ ) use  $CFA$ . Figure 4.16 shows interpolated and non-interpolated estimations with the  $CF(IL_{ref})$  2-reference base and the ideal estimation (using  $CF1\%$ ) obtained with all DRSsr setups. Figure 4.15 summarizes the average relative % error.

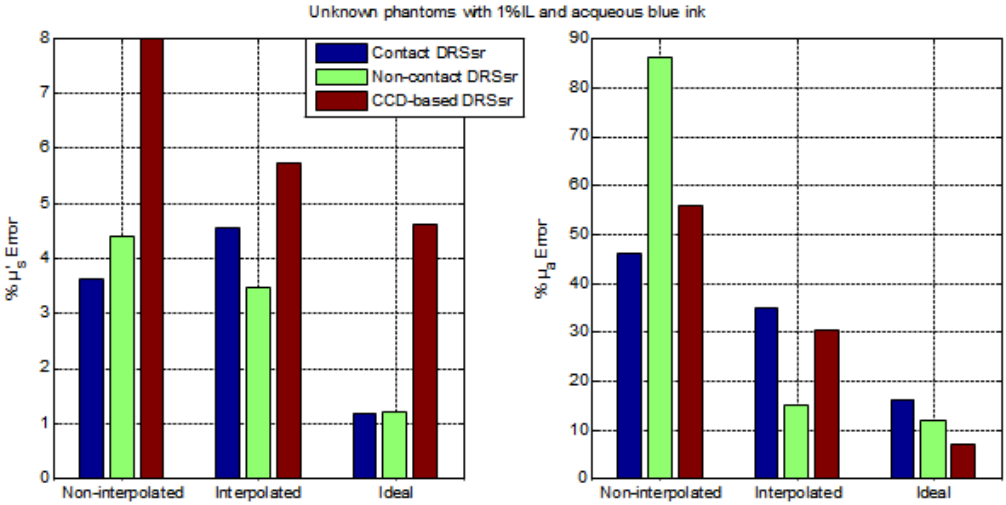
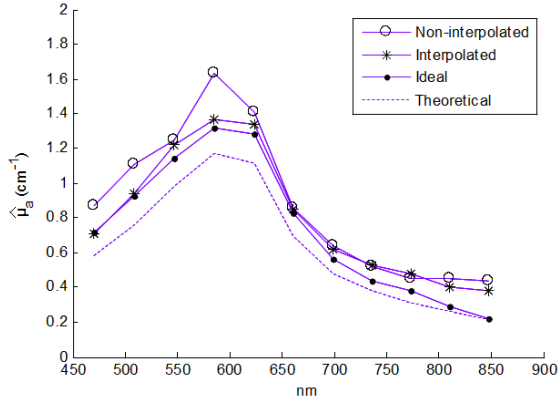
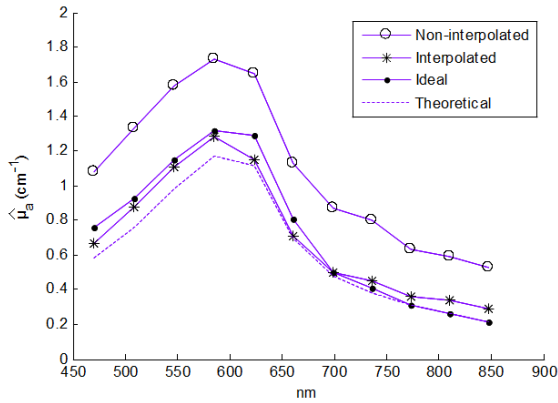


Figure 4.15: Average % error for non-interpolated, interpolated and ideal estimations of optical properties from a phantom with  $IL_{theo} = 1\%$  and dissolved blue pigment.

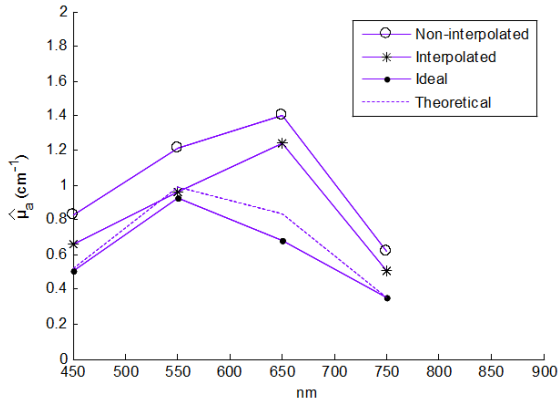
The results validate the interpolation strategy of the algorithm since it generally improves accuracy of optical properties when compared to non-interpolated estimations. The sole exception to this trend is *Contact DRSsr*  $\mu'_s$  estimation because of the discontinuity in its  $CF$ -reference base between  $IL = 0.5 - 1\%$  (see Figure 4.2) due to the limited accuracy of the Monte Carlo simulation at low scattering values ( $IL = 0.5\%$ ), which was already noticed (see Section 3.2.6).



(a) Contact DRSSr



(b) Initial Non-Contact DRSSr



(c) CCD-based DRSSr

Figure 4.16:  $\widehat{\mu}_a$  estimation with interpolated CFB of a phantom having  $IL_{theo} = 1\%$  and  $\mu_{a,theo}$  proper of blue pigment depicted in dotted lines.

### 4.5.6 Correction of Instrumental Variations

An additional section of the *ACA-Pro* approach considers the use of a single measurement of a common homogeneous material that characterizes instrumental conditions to calibrate from variations that occur between different experiments (refer to Section 4.4.3).

#### Extreme experimental variation

As a first validation stage of this calibration algorithm, we consider the *Contact DRSSr* setup only. In this study, a severe variation is simulated by deliberately provoking a change in signal intensity of  $S3$ ,  $S4$  and  $S5$  to affect the sensitivity both of  $\mu'_s$  and  $\mu_a$  estimation (see Figure 3.14). This is done by decentering the spectrometer fibre from the detection fibre bundles  $F3$ ,  $F4$  and  $F5$  by changing the corresponding alignment positions (see Section 3.2.2). A solid piece of white resin [Soloplast, 2015] having stable and homogeneous optical properties is used to characterize experimental conditions before and after the decentralization of fibres.

Figure 4.17 shows  $K_{t_0-t_1}$  (calculated according to Equation 4.1) for all  $F6 - F1$ . Notice that  $S3$ ,  $S4$  and  $S5$  decrease according to the decentralization of the fibres  $F3 - F5$  whilst all other remain almost constant (close to 1). Thereby, it can be said that resin measurements follow instrumental variations.

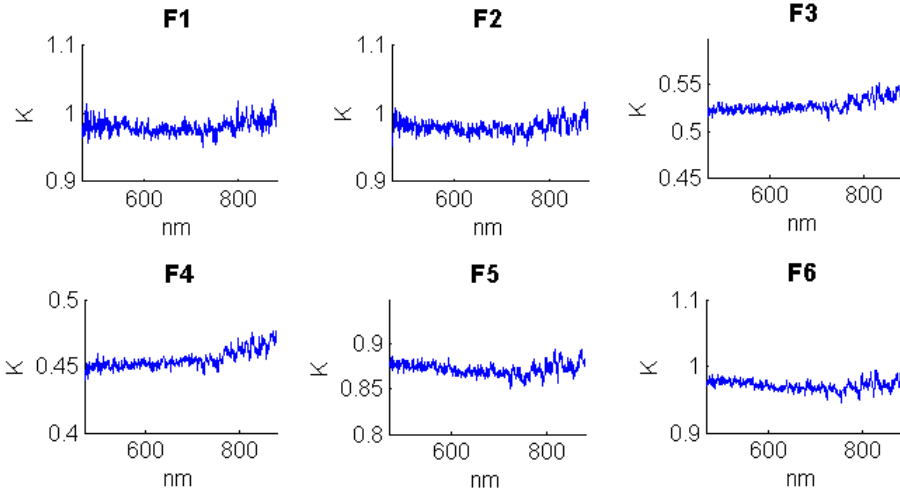
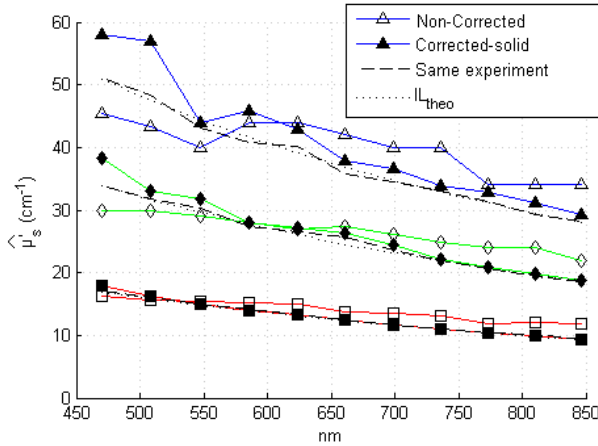


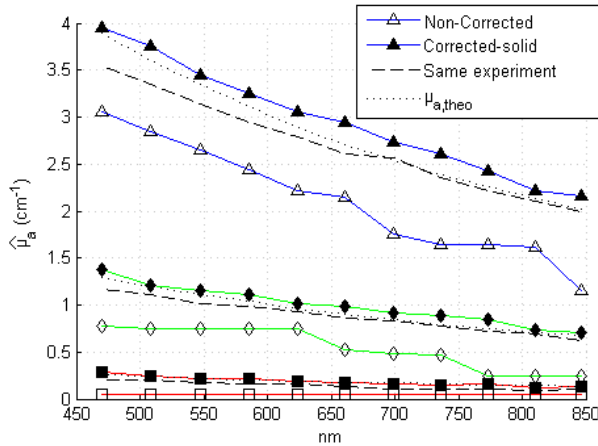
Figure 4.17:  $K_{t_0-t_1}$  Ratio of resin signals acquired at different experimental conditions.

Three different phantoms with  $IL_{theo} = 1, 2,$  and  $3\%$  and common  $\mu_{a,theo} = 1 \text{ cm}^{-1}$  are used to show the interest of the correction strategy for the  $\mu'_s$  estimation. Different phantoms with common  $IL_{theo} = 1\%$  and different  $\mu_{a,theo} = 0.2, 1,$  and  $3 \text{ cm}^{-1}$  are used to show the interest in the  $\mu_a$  estimation of the correction strategy. Figure 4.18 shows  $\widehat{\mu'_s}$  and  $\widehat{\mu_a}$  of the different phantoms (different colors and shapes) with the non-corrected signals (empty shapes) and corrected signals (black-filled shapes). Estimations under the same experimental conditions of the  $CF(IL_{ref})$  6-reference base are illustrated with

slashed black lines whilst theoretical optical properties are represented with black dotted lines.



(a)  $\widehat{\mu}'_s$  estimation of three unknown phantoms with  $IL_{theo} = 1, 2$  and  $3\%$  (different colors and shapes) and common  $\mu_{a,theo} = 1 \text{ cm}^{-1}$ .



(b)  $\widehat{\mu}_a$  estimation of three unknown phantoms with  $\mu_{a,theo} = 0.2, 1$  and  $3 \text{ cm}^{-1}$  (different colors and shapes) and common  $IL_{theo} = 1\%$ .

Figure 4.18: Optical properties  $\widehat{\mu}'_s$  and  $\widehat{\mu}_a$  estimations of unknown phantoms with different  $IL_{theo}$  and  $\mu_{a,theo}$  calibrated with signals measured under different and the same experimental conditions (slashed black lines) to the ones set to build the  $CF(IL_{ref})$  6-reference base. The effect of the conditions difference correction is represented with black-filled shapes and compared to the non-corrected signals represented with unfilled shapes. The legend is given for one phantom but the same line type code applies to all other phantoms.

Figure 4.19 sums up the  $\widehat{\mu}'_s$  and  $\widehat{\mu}_a$  average errors of the estimations from measurements taken with the same and different fibre positions, with and without correction.

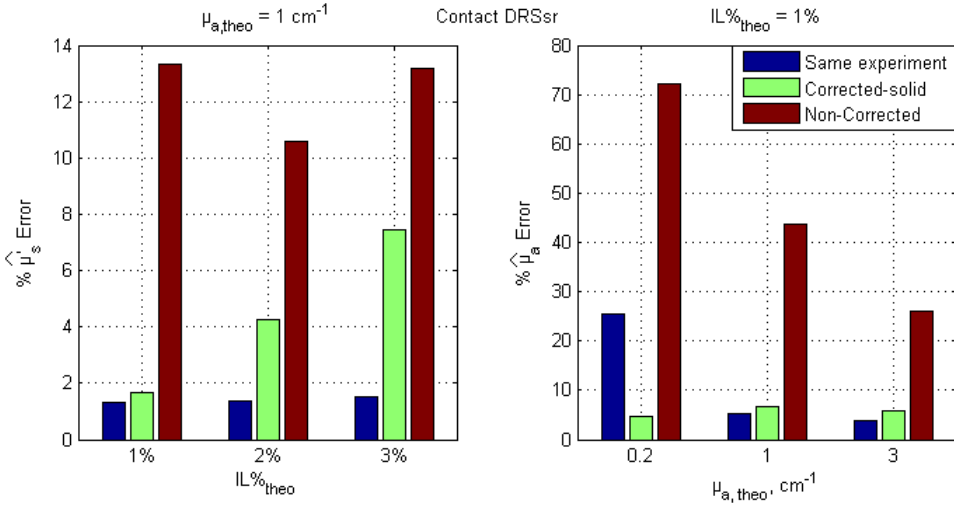


Figure 4.19: Average optical properties estimation relative error over the whole working spectrum with non-corrected and corrected signals from the different and the same experimental conditions to those of the  $CF(IL_{ref})$  6-reference base. *Contact DRSSr* measurements.

Figures 4.18 and 4.19 show the accuracy improvement in both optical properties estimation of corrected measurements with respect to non-corrected measurements. Estimations with corrected measurements lie closer to those obtained with measurements taken under the same experimental conditions. This results validate the correction strategy of experimental conditions variations.

To sum up, we have simulated an extreme change (unlikely to occur naturally) in experimental conditions by reducing  $S3$  and  $S4$  by 50% and  $S5$  by 15%, to test the capability of our strategy to correct from experimental variations. The obtained estimation results validate the correction approach. Moreover, we have demonstrated that the adoption of a solid material, measured only once to characterize each experimental condition, has the potential to replace liquid phantoms which pose temporal instability problems.

### Real daily experimental variations

In a second study, we considered less extreme real experimental variations and used, for precise correction, a more spatially homogeneous material than resin: the standard 99% reflecting Spectralon<sup>®</sup> fluoropolymer [Labsphere, 2016] (see Figure 4.20). Spectralon has a high reflecting efficacy and negligible diffuse reflectance, spatial optical homogeneity, and temporal optical stability.

To perform repetitive measurements of the Spectralon sample, necessary for a precise and robust correction, a special support, fixing the measurement distance and the Spectralon position, was built (see Figure 4.21). This support is used to calibrate the *Contact DRSSr* setup.

For the *initial Non-Contact DRSSr* setup, unfocused measurements of the Spectralon are performed at a fixed distance from the doublet pair by controlling the support table height.



Figure 4.20: 99% reflecting Spectralon<sup>®</sup> fluoropolymer [Labsphere, 2016].

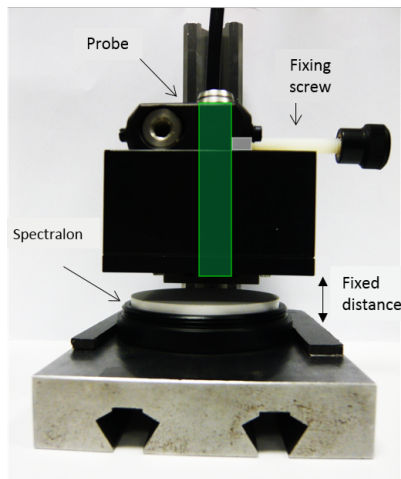


Figure 4.21: Built support fixing the DRSSr probe and the Spectralon position to keep a fixed measuring distance and allow for repetitive measurements.

Short-term instrumental stability is confirmed through the low signal error (see Figure 4.22) calculated for 6 normalized and treated measurements  $S_N$  (see Equation 3.2) taken along 45 minutes with the Spectralon support. Similar errors are obtained with the unfocused Spectralon measurements taken with the *initial Non-Contact DRSSr* setup. It is clear that errors increase for weaker signals (lower signal-to-noise ratio) such as the ones detected far from the source ( $F1 - F2$ ) and at lower wavelengths (470-500 nm).

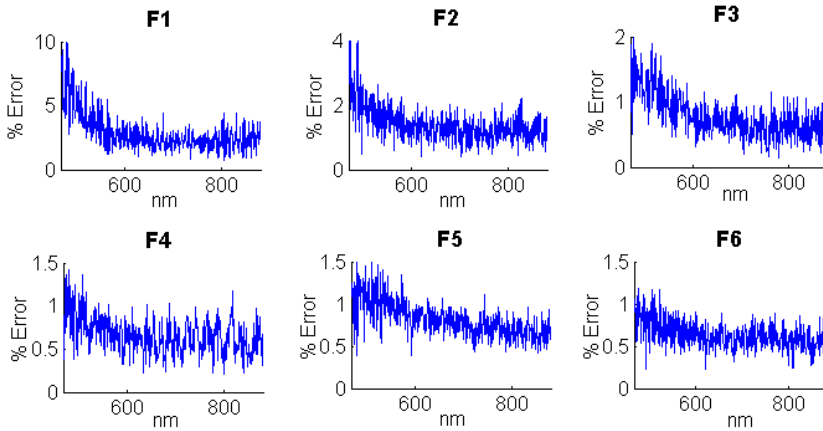


Figure 4.22: Relative error (%) of six different measurements taken on the Spectralon support to show measurement repetability and immediaty instrumental stability.

The minimal short-term measurement error allows to correct subtle real instrumental variations between two different measuring days. Derived Spectralon signal ratios  $K_{t_0-t_1}$  are shown for *Contact DRSSr* in Figure 4.23. Notice that  $K_{t_0-t_1}$  is close to 1 for  $F1 - F6$ , implying that minimal instrumental variations occurred.

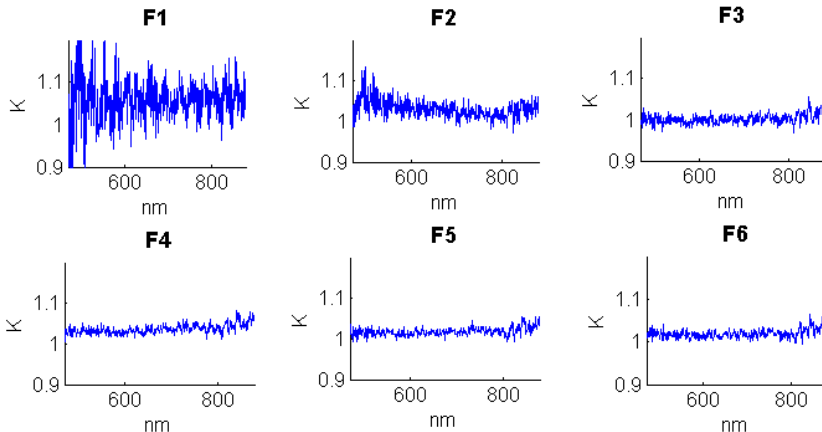


Figure 4.23:  $K_{t_0-t_1}$  ratio of Spectralon signals taken at different days.

Figure 4.24 shows the  $\widehat{\mu}_a$  estimation of unknown phantoms from *Contact DRSSr* measurements taken on the same or different day than the day in which the *CF*-reference base is measured. It is confirmed that the correction of experimental conditions with the Spectralon  $K_{t_0-t_1}$  reduces the estimation error of both optical properties (see Figure 4.25).

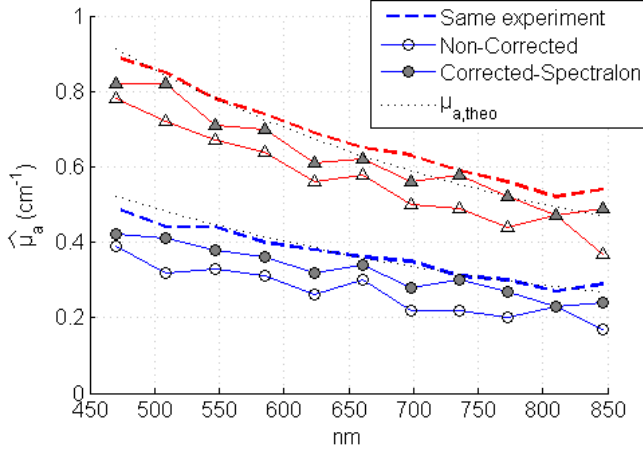


Figure 4.24:  $\widehat{\mu}_a$  estimation of unknown phantoms (with common  $IL_{theo} = 1.5\%$  and different  $\mu_{a,theo} = 0.4$  and  $0.7\text{ cm}^{-1}$  (at  $600\text{ nm}$ ) from *Contact DRSSr* measurements taken on the same (slashed lines) or different day to the *CF*-reference base. The correction of experimental variations for measurements taken on different days improves estimations (gray-filled shapes) compared to non-corrected signals (unfilled shapes). The legend is given for one phantom but the same line type code applies to all.

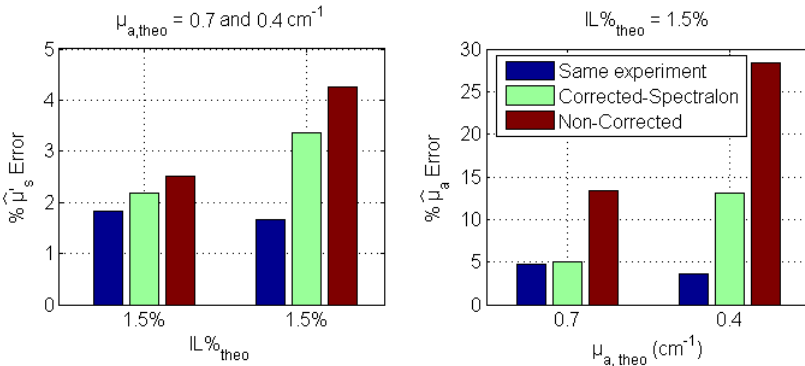


Figure 4.25: Relative optical properties estimation error averaged over the whole working spectrum corresponding to estimations shown in Figure 4.24.

The correction strategy has also been confirmed with the *initial Non-Contact DRSSr* setup through a similar decrease of the quantification error in both optical properties (results are not shown).

## 4.6 First probe measurements on biological samples

### 4.6.1 Heterogeneous Ham sample

The first biological sample that has been measured in this work is a heterogeneous flat slice of ham having areas with different types of fat and muscle. Figure 4.26 shows an example of one of the slices that were measured.

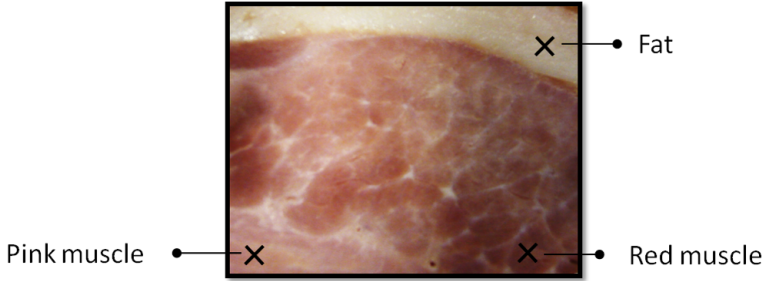


Figure 4.26: Image of the ham slice measured with both probe DRSsr systems on different types of tissues: fat, red and pink muscle.

### 4.6.2 Measurement procedure

The probe-based *Contact DRSsr* (see Section 3.2) and *initial Non-Contact DRSsr* (see Section 3.3) setups are used to acquire measurements with a non-cooled spectrometer *MAYA2000-Pro* detector.

Measurements are taken on different zones: fat, pink muscle and red muscle. For the comparison of both modalities, the surface heterogeneity of the tissue is considered. Therefore, five Contact measurements within the specified zone are taken and compared to the single focused Non-Contact measurement.

To focus the Non-Contact DRSsr setup on the sample, the minimal  $S_6$  intensity is used, as explained in Section 3.5.2.

### 4.6.3 Method

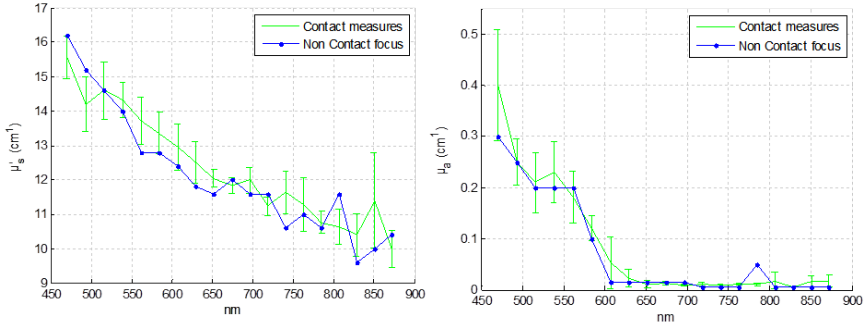
Signals are treated as described in Sections 3.2.3 and 3.3.5. For the instrumental calibration, the *ACA-Pro* algorithm, explained in Section 4.4, is used for both measurement modalities. To relate measurements to a *CF 6*-reference base built in a separate experiment, experimental variations are corrected with a common measurement on a reference intalipid phantom.

To analyse the effect of surface heterogeneities, the average and standard deviation of estimations with the various Contact measurements are calculated.

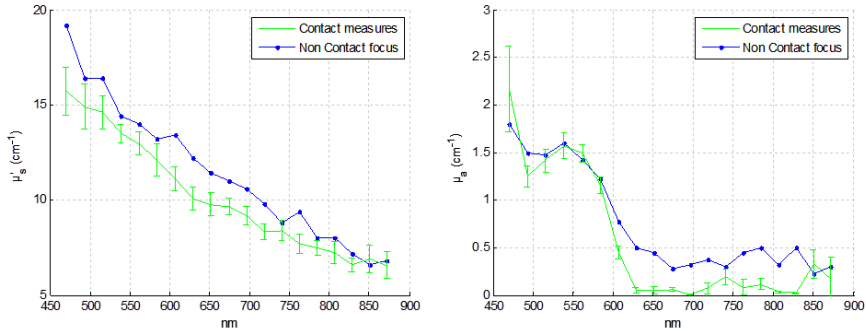
Because of the high sensitivity of  $\mu_a$  to the object plane height variations (see Section 3.5.2), we consider only a unique Non-Contact measurement taken at the focal plane for each zone.

### 4.6.4 Results and Discussion

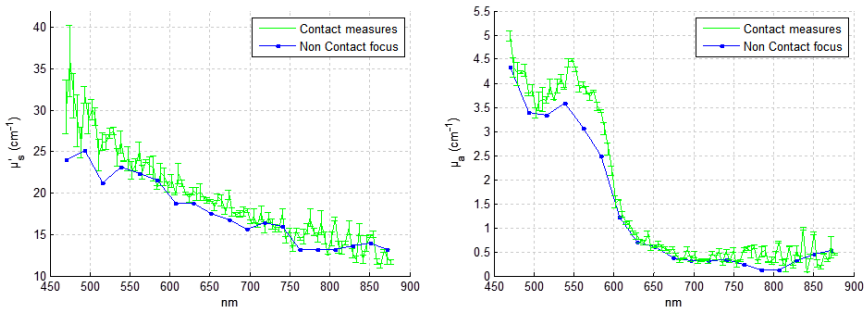
Figure 4.27 shows the average Contact estimations with corresponding standard deviation of fat, pink and red muscle compared to that of the focused Non-Contact measurement estimation.



(a) Fat



(b) Pink muscle



(c) Red muscle

Figure 4.27: Optical properties estimated with Contact measurements and focused initial Non-Contact measurement on different types of tissue.

Notice that the average Contact and single Non-Contact estimations superpose well. Minor differences are found when the absorption is too low as it is the case for fat and pink muscle after 600 nm. This is related to the instrumental noise originating from the non-cooled *MAYA2000-Pro* spectrometer detector used. To avoid this source of error in further measurements, we changed the spectrometer to the cooled *QE65000*.

Overall, the correspondence between the *initial Non-Contact DRSSr* and the well-established *Contact DRSSr* measurements has been validated.

## 4.7 Conclusion

We have presented an exhaustive comparison of the *ACA-Pro* calibration approach with Contact and Non-Contact measurement modalities of DRSSr and two different detectors: a spectroscopic fibre probe and a CCD.

The main advantage of the *ACA-Pro*, lies in the use of a unique Monte Carlo simulation with which measurements, taken with the different systems, have been fitted to derive optical properties. This was achieved through the compensation of the different non-modelled illumination profiles that originated from the components of the Non-Contact architectures, through a  $\mu'_s$ -based calibration procedure.

Intralipid phantoms with a wide range of scattering and absorption coefficients, comparable to that of biological tissues, have been measured to validate the calibration algorithm. Errors for Contact and Non-Contact probe-based setups remained below 4% and 8% for scattering and absorption properties, respectively. Further improvement on the estimation of  $\mu_a$  would be achieved by including a  $\mu_a$ -based calibration procedure to the original  $\mu'_s$ -based calibration of *ACA-Pro*.

The *ACA-Pro* algorithm was also validated with the *Non-Contact CCD-based DRSSr* that has been explored for a perspective integration in the final *Dual-Step* technique.

Moreover, the competence of the *ACA-Pro* algorithm was demonstrated with Non-Contact measurements and an adapted Non-Contact Monte-Carlo model that was built. Even though the adapted model improves quantification with a single reference phantom, *ACA-Pro* further optimizes absolute quantification.

Moreover, we have developed two strategies to reduce the amount of measurements and thereby manufacturing of liquid phantoms. The first was related to the use of interpolation between reference measurements with different scattering coefficients. The second dealt with the correction of intensity changes between measurements taken under different experimental conditions. For this purpose, we proposed the use of a single measurement characterizing each experimental condition. We have considered the measurement to be taken on a solid, optically stable, and homogeneous material (eg. standard Spectralon<sup>®</sup> fluoropolymer). This has the potential to fully substitute the use of liquid intralipid phantoms after a first instrumental calibration. Therefore, it is possible to bypass their related problems including temporal instability of optical properties, short-term conservation at low temperatures, and demanding manipulation. This approach poses the base for the development of a less demanding comparison technique between measurements taken at different time periods and subject to slight instrumental variations.

We have further validated the performance of the entire *ACA-Pro* algorithm with Contact and Non-Contact measurements in a biological sample. It is seen that Non-

Contact DRSsr estimations clearly relate to Contact DRSsr estimations.

In conclusion, the developed *ACA-Pro* algorithm is an extended calibration strategy that allows absolute quantification of optical properties of any DRSsr setup with a few reference phantoms measured only once. These reference measurements correct from the instrumental effects that are not modelled by the unique Monte Carlo simulation used. Additionally, *ACA-Pro* corrects from the instrumental variations that occur between experiments taken at different time periods with a single measurement of a common optically stable material.

The  $\mu'_s$ -based calibration procedure of *ACA-Pro* including the interpolation and correction of instrumental variations strategy is systematically used for the quantification of optical properties with all techniques considered in this work and discussed in the following Chapters.



# 5

## Large Field of View Multispectral Imaging

Multispectral Imaging (MSI) of a wide field of view cannot quantify both absolute optical properties. However, quantification of one optical property is possible if the other is known.

By assuming an a-priori modelled scattering coefficient  $\mu'_s$  with slow spatial variation, some groups ([Bjorgan et al., 2014], [Basiri et al., 2010], [Vogel et al., 2007] and [Zuzak et al., 2002]) fixed the same scattering coefficient on the whole imaged sample. Yet, because no direct measurement of  $\mu'_s$  is performed, only apparent or relative quantification of absorption is possible.

Distinctively, we propose to quantify absolute  $\mu'_s$  with DRSsr measurements to obtain absolute  $\mu_a$  quantification with MSI. The principle of the *Dual-Step* technique that we develop achieves wide-field quantification of optical properties based on punctual DRSsr measurements on specific zones. For this purpose, we have built a Large Field of View Multispectral Imaging (LFOV MSI) coupled to the *initial Non-Contact DRSsr* setup (described in Section 3.3) as shown in Figure 6.1.

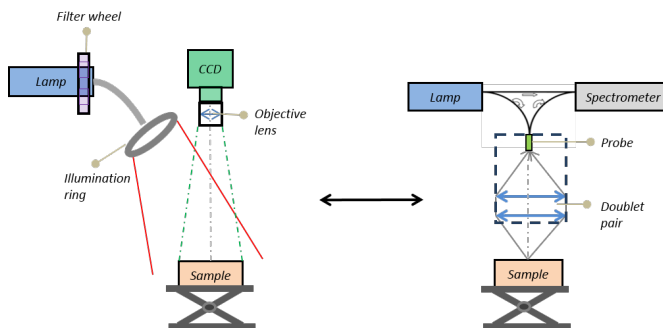


Figure 5.1: First *Dual-Step* setup combining *LFOV MSI* (left) and *initial Non-Contact DRSsr* (right) techniques.

In this Chapter we describe the LFOV MSI instrumental setup (Section 5.1) built, its measurement procedure (Section 5.2), and image processing (Section 5.3).

The method for optical properties quantification of the LFOV MSI technique is described in Section 5.4. Section 5.5 focuses on the  $\mu_a$  quantification capacity of MSI based on  $\mu'_s$  estimations provided by the *initial Non-Contact DRSSr* technique. Besides, the integration of the *ACA-Pro* algorithm in the MSI system, for further improvement of the absorption estimation, is explained and validated on homogeneous phantoms in Section 5.6.

An additional analysis of the spatial distribution of light in the sample is given in Section 5.7, describing also the optimization proposed through a pixel by pixel *ACA-Pro* calibration.

Section 5.8 evaluates the Depth of Field of the MSI technique with the  $\mu_a$  estimation error.

Section 5.9 demonstrates the wide field  $\mu_a$  quantification ability of LFOV MSI on a heterogeneous sample as a first result. Further results on real biological samples are considered in the next Chapter 6.

Finally, the conclusions of the technique are given in Section 5.10.

## 5.1 Instrumental Setup

After verifying the direct correlation between Spectral Imaging and Point Spectroscopy measurements (Appendix A.4), a staring modality of MSI (see Section 2.5.2) is adopted. The LFOV MSI instrumental setup built is illustrated in Figure 5.2. The system makes use of a 12-bit monochrome *VGA PixelFly* CCD detector, being a matrix of  $640 \times 480$  pixels with a pixel size of  $9.9 \mu m$  (see Appendix A.2.1). The lamp that is used for homogeneous illumination is a *KL2500 LCD Schott* source set to  $3000K$  of temperature for maximal spectral distribution. This is connected to a 6-LED illumination ring, which is inclined to avoid specular reflection of imaged phantoms.

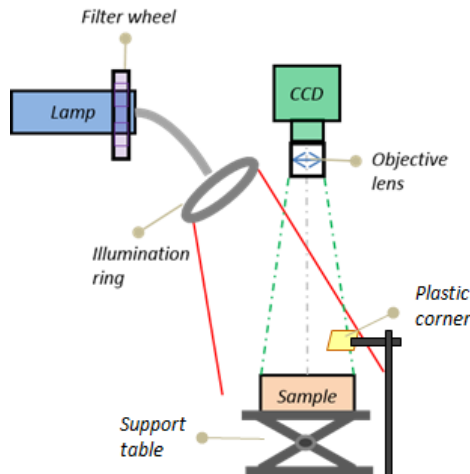


Figure 5.2: LFOV MSI setup.

A filter wheel has been customized to the lamp and the available filters to fasten them suitably and ensure no light leakage around, so that all light coming out of the lamp is filtered. Figure 5.3 shows the manufactured wheel with Delrin. Four filters in the visible range are used to acquire the first LFOV MSI measurements: 500, 550, 600 and 700 *nm*.



Figure 5.3: Customized filter wheel ensuring no light leakage around the filters.

A *Xenoplan 2.0/28* objective lens ensures a field of view (FOV) of  $50 \times 65 \text{ mm}^2$  (corresponding to a  $G=0.095$ ) at the focal plane, where the sample is placed.

Remark the small support fixing the plastic corner inside the field of view of the CCD, that is used for the indirect measurement and consequent correction of the source variations (refer to Section 5.3.3).

To ensure repeatability of measurements, the same dark ambient conditions are set. Therefore, we isolated the whole LFOV MSI system inside a black-cardboard structure.

## 5.2 Measurement Procedure

Images are acquired under the same conditions with an acquisition time  $t$  that is adapted to the dynamic range of the CCD detector. The focal plane of all objects is found as explained in the following Section 5.2.1. For each filtered light, sample images are acquired together with flat field images (see Section 5.2.2). Lastly, background images are taken for the entire range of integration time used.

### 5.2.1 Focusing

The object focal plane is identified by adjusting the support table height until a focused sharp image is obtained. The sample height around the object focal plane has a proportional effect on the intensity signal detected by the CCD. The measured intensity variation is shown in Figure 5.4 and it can be modelled through a simple linear equation. The latter is particularly useful for the correction of the surface curvature which will be developed in future work.

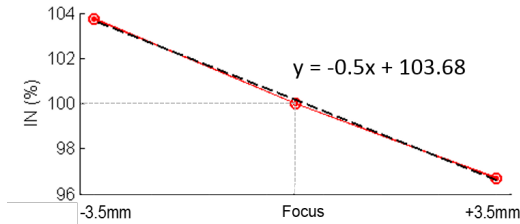


Figure 5.4: Percentage intensity variation with sample height ( $\pm 3.5\text{mm}$  around the focal plane).

The effect of this intensity variation on the  $\mu_a$  estimation is shown in Section 5.8.

### 5.2.2 Flat Field

Flat field images are acquired with the Spectralon<sup>®</sup> standard, described in Section 4.5.6 (see Figure 4.20) for each filtered light. The flat field images are used to correct reflectance images from the curved focal plane of the objective lens, the inclination of the illumination, and the filtering of light which provoke a varying intensity distribution on the object plane. The next Section 5.3.1 explains in detail the procedure for flat field correction.

## 5.3 Image Processing

### 5.3.1 Flat Field Correction

Flat field images  $S_{flat}$  (see Figure 5.5a) and sample intralipid images  $S$  (see Figure 5.5b) are corrected from the background  $S_{offset}$  taken with the corresponding integration time  $t$ . The blue squares on Figures 5.5 depict the useful area of the image, determined by

the Spectralon size, on which flat field correction is performed according to Equations 5.1 and 5.2.

$$FF = \frac{S_{flat} - S_{offset}}{\max(S_{flat} - S_{offset})} \quad (5.1)$$

$$S_c = \frac{S - S_{offset}}{FF \cdot t} \quad (5.2)$$

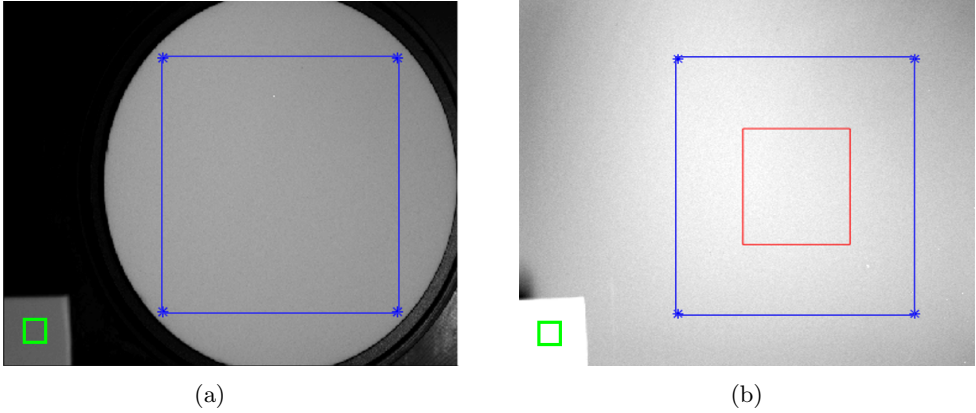


Figure 5.5: Blue squares show the area used for flat field correction. Smaller green squares define the common selected area of the plastic corner intensity that is averaged and used as an indirect measurement of the lamp (see Section 5.3.3). (a) Flat field image  $S_{flat}$  taken with the Spectralon. (b) Intralipid phantom image  $S$ . The red square defines the central selected area of  $150 \times 150$  pixels in which intensity is averaged (see Section 5.3.2).

### 5.3.2 Averaged intensity

After flat field correction, the intensity of an area of size  $T_x \times T_y$  is selected and averaged for further processing.

For a unique intensity with high SNR, individual to each imaged phantom, an area of  $T_x = T_y = 150$  is selected at the center of the image, as shown by the red square of Figure 5.5b.

For wide-field processing (refer to Section 5.6), smaller areas are considered. To keep the original spatial resolution, single pixels should be treated and  $T_x = T_y = 1$ . Yet, because the calculation time of individual pixels is too long, we considered mean pixels of the size  $T_x = T_y = 10$ .

The average reflection intensity  $S_a$  of the selected area is calculated through Equation 5.3.

$$S_a = \frac{\sum_{x=1}^{T_x} \sum_{y=1}^{T_y} S_c(x, y)}{T_x \cdot T_y} \quad (5.3)$$

### 5.3.3 Correction of Illumination fluctuations

The variation of illumination intensity should be compensated to allow the comparison of acquisitions and optimize the quantification accuracy. In practice, the average short-term source variability is measured to be  $< 1.8\%$  after a warm-up period of 6 minutes (see Figure 5.6). This variation may increase up to  $15.2\%$  when measured along different days.

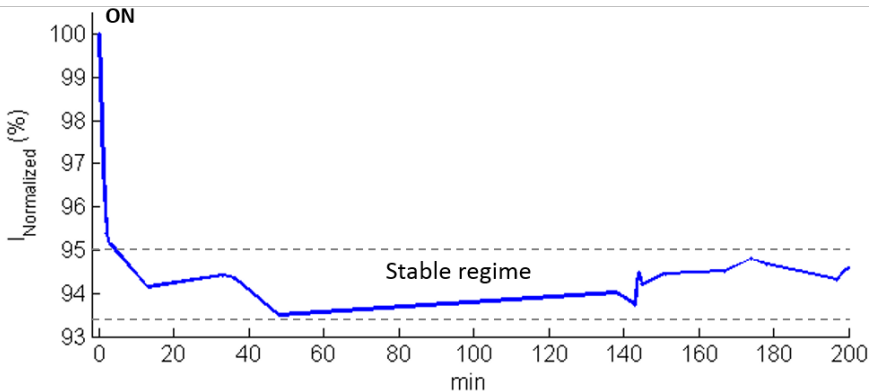


Figure 5.6: Lamp source variations over a period of 3 hours and 20 min after turning it on.

Ideally, the direct measurement of the source at each image acquisition should be used, as it is done in the probe DRSr measurement methodology (see Section 3.2.3). However, in the actual setup the direct source intensity measurement is not straightforward. Thus, we adopted an indirect measurement of the source through the average intensity  $I_s$  (corrected from the background and  $t$ ) of a common material, present in all images at the same place. For this, we chose a piece of cream-coloured plastic with a similar intensity response to our samples to ensure that it remains inside the dynamic range of each image. It is fixed at the opposite side of the source to avoid shadowing (see bottom left corner of Figures 5.5a and 5.5b) and its intensity is averaged across the same area (green square) on all images. The source variability correction is done according to Equation 5.4, where  $I_{s,1}$  and  $I_{s,2}$  are the average treated intensities of the common material in the first image  $Im_1$  and second image  $Im_2$ , respectively. Analogously,  $S_{a,1}$  and  $S_{a,2}$  are corrected and averaged reflectance signals of images  $Im_1$  and  $Im_2$ , respectively. For notation simplification purposes, we define the reflectance of  $Im_1$  corrected from the source fluctuations as  $S_N = S_{N,1}$ .

$$S_N = S_{N,1} = S_{a,1} \cdot \frac{I_{s,2}}{I_{s,1}} \quad (5.4)$$

In other words, the intensity of  $S_N$  is weighted with the factor  $I_{s,2}/I_{s,1}$  as if  $Im_1$  and  $Im_2$  images were taken on the same moment under the same illumination intensity. Thereby, all weighted reflectances  $S_N$  are comparable and their posterior processing can follow. The improvement of this treatment strategy in terms of absorption quantification is shown further in Section 5.6.3.

## 5.4 Method for the derivation of Optical Properties

### 5.4.1 Diffusion Model with homogeneous illumination

The forward model of this technique is chosen to be a well-established analytical expression of light transport in a homogeneous medium. The expression is based on the diffusion model derived by [Svaasand et al., 1995] and has been used for various multi-spectral imaging techniques such as the one developed by [Bjorgan et al., 2014] or SFDI [Cuccia et al., 2009], being the most advanced technique (refer to Section 2.5.4).

Diffuse reflectance  $R$ , originated from an isotropic illumination, is expressed as a function of the wavelength and the albedo  $a'$ , combining both optical properties  $\mu_a$  and  $\mu'_s$ . [Cuccia et al., 2009] extended the model to the spatial frequency domain. To do so,  $R_d$  is conveniently expressed as a function of the sinusoidal spatial frequency  $k$  of illumination. By supposing a planar illumination with frequency  $k = 0$ , the diffusion model  $R(0)$ , adapted to our technique, is obtained:

$$R(0) = \frac{3Aa'}{\sqrt{3(1-a') + 1}(\sqrt{3(1-a') + 3A})} \quad (5.5)$$

where  $A$  is the proportionality constant  $A = \frac{1-R_{eff}}{2(1+R_{eff})}$  ;

$R_{eff}$  is the effective reflection coefficient  $R_{eff} \approx 0.0636n + 0.668 + \frac{0.71}{n} - \frac{1.44}{n^2}$ ;

$n$  is the refractive index equal to 1.33 for water-based phantoms and equal to 1.37 for tissue samples;

$a'$  is the reduced albedo  $a' = \frac{\mu'_s}{\mu_{tr}}$ ;

and  $\mu_{tr}$  is the transport coefficient  $\mu_{tr} = \mu_a + \mu'_s$ .

Figure 5.7 shows the modelled diffuse reflectance in terms of optical properties  $\mu_a$  and  $\mu'_s$  that is saved in a Look-up-table LUT ( hence defined as  $R^{LUT}$ ) and used for data fitting with the measured and calibrated reflectance  $R_{CF}$  (see Section 5.4.2).

One of the advantages of this analytical model is that it requires little time to calculate  $R^{LUT}$  compared to a Monte-Carlo simulation.

As mentioned in Section 2.4, the limitation of the diffusion approximation at short distances (smaller than  $l'_s$ ) no longer exists with the homogeneous illumination and detection of MSI. Nevertheless, the approximation considers that scattering dominates over absorption. This is not always the case for skin, especially for dark skin phototypes and at  $\lambda < 600 \text{ nm}$  due to the high absorption of melanin and haemoglobin (see Figure 2.10). [Randeberg et al., 2005] approximated the error between the diffusion model and a Monte Carlo simulation for  $\lambda=400\text{-}850 \text{ nm}$ . They showed that the error can be reduced through the application of a constant scaling factor on the absorption coefficients of the diffusion model. As a first stage of this work and to determine the limitations of the model with our system, we have not explicitly implemented this constant scaling factor (see Section 5.5). Yet, in a second stage (see Section 5.6), we examine this absorption deviation with the advanced calibration procedure approach of *ACA-Pro*.

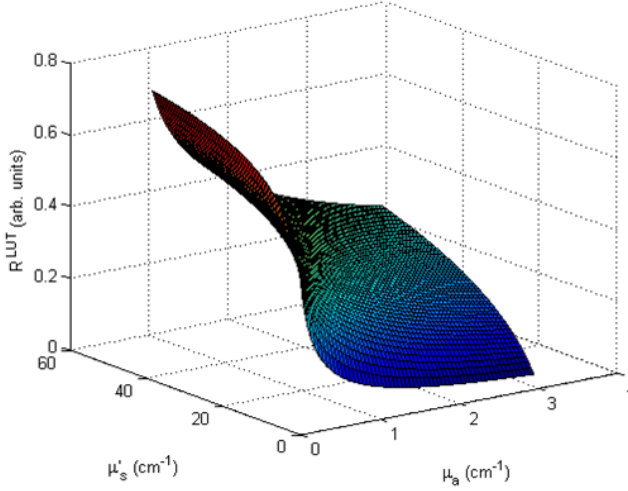


Figure 5.7:  $R^{LUT}$  built with the diffusion model for homogeneous illumination of Equation 5.5.

### 5.4.2 Instrumental Calibration

Similar to what is done in the Contact DRSSr method, we calibrate our measurements from the instrumental setup through the reflectance of a reference calibration phantom  $S_{N,ref}$  for which optical properties are known. The ratio of  $S_{N,ref}$  (averaged over the central part of the image, see red square of Figure 5.5) and the corresponding modelled  $R_{ref}^{LUT}$ , defines a correction factor  $CF$  (see Equation 5.6).

$$CF = \frac{R_{ref}^{LUT}}{S_{N,ref}} \quad (5.6)$$

The calibration is performed for each illumination wavelength and encompasses the constant instrumental effect such as the disregarded Quantum Efficiency of the CCD, numerical aperture of the objective lens, and illumination source intensity. To calibrate all measured reflectances  $S_N$  from the instrumental effect, their multiplication with the calibration factor  $CF$  is executed following Equation 5.7.

$$R_{CF} = S_N \cdot CF \quad (5.7)$$

### 5.4.3 Non-Uniqueness Problem

The corrected  $R_{CF}$  of an unknown phantom is close to an infinite number of particular modelled reflectances  $R^{LUT}$  which determine different unknown optical properties. This is due to the fact that the captured reflectance signal is a function of the albedo  $a'$  as mentioned in Section 5.4.1. Therefore, we approach the non-uniqueness problem stating that for the same reflectance measurement there exists an infinite number of possible  $\mu'_s - \mu_a$  couples [Arridge et al., 1998].

To clearly illustrate this effect, we calculate the Euclidian Norm of the difference between a single  $R_{CF}$  appertaining to a specific phantom, at a single wavelength  $\lambda$ , and all modelled  $R^{LUT}$ , according to the matrix  $\Delta_{Norm}(\mu_a, \mu'_s)$  of Equation 5.8.

$$\Delta_{Norm}(\mu_a, \mu'_s) = \sqrt{(R^{LUT}(\mu_a, \mu'_s) - R_{CF})^2} \quad (5.8)$$

As an example, we choose  $R_{CF}$  to be the reflectance of an unknown phantom having  $\mu_{a,theo} = 1 \text{ cm}^{-1}$  at  $600 \text{ nm}$  and  $IL_{theo} = 1.5\%$  calibrated with the  $CF$  of a reference phantom having  $\mu_{a,ref} = 0.4 \text{ cm}^{-1}$  at  $600 \text{ nm}$  and  $IL_{ref} = 1.5\%$ . Figure 5.8 shows the  $\Delta_{Norm}(\mu_a, \mu'_s)$  matrix for  $\lambda = 600 \text{ nm}$ . Red circles define the minimal difference values determining possible unknown  $\mu'_s - \mu_a$  couples which include the theoretical value, pointed by the green lines intersection and green arrow.

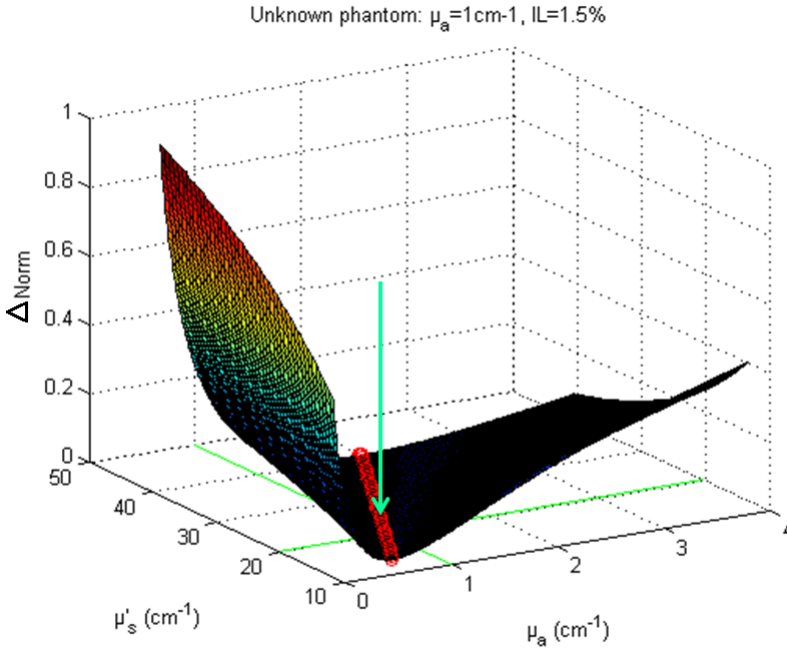


Figure 5.8: Normalized  $R^{LUT}$  model- $R_{CF}$  measurement difference showing all the possible  $\mu'_s - \mu_a$  couples with minimal difference in red circles.

Because of the non-uniqueness problem, measurements taken with the LFOV MSI setup cannot quantify both optical properties alone. This is why we developed a strategy of  $\mu_a$  quantification assuming a known scattering coefficient  $\mu'_{s,known}$ , explained in the next Sections 5.5 and 5.6.

## 5.5 Absorption Quantification

The known scattering value  $\mu'_{s,known}$  (or related  $IL_{known}$ ) determines a slice of the normalized difference  $\Delta_{Norm}$  matrix (illustrated in Figure 5.8) in terms of  $\mu_a$ . Figures 5.9 and 5.10 show an example of the  $\Delta_{Norm}$  slices for 3 wavelengths (500, 600 and 700 nm) of the same unknown phantom with theoretically known  $IL_{known} = 1.5\%$  and unknown  $\mu_{a,theo} = 1 \text{ cm}^{-1}$  at 600 nm. The red circles define the selected minimum value, or estimated  $\mu_a$  at each wavelength. The quantified errors of these estimations with respect to the theoretical values (black circles) are given further in Figure 5.13b.

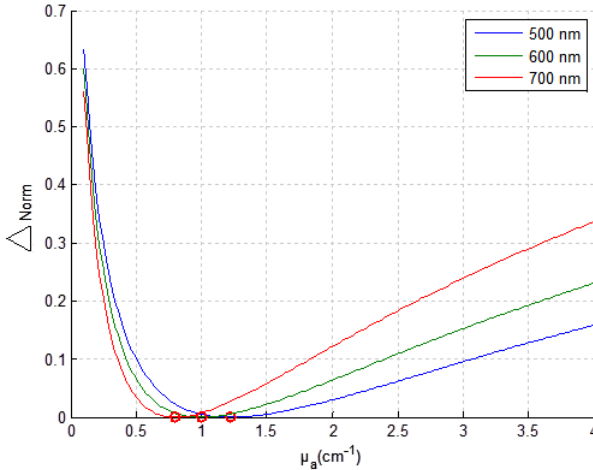


Figure 5.9:  $\mu_a$  estimation (red circles), of a phantom with  $IL_{known} = 1.5\%$  and  $\mu_{a,theo} = 1 \text{ cm}^{-1}$  at 600 nm. Refer to Figure 5.10 for a zoomed view.

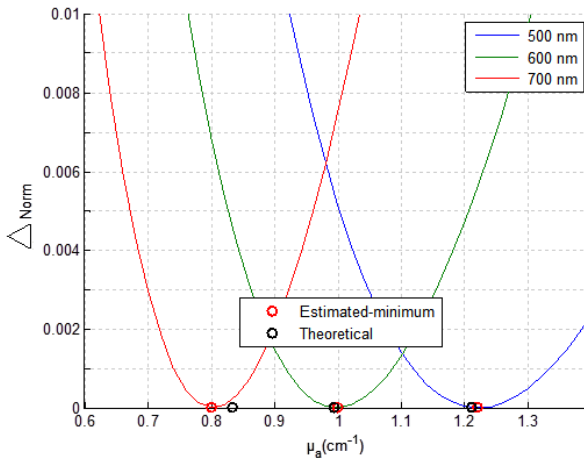


Figure 5.10:  $\mu_a$  estimation (red circles), with respect to theoretical values (black circles) of a phantom with  $IL_{known} = 1.5\%$  and  $\mu_{a,theo} = 1 \text{ cm}^{-1}$  at 600 nm.

To analyse the effect of fixing a wrong known scattering value  $IL_{known}$  on the  $\mu_a$  estimation, we considered phantoms having the same  $\mu_{a,theo} = \mu_{a,ref} = 0.4 \text{ cm}^{-1}$  at  $600 \text{ nm}$  and different scattering properties  $IL_{theo} = 1, 1.5, 2$  and  $3 \%$ . We fixed a single  $IL_{known} = IL_{ref} = 1.5 \%$  for all. Estimation results and spectrally-averaged relative errors of  $\mu_a$  are shown in Figure 5.11.

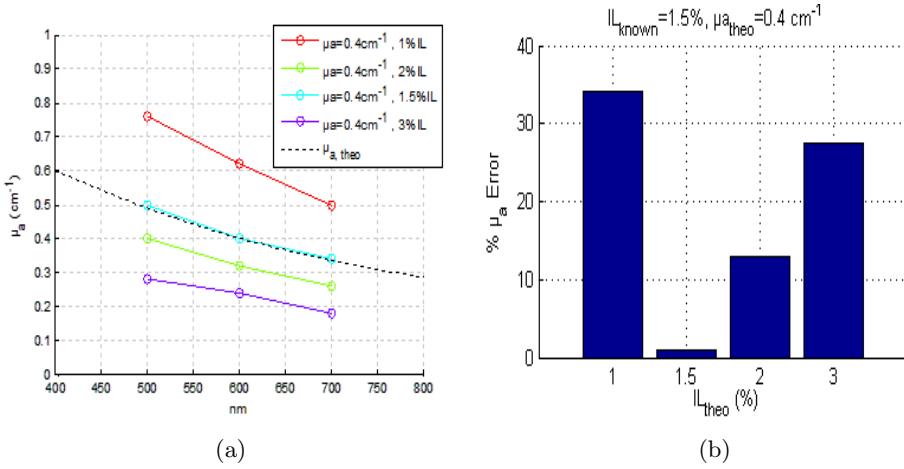


Figure 5.11: (a) Absorption quantification of phantoms having the same  $\mu_{a,theo} = 0.4 \text{ cm}^{-1}$  and different  $IL_{theo}$ , when fixing  $IL_{known} = 1.5\%$ . (b) Corresponding average relative absorption errors which are not acceptable for absolute quantification.

It is not surprising that minimal error is obtained with the phantom having  $IL_{theo} = IL_{known} = 1.5\%$ . For other phantoms, the estimation error generally increases as their  $IL_{theo}$  moves further from  $IL_{known} = 1.5\%$ . Supposing a wrong scattering property differing by 50% from  $IL_{theo}$  (eg.  $IL_{theo} = 1\%$ ), provokes relative estimation errors that can go beyond 30%, which are unacceptable for absolute absorption estimation. Thus, only relative quantification is possible.

Contrastingly, supposing the known scattering properties to be correct for each phantom,  $IL_{known} = IL_{theo}$ , greatly reduces the quantification errors. This is clearly illustrated in Figure 5.12.

Comparing  $\mu_a$  errors obtained with fixed  $IL_{known} = 1.5\%$  (Figure 5.11b) and those with a correct  $IL_{known} = IL_{theo}$  for each phantom (Figure 5.12b), it is clear that the absorption relative error is reduced to more than one third when using a correct  $IL_{known} = IL_{theo}$ . Consequently, to ensure the best quantification of absorption, a good estimation of the scattering coefficient is necessary.

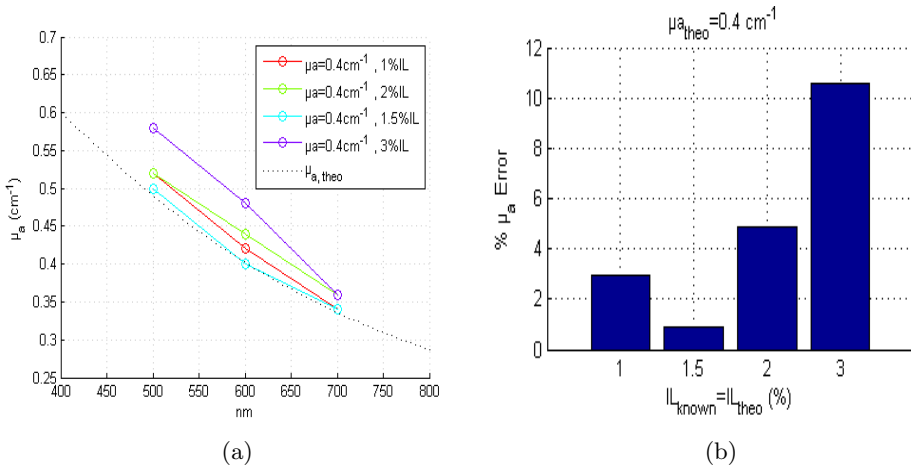


Figure 5.12: (a) Absorption quantification of phantoms having the same  $\mu_{a,theo} = 0.4\text{ cm}^{-1}$  and different  $IL_{theo}$ , with  $IL_{known} = IL_{theo}$ . (b) Corresponding average relative absorption errors.

Absorption estimation is also analysed for phantoms with the same scattering properties  $IL_{theo} = 1.5\%$  and different absorption properties. Setting  $IL_{known} = IL_{theo} = 1.5\%$ , the results shown in Figure 5.13 are obtained.

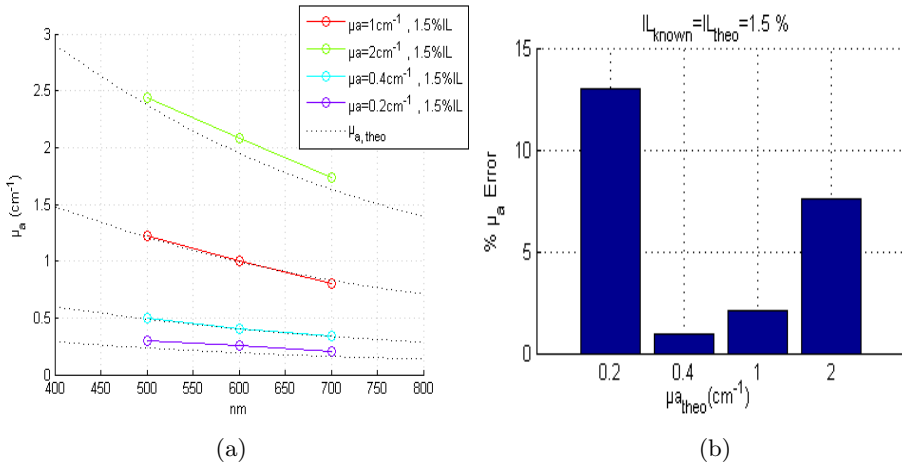


Figure 5.13: (a) Absorption estimation of various phantoms having different  $\mu_{a,theo}$  and the same  $IL_{known} = IL_{theo} = 1.5\%$  and supposing  $IL_{known} = IL_{theo}$  for all phantoms. (b) Corresponding average relative  $\mu_a$  errors.

The *Dual-Step* technique that we propose achieves appropriate scattering estimation through Non-Contact DRSSr measurements. The Non-Contact DRSSr technique achieves a maximum  $\mu'_s$  error of 3.3% at the focal plane (see Section 4.5.3). Keep in mind that this error would increase with non-focused measurements inside the DOF of 1.2 mm (see Section 3.5.2).

Figure 5.14 illustrates the increase in MSI  $\mu_a$  error when using  $IL_{known}$  values estimated with the Non-Contact DRSSr technique (at the focal plane, subject to 3.3 % error) compared to  $IL_{known} = IL_{theo}$ , for phantoms having different absorption and scattering properties.

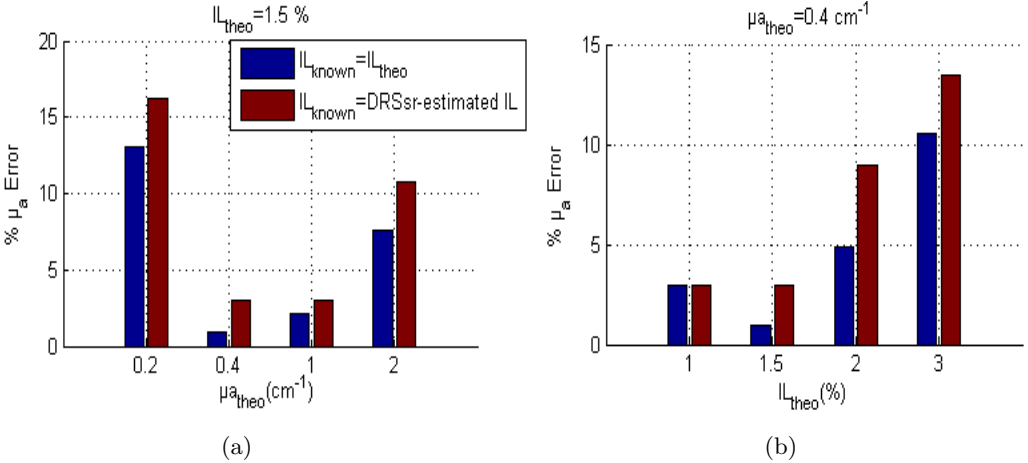


Figure 5.14: Relative  $\mu_a$  errors of (a) phantoms with different  $\mu_{a,theo}$  and common  $IL_{theo}$  (b) phantoms with different  $IL_{theo}$  and common  $\mu_{a,theo}$  when using  $IL_{known} = IL_{theo}$  or Non-Contact DRSSr-estimated  $IL$  with maximum error of 3.3%.

Overall, it is seen that  $\mu_a$  error increases due to the scattering  $\mu'_s$  estimation error of DRSSr, is lower than 4%.

Notice that the minimal estimation error of 1% is that of the phantom being identical to the reference phantom ( $\mu_{a,theo} = \mu_{a,ref} = 0.4 cm^{-1}$  and  $IL_{theo} = IL_{ref} = 1.5\%$ ). This error increases to 3% with the use of DRSSr-estimated scattering values.

Errors of phantoms different from the reference phantom generally increase as their optical properties move further from the reference. This is emphasized with the phantom having  $\mu_{a,theo} = 0.2 cm^{-1}$  and the other phantom having  $IL_{theo} = 3\%$ .

To illustrate this deviation and better understand the estimation errors, we consider optical properties of all phantoms known and derive the corresponding modelled reflectance  $R_{known}^{LUT}$ . This allows comparison of  $R_{ref}^{LUT}/R_{known}^{LUT}$  with  $S_{N,ref}/S_N$ . The comparison is used to test the linearity between model and measurements by looking at the fit with respect to the 1 : 1 ratio. Figure 5.15 shows these ratios for  $\lambda = 600 nm$ . Notice that the further optical properties (in pink) from the reference (in red) are the measurements that least fit to the 1:1 ratio (in dotted black line).

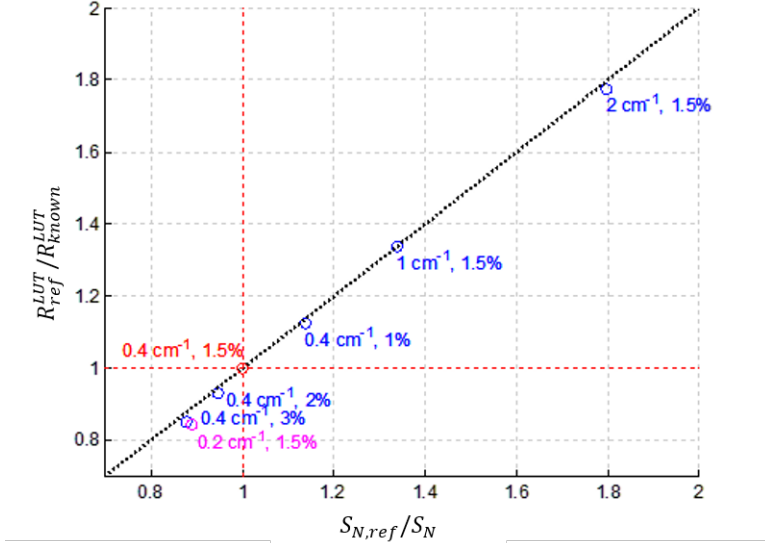


Figure 5.15: Linearity between normalized measurements and normalized modelled reflectance at  $\lambda = 600 \text{ nm}$ .

For a more quantitative analysis, relative percentage errors are calculated between  $R_{known}^{LUT}$  and  $R_{CF}$  and shown in Table 5.1.

Table 5.1: Relative errors between calibrated measurements  $R_{CF}$  and modelled values  $R_{known}^{LUT}$  for phantoms having the given  $\mu_a$  values at  $600 \text{ nm}$ . The same color code of Figure 5.15 is kept.

$\mu_a$ ( $\text{cm}^{-1}$ )	IL (%)	Relative error (%)
0.4	1.5	0 (reference)
0.4	1	1.3
0.4	2	1.7
0.4	3	3.4
1	1.5	0.3
2	1.5	1.4
0.2	1.5	5.6

These errors, resulting from the use of a single reference phantom, directly explain the  $\mu_a$  estimation errors shown in Figure 5.14.

Therefore, to improve  $\mu_a$  quantification, we propose to use several reference absorbing phantoms. In other words, the improvement is achieved by integrating the *ACA-Pro* algorithm (described in Chapter 4) to calibrate the MSI instrument according to absorption estimations. This is explained in the next Section 5.6.

## 5.6 Wide-field Absorption Optimization with ACA-Pro

The *ACA-Pro* algorithm, described in Chapter 4, proposes an optimal approach to calibrate the instrumental response. Applied to MSI, *ACA-Pro* is able to improve absorption quantification, which is initially limited by the diffusion model used (see Section 5.4.1). Figure 5.16 illustrates the flowchart of the *ACA-Pro*  $\mu_a$  quantification process applied to the MSI system of the *Dual-Step* technique, combining it with Non-Contact DRSSr. The *ACA-Pro* algorithm makes use of a *CF* reference base (see Section 5.6.1) built with reference phantoms having different known scattering and absorption properties. The selection of the best reference optical properties of the *CF* is performed in two steps. In a first step, the  $\widehat{\mu}'_s$  is estimated with Non-Contact DRSSr. In a second step, for the given scattering coefficient, the  $\widehat{\mu}_a$  estimation is upgraded according to the *ACA-Pro* algorithm approach (refer to Section 4.4).

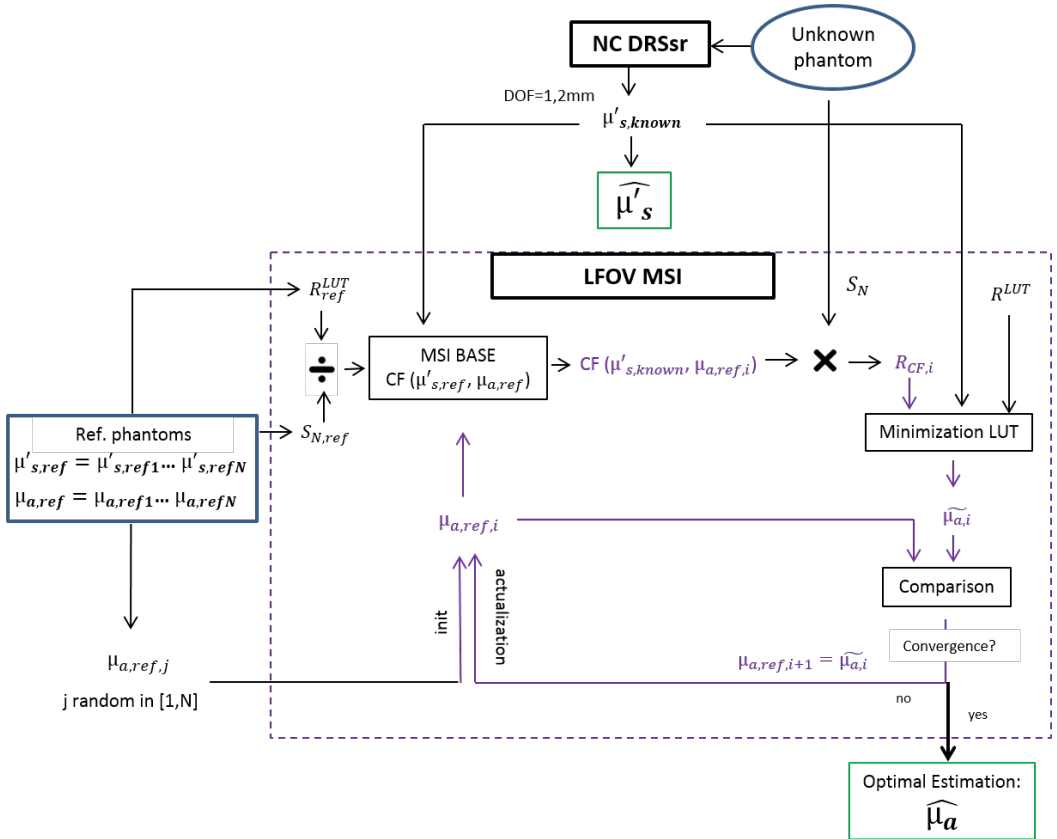


Figure 5.16: Flowchart describing *ACA-Pro* applied to MSI technique for absorption quantification based on the  $\widehat{\mu}'_s$  estimation of Non-Contact (NC) DRSSr technique.

*ACA-Pro* also allows to reduce the number of necessary reference phantoms through an interpolation strategy of both optical properties (refer to Section 5.6.2).

### 5.6.1 CF Reference base

An extensive phantom study is carried out to validate the absorption quantification improvement of *ACA-Pro* in LFOV MSI. Ten different reference phantom having two different scattering properties ( $IL_{ref} = 1$  and 1.5%) and five different absorption properties ( $\mu_{a,ref} = 0.4, 1.05, 2.84, 6.01, \text{ and } 10.4 \text{ cm}^{-1}$  at 600 nm), are used. The *CF* 10-reference base is built according to Equation 5.6 for the different considered phantoms and wavelengths  $\lambda$  (500, 550, 600 and 700 nm). Figure 5.17 shows the resulting *CF* 10-reference base according to  $\lambda$  and reference optical properties.

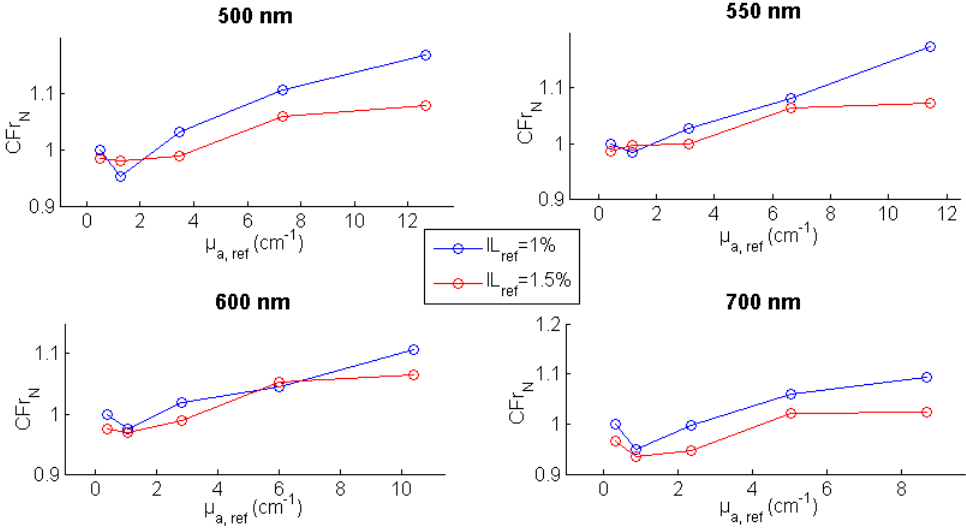


Figure 5.17: *CF* 10-reference base according to illumination  $\lambda$  built with ten reference phantoms having two different scattering properties ( $IL_{ref} = 1$  and 1.5%) and five different absorption properties  $\mu_{a,ref} = 0.4, 1.05, 2.84, 6.01, \text{ and } 10.4 \text{ cm}^{-1}$  at 600 nm.

Recall that the diffusion model used is not accurate for high absorption values (see Section 5.4.1). Therefore, as expected, *CF* depends on  $\mu_a$ , justifying the use of  $\mu_a$ -based *ACA-Pro* calibration.

Wide field  $\mu_a$  estimation is achieved by considering the average reflectance value of 10 pixels (refer to Section 5.3.2), calibrating it with a *CF*, and fitting it to  $R^{LUT}$ . To show the performance of *ACA-Pro*, an example of five unknown phantoms having the same  $IL_{theo} = 1\%$  (estimated with Non-Contact DRSr) and different  $\mu_{a,theo}$  are used. Their wide field  $\mu_a$  is estimated with the *CF* 10-reference base of Figure 5.17.

Figure 5.18 shows an example of estimated wide field  $\mu_a$  obtained for the lowest absorbing phantom considered with the appropriate *CF*. Notice that all quantified  $\widehat{\mu}_a$  pixels are around the theoretical value  $\mu_{a,theo}$  with an average error of 4% for all  $\lambda$ s.

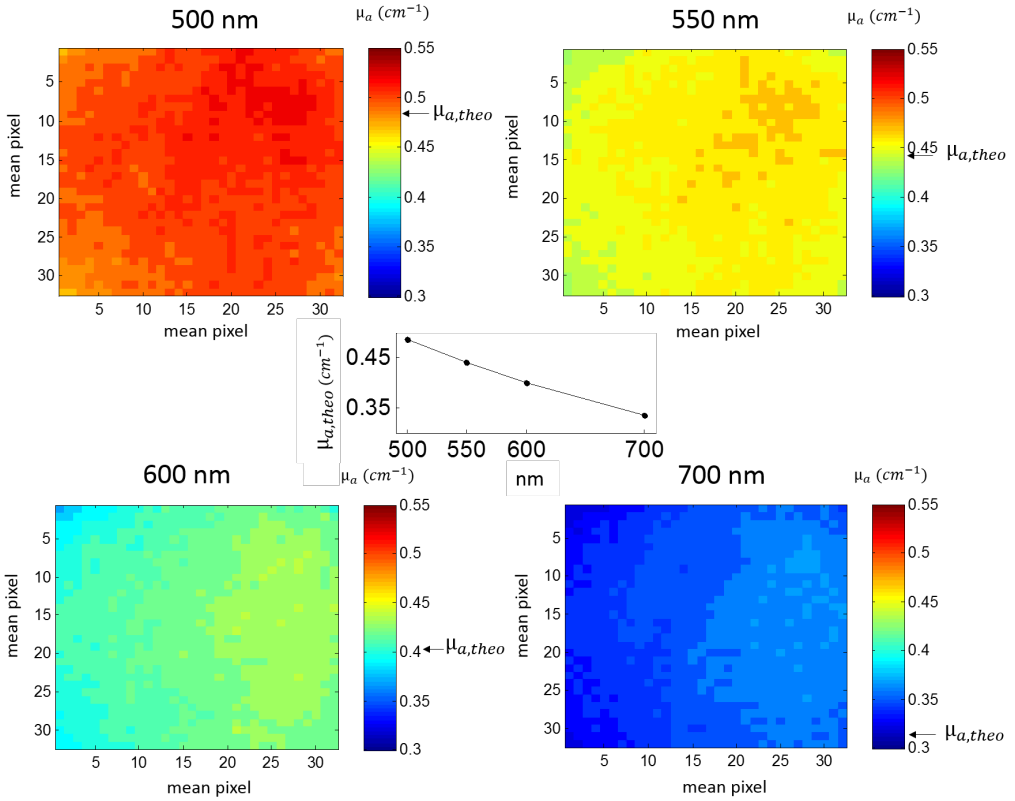


Figure 5.18: Wide field multispectral  $\widehat{\mu}_a$  quantification for an unknown phantom having  $\mu_{a,theo}$  specified by the central figure and marked by the black arrows on the colorbars.

Spatially averaged  $\widetilde{\mu}_a$  errors calculated at 550 nm with respect to  $\mu_{a,theo}$  for five unknown phantoms (with different  $\mu_{a,theo}$  and common  $IL_{theo} = 1\%$ ) calibrated with the entire  $CF$  10-reference base are shown in Figure 5.19. It is clear that minimal errors are obtained with the  $CF$  having the closest optical properties to the unknown phantom. Through a dichotomic procedure both on  $\mu'_s$  and  $\mu_a$ , *ACA-Pro* is able to automatically derive the optimal  $CF$  ( $CF_{opt}$ ) for each pixel of the image. Figure 5.20 summarizes the minimal spatially averaged  $\mu_a$  errors obtained with  $CF_{opt}$  for all phantom absorptions  $\mu_{a,theo}$  and  $\lambda$ . These results comprehensively validate the optimal calibration procedure of *ACA-Pro* and use of Non-Contact DRSr  $\mu'_{s,known}$  to estimate wide field  $\widehat{\mu}_a$  with an error  $< 5.5\%$  for the range of optical properties considered.

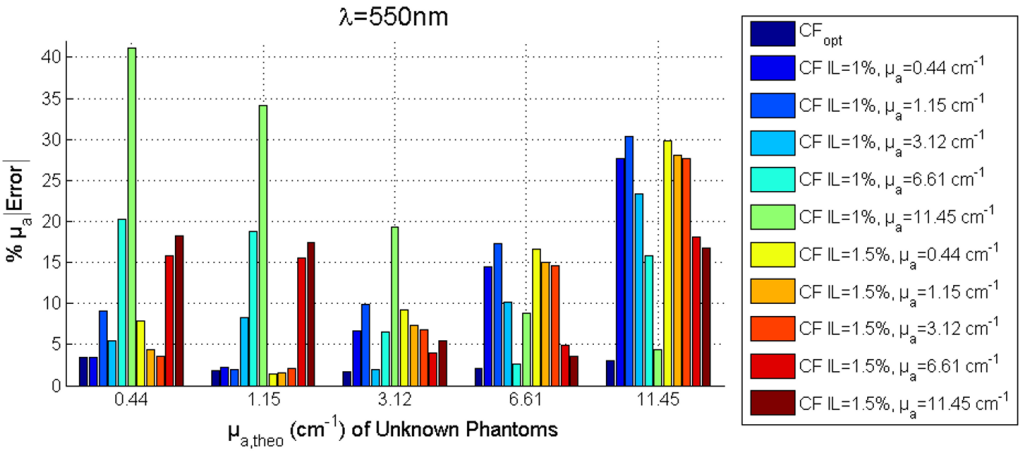


Figure 5.19: Average  $\widetilde{\mu}_a$  errors at 550 nm of unknown phantoms having different  $\mu_{a,theo}$  and common  $IL_{theo} = 1\%$ , calibrated with the  $CF$  10-reference base and the optimal  $CF_{opt}$  chosen by  $ACA-Pro$ .

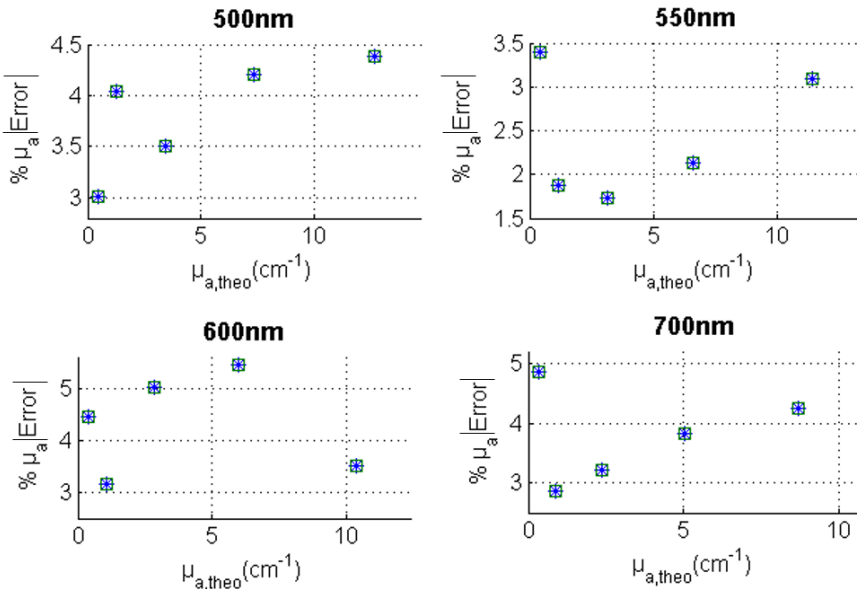


Figure 5.20: Average  $\widehat{\mu}_a$  errors of unknown phantoms having common  $IL_{theo} = 1\%$  and different  $\mu_{a,theo}$ , calibrated with  $CF_{opt}$  for all considered  $\lambda$ .

### 5.6.2 CF Interpolation

The linearity of the  $CF$  10-reference base with respect to  $\mu_{a,ref}$  (see Figure 5.17), allows to reduce the number of reference phantoms and derive the optimal  $CF$  through interpolation of both  $\mu'_s$  and  $\mu_a$ .

To show this, an unknown phantom having  $IL_{theo} = 1\%$  and  $\mu_{a,theo} = 3.12 \text{ cm}^{-1}$  is estimated with a  $CF$  2-reference base built with  $IL_{ref} = 1\%$  and  $\mu_{a,ref} = 1.15$  and  $6.61 \text{ cm}^{-1}$ . Figure 5.21 shows the wide-field relative  $\mu_a$  errors obtained with the use of the  $CF$  2-reference base and the interpolated  $CF$  ( $CF_{interp}$ ), at  $500 \text{ nm}$ . Notice that  $CF_{interp}$  achieves minimal wide-field error which is directly comparable to the average error obtained with  $CF$  proper of  $\mu_{a,ref} = 3.12 \text{ cm}^{-1}$  (error = 3.5%, see Figure 5.20 at  $500 \text{ nm}$ ). This result validates the interpolation strategy of *ACA-Pro* applied to LFOV MSI.

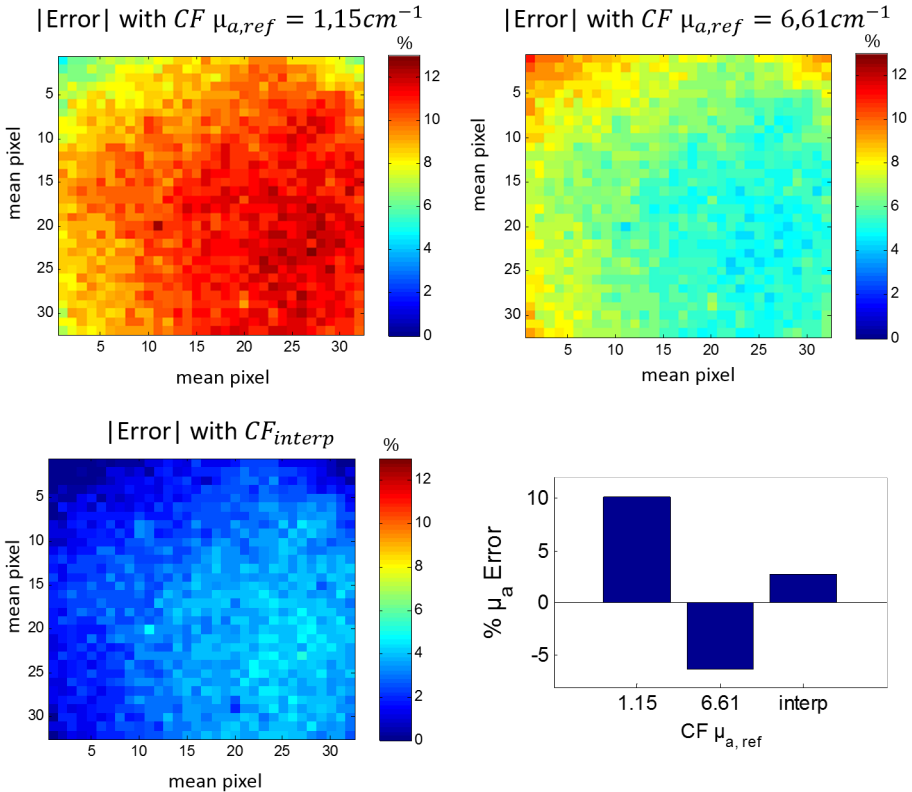


Figure 5.21: Wide field  $\widehat{\mu}_a$  error at  $500 \text{ nm}$  of an unknown phantom having  $\mu_{a,theo} = 3.12 \text{ cm}^{-1}$ , calibrated with the  $CF$  2-reference base built with  $\mu_{a,ref} = 1.15$  and  $6.61 \text{ cm}^{-1}$ , and the interpolated  $CF_{interp}$ .

An optimal choice of the minimal amount of reference phantoms used to build the  $CF$  reference base is necessary to optimally benefit from the interpolation strategy of *ACA-Pro*. This choice directly depends on the optical properties of interest.

### 5.6.3 Intensity variation correction

As mentioned in Section 5.3.3, images are corrected from the lamp intensity fluctuations through the indirect intensity measurement of a common material present in all images at the bottom left corner (see Figures 5.5a and 5.5b). This is particularly useful when using a  $CF$  reference base measured on a different day for which the illumination intensity variation is non negligible. To show this, we consider the case of an unknown phantom showing an intensity variation of 15% with respect to the  $CF$ -reference base measured on another day. Figure 5.22 illustrates the reduction in wide-field  $\widehat{\mu}_a$  error considering or not the correction of intensity variation at 500 nm.

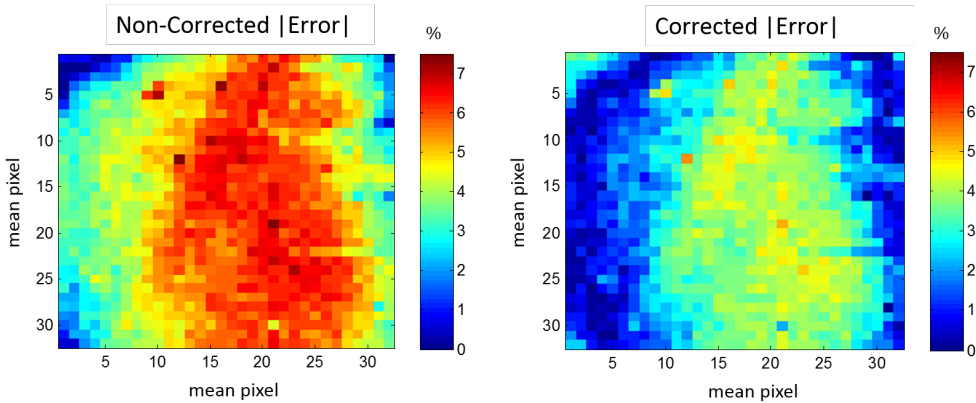


Figure 5.22: Wide-field  $\widehat{\mu}_a$  relative error at 500 nm obtained with or without the correction of the lamp fluctuation for an unknown phantom with  $\mu_{a,theo} = 1.27 \text{ cm}^{-1}$  and  $IL_{theo} = 1\%$ . Through the correction of fluctuations the average error is reduced of about 2.2%.

In average, estimation errors are reduced by 2.2%, validating the indirect measurement protocol of the source fluctuations and correction process between images.

## 5.7 Spatial distribution optimization

Section 5.6.1 shows that the achieved  $\widehat{\mu}_a$  error averaged over the whole image is  $< 5.5\%$  for the range of optical properties and wavelengths considered. Further improvement on this estimation should focus in the optimization of the spatial distribution. Indeed, the spatially heterogeneous diffuse reflectance originated from the inclined illumination is not corrected by the non-diffusing (reflectance) Spectralon flat field images.

To better understand this effect, let us have a closer look at Spectralon and intralipid phantom images (see Figure 5.23). For a comparative study, we consider images of a sample intralipid phantom  $IP_1$  (with  $IL_{theo} = 1.5\%$  and  $\mu_{a,theo} = 0.7 \text{ cm}^{-1}$ ), a different intralipid phantom  $IP_2$  (with same  $IL_{theo} = 1.5\%$  and  $\mu_{a,theo} = 0.4 \text{ cm}^{-1}$ ), and the standard Spectralon.

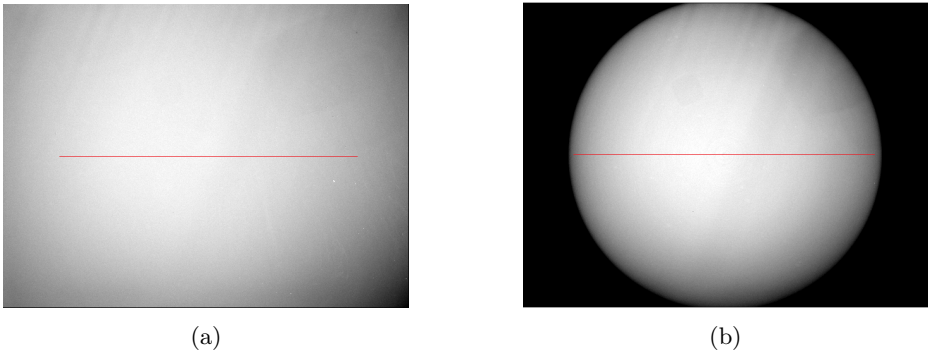


Figure 5.23: Reflectance images of (a) Intralipid Phantom (b) Spectralon.

The central horizontal profile (illustrated by the red line on images of Figure 5.23) of the sample intralipid  $IP_1$  image and the smoothed central profiles of  $IP_2$  and the Spectralon are normalized and compared in Figure 5.24a. The corresponding ratio of profiles with respect to  $IP_1$  are illustrated in Figure 5.24b.

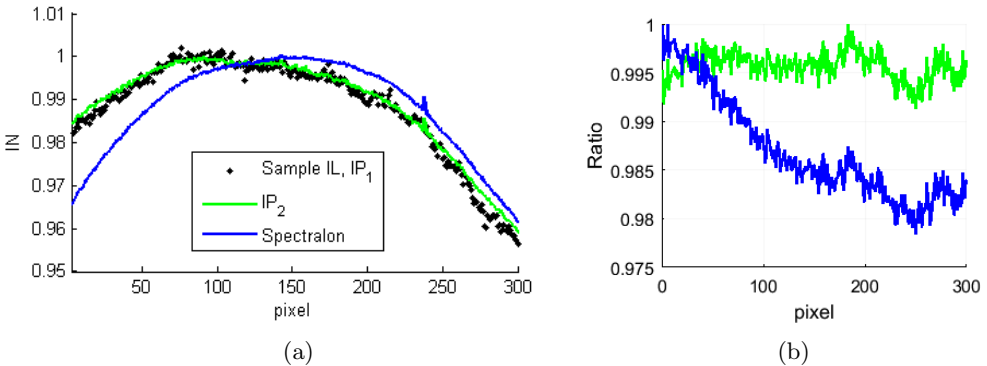


Figure 5.24: (a) Profile of  $IP_1$  and smoothed profiles of a  $IP_2$  and the standard Spectralon. (b) Corresponding profile ratios relative to that of  $IP_1$ .

Notice that the profiles differ between the highly reflectance diffusing intralipid and non-reflectance diffusing Spectralon. In other words, the diffuse reflectance that occurs in the intralipid only is imperceptible in the reflective Spectralon. The mathematical analysis of the signals measured on the intralipid ( $S_{IL}$ ) and the Spectralon ( $S_{Spec}$ ), shown in Figure 5.24a, combines the signals originating from the source ( $S_{source}$ ), the impulse response function of the system ( $IRF$ ), a factor proper to the surface of the sample ( $\gamma$ ), and, in the case of the intralipid, the resulting diffuse reflectance ( $R_{IL}$ ) (see Equation 5.9).

$$\begin{aligned} S_{IL} &= S_{source} \times IRF \times \gamma_{IL} \times R_{IL} \\ S_{Spec} &= S_{source} \times IRF \times \gamma_{Spec} \end{aligned} \quad (5.9)$$

Therefore, the ratio  $S_{IL}/S_{Spec}$  (shown in blue, Figure 5.24b) encompasses not only the constant surface ratios  $\gamma_{IL}/\gamma_{Spec}$  but also the spatially heterogeneous distribution of  $R_{IL}$  emerging from the inclined illumination (see Equation 5.10).

$$Ratio = \frac{S_{IL}}{S_{Spec}} = \frac{\gamma_{IL}}{\gamma_{Spec}} \times R_{IL} \quad (5.10)$$

This explains the lack of spatial uniformity of the Ratio  $S_{IL}/S_{Spec}$ .

In analogy to the non-modelled illumination profile of Non-Contact DRSSr techniques (see Section 3.5.1) in the Monte Carlo simulation, the non-modelled inclined illumination of the LFOV MSI setup, results in different diffuse reflectances according to the optical properties of the phantom. This non-constant effect cannot be corrected by the single  $CF$  that has been used and which is spatially averaged at the center of each image (see Section 5.4.2).

Recall from Chapter 4 that the *ACA-Pro* calibration in Non-Contact DRSSr techniques uses a  $CF$  individual to optical property, wavelength, and  $SD$  distance to completely correct the non-modelled illumination profile.

Applying the same concept to MSI, we propose to adjust the heterogeneous spatial distribution of wide field  $\widehat{\mu}_a$  by using a  $CF$  individual not only to each optical property and wavelength, but also to each pixel. In this way, the *ACA-Pro* calibration includes the constant deviation between measurement ( $S_{N,ref}$ ) and model ( $R_{ref}^{LUT}$ ), and also the heterogeneous spatial distribution of the diffuse reflectance emerging from the non-modelled inclined illumination. This calibration procedure would considerably reduce the spatial distribution of the estimation error of wide-field  $\mu_a$  due to the spatial illumination variation and should be contemplated as a perspective improvement (see Section 7.2.2).

## 5.8 Depth of Field

As explained in Section 5.2.1, the distance sample - objective lens has a proportional effect on the intensity variation. To define an acceptable depth of field (DOF), we quantified the  $\mu_a$  error originated by this intensity variation at  $\lambda=500\text{ nm}$ . A reference phantom having  $\mu_{a,ref} = 0.4\text{ cm}^{-1}$  at  $600\text{ nm}$  and  $IL_{ref} = IL_{known} = 1\%$  (estimated by Non-Contact DRSsr), is placed at the focal plane. The corresponding  $CF$  is used to calibrate images of the same phantom placed at  $\pm 3.5\text{ mm}$  around the focal plane. Thereby, the total  $\mu_a$  error of the *Dual-Step* technique, due to difference in plane heights, can be calculated.

Figure 5.25 shows the relative  $\mu_a$  error with respect to the theoretical value and averaged over the quantified calculated images. As expected, the  $\mu_a$  estimation decreases with height, since the intensity increases as the sample approaches the source. According to these results, a convenient DOF of  $3\text{ mm}$  can be defined to limit the  $\mu_a$  error to  $\pm 5\%$  (see green lines). Therefore, the final DOF of the *Dual-Step* technique is defined by the  $4.1\%$  estimation error of  $\mu'_s$  with Non-Contact DRSsr for  $1.2\text{ mm}$  (see Section 3.5.2). With this DOF the wide field  $\mu_a$  estimation error with MSI is  $< 5\%$ .

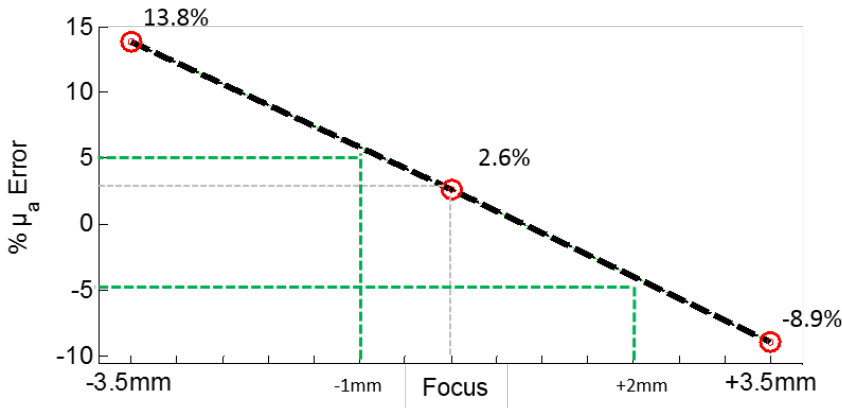


Figure 5.25:  $\mu_a$  error originated from the intensity variation at different planes ( $\pm 3.5\text{ mm}$  around the focal plane).

Yet, to further reduce the  $\mu_a$  error in biological non-flat samples, the detection of the sample's curvature is necessary for correction with the linear intensity-height equation (see Figure 5.4). This should be a focus of further development and will be discussed in Section 7.2.2.

## 5.9 Measurement of a heterogeneous medium

A home-made gelatine-based heterogeneous phantom with different absorbing and scattering zones has been used to test the ability of LFOV MSI to quantify  $\mu_a$  in the different zones of the same image (see Figure 5.26). Reference optical properties of the zones in the phantom are estimated with Contact DRSsr. Reference DRSsr  $\mu'_s$  are used as  $\mu'_{s,known}$  values to estimate wide-field  $\mu_a$  with MSI. These MSI  $\mu_a$  estimations are subsequently validated with reference DRSsr  $\mu_a$  estimations.

Absorption of the zones in the phantom depends on the different concentrations of ‘VAHINE’ red ink or *HP-printer* blue ink used. Scattering depends on the amount of diffusive milk and edible gelatine used. Blue shapes are made of different concentrations of blue ink and the same milk-gelatine mixture, whilst the pink background is made of a low concentration of red ink and a different milk-gelatine mixture. Notice that some pink background mixture invades the surface of the blue shapes.

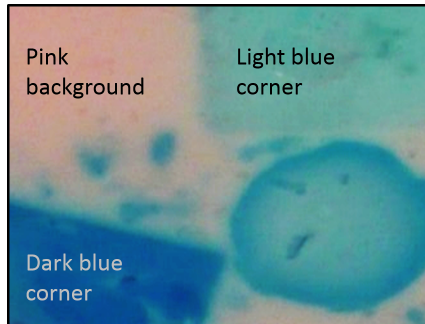


Figure 5.26: Home-made gelatine-based heterogeneous phantom composed of different optical properties  $\mu_a$  and  $\mu'_s$ .

Contact DRSsr measurements have been taken (on similar areas than the ones imaged) of the pink background mixture, the dark blue, and the lighter blue shapes. Figure 5.27 shows the estimated reference optical properties.

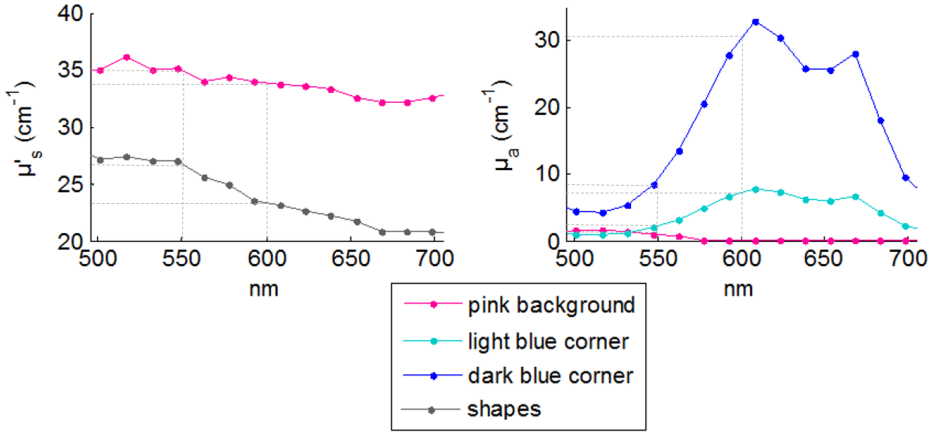


Figure 5.27: Contact DRSSr estimated  $\mu'_s$  (left) and  $\mu_a$  (right) properties of the different zones (background and light blue or dark blue shapes) on the heterogeneous gelatine-based phantom.

### 5.9.1 Image acquisition

Filters of 550 nm and 600 nm are chosen for LFOV MSI, because at these wavelengths there is a clear difference of the absorption signature of the various zones (see grey dotted lines of Figure 5.27). Images with these filtered light are acquired and treated as explained in Sections 5.2 and 5.3 and shown in Figure 5.28. Notice that some small areas have a wrong reflectance intensity value because of specular reflections caused by air bubbles or sample holes. The small specular reflections are bypassed through a filter algorithm that accords the minimal value of a mask to the center pixel. Yet, because the correction of the surface curvature of the sample has not been considered in this case, the quantification of holes is not possible.

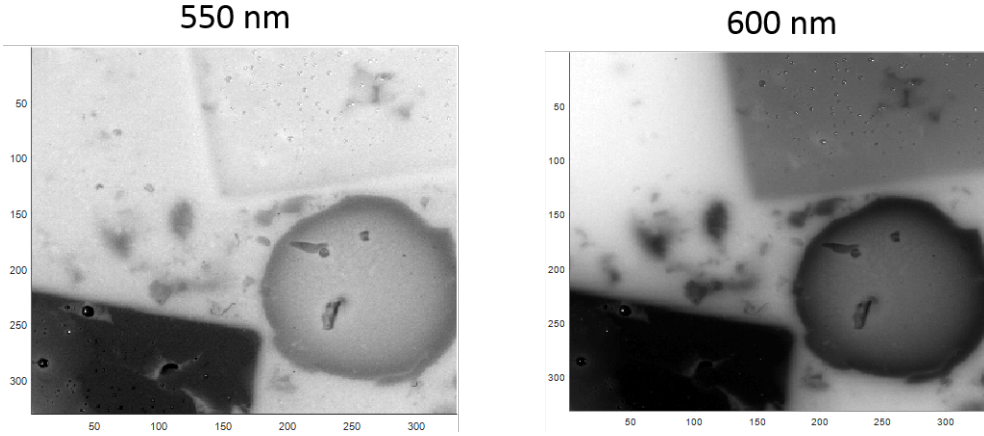


Figure 5.28: Treated images of the heterogeneous phantom under 550 and 600 nm filtered illumination.

### 5.9.2 Wide-field absorption quantification

The first step in the quantification of wide-field  $\widehat{\mu}_a$  with LFOV MSI is to give a  $\mu'_{s,known}$  value to each pixel of the image. The  $\mu'_{s,known}$  map is built with an intensity-based segmentation procedure, based on the high contrast of the 600 nm image and the *Otsu* method. DRSSr estimated  $\widehat{\mu}'_s$  values are set for each segmented homogeneous zone (background and shapes) as illustrated in Figure 5.29.

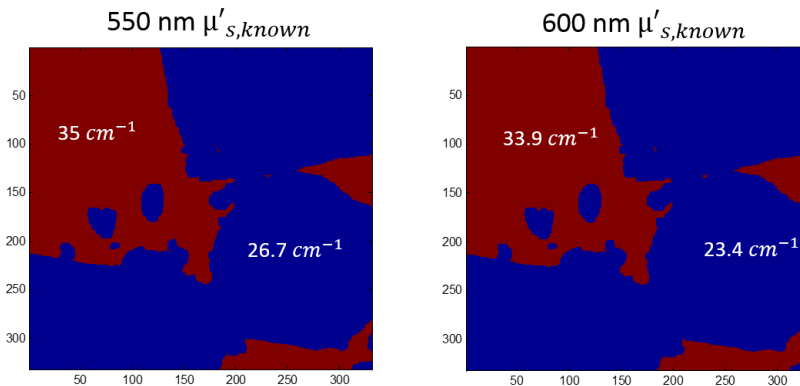


Figure 5.29:  $\mu'_{s,known}$  map for 550 and 600 nm.

This quantitative multispectral  $\mu'_{s,known}$  map, together with the *CF*-reference base is used to calibrate single pixel of images according to *ACA-Pro* (refer to Section 5.6) and optimally quantify wide-field  $\widehat{\mu}_a$  (see Figure 5.30). Notice that the quantitative  $\widehat{\mu}_a$  maps show values corresponding to the Contact DRSSr-estimated  $\widehat{\mu}_a$  of the different zones shown in Figure 5.27. These results ultimately validate the wide-field  $\mu_a$  quantifi-

cation ability of LFOV MSI based on an a-priori built  $\mu'_{s,known}$  map and the *ACA-Pro* calibration.

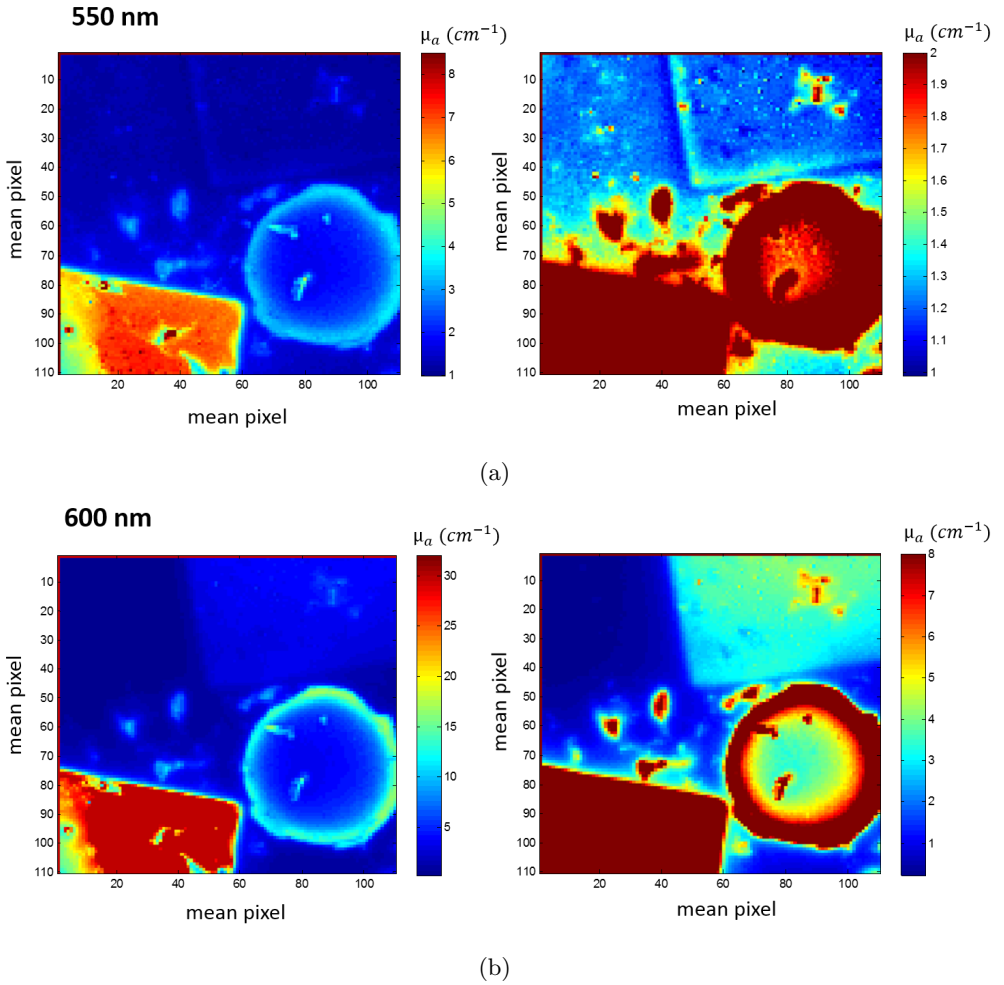


Figure 5.30: Wide field  $\mu_a$  shown with two different scales (left-right) to enhance visualization. (a) 500 nm and (b) 600 nm.

The analysis of quantitative  $\widehat{\mu}_a$  maps at 550 nm and 600 nm is taken a step further with the calculation of relative concentrations of blue and red inks. This is based on linear combinations of spectral unmixing (see Equation 5.11). According to Equation 2.4, the estimated  $\mu_a$  at each wavelength ( $\mu_{a,550}$  and  $\mu_{a,600}$ ) is expressed as a linear combination of the relative extinction coefficient  $\varepsilon_R$  of red and blue ink multiplied by their corresponding concentrations  $C_{red}$  and  $C_{blue}$ . In this case, no theoretical quantification of  $\varepsilon_R$  is available and thus has been replaced by Contact DRSSr  $\mu_a$  signatures of the background and the light blue zones (refer to right Figure 5.27).

$$\begin{aligned}\mu_{a,550} &= \mu_{a,red,550} \cdot C_{red,550} + \mu_{a,blue,550} \cdot C_{blue} \\ \mu_{a,600} &= \mu_{a,red,600} \cdot C_{red,600} + \mu_{a,blue,600} \cdot C_{blue}\end{aligned}\tag{5.11}$$

$C_{red}$  and  $C_{blue}$  are calculated for each pixel to build the concentration maps, shown in Figure 5.31. Notice the correct distribution of red ink on the pink background mixture and the blue ink on the shapes. Mixtures of red and blue ink are present at the border and the surface of shapes, as expected. Areas corresponding to holes are not quantitative because of shadow and curvature artefacts.

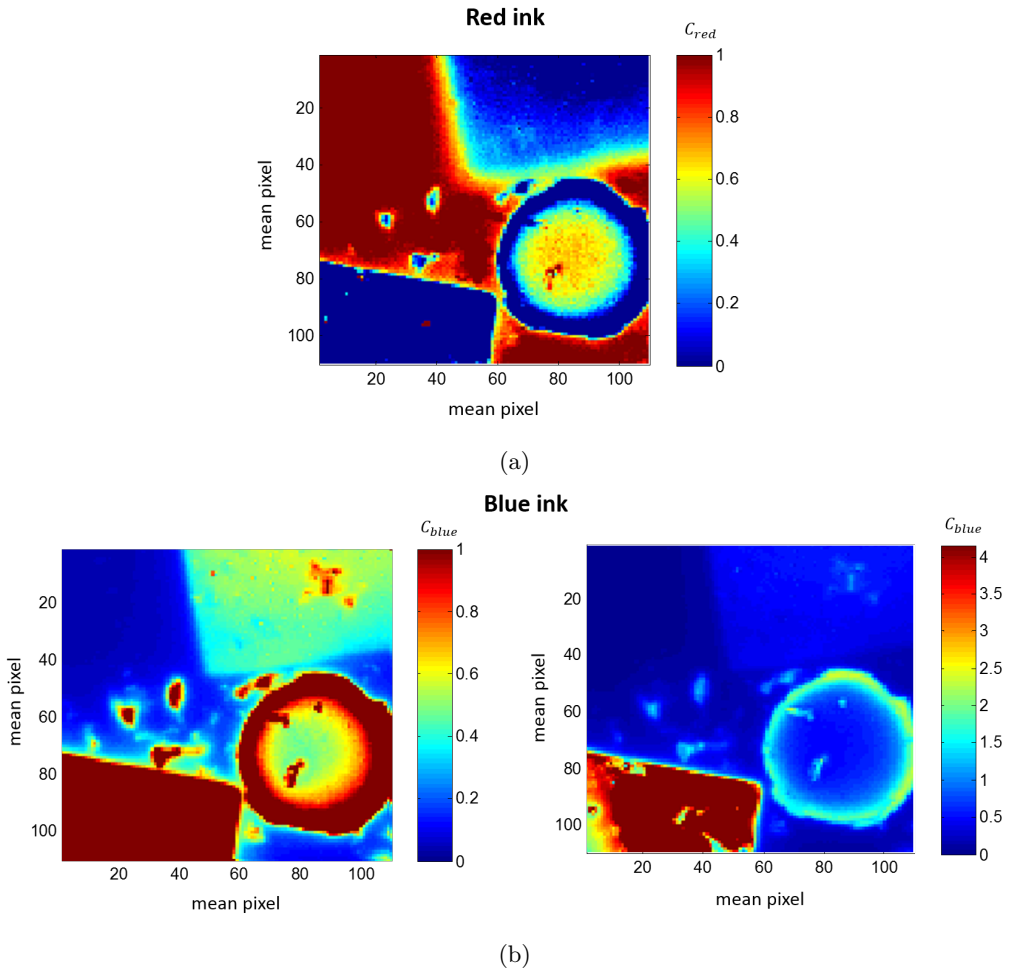


Figure 5.31: Relative concentration of (a) red ink (b) blue ink, shown with two different scales for visual enhancement.

## 5.10 Conclusion

In this Chapter we have described the Multispectral Imaging (MSI) setup used to cover a Large Field of View (LFOV). We have also validated a method for wide field imaging quantification of absorption using an isotropic illumination model and considering the scattering properties of the sample to be known.

We have shown that supposing wrong scattering properties, provoke estimation errors that hinder absolute quantification of absorption. A-priori known scattering properties should approach the theoretical ones to achieve acceptable estimation errors that allow absolute absorption quantification. With the *Dual-Step* technique we propose, scattering properties are estimated with Non-Contact DRSr.

We also noticed a deviation between the isotropic illumination model and measurements that degrades the  $\mu_a$  quantification of samples having optical properties far from the reference, used for calibration. This is directly related to the accuracy limitation of the diffusion model in media in which scattering does not outweigh absorption properties. To overcome this limitation, we integrated the *ACA-Pro* algorithm for instrumental calibration according to optical properties. We have shown and validated the optimal wide field absorption quantification of *ACA-Pro*, including the use of a correction factor *CF* reference base, *CF* interpolation, and correction of illumination intensity fluctuations between images. Using the Non-Contact DRSr estimated  $\mu'_s$  and *ACA-Pro*, average  $\mu_a$  relative error achieved for a large range of well-characterized homogeneous intralipid phantoms is less than 5.5%. To further reduce this error, a spatially distributed correction factor *CF* should be used to take into account the non-homogeneous non-modelled spatial illumination.

We also showed the wide-field  $\mu_a$  quantification capacity of LFOV MSI in a first heterogeneous phantom with different  $\mu'_s$  and  $\mu_a$  properties. The calculated quantitative  $\mu_a$  maps allowed to derive concentration maps of the different absorbing chromophores. These quantitative results on the heterogeneous medium have encouraged the measurement of biological samples with our technique, shown in the next Chapter 6.

# 6

---

## Optical properties quantification of biological tissue with Dual-step technique

This Chapter describes the final *Dual-Step* Multispectral Imaging technique which couples the *initial Non-Contact DRSSr* (described in Section 3.3) with LFOV MSI (described in Chapter 5). The technique achieves wide-field quantification of optical properties through an initial estimation of scattering with Non-Contact DRSSr used to quantify absorption with LFOV MSI.

The final assembled instrumental setup, combining the Non-Contact DRSSr system with the LFOV MSI system is described in Section 6.1.

The approach has been validated with measurements on biological models. These include: three different *ex-vivo* human abdominal skin samples (Section 6.2.1) and three *in-vivo* rat skin models (Section 6.2.2). The latter include two different inflammation models which are of particular interest for future medical application.

The general measurement procedure used for all biological samples is detailed in Section 6.3.

Section 6.4 describes the signal and image processing that has been implemented previous to the use of *ACA-Pro* for the optimal quantification of wide field absorption (Section 6.5).

Sections 6.6 and 6.7 interpret the absorption quantification results of each *ex-vivo* human skin and *in-vivo* rat skin models, respectively.

Section 6.8 terminates with the discussion and conclusions that can be drawn from the biological sample results, obtained with the *Dual-Step* Multispectral Imaging technique.

## 6.1 Instrumental Setup

The final instrumental system of the *Dual-Step* technique is shown in Figure 6.1. Individual detailed descriptions of the coupled setups are given in Section 3.3.1, for Non-Contact DRSsr, and Section 5.1, for LFOV MSI. For LFOV MSI, the wavelengths of filters chosen are 500, 550, 600, and 700 nm, to allow optimal contrast of skin chromophores (see Figures 2.10 and 2.12b).

The focal distance of the objective lens used in MSI, and the doublet pair used in Non-Contact DRSsr, are fixed to settle a common focal plane (illustrated with the green line). The sample object is placed on a translation stage and moved in the  $x$  and  $y$  directions, according to a developed *LabView* interface program.

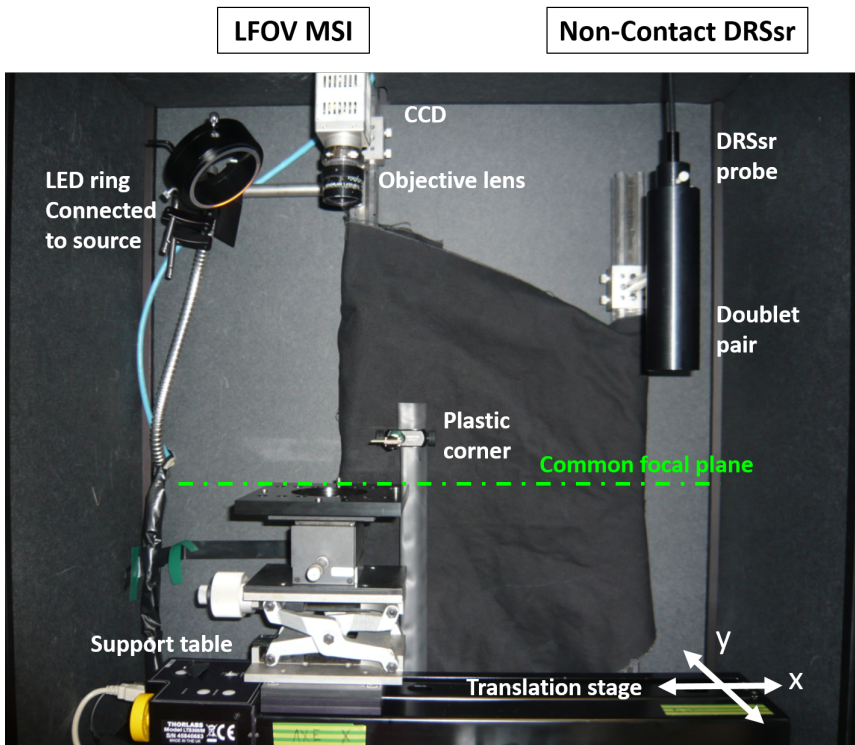


Figure 6.1: Real *Dual-Step* setup combining initial Non-Contact DRSsr with LFOV MSI systems. The common focal object plane to both techniques is delineated in green. The sample object is moved between them (in  $x$ - $y$  directions) with the translational stage.

The whole system is isolated inside a black-cardboard structure and reflecting components are covered with a black cloth or plastic to ensure no uncontrolled reflections and set the same dark ambient conditions for all measurements.

## 6.2 Samples

The biological samples that are measured with the *Dual-Step* technique are: three *ex-vivo* human skin samples and three *in-vivo* rat skin models. These are respectively described in the following Sections 6.2.1 and 6.2.2.

Additional intralipid phantoms (refer to Section 6.2.3) have been manufactured and measured to build a *CF*-reference base necessary for *ACA-Pro* calibration of all techniques.

### 6.2.1 *Ex-vivo* Human abdominal skin

Three different skin samples of human abdomen were purchased from the biochemistry laboratory *BIOPREDIC INTERNATIONAL* (Saint-Grégoire, France).

The skin samples include the full thickness of skin with underlying adipose tissue.

The first sample (Figure 6.2a) is a  $2 \times 3 \text{ cm}^2$  homogeneous piece of caucasian skin of Phototype 2. This is used as the first homogeneous model representative of a low skin absorption range.

The second sample (Figure 6.2b) is a  $2 \times 3 \text{ cm}^2$  piece of caucasian skin of Phototype 2 with stretch marks naturally present and visible. This is used as the heterogeneous model representative of a low skin absorption range.

The third sample (Figure 6.2c) is a  $3 \times 3 \text{ cm}^2$  homogeneous piece of african skin of Phototype 5. This is used as the second homogeneous model representative of a higher skin absorption range.

On each sample, Non-Contact DRSr scan (NC scan) is performed on the positions shown by the red line and the considered field of view for MSI is illustrated with a blue square.

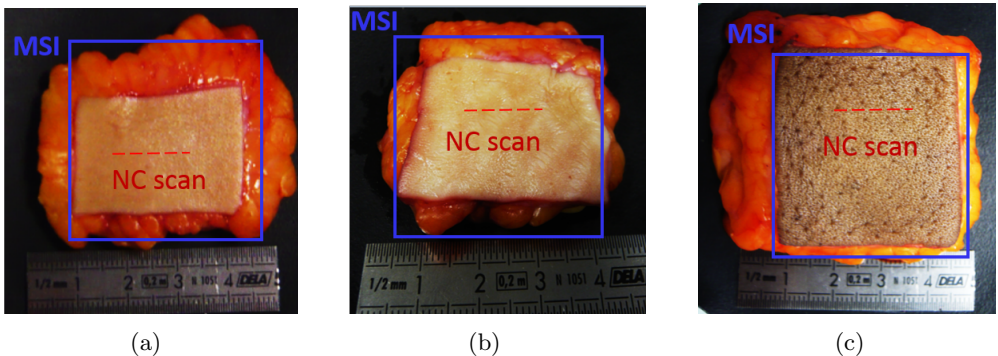


Figure 6.2: Samples of abdominal human skin used as (a) Homogeneous model of Phototype 2 (b) Heterogeneous model of Phototype 2 (c) Homogeneous model of Phototype 5.

All samples were decontaminated before surgery with chlorhexidine alcohol and conserved at a storage temperature of  $-20 \text{ }^\circ\text{C}$ . The frozen samples were delivered in less than 6 hours, during which the temperature was kept lower than  $0 \text{ }^\circ\text{C}$ . As soon as they

were received in our laboratory, they were re-frozen until use. No additional treatment has been performed.

### 6.2.2 *In-vivo* rat models

Three *Lister Hooded* adult rats were purchased from the laboratory *Charles River* (Saint-Germain-Nuelles, France) and bred at the Institute of Advanced Biosciences *Albert Bonniot* (La Tronche, France).

Animal experiments were conducted in accordance with the Institutional European guidelines and approved by the Regional Ethics Committee and the French Ministry of Education and Research.

For all manipulations, rats were anaesthetized with isoflurane/oxygen 3.5% for induction and 1.5% thereafter. The day previous to the experiment, the rats were shaved with a hair clipper and depilatory cream to allow measurements on the bare soothed skin of the zones of interest.

Figure 6.3 shows the three rats used for the *in-vivo* heterogeneous models. The position of the Non-Contact DRSSr scan (NC scan), performed on each sample, is illustrated with a red line and the quantified field of view of MSI is depicted with a blue square.

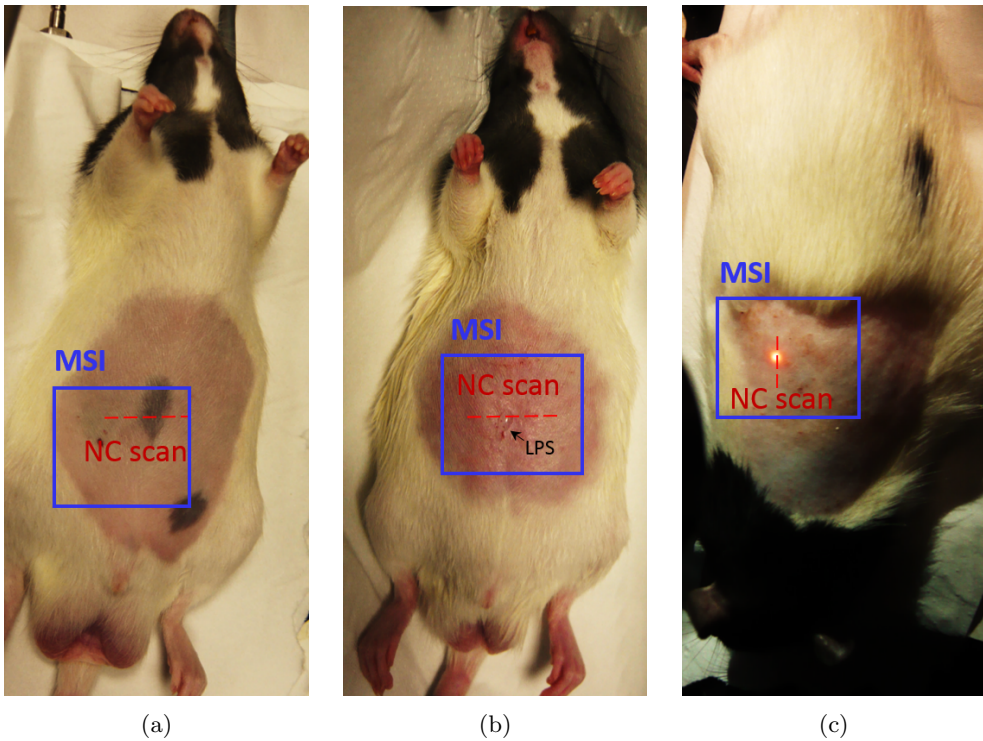


Figure 6.3: In-vivo rat skin models (a) Bi-coloured model (b) Inflammation Type 1 model (c) Inflammation Type 2 model.

The first model (Figure 6.3a) is a bi-coloured model for which a black mark in the white abdomen of the rat is scanned and imaged.

The second model (Figure 6.3b) is an inflammation model Type 1, proposed by [Kim et al., 2015]. The inflammatory response is provoked with lipopolysaccharide (LPS), a gram negative bacterial membrane that has been widely used in inflammatory studies [Diks et al., 2001]. For our model, a 20  $\mu$ l drop of LPS has been topically applied on the rat's abdomen. Previous to application of LPS, the zone on the rat's abdomen is pricked a few times with a syringe needle for faster integration. The action period of inflammation is within 30 min - 1 hour.

The third model (Figure 6.3c) is an inflammation model Type 2 which has been provoked through supplementary unequal shaving of the rat's back with the same depilatory cream and hair clipper to the ones used the previous day.

### 6.2.3 Reference samples

For *ACA-Pro* calibration of DRSsr (refer to Chapter 4) and LFOV MSI (refer to Section 5.6), ten intralipid phantoms are manufactured, as described in Section 2.3.1. The selected reference optical properties of the phantoms, are summarized in Table 6.1.

Table 6.1: Reference Optical properties of the *CF* reference base.

Phantom #	$IL_{ref}$	$\mu_{a,ref}$ at 600 nm
<b>1</b>	<b>1%</b>	<b>0.4 <math>cm^{-1}</math></b>
<b>2</b>	<b>1%</b>	<b>1 <math>cm^{-1}</math></b>
<b>3</b>	<b>1%</b>	<b>2.84 <math>cm^{-1}</math></b>
<b>4</b>	<b>1%</b>	<b>6.1 <math>cm^{-1}</math></b>
<b>5</b>	<b>1%</b>	<b>10.4 <math>cm^{-1}</math></b>
<b>6</b>	<b>1.5%</b>	<b>0.4 <math>cm^{-1}</math></b>
<b>7</b>	<b>1.5%</b>	<b>1 <math>cm^{-1}</math></b>
<b>8</b>	<b>1.5%</b>	<b>2.84 <math>cm^{-1}</math></b>
<b>9</b>	<b>1.5%</b>	<b>6.1 <math>cm^{-1}</math></b>
<b>10</b>	<b>1.5%</b>	<b>10.4 <math>cm^{-1}</math></b>

Additionally, a measurement of the standard Spectralon (see Figure 4.20) is performed with DRSsr to correct the intensity variations (Int. var.) with *ACA-Pro* (see Section 4.5.6). It is also imaged with LFOV MSI to perform the Flat Field correction (see Section 5.2.2).

All samples are measured according to the protocol described in the next Section 6.3 to build the *CF* reference base, proper to each technique.

### 6.3 Measurement Procedure

In this study, the *Dual-Step* approach, coupling Non-Contact DRSSr and LFOV MSI techniques, is validated with respect to the pre-existing and well-established *Contact DRSSr* system.

Apart from the skin samples, measurements of the reference samples (intralipid phantoms and Spectralon) are performed.

The entire reference phantom base (Table 6.1) is measured with all techniques only once to build the general *CF* reference base. However, together with each biological sample, three selected phantoms (# 1, 2, and 6, delineated in bold) are also measured to build a reduced *CF* reference base used to control individual measurement conditions. These selected phantoms and the considered biological sample define an individual measurement set.

An appropriate sequence of measurements with the three techniques (Contact DRSSr, Non-Contact DRSSr, and MSI) on the three samples (skin (*in-vivo* and *ex-vivo* models), intralipid phantoms, and Spectralon) is followed to ensure:

- Position correlation between Non-Contact DRSSr scan measurements and LFOV MSI images.
- The same measurement conditions (dark and instrumental conditions) for the single biological sample and the three selected intralipid phantoms of the individual measurement set.

Firstly, Contact DRSSr measurements are taken on intralipid phantoms, according to the procedure described in Section 3.2.2, on the standard Spectralon, with the support shown in Figure 4.21, and at three measurements of the various zones of interest on the biological skin sample, as illustrated in Figure 6.4. All these measurements are acquired under the same dark conditions and are used to quantify  $\mu_a(\lambda)$  and  $\mu'_s(\lambda)$ .

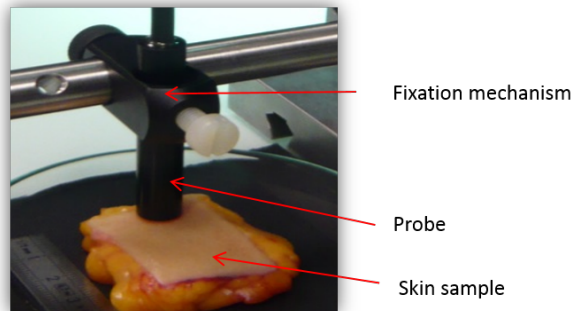


Figure 6.4: Fixed DRSSr probe positioned in contact with the skin sample to be measured.

Secondly, the same DRSSr probe used for Contact DRSSr, is inserted in the framework of Figure 3.20 for Non-Contact DRSSr measurements. Beforehand, the height of

the support table is adjusted for samples to be at the common focal plane with the minimal  $S6$  signal, according to the procedure described in Section 3.5.2. Measurements are then acquired as described in Section 3.3.4. After intralipid phantoms and Spectralon measurements, the biological sample is placed on the support table and focused at the central point of the Non-Contact DRSsr scan (illustrated with a red line on Figures 6.2 and 6.3). Since the probe is fixed inside the Non-Contact DRSsr framework and no ambient light enters the setup, the same exact conditions are ensured for all measurements. Under these conditions, both optical properties  $\mu_a(\lambda)$  and  $\mu'_s(\lambda)$  are estimated. Keep in mind that Non-Contact DRSsr achieves good estimations of  $\mu'_s(\lambda)$  (error < 4.1%) for a DOF of 1.2 mm (Section 3.5.2). However,  $\mu_a(\lambda)$  estimations are optimal at the focal plane only and are rapidly overestimated with slight depressions of the sample.

Thirdly, the support table, on which the sample skin has been placed at the common focal plane, is moved with the translation stage under the CCD for LFOV MSI measurements. Special care is made for the sample not to move on the support table, so that the Non-Contact DRSsr scan positions can be directly identified in the acquired MSI images (refer to Section 6.4.2). Subsequently, the skin sample is removed from the support table and focused intralipid phantoms are measured under the same dark conditions. The acquired MSI images are used for the wide field quantification of  $\mu_a(\lambda)$  with the a-priori DRSsr estimation of  $\mu'_s(\lambda)$ .

Table 6.2 summarizes the measurement sequence of an individual measurement set and indicates the related specific purpose.

Table 6.2: Measurement sequence (Seq.) for an individual measurement set

Seq.	Technique	Conditions	Sample	Purpose
1	Contact DRSsr	Same dark	Skin	$\mu_a$ and $\mu'_s$
2			Phantoms	<i>ACA-Pro CF</i> -base
3			Spectralon	<i>ACA-Pro Int.</i> var.
4	Non-Contact DRSsr	Same dark, Fixed Probe, Adapted Focus	Phantoms	<i>ACA-Pro CF</i> -base
5			Spectralon	<i>ACA-Pro Int.</i> var.
6		Same dark, Fixed Probe, Common Focal Plane	Skin	$\mu_a$ and $\mu'_s$
7	LFOV MSI	Same dark, Common Focal Plane	Skin	$\mu_a$
8		Same dark,	Phantoms	<i>ACA-Pro CF</i> -base
9		Adapted Focus	Spectralon	Flat Field

## 6.4 Signal and Image Processing

Contact and Non-Contact DRSSr measurements are treated as described previously in Sections 3.2.3 and 3.3.5, respectively.

LFOV MSI images are treated according to the fundamental corrections described in Section 5.3. Additionally, the specular reflections at the sample surface, seen in MSI images of biological samples, should be corrected to improve  $\widehat{\mu}_a$  quantification, as explained in Section 6.4.1.

For what concerns the *Dual-Step* technique, a supplementary procedure of image processing is required to correlate positions between the Non-Contact DRSSr scan and MSI images. This is explained in Section 6.4.2.

### 6.4.1 Filtering of Specular Reflections

Despite the inclination of the source, we observe specular reflections on the surface of the biological samples which degrade the quantification of absorption. To reduce the specular effect, we use a filter function. The function uses a  $3 \times 3$  kernel, which is swept throughout the entire image assigning the minimal value of pixels in the mask to the central pixel. Figure 6.5 shows the difference on an example image (at 500 nm) before and after filtering.

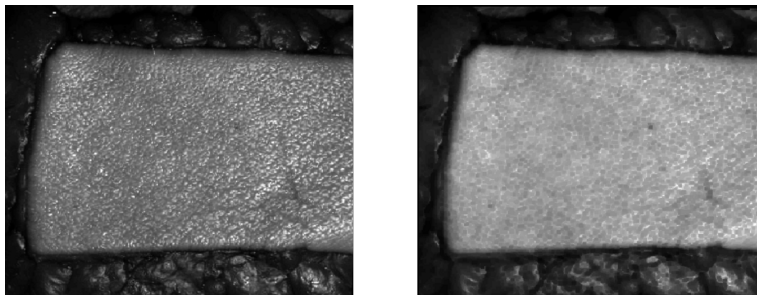


Figure 6.5: Left: Original image at 500 nm, Right: Same image after application of the specular filter.

The effect of this filter on the  $\widehat{\mu}_a$  estimation is further analysed in Section 6.5.2.

### 6.4.2 Position Correspondence

The first step of position correlation for the *Dual-Step* approach is to obtain a unique coordinate axis of the entire system. Hence, the tilt of the CCD with respect to the translation stage axis is corrected with an affine transform. For this, a grid paper is positioned on the support table and fixed along the translation stage axis with the use of the illumination projection of the Non-Contact DRSSr. The support table is then moved with the translation stage under the CCD and an image is acquired. This image is used together with a pre-built aligned grid to manually select corresponding pair points, as depicted in Figure 6.6. The coordinates of the selected points derive the affine transform which is methodically applied to all images.

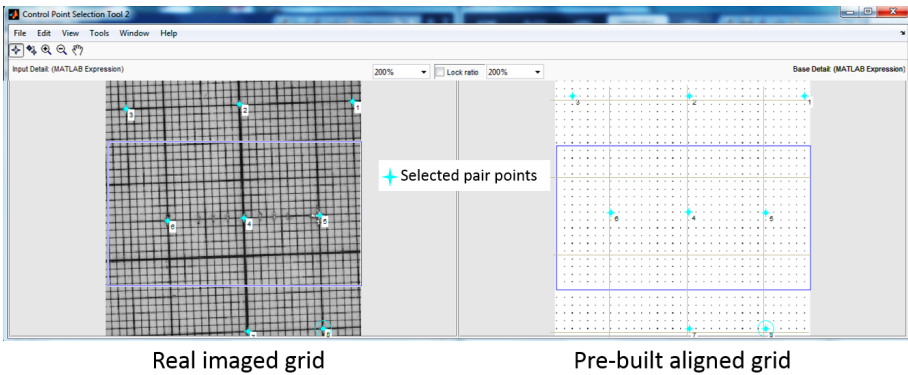


Figure 6.6: Example of the manually selected corresponding points (in cyan) in the real imaged grid (left) and the pre-built aligned grid (right).

The second step of position correlation consists in identifying the Non-Contact scan points in the MSI image. For this, we use a grid paper on which the starting and ending points of the scan are manually drawn. The image of this paper allows the manual selection of the points to obtain their coordinates. Figure 6.7 shows an example of the scan points identification on one of the skin sample images.

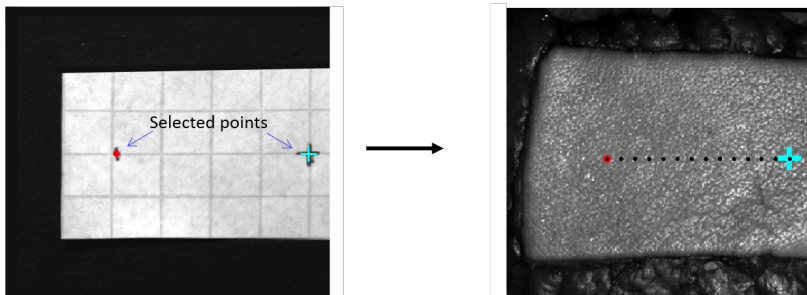


Figure 6.7: Affine transformed images showing the matching points (black dots) of the Non-Contact DRSSr scan, starting with the cyan cross and ending at the red dot on the grid paper and on the sample.

Now, the Non-Contact DRSSr scan point measurements previously validated with the reference Contact DRSSr (see Section 6.5.1) can be directly used for the quantification of the corresponding pixel line in the MSI image as shown in Section 6.5.2.

## 6.5 Quantification of optical properties

The quantification method is described separately for Contact and Non-Contact DRSSr, settling the reference estimations (Section 6.5.1) which are then used by LFOV MSI, according to the *Dual-Step* technique, for absorption quantification (Section 6.5.2). To facilitate the explanation, we have used the measurements of the homogeneous human skin sample of Phototype 2. The same procedure is applied to all other *ex-vivo* human skin samples (Section 6.6) and *in-vivo* rat skin models (Section 6.7).

### 6.5.1 DRSSr

Individual measurement sets of Contact and Non-Contact DRSSr are calibrated according to *ACA-Pro* with the entire general *CF*-reference base (of Table 6.1), through the correction of instrumental variations with the Spectralon measurements (refer to Section 4.5.6). Because the individual measurement sets are measured in a special *L2* room, adapted for the manipulation of human samples, and the reference phantoms of the general *CF*-base are measured after moving the entire instrumental system to a different room, the main source of instrumental variations is the system transfer. The correction of instrumental variations is validated with the phantom #2 ( $IL_{theo} = 1\%$  and  $\mu_{a,theo} = 1 \text{ cm}^{-1}$  at  $600 \text{ nm}$ ) which is defined as unknown and is calibrated either with the general *CF*-base requiring correction, or with the individual measurement set *CF*-base. The fitting of DRSSr calibrated signals to the forward Monte-Carlo model (refer to Section 3.2.4) results in quantified optical properties with negligible difference (results not shown) between the different *CF*-reference bases used. This validates the performance of the *ACA-Pro* in the context of real experimental variations.

Figure 6.8 shows an example of the average Contact and Non-Contact DRSSr measurements on the homogeneous skin sample of Phototype 2. Error bars of Contact and Non-Contact DRSSr measurements correspond to the standard deviation calculated with twelve measurements (three measurements of four considered zones along the scan).

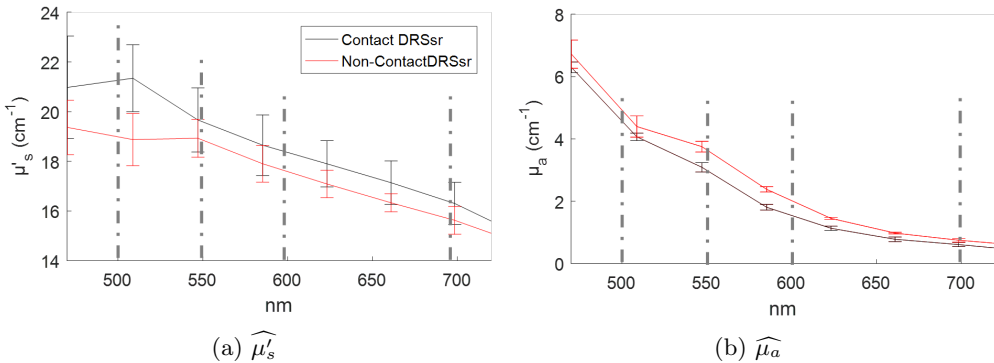


Figure 6.8: Contact and Non-Contact DRSSr optical properties estimations of homogeneous skin model of Phototype 2.

Note that Contact and Non-Contact DRSSr estimations have a similar tendency and their bar errors mostly overlap. Full correspondence is not achievable because measurements with both DRSSr techniques are taken on the same average zones but not

exactly at the same points. Therefore, slightly different volumes of tissue are inspected.

Therefore, these results validate the estimations of Non-Contact DRSSr with the reference Contact DRSSr technique.

### 6.5.2 *Dual-Step* technique

According to the *Dual-Step* technique, MSI makes use of the validated and interpolated Non-Contact DRSSr optimal  $\widehat{\mu}'_s$  estimation, set as  $\mu'_{s,known}$  to spatially estimate  $\widehat{\mu}_a$  (as explained in Section 5.6). As an example, the  $\mu'_{s,known}$  estimations of the Non-Contact DRSSr scan (with a constant step of 1.5 mm) are interpolated and imaged in Figure 6.9 on top of the treated images of the homogeneous model of Phototype 2. As expected,  $\mu'_{s,known}$  estimations are homogeneous, with a maximum relative deviation of 5.5% at 500 nm which decreases for other  $\lambda$ .

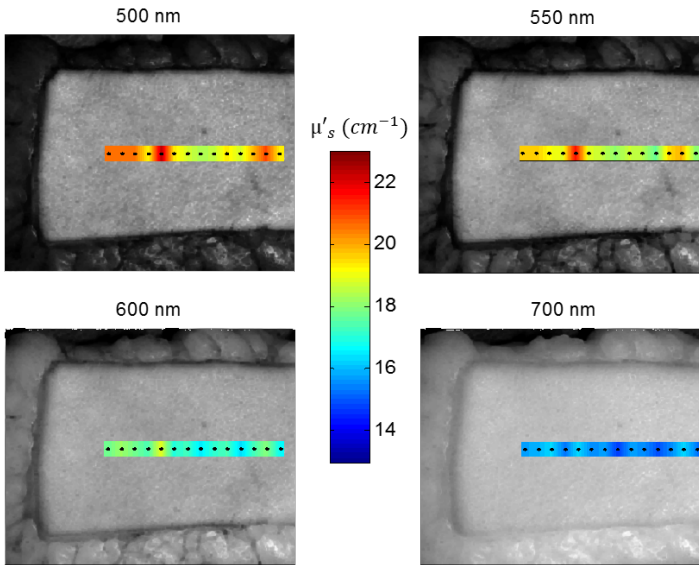


Figure 6.9: Treated images of the homogeneous skin model of Phototype 2. Superimposed to the images are the  $\mu'_{s,known}$  estimations obtained with spatially interpolated Non-Contact DRSSr scan measurements (illustrated with black dots).

These punctual  $\mu'_{s,known}$  estimation values are interpolated and used to derive the corresponding  $\widehat{\mu}_a$  with MSI. For this, *ACA-Pro* corrects each pixel from the source intensity fluctuations (refer to Section 5.3.3) and calibrates it with the entire *CF*-reference base of Table 6.1 as described in Section 5.6. Each calibrated pixel is then fitted to the forward analytical model, defined in Section 5.4.1, to derive  $\widehat{\mu}_a$  estimations.

Figure 6.10 shows MSI  $\widehat{\mu}_a$  estimations together with punctual Non-Contact DRSSr  $\widehat{\mu}_a$  estimations of the corresponding scanned line. The first MSI  $\widehat{\mu}_a$  estimations, shown in blue, show a general underestimation due to the increase in intensity originated from the non-negligible specular reflections (SR) at the surface of the sample. The estimations are improved with the specular filter (see Section 6.4.1), shown in red. It is observed that the underestimation is more significant at 700 nm. An analysis of this effect is given further.

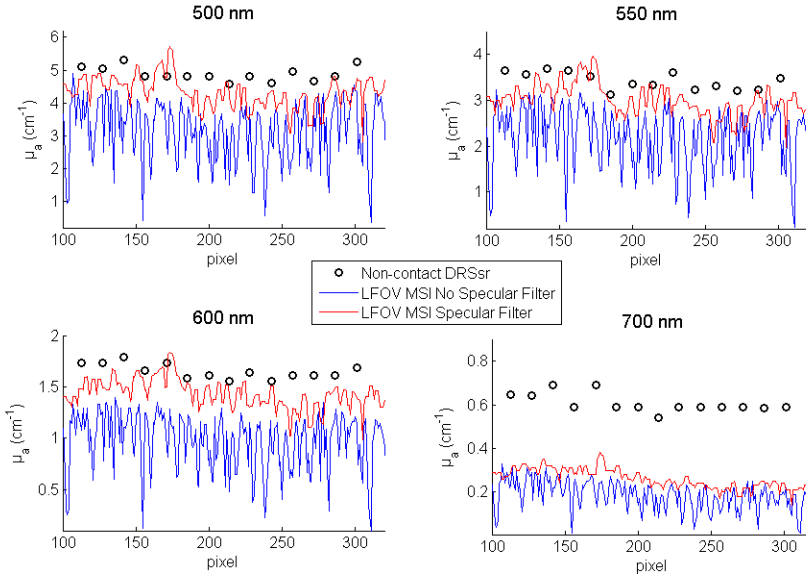


Figure 6.10: Absorption quantification profile of homogeneous skin of Phototype 2 image with Non-Contact DRSSr (black circles) and MSI, with (red line) or without (blue line) specular filtering.

It is clear that specular filtering ameliorates the original large underestimation and ‘speckle’ impression of MSI  $\widehat{\mu}_a$ . Still, it does not eliminate the entire effect of SR. Indeed, the ratio of interpolated Non-Contact DRSSr / filtered MSI  $\widehat{\mu}_a$  estimations, shown in Figure 6.11a, is not uniformly at 1. Notice that the pattern of ratios is very similar at all  $\lambda$ , confirming the particular SR effect. To consider this specular effect, we choose to use the ratio of a single  $\lambda$  (550 nm) to correct all MSI  $\widehat{\mu}_a$  estimations. An example of this correction is shown in green in Figure 6.12.

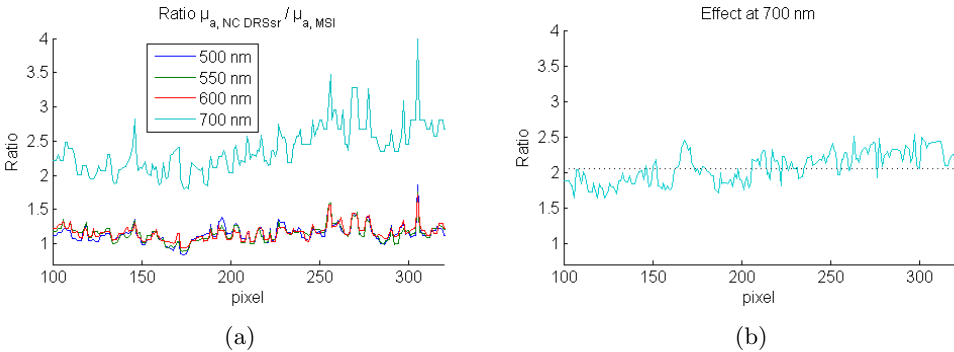


Figure 6.11: (a) Ratio of Non-Contact DRSSr / MSI  $\widehat{\mu}_a$  estimations of homogeneous model of Phototype 2 (see Figure 6.10). (b) Division of 700 nm / 550 nm ratios to derive the average correction factor of the 700 nm effect.

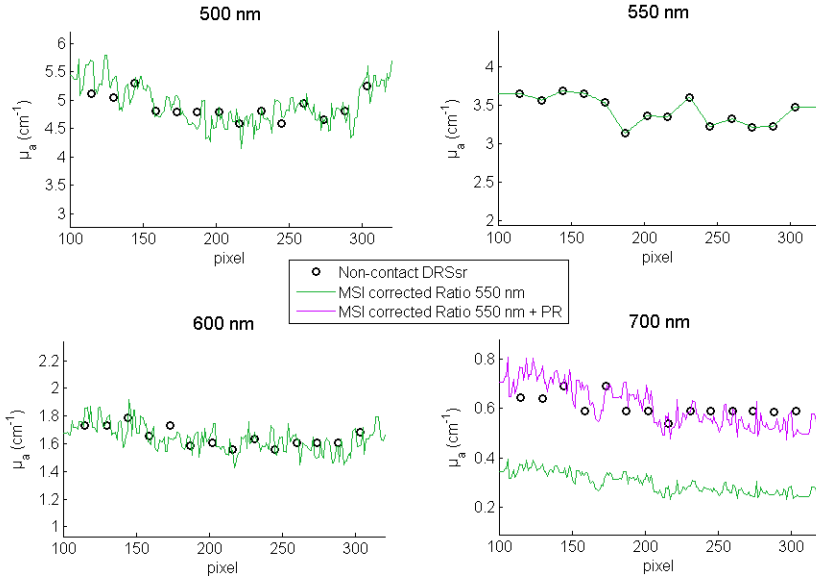


Figure 6.12: Absorption quantification profile of homogeneous skin, Phototype 2 with Non-Contact DRSSr and MSI corrected with the pre-calculated ratios shown in Figure 6.11). Green estimations are corrected from SR with the Ratio of 550  $nm$  shown in Figure 6.11a. Violet estimations are adjusted with the factor shown in Figure 6.11b.

We note that the obtained MSI  $\widehat{\mu}_a$  is still underestimated with respect to Non-Contact DRSSr  $\widehat{\mu}_a$ . This is directly related to the higher ratio amplitude at 700  $nm$  of Figure 6.11a. In an attempt to quantify this effect, we determine another correction factor through the division of the 700  $nm$  ratio and the 550  $nm$  ratio. The resulting factor, shown in Figure 6.11b, is spatially averaged and also used to adjust MSI  $\widehat{\mu}_a$  estimations at 700  $nm$  to the parasite reflections of Non-Contact DRSSr, as illustrated in violet in Figure 6.12. A possible explanation of this effect (to be verified in perspective work, Section 7.2.3) is the overestimation of  $\mu_a$  by Non-Contact DRSSr due to the low signal-to-noise ratio (SNR) resulting from the low source emission and high doublet pair parasite reflection (PR) at  $\lambda \geq 700$   $nm$  (see Section 3.3.3).

Since corrected MSI  $\widehat{\mu}_a$  follows the punctual Non-Contact DRSSr  $\widehat{\mu}_a$  estimations at  $\lambda=500, 600,$  and  $700$   $nm$ , the common SR pattern (calculated with a different  $\lambda=550$   $nm$ ) is validated and the DRSSr effect at 700  $nm$  is properly compensated. Keep in mind that these corrections are performed for representation purposes mainly. Further authentication of the SR ratio correction capability should be considered. Alternatively, the use of polarized light in a perspective instrumental *Dual-Step* setup would completely avoid the SR effect (refer to 7.2.2). Moreover, a doublet pair treated for the whole spectral range would result in no PR of Non-Contact DRSSr (refer to Section 7.2.1).

The spatial average of corrected MSI  $\widehat{\mu}_a$  estimations (see Figure 6.12) are directly compared to averaged Contact and Non-Contact DRSSr  $\widehat{\mu}_a$  estimations as illustrated in Figure 6.13. With these results, the  $\mu_a$  quantification ability in biological samples of the developed *Dual-Step* technique is confirmed.

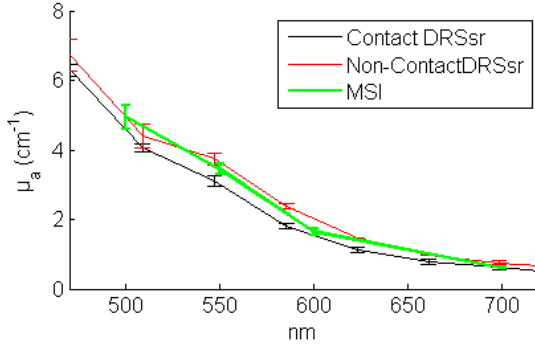


Figure 6.13: Average absorption quantification of homogeneous model of Phototype 2 with Contact DRSSr, Non-Contact DRSSr, and corrected MSI.

The validation of this absorption quantified scanned line with MSI is extended to a wide field in the next Section 6.5.3.

### 6.5.3 Wide field quantification of $\mu_a$

According to the small  $\widehat{\mu}'_s$  variations (maximum deviation of 5.5 %) of Non-Contact DRSSr on the homogeneous skin sample of Phototype 2 (see Figure 6.9), the scattering properties are considered constant for the whole sample. Thereby, the average Non-Contact DRSSr  $\widehat{\mu}'_s$  is set as  $\mu'_{s,known}$  on all pixels and used for the wide field quantification of  $\widehat{\mu}_a$  with MSI (see Figure 6.14).

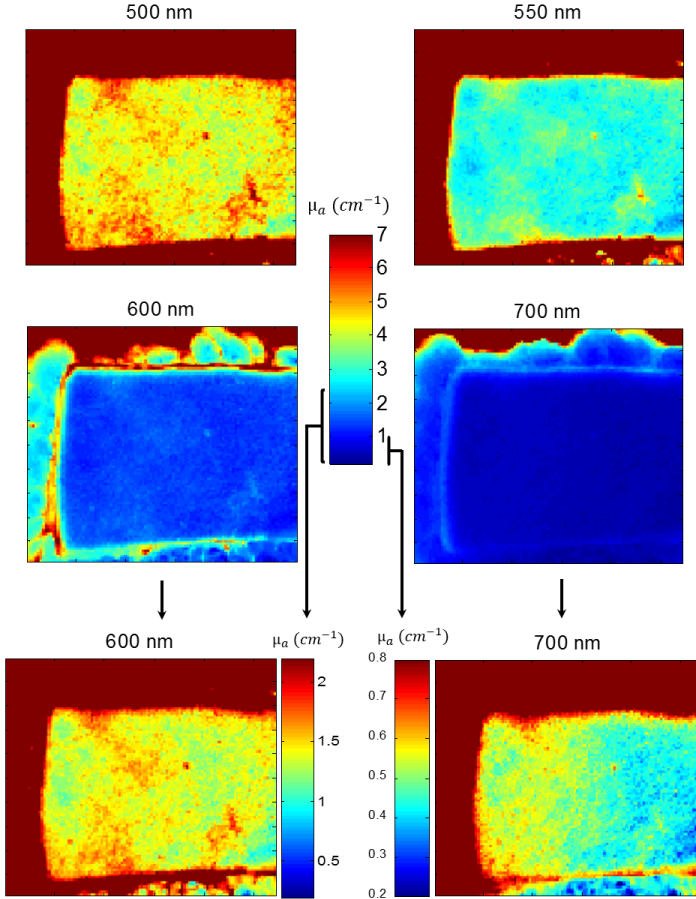


Figure 6.14: Wide-field absorption quantification of homogeneous model of Phototype 2, considering a unique average of Non-Contact DRSSr estimated  $\widehat{\mu}'_s = \mu'_{s,known}$  (Figure 6.8a). The same scale is considered for the top four images at all  $\lambda$ s and an additional zoom of the scale is done for images at 600 and 700  $nm$ .

Notice that, in general, quantitative  $\widehat{\mu}_a$  values are correct on the whole imaged sample and its expected homogeneity is confirmed. Some artefacts are present in wrinkles or sample depressions which show an intensity reduction not only due to the curvature (see Figure 5.25), but mostly due to the resulting shadow, provoking an overestimation of  $\mu_a$ . This error will be considered in a perspective technique (refer to Section 7.2.2).

## 6.6 Validation of *Dual-Step* technique using *ex-vivo* human skin samples

### 6.6.1 Heterogeneous skin model, Phototype 2

The skin sample with stretch marks and Phototype 2 (see Figure 6.2b) is used as the heterogeneous model. Treated images taken at the four different  $\lambda$ s are shown in Figure 6.15 together with the  $\widehat{\mu}'_s$  estimations of the Non-Contact DRSsr scan (with a constant step of 1 or 0.5 mm), having a maximum relative error of 8.3 %. Notice that the contrast of the stretch marks is seen in all images. However, this contrast is not obvious along the scanned Non-Contact DRSsr  $\widehat{\mu}'_s$ . This is due to the size of the inspected DRSsr volume being larger than the stretch marks. Moreover, the direction of the scan impairs the specificity of the estimations. Therefore, as a first perspective attempt to estimate the characteristic optical properties of stretch marks and surrounding tissue with the current Non-Contact DRSsr setup, we would propose to perform a scan in the direction of the tissue variations, as shown in Figure 6.16.

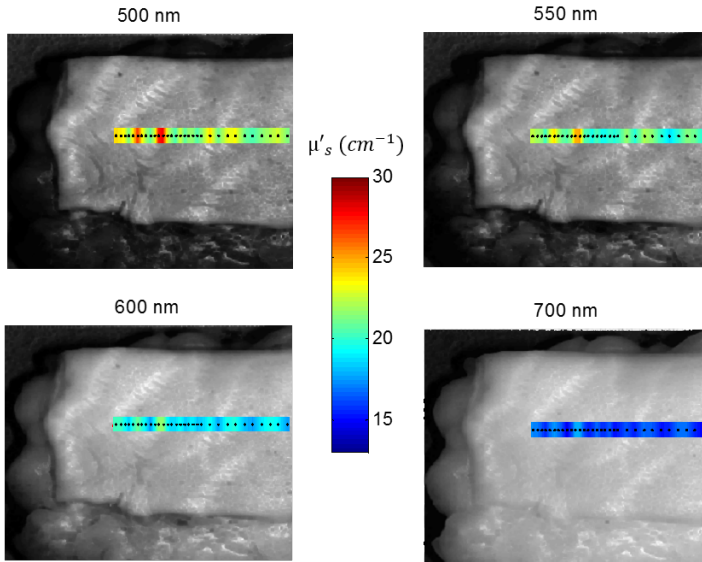


Figure 6.15: Treated images of heterogeneous model of Phototype 2. Superimposed are the  $\mu'_{s,known}$  estimations obtained with interpolated Non-Contact DRSsr scan measurements (illustrated with black dots).

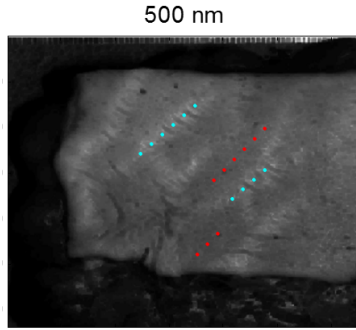


Figure 6.16: Proposed Non-Contact DRSsr scan to determine the characteristic optical properties of stretch marks (cyan dots) and surrounding tissue (red dots).

Because the performed scan does not allow the identification of optical properties proper to the stretch marks and the surrounding tissue, we make use of the average estimations on the sample to continue the analysis. Average Non-Contact DRSsr estimations of both optical properties are validated with respect to the Contact DRSsr ones, as shown in Figure 6.17. Error bars of Contact and Non-Contact DRSsr measurements correspond to the standard deviation calculated with nine measurements (three measurements of three considered zones along the scanned line) and are seen to overlap.

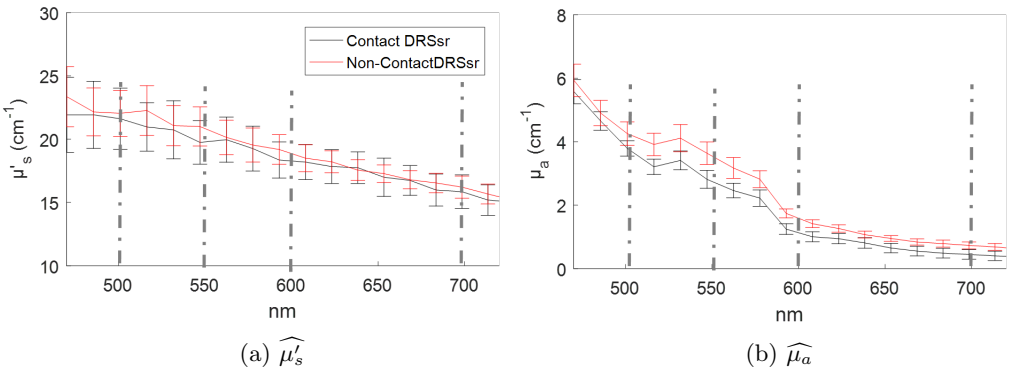


Figure 6.17: Contact and Non-Contact DRSsr optical properties estimations of heterogeneous model of Phototype 2.

### Scanned line $\mu_a$ estimation

The Non-Contact DRSsr estimated  $\mu'_{s,known}$  individual values (see Figure 6.15) are used to estimate the corresponding  $\widehat{\mu}_a$  with MSI with which the effects of SR (see Figure 6.18a) and of PR at 700 nm (see Figure 6.18b) are derived. Notice that with this heterogeneous sample, the effect of SR is more disparate than that of the homogeneous sample (see Figure 6.11a) due to the different surface tissue structure between stretch marks and surrounding skin.

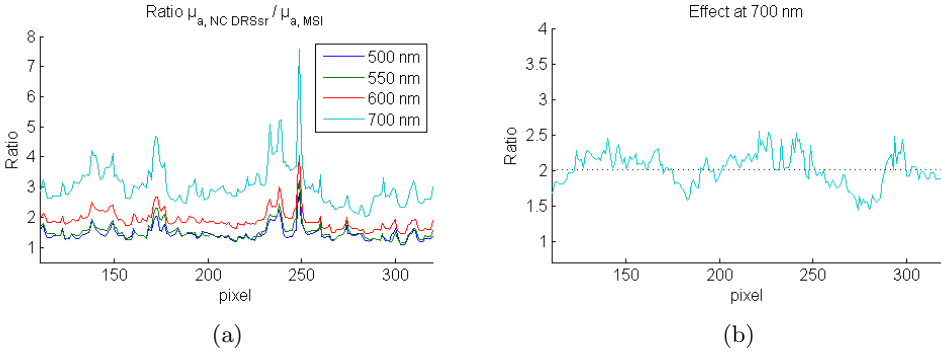


Figure 6.18: (a) Ratio of Non-Contact DRSsr / MSI  $\widehat{\mu}_a$  estimations of heterogeneous model of Phototype 2, used to correct SR. (b) Division of 700 nm / 550 nm ratios to derive the average correction factor of the 700 nm effect.

MSI  $\widehat{\mu}_a$  estimations corrected with the 550 nm ratio (Figure 6.18a) and from the 700 nm effect (Figure 6.18b) are shown in green and violet, respectively, in Figure 6.19 together with the punctual Non-Contact DRSsr  $\widehat{\mu}_a$  estimations. The slight underestimation of  $\mu_a$  at 600 nm is directly related to the slightly higher ratio of Figure 6.18a, that perfectly corrects the SR pattern but does not correct the exact SR intensity. Yet, note how the corrected MSI  $\widehat{\mu}_a$  at  $\lambda=500, 600,$  and  $700$  nm follow the same spatial pattern to that estimated with the Non-Contact DRSsr scan, according to the stretch marks of generally lower absorption, indicated by the yellow arrows. Thereby, the difference in  $\mu_a$  between the stretch marks and surrounding skin is clear.

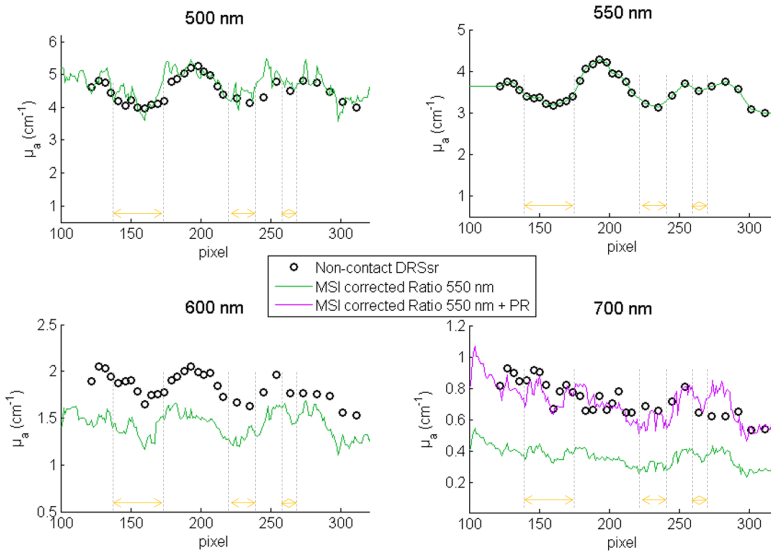


Figure 6.19: Absorption quantification of scanned line in heterogeneous model with Non-Contact DRSSr and MSI corrected (with the pre-calculated ratios shown in Figure 6.18). Green estimations are corrected from SR with the Ratio of 550 nm (Figure 6.18a). Violet estimations are adjusted with the factor of Figure 6.18b. Dotted lines and yellow arrows indicate the position of the stretch marks.

These MSI estimations are spatially averaged and compared to the reference Contact and Non-Contact DRSSr estimations in Figure 6.20. The strong correlation of estimated  $\widehat{\mu}_a$  with the three techniques is confirmed for all  $\lambda$ .

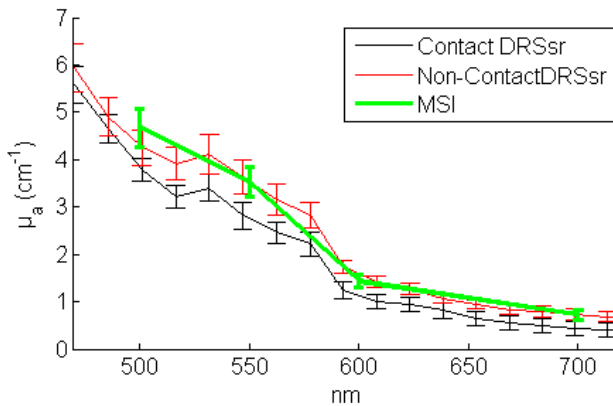


Figure 6.20: Average Absorption quantification of heterogeneous model with Contact DRSSr, Non-Contact DRSSr, and corrected MSI.

### Wide-field $\mu_a$ estimation

As a first stage towards wide-field quantification, we suppose that the whole sample has the same  $\mu'_{s,known}$  because the performed Non-Contact DRSSr measurements do not allow the identification of  $\widehat{\mu}'_s$  proper to the stretch marks and to the surrounding tissue (see Figure 6.15). We are conscious that omitting the specific  $\mu'_s$  values, will affect the quantification of  $\mu_a$ . Yet, until a more appropriate scan will be performed (eg. see Figure 6.16), the segmentation of  $\widehat{\mu}'_s$  should be a focus of perspective work (refer to Section 7.2.3), since it is not straightforward. Thus, we use a unique  $\widehat{\mu}'_s$  value, averaged over the entire Non-Contact DRSSr scan (see Figure 6.15), and set it for the whole sample as  $\mu'_{s,known}$ . This is how the wide-field  $\widehat{\mu}_a$ , illustrated in Figure 6.21, is derived.

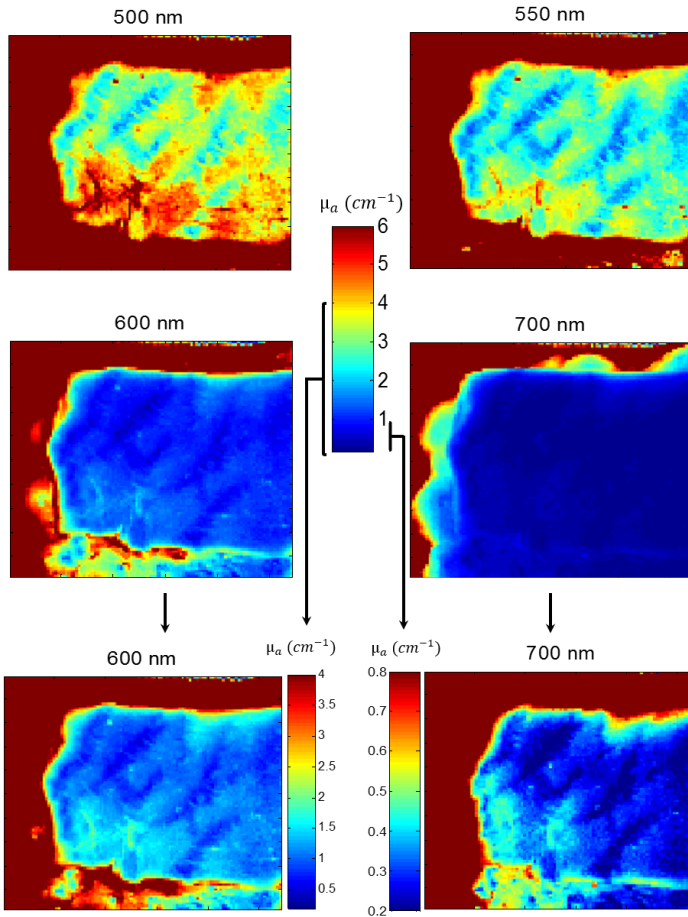


Figure 6.21: Wide-field absorption quantification of homogeneous skin sample of Phototype 2, considering a unique average of Non-Contact DRSSr estimated  $\widehat{\mu}'_s = \mu'_{s,known}$  (see Figure 6.17a). The same scale is considered for the top four images at all  $\lambda$ s and additional zoom of the scale is done for images at 600 and 700 nm.

These quantified  $\widehat{\mu}_a$  maps show a range of absolute values of the surrounding skin similar to that of the homogeneous skin sample (see Figure 6.14), validating the same optical properties range of skin with no stretch marks. Moreover, the expected reduction of  $\widehat{\mu}_a$  at the stretch marks is seen, confirming the contrast previously seen in Figure 6.19. Quantitative absorption values are correct except for the zone with a depression at the sample's bottom left corner due to the uncorrected shadow and slight sample's curvature.

### 6.6.2 Homogeneous skin model, Phototype 5

The second homogeneous model is the skin sample of Phototype 5 (Figure 6.2c) which has been considered to cover a higher absorption range of skin. Treated images at all  $\lambda$ s, together with the Non-Contact DRSSr scan (with a constant step of 5 or 0.5 mm) obtaining  $\widehat{\mu}'_s = \mu'_{s,known}$ , are shown in Figure 6.22. Because of the local overestimation seen at a specific hot spot (in the center right of the scan), the maximum relative error of  $\mu'_{s,known}$  is as high as 14.3% at 500 nm.

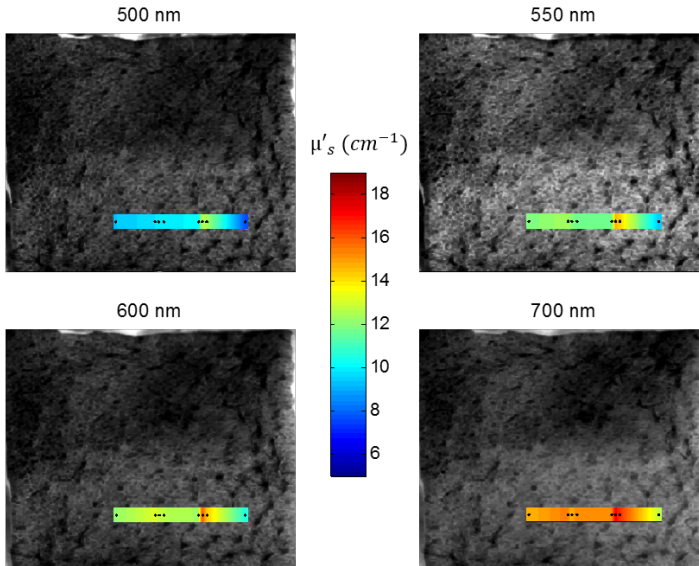


Figure 6.22: Treated images of the homogeneous skin of Phototype 5. Superimposed  $\mu'_{s,known}$  estimations obtained with interpolated Non-Contact DRSSr scan measurements (illustrated with black dots).

Optical properties estimations of Non-Contact DRSSr are compared to Contact DRSSr in Figure 6.23. Error bars of Contact and Non-Contact DRSSr measurements correspond to the standard deviation calculated with nine measurements (three measurements of three considered zones along the scanned line).

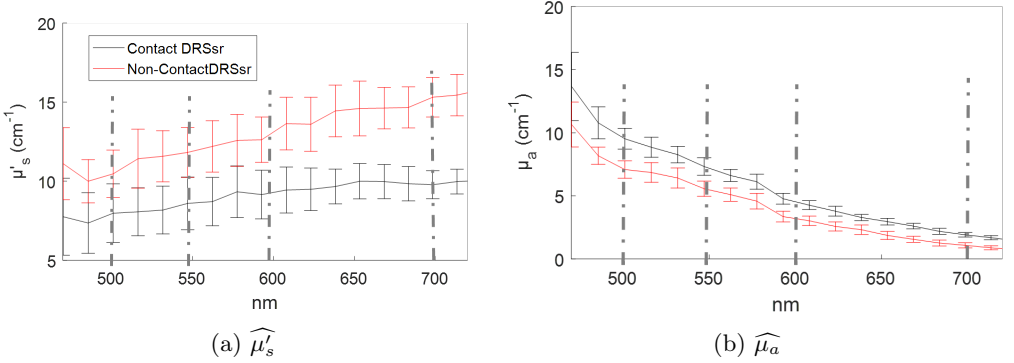


Figure 6.23: Average Contact and Non-Contact DRSSr optical properties estimations of homogeneous model, Phototype 5.

From Figure 6.23b, it can be said that absorption estimations obtained with Non-Contact and Contact DRSSr  $\widehat{\mu}_a$  estimations follow the same behaviour. Notice that as expected, the higher concentration of melanin in this sample of Phototype 5 corresponds to a higher absorption estimation when compared to the previous skin samples of Phototype 2 (Figures 6.8b and 6.17b).

For what concerns  $\mu'_s$ , remark the different signature of this high absorbing sample (Figure 6.23a) with respect to skin of Phototype 2 (Figures 6.8a and 6.17a). Explanations for this effect are not very clear but a hypothesis we have is linked to the limitation of  $R^{LUT}$  at low scattering values, as described in Section 3.2.6. Moreover, overestimation of  $\mu'_s$  with Non-Contact DRSSr is seen, possibly due to the low SNR resulting from the high absorbing sample. A detailed analysis of these aspects, including the confirmation of the  $\mu'_s$  signature and the appropriate calibration of Non-Contact DRSSr measurements, should be investigated for the perspective technique. However, even though  $\widehat{\mu}'_s$  estimations are not optimal with DRSSr, we have used them for the validation of principle of  $\mu_a$  quantification of the *Dual-Step* technique only, and we do not expect to obtain absolute quantification for this case.

### Scanned line $\mu_a$ estimation

The Non-Contact DRSSr  $\widehat{\mu}'_s$  estimated scan is used for a first estimation of  $\widehat{\mu}_a$  with MSI. The latter is used to derive the correction ratios of SR and 700 nm effect shown in Figure 6.24. Notice, that the amplitude of SR at the sample's surface is very low since the average correction ratio is very close to 1 (Figure 6.24a).

Estimations of MSI  $\widehat{\mu}_a$  corrected with the 550 nm ratio are shown in green in Figure 6.25. The 700 nm effect is considered with the average factor of Figure 6.24b and adjusted MSI estimations are shown in violet in Figure 6.25.

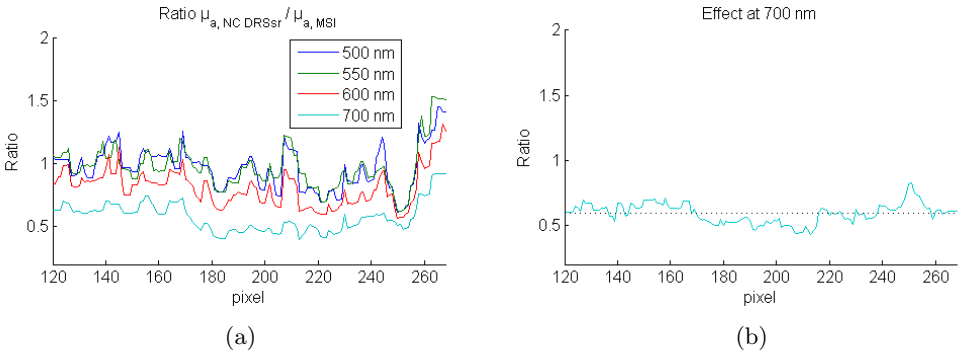


Figure 6.24: (a) Ratio of Non-Contact DRSSr / MSI  $\widehat{\mu}_a$  estimations of homogeneous model of Phototype 5, used to correct from SR effects. (b) Division of 700 nm / 550 nm ratios to derive the average correction factor of the 700 nm effect.

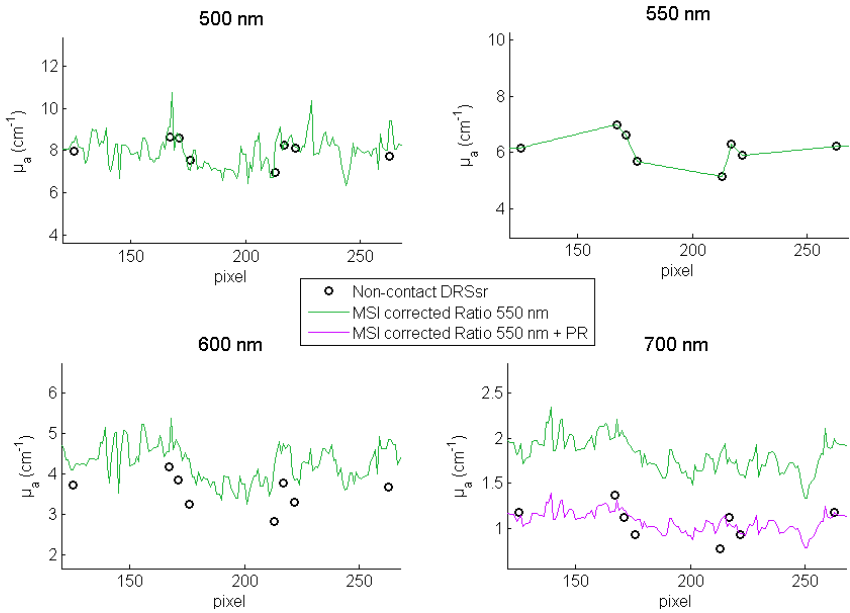


Figure 6.25: Absorption quantification of scanned line in homogeneous model of Phototype 5 with Non-Contact DRSSr and MSI corrected with the pre-calculated ratios shown in Figure 6.24). Green estimations are corrected from SR with the Ratio of 550 nm (Figure 6.24a. Violet estimations at 700 nm are adjusted with the factor of Figure 6.24b.

Overall, the spatial correspondence between MSI corrected and Non-Contact DRSSr  $\widehat{\mu}_a$  estimations is confirmed for  $\lambda = 500, 600, \text{ and } 700 \text{ nm}$ . Therefore, spatially averaged and corrected  $\widehat{\mu}_a$  estimations of MSI at each  $\lambda$  are compared with estimations of Contact and Non-Contact DRSSr techniques (see Figure 6.26).

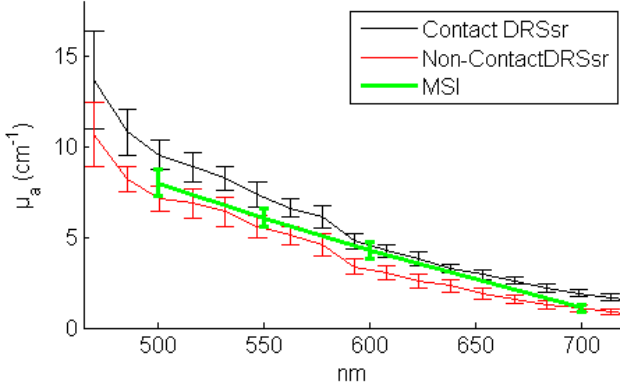


Figure 6.26: Average Absorption quantification of homogeneous model of Phototype 5 with Contact DRSsr, Non-Contact DRSsr, and corrected MSI.

These results are encouraging for the  $\widehat{\mu}_a$  quantification of MSI in highly absorbing samples, with the given correction method.

### ***Wide-field $\mu_a$ estimation***

As seen from Figure 6.22, the  $\mu'_{s,known}$  is generally homogeneous at all  $\lambda$  if the hot spot is overlooked. Therefore, the average  $\widehat{\mu}'_s$  estimation is set as the  $\mu'_{s,known}$  for the whole sample. Nevertheless, we are aware that some  $\mu'_s$  differences might exist between the skin and the darker spots. To validate this, a higher spatial resolution on the  $\mu'_s$  estimations would be needed. Indeed, the current inspected area with Non-Contact DRSsr for  $\mu'_s$  estimation (performed with *F5-F3*) has a diameter of 2.88 mm (*F3*, see Figure 3.4), which is larger than the dark spots in the order of 1 mm. Therefore, a more resolved and optimized segmentation of  $\widehat{\mu}'_s$  for the different zones of the samples should be a focus of perspective work to ensure minimal absolute quantification error (refer to Section 7.2.3).

For the moment, preliminary results of wide-field MSI  $\widehat{\mu}_a$  are derived from a homogeneous averaged  $\mu'_{s,known}$  value and are shown in Figure 6.27.

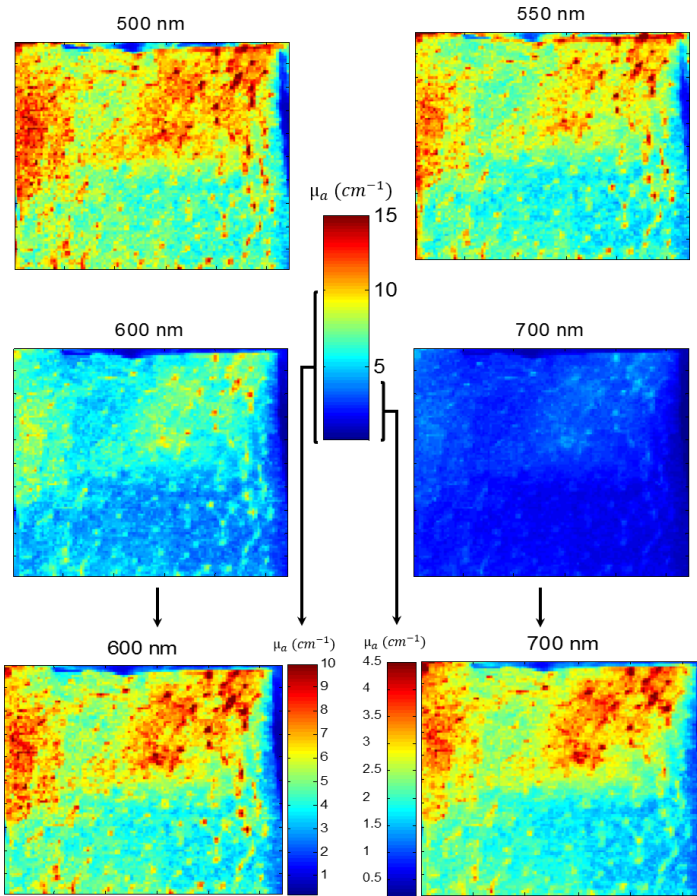


Figure 6.27: Wide-field absorption quantification of the homogeneous model of Phototype 5, considering a unique average of Non-Contact DRSSr estimated  $\mu'_{s,known}$  (see Figure 6.23a).

Overall, estimated  $\widehat{\mu}_a$  is considered homogeneous in the flat bottom zone that is scanned and set at the focal plane. Apart from the skin depressions affected by shadow at the top corners of the imaged sample that show an overestimated  $\mu_a$ , the quantitative  $\widehat{\mu}_a$  maps are within a correct range of values at all  $\lambda$ s. Thereby, the wide field absorption quantification ability of the *Dual-Step* technique is confirmed for such high absorbing samples.

## 6.7 Validation of *Dual-Step* technique using *in-vivo* rat skin models

### 6.7.1 Bi-coloured model

A black mark on the abdomen of a living anesthetized rat is used as the bi-coloured model (see Figure 6.3a). Treated images of the abdomen (see Figure 6.28) show a shadowed left-hand side of the image at all  $\lambda$ s due to the sample's curvature and the illumination originating from the right-hand side of the image. Superimposed Non-Contact DRSSr scan (with steps of 2.85, 1, and 1.85 mm)  $\mu'_{s,known}$  estimations span the black mark and white skin and show a clear difference between these. Keep in mind that the focal plane of the Non-contact DRSSr measurements is set for the central measurement, on the black mark as shown on the right of Figure 6.28. Moreover, even though we made an effort to improve the flatness of the imaged zone, some shadow is still present at the left-hand side of the image.

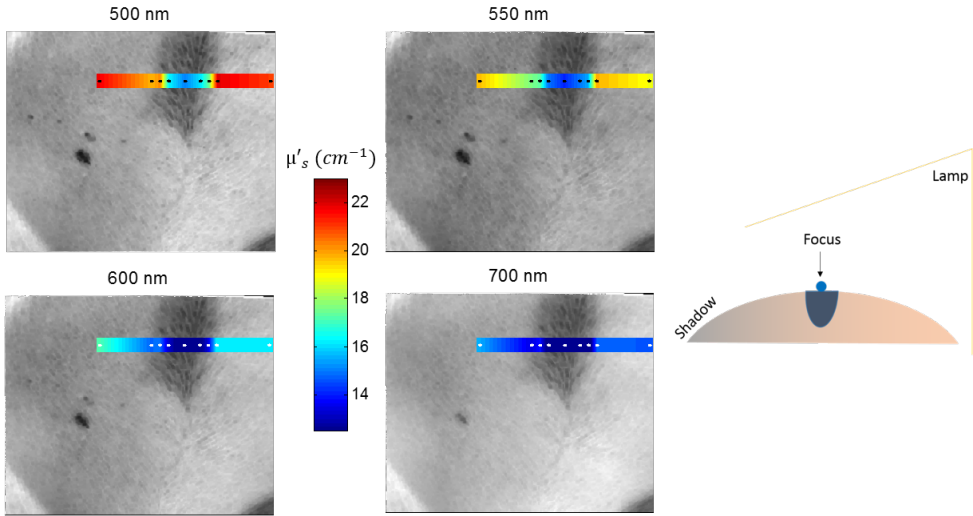


Figure 6.28: Treated images of the bi-coloured rat model. Superimposed  $\mu'_{s,known}$  estimations obtained with interpolated Non-Contact DRSSr scan measurements (illustrated with black/white dots). To the right, a sketch of the curved profile is given, showing the shadow effect and the focused central point of the NC scan.

The single Non-contact DRSSr optical properties estimations of the black mark (three central points of the scan) and the white skin (extreme points of the scan) are confirmed with the average Contact DRSSr estimation of three measurements taken on the black and white zones, with their corresponding standard deviation (see Figure 6.29).

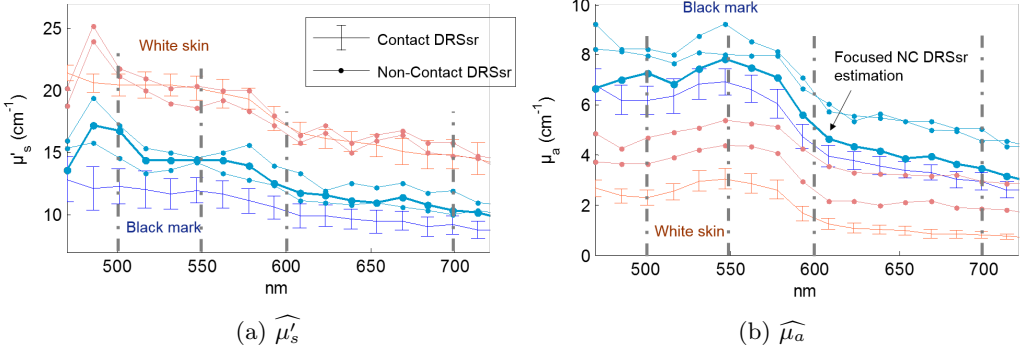


Figure 6.29: Optical properties estimations of the black mark (blue) and surrounding white skin (pink) with the average of three Contact DRSr measurements (per zone) and individual Non-Contact DRSr measurements taken on the three central points of the scan (for the black mark) and two extreme points of the scan (for white skin). The thicker line in both graphs corresponds to the estimations at the central focused point of the scan (see right sketch of Figure 6.28).

In terms of  $\hat{\mu}'_s$  (see Figure 6.29a), Non-contact DRSr estimation values and contrast between the black mark and white skin are well validated by Contact DRSr estimations.

The comparison of  $\hat{\mu}_a$  estimated with Contact and Non-Contact DRSr (see Figure 6.29b), reveals an overestimation of Non-Contact DRSr  $\mu_a$  at all  $\lambda$ . This is explained with the fact that the focal plane is set for a unique point at the center of the black mark (see Figure 6.28), obtaining the closest  $\mu_a$  estimation to Contact DRSr (see bold blue estimation of Figure 6.29b, pointed out by the black arrow). Because of the sample's curvature, the other measured points are not at the object plane. As previously seen in Section 3.5.2 and more concisely in Figure 3.50,  $\hat{\mu}_a$  estimations with Non-Contact DRSr are very sensitive to the sample's height. Thereby, a depression of the sample, quickly provokes an overestimation of  $\hat{\mu}_a$ . The overestimation error seen in Figure 6.29b clearly corresponds to the curvature range of the rat's abdomen scan ( $> 1$  mm).

Otherwise, both Contact and Non-Contact DRSr show an increase of  $\mu_a$  at all  $\lambda$  of the black mark, according to the increase of melanin concentration (refer to its signature shown in Figure 2.10).

### Scanned line $\mu_a$ estimation

A first estimation of  $\widehat{\mu}_a$  with MSI based on the scanned Non-Contact DRSSr  $\mu'_{s,known}$ , derives the correction ratio shown in Figure 6.30.

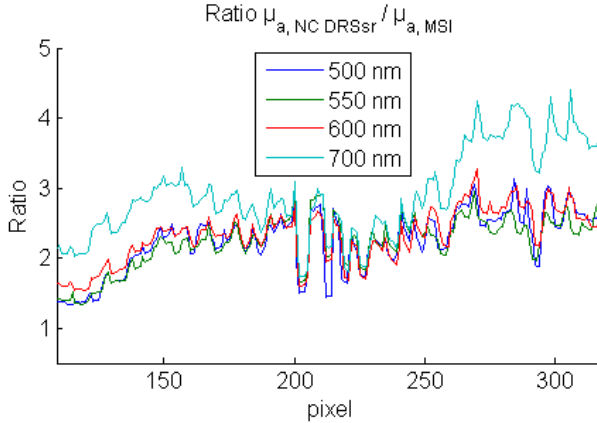


Figure 6.30: Ratio of Non-Contact DRSSr / MSI  $\widehat{\mu}_a$  estimations used to correct SR effects.

Notice that the SR effect included in the correction ratio is higher than on the previous human skin samples (see Figures 6.11a, 6.18a, and 6.24a). Also, a difference is clear in the middle of the profile, corresponding to the black mark position. Moreover, the shadow effect at the left-hand side (see Figure 6.28) is also detected with the decrease of the correction ratio.

MSI  $\widehat{\mu}_a$  estimations corrected with the 550 nm ratio (Figure 6.30) are shown together with Non-Contact DRSSr  $\widehat{\mu}_a$  estimations in Figure 6.31. Notice that the same spatial distribution is effectively followed at all  $\lambda$ s, confirming the width of the central black mark  $\approx 8.5$  mm (80 pixels, recall that G is 0.095 and pixel size is 9.9  $\mu$ m).

Corrected MSI  $\widehat{\mu}_a$  estimations are spatially averaged for the black mark ( $190 < \text{pixel} < 230$ ) and the non-shadowed scanned white skin ( $280 < \text{pixel} < 320$ ). These values are validated with Contact and Non-Contact DRSSr estimations in Figure 6.32.

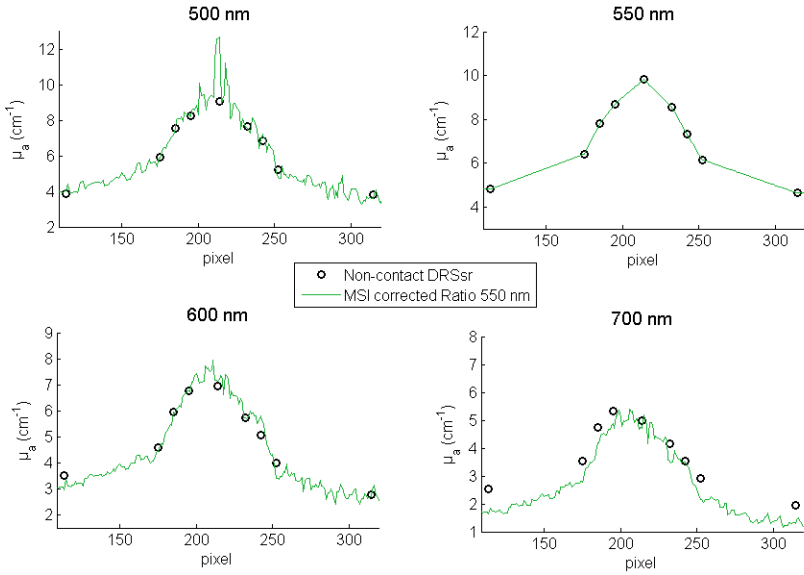


Figure 6.31: Absorption quantification of scanned line in bi-coloured *in-vivo* rat skin model with Non-Contact DRSSr and MSI corrected with the 550 nm ratio (shown in Figure 6.30) from SR and shadow effects.

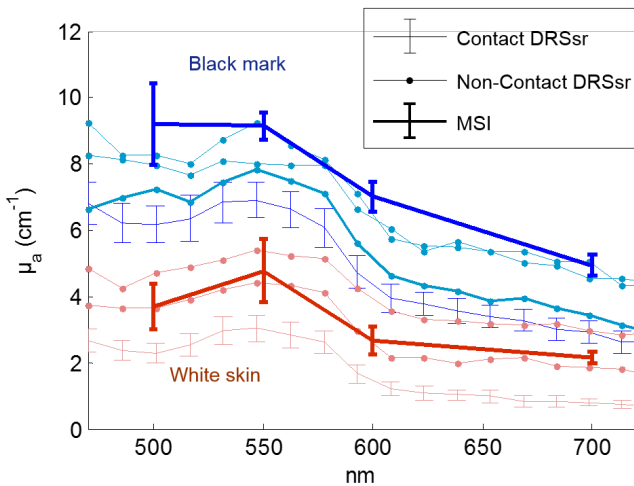


Figure 6.32: Average Contact DRSSr and MSI with individual Non-Contact DRSSr  $\widehat{\mu}_a$  estimations. The black mark is represented in blue, whilst the surrounding white skin is represented in pink-red.

### Wide-field $\mu_a$ estimation

The estimations of  $\mu'_s$  with Contact and Non-Contact scan DRSSr (see Figure 6.29a) clearly show the contrast ( $> 25\%$ ) between the black mark and the surrounding white skin at all considered  $\lambda$ s. Therefore, for wide-field  $\widehat{\mu}_a$  quantification, the appropriate averaged Non-contact DRSSr  $\widehat{\mu}'_s$  value is set for the different zones. These zones are determined through the segmentation of a reflectance image at  $\lambda=700\text{ nm}$ , because it is the least sensitive to the absorption signature of chromophores (see Figure 2.10) and thereby the most sensitive to changes in scattering properties. The segmentation method is based on the *Otsu* multi-threshold algorithm and has been adapted to the image to obtain a clear separation of the black and white skin zones. Figure 6.33 shows the segmented image for which the shadow effect is overlooked.

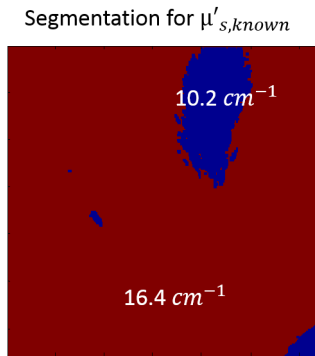


Figure 6.33: Reflectance Segmentation of the image taken at  $700\text{ nm}$  for which the shadow at the left-hand side of the image is ignored. As an example, values shown correspond to the  $\mu'_{s,known}$  at  $700\text{ nm}$ .

This segmented image is used to create the  $\mu'_{s,known}$  map according to the average Non-Contact DRSSr estimations in the black mark and the surrounding white homogeneous skin (see Figure 6.29a). An example of  $\mu'_{s,known}$  at  $700\text{ nm}$  is shown in Figure 6.33. According to the  $\mu'_{s,known}$  map at all  $\lambda$ , the estimation of  $\widehat{\mu}_a$  is performed for all pixels of the image. The resulting wide-field  $\widehat{\mu}_a$  quantification is shown in Figure 6.34.

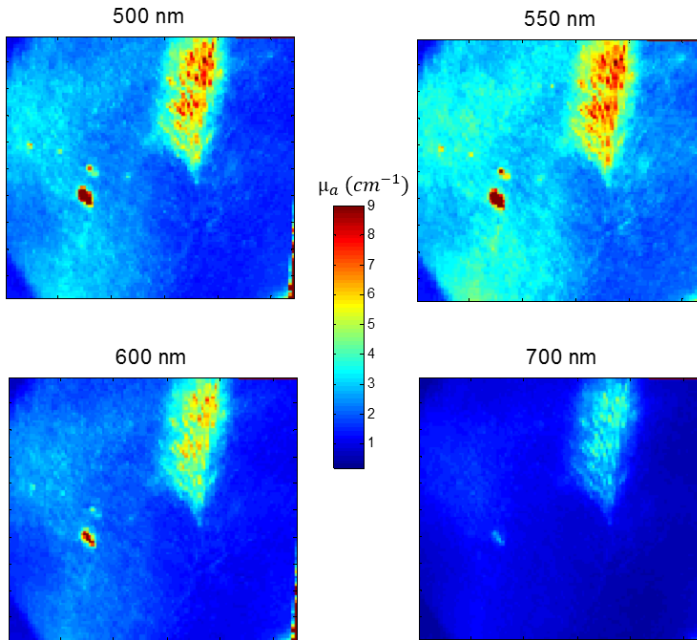


Figure 6.34: Wide-field absorption quantification, considering the  $\mu'_{s,known}$  map shown in Figure 6.33.

Even though, the shadow artefacts provoke  $\widehat{\mu}_a$  overestimation at the left-hand side of the image, these quantified  $\widehat{\mu}_a$  maps show a clear spatial correspondence and a similar range of absolute  $\widehat{\mu}_a$  values to that shown in Figure 6.32 for all  $\lambda$  for the different non-shadowed zones of the sample.

### 6.7.2 Inflammation model Type 1

The second rat (see Figure 6.3b) is used for the inflammation model of Type 1, previously explained in Section 6.2.2. Figure 6.35 shows the irritating LPS drop that was topically applied on the center of the rat's abdomen.



Figure 6.35: LPS 20  $\mu\text{l}$  drop placed on the shaved abdomen of the rat used for the inflammation model of Type 1.

Treated MSI images at the different illuminating  $\lambda\text{s}$  are shown in Figure 6.36. Notice the present shadow at the left part of the image. The performed Non-Contact DRSSr scan (with steps of 4 and 2 mm), superimposed on the images, spans the position of the drop, shown with cyan dotted margins. The Non-Contact DRSSr estimated  $\widehat{\mu}'_s$  show a slight difference (maximum relative error of 8.4%) between the left and center-right side of the drop, suggesting an inflammation effect at the drop position which has diffused to the right. However, this effect remains a hypothesis since it has not been confirmed with histological measurements.

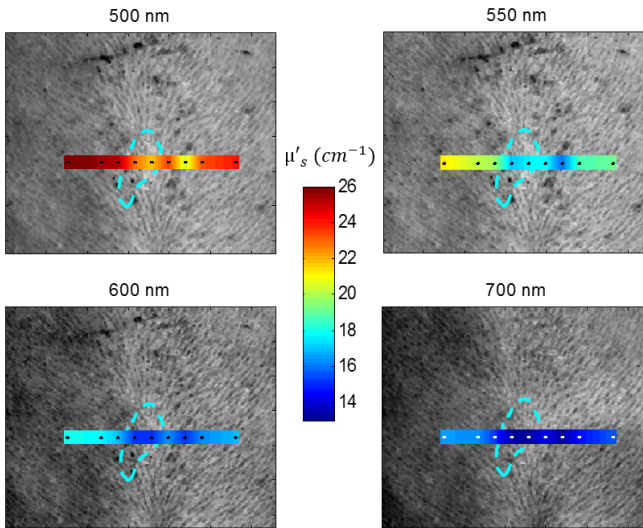


Figure 6.36: Treated images of the *in-vivo* inflammation rat model Type 1. Superimposed  $\mu'_{s,known}$  estimations obtained with interpolated Non-Contact DRSSr scan measurements (illustrated with black/white dots).

The non-existing visual difference between inflamed and non-inflamed skin make the acquisition of measurements difficult on the two zones with Contact-DRSsr. Therefore, the Contact DRSsr estimations shown in Figure 6.29 give the average range and standard deviation of optical properties (corresponding to three measurements per zone) but are not indicative of the difference between inflamed and non-inflamed skin. The case of Non-Contact DRSsr is different since the measurement positions have been strictly controlled with the translation stage. This allows the separation of measurements taken inside (two central scan points) or outside (extreme scan points) the zone where the drop was applied. Thereby, according to the Non-Contact DRSsr scan, some slight diminution in both optical properties is seen between inflamed and non-inflamed skin. Compared to Contact DRSsr, Non-Contact DRSsr  $\widehat{\mu}'_s$  estimations are validated, whilst a general overestimation of  $\mu_a$  is noticed due to the sample's curvature.

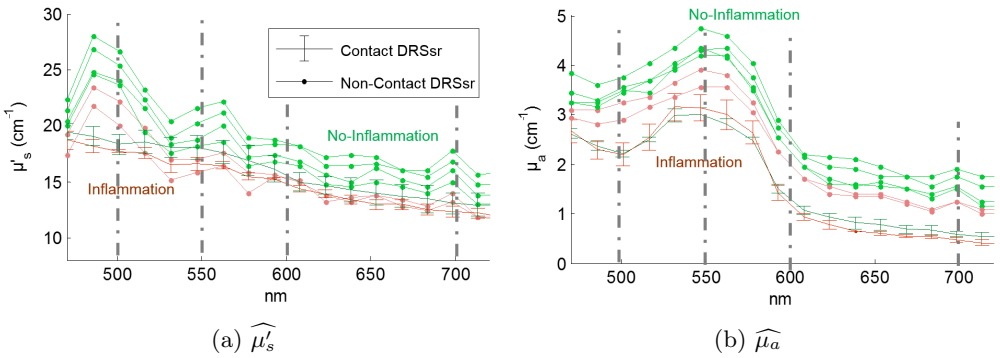


Figure 6.37: Optical properties estimations of inflammation model Type 1 with the average of three measurements taken with Contact DRSsr and individual Non-Contact DRSsr measurements on the zones. The inflamed zone is represented in pink-brown whilst non-inflamed zone is represented in green.

It is interesting to notice that the optical properties values of the non-inflamed skin (in green of Figure 6.37) are of the same order than the non-inflamed white skin of the previous bi-coloured model (pink estimations shown in Figure 6.29). This confirms the coherence of both optical properties estimations on the skin of two different rats.

### Scanned line $\mu_a$ estimation

The validated Non-Contact DRSsr  $\widehat{\mu}'_s$  scanned estimations (shown in Figure 6.36) are used as  $\mu'_{s,known}$  to derive a first  $\widehat{\mu}_a$  estimation with MSI of the corresponding scanned line in the image. The latter determines the  $\mu_a$  correction ratios shown in Figure 6.38.

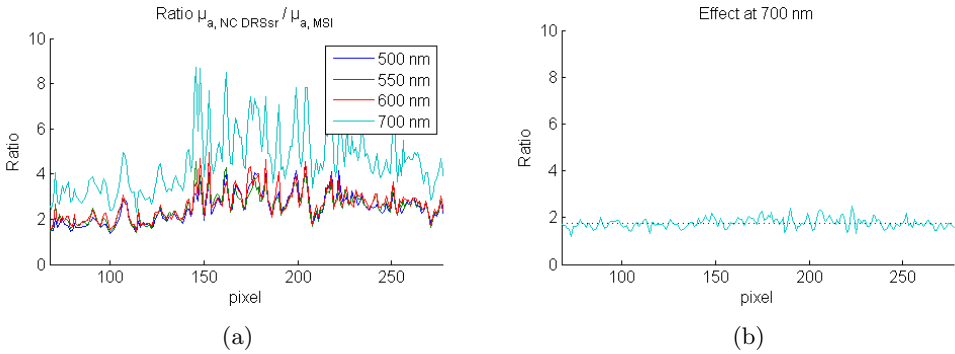


Figure 6.38: (a) Ratio of Non-Contact DRSSr / MSI  $\widehat{\mu}_a$  estimations of inflammation model Type 1, used to correct from SR and shadow effects. (b) Division of 700 nm / 550 nm ratios to derive the average correction factor of the 700 nm effect.

Corrected MSI with the ratios of Figure 6.38 and Non-Contact  $\widehat{\mu}_a$  estimations of the scanned line are shown in Figure 6.39.

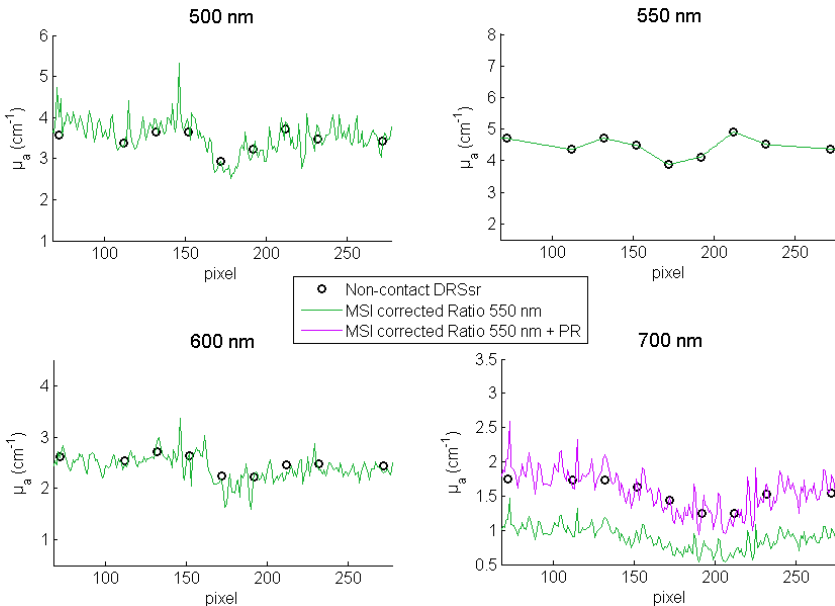


Figure 6.39: Absorption quantification of scanned line in inflammation Type 1 model with Non-Contact DRSSr and MSI corrected with the pre-calculated ratios shown in Figure 6.38). Green estimations are corrected from SR with the Ratio of 550 nm (Figure 6.38a). Violet estimations at 700 nm are adjusted with the factor of Figure 6.38b.

Notice how well the MSI adjusted estimations correlate to Non-Contact DRSSr estimations at  $\lambda=500, 600,$  and  $700$  nm. All estimations show a slight reduction of  $\mu_a$  at the center of the profile ( $150 < \text{pixel} < 200$ ), corresponding to the area where the LPS drop has been applied.

Spatially averaged MSI  $\widehat{\mu}_a$  in the identified central inflamed zone ( $160 < \text{pixel} < 200$ ) and the non-shadowed right-hand side zone ( $220 < \text{pixel} < 260$ ) is compared to the  $\widehat{\mu}_a$  estimated with Non-Contact DRSsr in Figure 6.40. With these results, the slight reduction of  $\widehat{\mu}_a$  due to inflammation is clear.

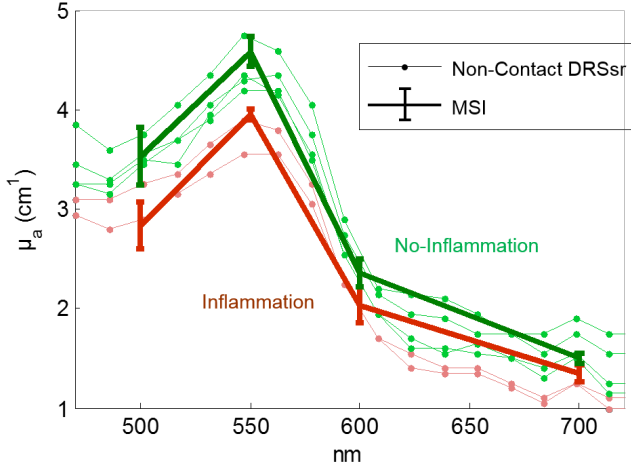


Figure 6.40: Averaged MSI with individual Non-Contact DRSsr  $\widehat{\mu}_a$  estimations for inflamed (pink-brown) and non-inflamed (green) skin.

### Wide-field $\mu_a$ estimation

According to the difference (relative variation of 8.4%) of  $\widehat{\mu}'_s$  estimations with Non-Contact DRSSr (see Figure 6.37a) between inflamed and non-inflamed skin, two cases are considered. The first case overlooks the  $\mu'_s$  measured contrast between inflamed and non-inflamed zones and sets a unique average  $\widehat{\mu}'_s$  estimation as the  $\mu'_{s,known}$  for the whole sample area. Although more straightforward, this supposition limits the absolute wide-field quantification of  $\mu_a$ , since it will be affected by a cross-talk with the  $\mu'_{s,known}$  inaccuracy. The second case, considers the slight  $\mu'_s$  measured contrast by using two averaged  $\widehat{\mu}'_s = \mu'_{s,known}$  estimations for inflamed and non-inflamed skin.

The first supposition, in which the same average  $\mu'_{s,known}$  is set for the whole sample, calculates the quantitative  $\widehat{\mu}_a$  wide-field maps shown in Figure 6.41. The shadow effect in the left-hand side of the image is hidden to improve visualization. The results show a slight reduction of  $\widehat{\mu}_a$  in the central area at all  $\lambda$ , corresponding to the inflammation zone provoked by the LPS drop. Notice that at 700 nm, this reduced  $\widehat{\mu}_a$  extends towards the right-hand side of the image.

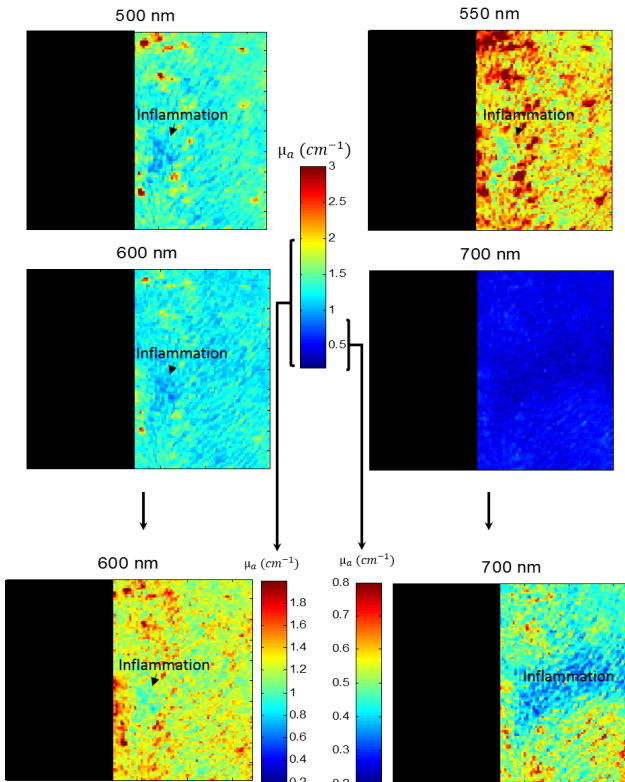


Figure 6.41: Wide-field absorption quantification, considering a unique average of Non-Contact DRSSr estimated  $\mu'_{s,known}$  (see Figure 6.37a) at each wavelength. The same scale is considered for the top four images at all  $\lambda$ s and an additional zoom of the scale is done for images at 600 and 700 nm.

Remark the clear  $\widehat{\mu}_a$  contrast of the inflamed zone with respect to the non-inflamed zone. With these preliminary results we show the great interest of the *Dual-Step* technique, being able to quantitatively discriminate non-visual effects of inflammation. Yet, as mentioned before, the estimated  $\widehat{\mu}_a$  values are affected by the cross-talk originated from the inaccurate supposition of  $\mu'_{s,known}$ . Thereby, the contrast seen in Figure 6.41 is not only due to the natural contrast of  $\widehat{\mu}_a$  but also that of  $\widehat{\mu}'_s$ .

This is why, to approach absolute  $\mu_a$  values, independent from  $\mu'_s$ , we explored the second case, which considers the different  $\mu'_{s,known}$  in inflamed and non-inflamed skin. For wide-field  $\widehat{\mu}_a$  quantification with both  $\mu'_{s,known}$ , a spatial segmentation of both zones is necessary and is performed based on the reflectance image taken at 700 nm because it shows the highest intensity contrast (see Figure 6.42) between the supposed inflamed and non-inflamed zones. Keep in mind that this supposition of spatial inflammation has not been validated with other techniques and that the segmentation method should be improved. Yet, we make use of it because the objective of this study is merely to explore the  $\widehat{\mu}_a$  quantification capability of the *Dual-Step* technique.

Segmentation for  $\mu'_{s,known}$

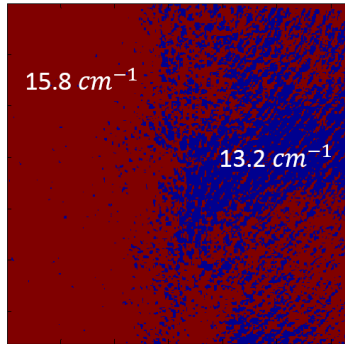


Figure 6.42: Reflectance segmentation of the image taken at 700 nm and neglecting the shadow at the left-hand side of the image. As an example, scattering  $\mu'_{s,known}$  values are given for 700 nm.

The segmented image is used to create the  $\mu'_{s,known}$  map according to the average of Non-Contact DRSSr estimations of the inflamed and non-inflamed zones (see Figure 6.37a) at each  $\lambda_s$ . An example of  $\mu'_{s,known}$  values on the segmented map at 700 nm are shown in Figure 6.42.

The wide-field estimation of  $\widehat{\mu}_a$  with MSI, based on this  $\mu'_{s,known}$  map, is shown in Figure 6.43. In general, it is observed that estimated  $\widehat{\mu}_a$  values are decreased with respect to the first case (Figure 6.41), confirming the cross-talk effect of  $\mu'_{s,known}$  on the estimation of  $\widehat{\mu}_a$ . Therefore, by considering a more accurate  $\mu'_{s,known}$ , we consider these  $\widehat{\mu}_a$  to be more absolute than the previous  $\widehat{\mu}_a$ , calculated with an average  $\mu'_{s,known}$ . Also, notice that, because the  $\mu'_{s,known}$  crosstalk effect on  $\mu_a$  is reduced, the contrast between inflamed and non-inflamed zones is also reduced. Certainly, the contrast of absolute optical properties of this inflammation model, would increase with a longer time could be granted for LPS to act.

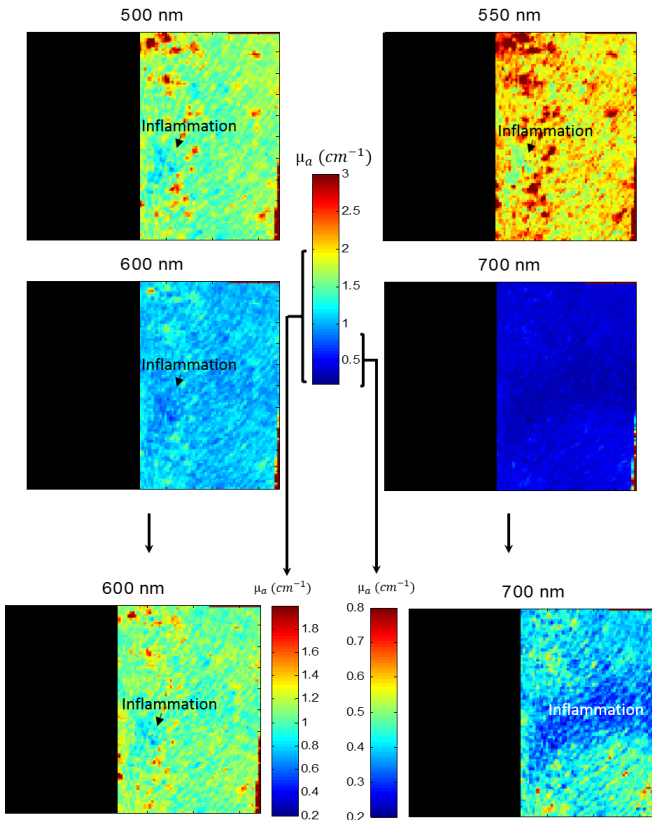


Figure 6.43: Wide-field absorption quantification, considering the  $\mu'_{s,known}$  map shown in Figure 6.42. The same scale is considered for the top four images at all  $\lambda$ s and an additional zoom of the scale is done for images at 600 and 700  $\text{nm}$ .

In summary, it can be said that the *Dual-Step* technique allows to see the slight  $\widehat{\mu}_a$  reduction at the inflammation site which is not perceptible to the naked eye. This shows the interesting potential of the *Dual-Step* technique for the clinical diagnosis of non-perceptible inflammation symptoms.

### 6.7.3 Inflammation model Type 2

The third rat (see Figure 6.3c), is adopted for an inflammation model of Type 2. As previously described in Section 6.2.2, this inflammation is provoked with additional shaving of the rat's back skin. Treated images at the different  $\lambda$ s are shown in Figure 6.44. Notice the different contrasts of the inflammation marks at the middle-top of the images taken with  $\lambda = 500 - 550 - 600 \text{ nm}$  and the black marks at the bottom right and middle left of images taken with  $\lambda = 600 - 700 \text{ nm}$ .

For what concerns the Non-Contact DRSSr scan (with steps of 2, 1.5, and 0.5 mm), spanning an inflammation mark, the determined  $\mu'_{s,known}$  estimations are considered homogeneous throughout the whole sample at all  $\lambda$ s with a maximum relative error of 4.1% at 550 nm.

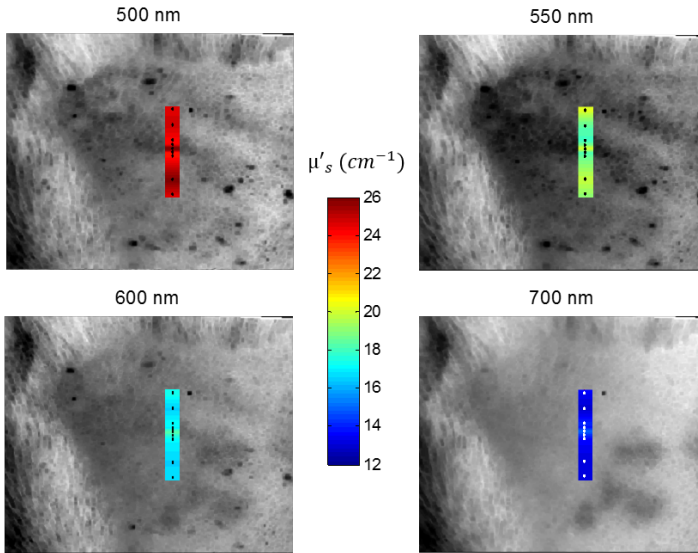


Figure 6.44: Treated images of the *in-vivo* inflammation rat model Type 2. Superimposed are the  $\mu'_{s,known}$  estimations obtained with interpolated Non-Contact DRSSr scan measurements (illustrated with black/white dots).

The homogeneous scattering individual estimations of Non-Contact DRSSr of each zone are clearly validated with Contact DRSSr average and standard deviation of three measurements per zone (see Figure 6.45a). In the case of absorption (see Figure 6.45b), Non-Contact DRSSr  $\mu_a$  overestimation is observed as in the previous rat models, due to the sample's curvature and shadow effect. However, the same behaviour is noticed for both Contact and Non-Contact DRSSr estimations. Notice that all  $\widehat{\mu_a}$  values at  $\lambda < 600 \text{ nm}$  are higher for inflamed skin, according to the increase of haemoglobin.

It is particularly interesting to remark that the homogeneous  $\widehat{\mu'_s}$  and the  $\widehat{\mu_a}$  difference in this inflammation model are in opposition to the inflammation model of Type 1, in which the inflamed zone features lower scattering and absorption than the non-inflamed zone (see Figure 6.40).

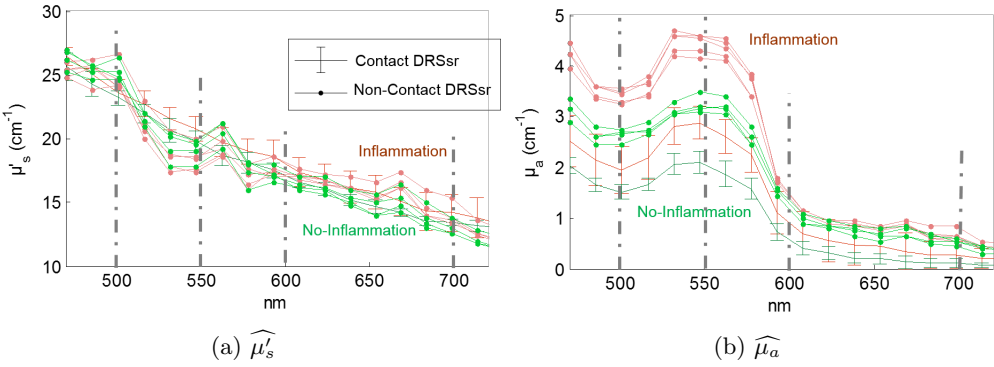


Figure 6.45: Optical properties estimations of inflammation model Type 2 with average of three measurements with Contact DRSr and individual measurements with Non-Contact DRSr on the zones. The five central points of the Non-Contact DRSr scan are considered to be inside the inflamed zone (pink) and the four extreme points of the scan are considered for the non-inflamed zone (green).

**Scanned line  $\mu_a$  estimation of inflammation**

Validated Non-Contact DRSr  $\widehat{\mu}'_s$  estimations are used to quantify  $\widehat{\mu}_a$  with MSI through the same scanned line. The latter derives the  $\mu_a$  correction ratios shown in Figure 6.46.

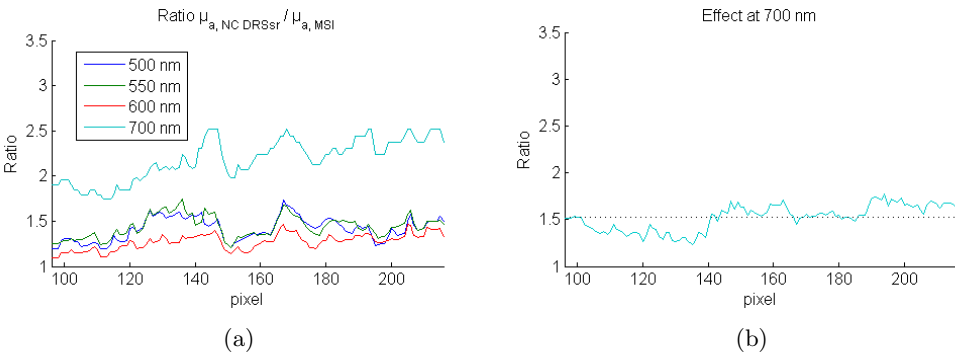


Figure 6.46: (a) Ratio of Non-Contact DRSr / MSI  $\widehat{\mu}_a$  estimations of inflammation model Type 2, used to correct SR and shadow effects. (b) Division of 700 nm / 550 nm ratios to derive the average correction factor of the 700 nm effect.

The corrected MSI  $\widehat{\mu}_a$  is shown together with Non-Contact DRSr  $\widehat{\mu}_a$  estimations in Figure 6.47. Remark the spatial correspondence of estimations with both techniques at  $\lambda=500$  and  $600$  nm. The slight overestimation of  $\mu_a$  at  $600$  nm is related to the lower ratio (see Figure 6.46a) that does not completely compensate the SR intensity. Expected increased  $\widehat{\mu}_a$  values are seen for the thin inflammation mark (of width  $\approx 4$  mm) at  $\lambda=500-550$  nm, less at  $\lambda=600$  nm and not at all at  $700$  nm.

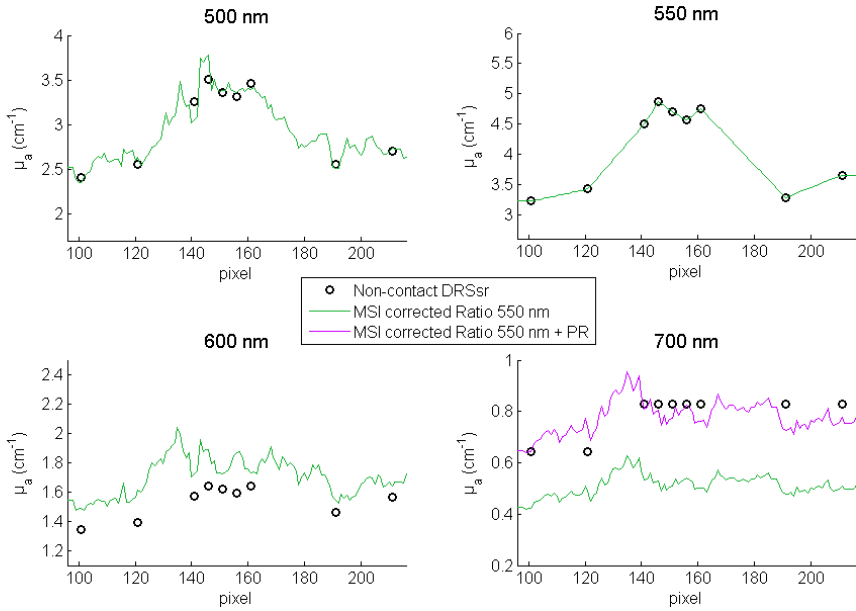


Figure 6.47: Absorption quantification of scanned line in inflammation Type 2 model with Non-Contact DRSSr and MSI corrected with the pre-calculated ratios shown in Figure 6.46). Green estimations are corrected from SR and shadow effects with the Ratio of 550 nm (Figure 6.46a. Violet estimations are adjusted with the factor of Figure 6.46b.

MSI  $\widehat{\mu}_a$  estimations are spatially averaged at the central zone ( $140 < \text{pixel} < 160$ ) to define the  $\widehat{\mu}_a$  proper to the thin inflamed mark and at the non-shadowed zone ( $180 < \text{pixel} < 220$ ) to define that proper to the non-inflamed skin. These results are compared to Non-Contact DRSSr  $\widehat{\mu}_a$  estimations in Figure 6.48.

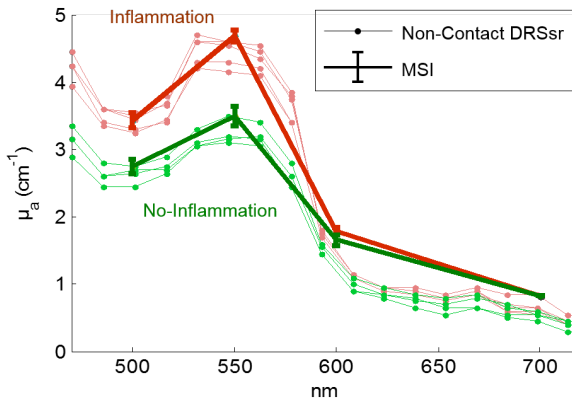


Figure 6.48: Spatially averaged MSI with individual Non-Contact DRSSr  $\widehat{\mu}_a$  estimations for inflamed (pink-brown) and non-inflamed (green) skin.

### Black mark $\mu_a$ estimation

Additionally, a single Non-Contact DRSsr measurement has been performed on a black mark of the rat's back (see bottom right corner of the 700 nm image of Figure 6.44). Comparing optical properties estimations, it is seen that its scattering coefficient is identical to that of white skin (see Figure 6.49a). In what concerns absorption (see Figure 6.49b), the black mark shows a general higher  $\widehat{\mu}_a$  than non-inflamed white skin, at all  $\lambda$ , according to the increase of melanin (refer to the chromophore signature of Figure 2.10).

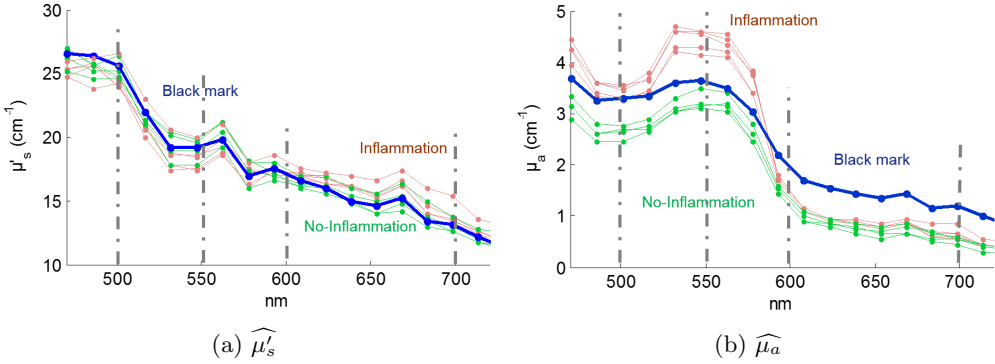


Figure 6.49: Non-Contact DRSsr optical properties estimations of the black mark (blue) compared to inflamed (red) and non-inflamed skin (green).

Since the higher contrast of inflammation lies at  $\lambda < 580$  nm, the higher contrast for the black mark lies at  $\lambda > 580$  nm. Indeed, the black marks are most distinguishable in the wide-field  $\widehat{\mu}_a$  quantification at  $\lambda=600$  and 700 nm shown in the next paragraph (see Figure 6.50).

Note that the scattering properties of this black mark are very different to those of the black mark in the bi-coloured model. This opens the door to an interesting discrimination potential of different chromophores. Further analysis on this could be performed with a depth approach in future work (refer to Section 7.2.3).

### Wide-field $\mu_a$ estimation

Since a negligible  $\widehat{\mu}'_s$  difference (maximum relative error of 4.1%) is obtained with Non-Contact DRSSr validated measurements at the different zones (see Figure 6.45a and 6.49a), the average  $\widehat{\mu}'_s$  value is used as  $\mu'_{s,known}$  for the whole imaged sample. The resulting wide-field  $\widehat{\mu}_a$  at all  $\lambda$ s is shown in Figure 6.50. Notice the different expected contrasts of the inflamed skin at  $\lambda = 500, 550,$  and  $600 \text{ nm}$  and the black marks at  $\lambda = 600$  and  $700 \text{ nm}$ . Areas with hair should be ignored.

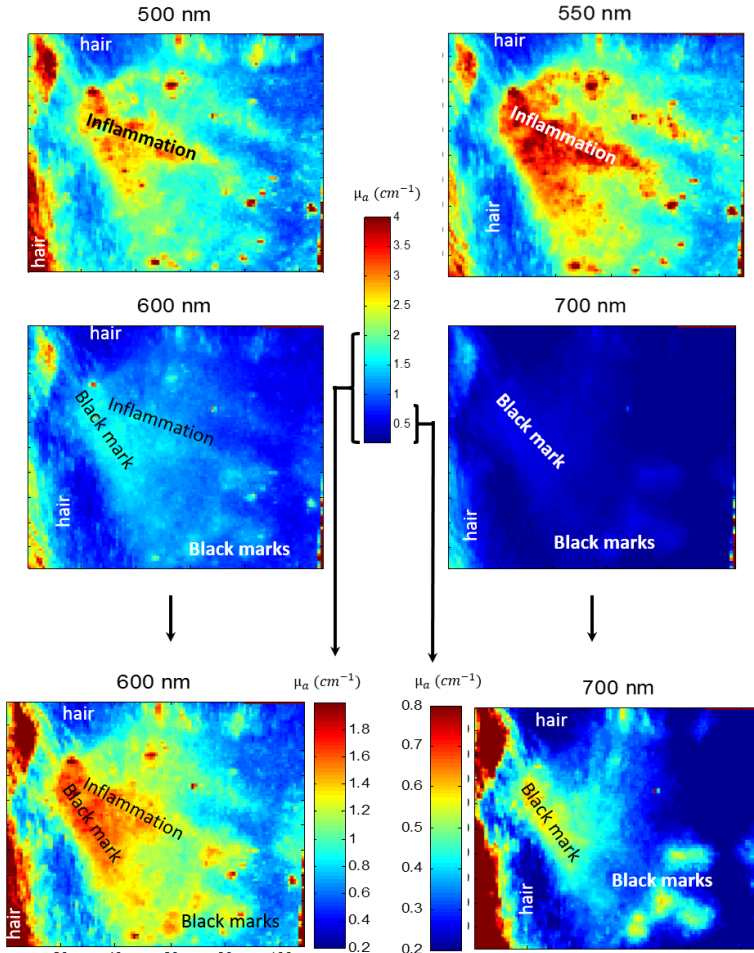


Figure 6.50: Wide-field absorption quantification, considering a unique Non-Contact DRSSr averaged  $\mu'_{s,known}$  (see Figure 6.45a). The same scale is considered for the top four images at all  $\lambda$ s and an additional zoom of the scale is done for images at 600 and 700  $\text{nm}$ .

The quantitative  $\widehat{\mu}_a$  maps show correct spatial correspondence of the considered field (with no hair) and at all  $\lambda$ s. Moreover, the range of absolute values in non-inflamed

skin is similar to that of the previous models (see Figures 6.34 and 6.43). Notice that quantitative absorption maps reveal a black mark (see 600 and 700 *nm* contrast ) with inflammation (see 500, 550, and 600 *nm* contrast).

## 6.8 Discussion and Conclusion

In this Chapter, we have applied the *Dual-Step* technique and shown its quantification potential on six different and pertinent skin models. Three of them were based on *ex-vivo* human abdominal skin samples with two different Phototypes (2 and 5) and either homogeneous or heterogeneous real surface patterns. The other three were based on *in-vivo* skin of three different rats, used for a bi-coloured model and for two different inflammation models.

The scattering parameters estimated with Non-Contact DRSsr scan on the different samples are thoroughly validated with the reference Contact DRSsr measurements. However, since Non-Contact DRSsr measurements are performed at a fixed plane, the larger the sample's curvature (eg. rat's abdomen or back), the higher the absorption quantification error of Non-Contact DRSsr is. Besides, at  $\lambda > 700 \text{ nm}$  Non-Contact DRSsr absorption estimations are probably affected by the low signal-to-noise ratio (SNR) due to the lower signal of the lamp the parasite reflections of the doublet pair at the given spectral range.

The *Dual-Step* technique makes use of the optimally estimated scattering properties by Non-Contact DRSsr scan, to quantify absorption with MSI on the corresponding scanned line. These MSI absorption estimations at the considered  $\lambda$  (500, 550, 600, and 700 nm) follow the same spatial patterns as Non-Contact DRSsr. Estimated MSI  $\mu_a$  is generally underestimated because of the specular reflection which depends on the sample's surface. A developed filter algorithm reduced this effect but was not enough to overcome it.

To compensate for the low SNR at 700 nm of Non-Contact DRSsr and the specular reflection of MSI measurements, correction ratios were calculated with the  $\widehat{\mu}_a$  estimations of both techniques. With this adjustment, obtained results showed good quantitative correspondence with Contact DRSsr and were used as part of the validation of principle study. Perspective work should focus on the improvement of optical properties estimations by changing the doublet pair of Non-Contact DRSsr to another one having an anti-reflection treatment also for  $\lambda > 700 \text{ nm}$ . To optimally correct measurements from specular reflections, further investigation on the feasibility of the correction ratio, calculated with a single  $\lambda$  (in this case 550 nm) and used for all other  $\lambda$  (in this case 500, 600, 700, nm), would be interesting to explore, due to the simplicity of the approach. Alternatively, a more complicated and expensive instrumental solution would consider the integration of a polariser in the setup to completely avoid specular reflection.

Apart from the quantification of the scanned line spanning the zones of interest, wide-field quantification of both optical properties has been investigated. According to the variation of Non-Contact DRSsr  $\widehat{\mu}'_s$  estimations in the different zones, either a unique average  $\mu'_{s,known}$  is considered for the whole sample, or individual  $\mu'_{s,known}$  values are set for the different zones. For the latter, an intensity-based segmentation of the reflectance image at 700 nm is proposed to build the  $\mu'_{s,known}$  map. The reflectance image at 700 nm is selected to move further away from haemoglobin absorption peaks and approach the differences of reflectance caused mostly due to  $\mu'_s$  changes. This spatial  $\mu'_{s,known}$  map has been used to subsequently quantify wide-field  $\widehat{\mu}_a$  for all imaged samples. Even though we made an effort to inspect the flattest zones of the samples, a shadowing effect was still present due to the natural curvature. Shadow at certain depressions of the sample is the major artefact affecting wide-field  $\widehat{\mu}_a$  quantification since it provoked a reduction

in the intensity which directly generated a  $\widehat{\mu}_a$  overestimation. This effect should be avoided with a better illumination in the perspective instrument (see Section 7.2.2).

The preliminary results that we obtained are very interesting. For instance, it was seen that estimated optical properties are coherent on the same skin type of different samples. Indeed, the scattering and absorption optical properties of caucasian human skin with no stretch marks are of the same range in the homogeneous and heterogeneous models. Likewise, non-inflamed skin of the three rats show similar scattering and absorption values.

We also showed that the two considered rat skin inflammation models (Type 1 and 2) featured different quantitative optical properties. This is a promising result that approves the interest of achieving absolute optical properties quantification to perform a more accurate diagnosis of different superficial lesions. Moreover, it is of special interest to mention the quantitative discrimination that this technique was able to provide for the commonly used inflammation model Type 1 showing no contrast to the naked eye.

When comparing the black mark on the rat skin of the bi-coloured model with that of the inflammation of Type 2 model, we observed that the scattering properties were very different. These results should be further analysed with the depth-resolution analysis offered by DRSSr modality (refer to Section 7.2.3). Also, more experiments, completed with histological measurements, would be interesting to pursue this investigation.

Furthermore, with the measurements of the inflammation Type 2 model, we showed the ability of the *Dual-Step* technique to detect not only inflamed zones and black marks separately but also inflammation on the black mark, with no cross-talk between them.

We also introduced the interest of the high spatial resolution of the *Dual-Step* technique. Recall that scattering properties are estimated with the *initial Non-Contact DRSSr* to allow absorption estimations with LFOV MSI. According to the higher sensitivity to  $\widehat{\mu}'_s$  of short source-detector (SD) distances in DRSSr, an analysis of the shortest distances achieving optimal estimation of  $\widehat{\mu}'_s$  and the diameter of the excitation fibre, would define the best spatial resolution of the technique. This will certainly be smaller than 2.88 mm, which is the actual maximal fibre ring diameter (F3) used for  $\widehat{\mu}'_s$  estimation (see Figure 3.14). Based on these absolute  $\widehat{\mu}'_s$  estimations, absolute  $\widehat{\mu}_a$  estimations can be obtained with LFOV MSI for each pixel with a size controlled by the magnification of the optical system which can be as small as the CCD's pixel size of 9.9  $\mu\text{m}$ . This provides a much more precise analysis than Contact DRSSr and has been visualized with some of the heterogeneous biological samples with thin different structures considered in this study. What is more attractive, is that no prerequisite on the scattering or absorption contrast between the small structure and surrounding medium is required to obtain absolute quantitative optical properties, as it is the case for the *SFDI* study [Laughney et al., 2013].

In conclusion, the obtained preliminary results of this study have shown the potential for the wide-field resolved quantification of scattering and absorption properties of the *Dual-Step* technique in biological skin models. Particularly appealing is the interest of the developed technique not only for the clinical diagnosis of visual superficial abnormalities but also for those that are imperceptible to the naked eye. Further measurements and analysis would be necessary to optimize the technique as explained in the next Chapter 7.

---

# Conclusions and Perspectives

## 7.1 Conclusions

In this work, we proposed a *Dual-Step* technique capable of quantifying absolute scattering and absorption optical properties of biological tissue in a wide field of view through non-contact measurements. With these features we aspired to provide an accurate, non-invasive, and wide field clinical diagnosis of superficial lesions of skin such as skin inflammation.

Some existing techniques rely on the absolute quantification capability of punctual spectroscopic techniques like Diffuse Reflectance Spectroscopy (DRS). Punctual DRS systems achieve accurate absolute estimations of optical properties but require a long time to spatially scan a wide zone of interest. Other approaches consider Multispectral Imaging (MSI) covering a large field of view (LFOV) with homogeneous illumination, which can provide relative but not absolute estimations of optical properties. Thereby, the accuracy of MSI techniques is not optimal.

The *Dual-Step* technique we proposed relies on the combination of a Non-Contact modality of punctual Spatially-resolved Diffuse Reflectance Spectroscopy (DRSsr), being more robust than DRS, with LFOV MSI. Quantification is based on the scattering estimation of Non-Contact DRSsr which is subsequently used to achieve absolute wide-field estimation of absorption with LFOV MSI.

In the first part of this work, we focused on the development of two different Non-Contact DRSsr instrumental setups, with a working spectral range of 470-880 *nm*. These were based on the geometrical dimensions and quantification method of an existing and well-established *Contact DRSsr* system to facilitate comparison by ensuring that the same sample volume is inspected and that measured signals can be fitted to the same Monte Carlo model. The first developed setup is a probe-based Non-Contact DRSsr defined as the *initial Non-Contact DRSsr* which is integrated in the *Dual-Step* technique developed in this work. The second developed setup is the *CCD-based Non-Contact DRSsr*, which was investigated for the advantages it would offer in the integration of a perspective *Dual-Step* technique.

The developed Non-Contact DRSsr setups posed new instrumental and methodolog-

ical challenges that were solved to allow robustness of data acquisition and subsequent quantification of optical properties.

The instrumental challenge dealt with the sensitivity of measurements to the positioning of the object plane. Thereby a robust focusing protocol was set to determine the focal plane. It was identified that absorption estimations require a strict positioning of the sample at the focal plane. In contrast, scattering estimations with an acceptable spectrally averaged error of 4.1 % allow for a convenient object plane range of 1.2 mm, determined to be the depth of field (DOF) of the *initial Non-Contact DRSSr* technique.

The methodological challenges comprised the optical component's spectral effect and spatial alterations on projected beams which are not considered in the Monte Carlo model. Because the spectral effect remains constant for all measurements, a basic calibration procedure was able to correct this effect. However, the spatial alterations of the projected beams provoke a non-modelled diffuse reflectance that depends on the sample's optical properties. To correct this non-constant effect, we developed a new calibration methodology defined as the *Adaptive Calibration Algorithm and Protocol (ACA-Pro)*. The algorithm uses a few reference phantoms, with known optical properties, to derive correction factors that calibrate measurements of any sample through an interpolation approach. The main advantage of *ACA-Pro* is that it allows quantification of optical properties with any DRSSr measurement modality (Contact or Non-Contact) and a unique Monte Carlo simulation modelled under contact conditions. Thereby, time-consuming Monte Carlo simulations are not necessary for each instrumental setup. *ACA-Pro* has been thoroughly validated with all DRSSr systems considered in this work based on the calibration of the scattering properties. The resulting estimation errors of absorption and scattering for the *initial Non-Contact DRSSr system* are inferior to 7.6% and 3.3%, respectively, at the focal plane. Moreover, the *ACA-Pro* algorithm integrates a calibration procedure of instrumental variations (i.e. between different experiments) which avoids the measurements of reference phantoms at each experimental session. The entire algorithm has been validated not only on phantoms but also on *ex-vivo* and *in-vivo* biological samples.

In the second part of this work, we considered the development of the LFOV MSI instrumental setup and wide-field absorption quantification method. The instrumental setup was established on a staring MSI technique covering a field of view of  $5 \times 6.5 \text{ cm}^2$ . Filters used for the spectral scan were chosen to be at 500, 550, 600, and 750 nm according to the chromophores of interest (mainly oxy, deoxy- haemoglobin, and melanin). The absorption quantification method of MSI adopted a commonly used diffusion model coupled with an estimation of scattering properties with the *initial Non-Contact DRSSr* system. To overcome the limitations of the diffusion model in the estimation of absorption, we included a  $\mu_a$ -based *ACA-Pro* calibration procedure. Together with a developed method for correction of source fluctuations, *ACA-Pro* achieved quantitative errors inferior to 5.3% for the entire field of view, absorption range, and all wavelengths considered, of flat characterized phantoms. We also considered an heterogeneous gelatine-based phantom to quantify wide-field absorption properties from which spatial maps of ink concentration were derived.

In the final stage of this work, we used the *Dual-Step* technique combining *initial Non-Contact DRSSr*, to estimate scattering and allow absorption estimations with LFOV MSI. The potential of the method in the quantification of optical properties of tissue was

assessed using *ex-vivo* human skin samples and *in-vivo* rat skin models. Human samples included two homogeneous samples of low and high absorbing ranges (Phototype 2 and 5) and a heterogeneous sample with stretch marks. *In-vivo* models of rat skin included a bi-coloured zone, an imperceptible inflammation reaction, and a visible inflammation manifestation.

Scattering properties estimated with *initial Non-Contact DRSSr* were validated with *Contact DRSSr* on different zones of all measured samples. To allow wide-field quantification of scattering, an image segmentation approach was developed to determine the zones of the image with different scattering properties. The approach was based on the image acquired at 700 nm because this wavelength is the most sensitive to the reflectance contrasts that are directly associated to scattering changes. Non-Contact DRSSr scattering estimations were assigned according to the resulting segmented zones to create the absolute quantitative scattering maps.

The Non-Contact DRSSr scattering estimations allowed a first quantification of absorption with MSI which was subsequently corrected from the unfiltered specular reflections and adjusted to the 700 nm effect (probably originating from the parasite reflections of the Non-Contact DRSSr doublet). Thereby, the wide-field absorption quantification of all samples with MSI has been confirmed with respect to Contact and Non-Contact DRSSr. With this method, we validated the absorption quantification capacity of the *Dual-Step* technique.

The obtained preliminary results on biological samples are promising. Optical properties estimation on the same skin type were coherent between different *ex-vivo* samples (eg. caucasian skin) or *in-vivo* models (eg. white skin of the three rats). Thus, the difference in optical properties, observed between the black marks of two *in-vivo* rat skin models, is reliable. Moreover, in one of the rat inflammation models, the technique detected, with no cross-talk, the presence of inflammation on the black mark. Comparing the two measured inflammation models, a quantitative discrimination of optical properties was observed. Particularly interesting is the quantified optical property contrast measured by the *Dual-Step* technique and not discernible by the human eye in one of the *in-vivo* inflammation skin models. This shows the potential of the developed *Dual-Step* technique for the clinical diagnosis of superficial lesions, imperceptible to the naked eye.

In conclusion, we have developed a new Multispectral Imaging technique capable of providing absolute wide-field quantification of optical properties with non-contact measurements. We have obtained absolute quantification of the technique with well-characterized known phantoms, whilst a preliminary validation of the technique has been shown with three pertinent *ex-vivo* and three *in-vivo* skin samples. Yet, further experiments are needed to prove the absolute quantification on biological samples. Spatial maps of a few chromophores concentration were obtained with a heterogeneous gelatine-based phantom. Using the same unmixing method, chromophore concentration maps of biological samples can be easily derived. Thus, we have demonstrated the potential of the *Dual-Step* technique as an accurate, wide field, and non-invasive optical diagnosis tool.

The absolute quantification of optical properties obtained with characterized intralipid phantoms and the encouraging results on biological samples can be used to define new interesting directions for future developments.

The main instrumental advancements deal with the development of a parallel illumination *CCD-based DRSsr* technique, a homogeneous illumination to avoid shadowing in the LFOV MSI setup, and an intelligent coupling of the optimized setups for the *Dual-Step* technique.

The main methodological evolutions consider the development of a method achieving depth-resolution of optical properties with DRSsr, the correction for specular reflections in MSI images, and the optimal establishment of a  $\mu'_s$ -based segmentation algorithm of the *Dual-Step* technique.

These should be the focus of perspective work, detailed in the following Section 7.2.

## 7.2 Perspectives

To further evolve the *Dual-Step* technique towards a real clinical instrument, we propose various instrumental and methodological improvements. Some of these are focused on the composing *initial Non-Contact DRSSr* (Section 7.2.1) and LFOV MSI (Section 7.2.2) techniques individually. Additional improvements of the combining *Dual-Step* technique are given in Section 7.2.3.

### 7.2.1 Non-Contact DRSSr perspectives

#### *Instrumental perspectives*

Instrumental improvements of Non-Contact DRSSr aim to reduce undesirable signals and facilitate focusing of projected beams on the sample.

One of the undesirable signals of *initial Non-Contact DRSSr* include parasite reflections originated at the doublet for  $\lambda > 700 \text{ nm}$  (see Section 3.3.3). These parasite reflections are inconvenient because they have to be measured at each experiment session and they reduce significantly the signal to noise ratio. Therefore, a change of doublet pair with anti-reflection coating for the entire working spectral range should be considered in a perspective setup.

Moreover, the undesirable spatial spread of the illumination beam projection of Non-Contact DRSSr setups (see Figure 3.38) should be truncated to approach the modelled signals of the Monte Carlo simulation. This would benefit *ACA-Pro* calibration by extending the optical properties range that achieve optimal quantification with correction factors. A first progress of the *CCD-based DRSSr* illumination profile has been obtained by adding a diaphragm in the illumination path as described in Appendix A.5. A more advanced setup would avoid the use of a beamsplitter giving rise to unwanted parasite reflections (see Section 3.37) through the inclination of the illumination beam. Some groups ([Reif et al., 2007], [Zhu et al., 2011]) have already considered various tilt angles of the illumination beam in DRS. An investigation of the specific angles needed for the advanced *CCD-based DRSSr* setup should be performed in terms of instrumental arrangement and Monte Carlo model.

Further refinement of the illumination profile should be envisaged in all Non-Contact DRSSr setups with the reduction of spherical aberration with an aspheric lens. Measurements on characterized phantoms should be performed with this corrected illumination projection to confirm the estimation improvement of optical properties. Moreover, this correction will most probably improve the depth of field of the technique. The latter will have to be accurately determined with the optical properties estimation error of several unknown phantoms calibrated with different reference phantoms.

As explained in Section 3.4, the use of a CCD detector instead of a probe detector for Non-Contact DRSSr, should be considered for the various advantage it offers in a perspective integration of the *Dual-Step* technique.

Once the advanced setup of punctual *CCD-based DRSSr* will be validated, it is attractive to imagine a parallel DRSSr measurement with the use of an illumination point grid projected on the sample as shown in Figure 7.1. This setup would make use of an inclined illumination focused through multiple aspheric microlenses and diaphragms to reduce the spatial spread of individually projected filtered beams. For this, the utilization of an autofocus system, proper to each illumination beam, is necessary for samples having a curvature higher than the depth of field defined as  $1.2\text{ mm}$  for appropriate  $\widehat{\mu}_s'$  estimation (refer to Section 3.5.2).

Moreover, the setup should integrate the indirect measurement of the illumination intensity through a fixed calibration material (plastic corner) to correct from intensity fluctuations. This correction strategy has already been used and validated in the LFOV MSI technique developed in this work (refer to Section 5.3.3).

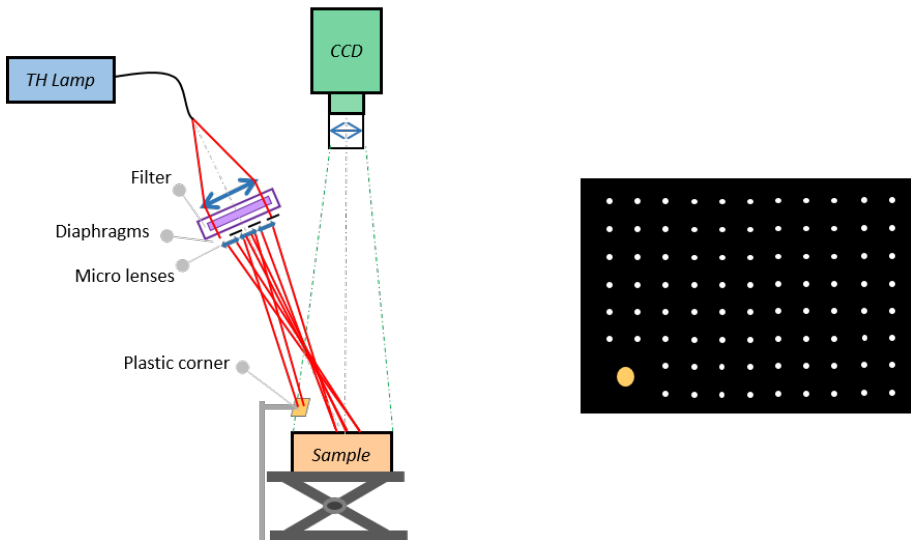


Figure 7.1: Left: CCD-based DRSSr setup with multiple inclined illumination points focused on the sample. Notice the fixed plastic corner to indirectly measure the source intensity. Right: Grid of focused illumination points on the sample (white points) and indirect source measurement on plastic corner (circle on the bottom left corner.)

The distances between illumination points should be optimized according to the spatial reflectance decay used to recover optical properties. Ideally, the acquisition of the spatial reflectance decay around each point should be automated with the acquisition of images at specific integration times, adapted to the sample and the dynamic range of the CCD. Also, the spectral scan (filter change) should be automated. Both of these controls are essential to reduce measurement duration and progress towards real-time acquisition.

### Methodological perspectives

Estimation accuracy of optical properties with the developed method for DRSSr depends on the forward model (Monte-Carlo simulation) and the calibration procedure *ACA-Pro*. Both of these aspects could be ameliorated to reduce the estimation error and improve the efficiency of the diagnosis.

We have shown that the adopted Monte Carlo simulation has accuracy limitations at the low scattering range ( $\mu'_s < 10 \text{ cm}^{-1}$ ). Hence, this constraint should be further analysed. As a starting point of this analysis, a comparison of the estimation error obtained with a Monte Carlo simulation or with the diffusion model should be done for optical property estimations at this low scattering range. Subsequently, the limits of the scattering model of [Van Staveren et al., 1991] used for intralipid should be examined. The investigation should be extended towards measurements of high absorbing samples such as the dark skin sample of Phototype 5, to verify the obtained scattering estimations (refer to Section 6.6.2).

In terms of the calibration procedure, we have shown that the estimation of absorption changes according to the absorption properties of the reference phantom (see Section 4.5.3). Thereby, to achieve the best estimation of optical properties, *ACA-Pro* should be based not only on scattering, as it has been done (Section 4.5.2), but also on absorption properties.

Besides, to fully benefit from the interpolation strategy of *ACA-Pro*, the optimal choice of reference phantoms used to build the *CF* reference base, should be done according to the optical property range of interest and the modelled reflectance response  $R^{LUT}$ .

## 7.2.2 LFOV MSI Perspectives

### *Instrumental perspectives*

Instrumental improvements of the developed LFOV MSI setup should be considered to avoid unwanted effects of specular reflections and shadow. Figure 7.2 illustrates the advanced LFOV MSI setup with the main ameliorations for this end.

First of all, specular reflections that do not allow accurate estimation of  $\widehat{\mu}_a$ , should be corrected. In a first stage, it would be interesting to explore the Non-Contact / MSI  $\mu_a$  ratio at one  $\lambda$  that derives the specular reflection pattern to correct the specular effect at other  $\lambda$ , as shown in Section 6.5.2. The simplicity of the approach should motivate the optimization of the correction method. Alternatively, the standard solution, more complicated and expensive, from an instrumental point of view, would consider the integration of a polariser in the instrumental LFOV MSI setup (see yellow element of Figure 7.2), to completely avoid specular reflections.

Second, a homogeneous central illumination should be considered to avoid shadow effects originating from the inclination of the illumination source that are difficult to correct a-posteriori. A plausible solution for this is to illuminate the sample perpendicularly by placing the illumination ring around the CCD detector as shown in Figure 7.2. An optimization of the numerical aperture and distance of the illumination ring is necessary to ensure the best illumination homogeneity.

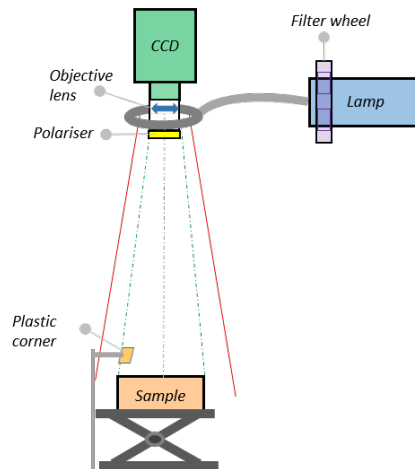


Figure 7.2: Advanced LFOV MSI setup with a homogeneous central illumination, to diminish shadow effects and polariser to avoid specular reflections.

In analogy to the perspective Non-Contact DRSr setup, to progress towards real-time acquisition, the spectral scan (filter change) and image acquisition with adapted integration time (according to the sample and dynamic range of the CCD) should be automatised.

### Methodological perspectives

The methodological perspectives of the LFOV MSI technique encompass calibration improvements and curvature correction of the sample.

Regarding the calibration improvements, we propose to perform an *ACA-Pro* calibration for each pixel of the image, as explained in Section 5.7, to compensate for illumination spatial nonuniformity.

Moreover, in analogy to the *ACA-Pro* calibration for DRSsr, an optimal benefit of the interpolation strategy would be obtained with an intelligent choice of the reference phantoms used to build the *CF* reference base adapted to the optical property range of interest.

As seen in Chapter 6, quantification of multispectral images are affected by the curvature of the sample itself and its consequences, mainly shadowing. A clear example is shown in Figure 7.3 with the image at 500 nm of the heterogeneous sample of human skin (Section 6.6.1). Note that the absorption of the depressions at the bottom and top left corners of the sample are overestimated (see Figure 7.3b) because they correspond to an intensity diminution of the acquired image (see Figure 7.3a).

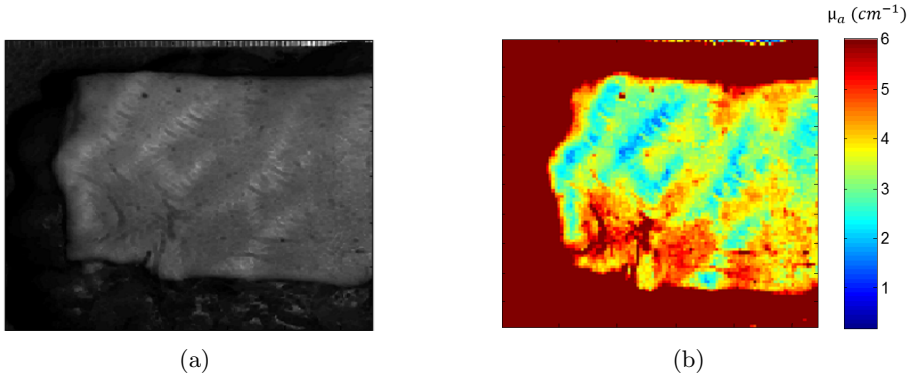


Figure 7.3: (a) Treated image and (b) Wide field  $\mu_a$  estimation at 500 nm.

Apart from avoiding shadowing with a homogeneous illumination, as explained previously, a curvature optical profiling method could be considered to perform correction of these artefacts. Correction would be based on a more detailed intensity-height function than the one that has been measured and discussed in Section 5.2.1.

### 7.2.3 *Dual-Step* technique Perspectives

#### *Instrumental perspectives*

The advanced instrumental version of the *Dual-Step* technique should combine the gridded *CCD-based DRSsr* system (see Figure 7.1) and the improved LFOV MSI setup (see Figure 7.2), as shown in the simplified diagram in Figure 7.4. Notice that in this setup, the translation stage is no longer needed for the position correlation between both techniques.

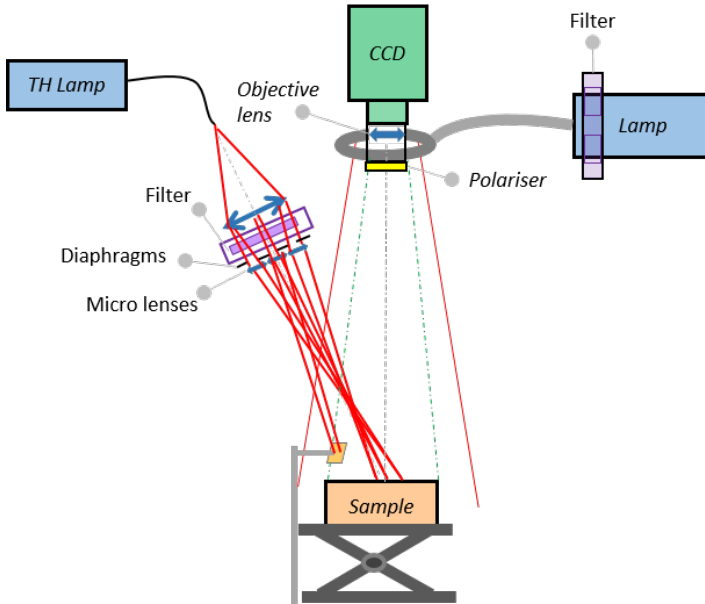


Figure 7.4: Simplified diagram of the ideal setup for the *Dual-Step* technique.

The characteristics of the common objective lens should be chosen according to a compromise between the spatial resolution of the DRSsr reflectance decay that allows optimal quantification of optical properties, distance/compactness instrumental requirements, and field of view covered by the MSI technique. This is of particular interest in the approach of a medical application, in which the development of a compact and ergonomic instrument is essential.

Moreover, automatised measurement acquisition of the *Dual-Step* technique according to a clear measurement protocol, is essential towards real-time performance in the clinical domain.

### Methodological perspectives

The advanced version of the *Dual-Step* system combines all improvements of *Non-Contact CCD-based DRSSr* described in Section 7.2.1 and LFOV MSI detailed in Section 7.2.2.

Since the *Dual-Step* technique is based on punctual measurements of Non-Contact DRSSr for wide-field scattering quantification, the most urging development should focus on the rapid acquisition of this wide-field scattering map. Instead of a long-time scan of punctual Non-Contact DRSSr, we propose to perform the minimal essential number of punctual DRSSr measurements on zones of the sample having the same scattering properties. For this, the development of a robust  $\mu'_s$ -based segmentation algorithm is required. As seen in Sections 6.7.1 and 6.7.2, the first development of the segmentation method is based on the 700 nm image because it is the least sensitive of the considered wavelengths to absorbing chromophore changes (eg. oxy- and deoxy-haemoglobin). Accordingly, reflectance intensity changes of the 700 nm image were supposed to be directly related to scattering changes and less affected by absorption changes. The segmentation algorithm we used is based on the *Otsu* method with varying number of thresholds.

A more rigorous investigation of the spatial variations of scattering in a wide range of biological skin samples is needed to evolve the segmentation method. For this, an appropriate direction of the Non-Contact DRSSr scan, according to the heterogeneities of the sample, could be used, and the size of the DRSSr inspected volume, limiting the spatial resolution of estimated optical properties, could be optimized. With this approach in mind, it would be interesting to analyse the heterogeneous human skin sample (refer to Section 6.6.1) with a spatial  $\mu'_{s,known}$  map.

Furthermore, a corresponding meticulous analysis of the spectral variations of scattering properties on different samples would be interesting to choose the most pertinent wavelengths on which an optimized segmentation method could be established.

These aspects are important to improve the accuracy of the segmentation that directly affects the wide-field quantification of the *Dual-Step* technique not only of scattering but also of absorption since the latter is based on the former.

It is known that bulk optical properties derive chromophore concentrations which are affected by the epidermal thickness variations [Saager et al., 2011]. Therefore, layer-resolved quantification of optical properties is one of the main investigations to follow to enhance the diagnosis accuracy of the *Dual-Step* technique in the clinical domain. Indeed, layer-resolved optical properties allow to detect more subtle alterations occurring in early-stage lesions such as cancer [Zhu et al., 2011].

The *Dual-Step* layer-resolution of quantified optical properties relies on the punctual DRSSr technique, as it has been studied by many groups ([Zhu et al., 2011], [Yu et al., 2014], [Koenig et al., 2015], [Wang et al., 2016]). The principle is based on the use of the different SD distances to investigate different volume depths. To illustrate this, we estimated optical properties with different fibre rings of the *Contact DRSSr* technique. A clear example is shown with absorption estimations on white skin (Figure 7.5) of the bi-coloured *in-vivo* rat model.

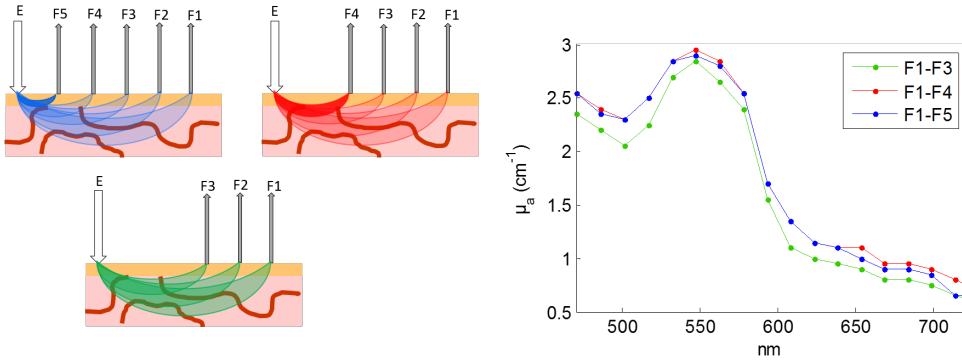


Figure 7.5: Left: Simplified illustration of the top absorbing epidermis layer and dermis underneath of the white rat skin. Right: Estimated absorption properties considering different fibre rings signals  $F$ .

Figure 7.5 illustrates photon paths through the tissue for each SD distance ( $F5 - F1$ ). Note that  $F1$  detects photons that have travelled deeper into the tissue, whilst those detected by  $F5$  interrogate a more superficial volume. Because of the higher melanin concentration, the top epidermis layer has a higher absorption than the dermis layer underneath. Correspondingly, photons that scrutinize mainly the epidermis superficial layer and are detected by  $F5$  and  $F4$ , estimate a higher absorption than photons who have travelled deeper and are detected by  $F3 - F1$ . The influence of  $F5$  and  $F4$  in the higher absorption estimation is clear in Figure 7.5.

These estimations exemplify the different sensitivities that SD distances have to optical properties individual to layers in depth. Certainly, the more SD distances, the better the depth resolution of quantification is. Hence, the use of a CCD detector providing a continuous spatial reflectance decay offers the best depth resolution, limited only by the object pixel size. The latter can be easily changed by changing the magnification of the detection optical system. This is why, the depth resolution capacity of optical properties estimation should be developed with the more flexible *CCD-based DRSSr* technique. Keep in mind that an essential requirement to allow depth-resolution of both optical properties is to ensure that the illumination point is perfectly focused.

Furthermore, the angled illumination of the perspective *CCD-based DRSSr* system (see Figure 7.1) could be exploited to restrict transport of detected light to the top layers, and increase corresponding depth resolution as has been done by [Wang et al., 2016]. However, a compromise of the illumination angle should be done between depth resolution and the maximum detectable depth of the technique.

As mentioned earlier, to approach real-time performance, the automatism of the optimal measurement protocol of the *Dual-Step* technique should be established in perspective work. To start off, the MSI images used for the  $\mu'_s$ -based segmentation method (to be developed) should be acquired and a single position of the segmented zones with different  $\mu'_s$  should be identified. Next, Non-Contact *CCD-based DRSSr* measurements would be performed. Depending on the punctual or grid illumination of the *CCD-based DRSSr* system, two options are possible. In the case of a unique punctual illumination, consecutive DRSSr measurements should be taken on each segmented zone (at the previously identified positions) to estimate scattering properties. In the case of a grid illumination, parallel DRSSr measurements would estimate a discrete scattering map in one go which would be interpolated with the  $\mu'_s$  segmented image. All DRSSr measurements should be ensured within a depth of field of 1.2 mm. Eventually, multispectral images would be acquired followed by the curvature profiling. Based on the  $\mu'_s$  quantitative maps and the curvature correction, absolute quantitative maps of  $\mu_a$  would be achieved.

Further information on layer-resolved quantitative optical properties can be then acquired with auto-focused DRSSr measurements, either on a determined zone or on the whole image. The latter would obviously be faster with a grid illumination *CCD-based DRSSr* setup performing focused parallel measurements, than with a single focused scan. Punctual estimations of optical properties would then be interpolated with the help of the wide-field map of bulk optical properties obtained previously.

An important advancement towards clinical diagnosis is to use the resulting quantification of optical properties to derive clinically significant parameters such as different chromophores (eg. oxy-, deoxy-haemoglobin, and melanin) concentration from absorption and tissue structure from scattering. The calculation of optimal estimations of chromophore concentration would be based on the same unmixing method that was used to derive the various ink concentration maps of the measured heterogeneous gelatine-based phantom. Obviously, the calculations should target the given chromophores and tissue structural changes that reveal important diagnosis information. For this, an appropriate choice of spectral ranges is required.

To approach real-time clinical diagnosis, it is essential to accelerate all measurements and calculations. The minimal number of measurements should be therefore performed and treated in an automatic manner to avoid not only human delay but also human error. Ideally, fast calculation algorithms should be ready to provide real-time wide-field chromophore concentration and tissue structure maps.

Once the aforementioned aspects will be developed, the *Dual-Step* technique should be compared to the state of the art technique (ie. SFDI).



# A

## Appendix

### A.1 Contributions to the current DRSSr procedure

#### A.1.1 Reduction of numerical noise

The discretization step of the range  $[\mu_s, \mu_a]$ ,  $\Delta\mu_s$  and  $\Delta\mu_a$ , used to generate the LUT with the Monte Carlo simulation, may induce numerical artefacts in the estimation of optical properties (see Figure A.1, left). This numerical noise is reduced with the optimized interpolation (smaller discretization step) of the  $[\mu_s, \mu_a]$  range (see Figure A.1, right).

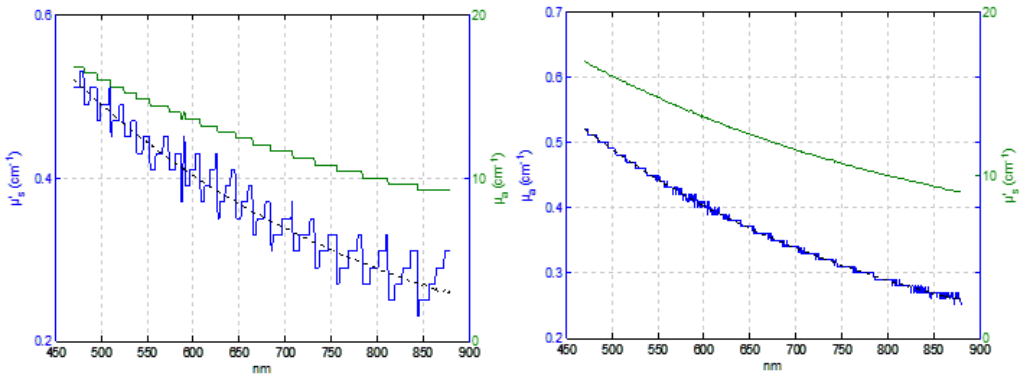


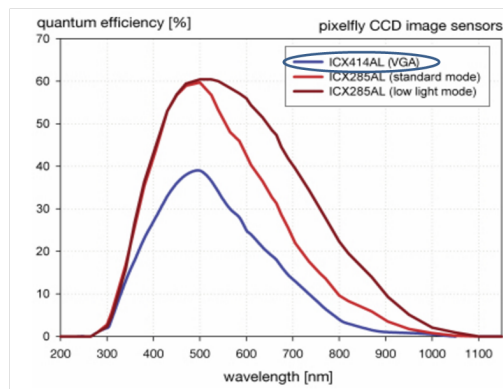
Figure A.1: Optical properties estimation with the original LUT (left), having a step size of  $2 \text{ cm}^{-1}$  in  $\mu_s$  and  $0.02 \text{ cm}^{-1}$  in  $\mu_a$ , and the new interpolated LUT having a smaller step size in  $\mu_s$  of  $0.2 \text{ cm}^{-1}$  and of  $0.01 \text{ cm}^{-1}$  in  $\mu_a$ .

## A.2 Detectors' specifications

### A.2.1 PixelFly VGA CCD

	unit	setpoint	pixelfly VGA
region of interest			no
extinction ratio		@ 1ms exposure time	1 : 2000
non linearity (differential)	%	full temperature range	< 2
uniformity darkness DSNU <sup>3</sup>	count	@ 90% center zone	1
uniformity brightness PRNU <sup>4</sup>	%	typical	1.0
trigger, auxiliary signals		internal / external	software / TTL level, 24V
power consumption	W		12
power supply	VAC		via PCI board
camera dimensions (w x h x l)	mm <sup>3</sup>		39 x 39 x 53
weight	kg	camera	0.26
operating temperature range	°C		+10 .. +40
operating humidity range	%	non condensing	10 .. 90
storage temperature range	°C		-20 .. +70
optical input			c-mount
optical input window			fused silica
data interface			PCI, compact PCI
interframing time	µs		5
CE certified			yes

technical data			
	unit	setpoint	pixelfly VGA
resolution (hor x ver) <sup>1</sup>	pixel		640 x 480
pixel size (hor x ver)	$\mu\text{m}^2$		9.9 x 9.9
sensor format / diagonal	inch / mm		1/2" / 7.9
quantum efficiency	%	@ 500nm typical	40
full well capacity	$e^-$		30 000
image sensor			ICX414AL
dynamic range	dB	CCD + camera	68.7
dynamic range A/D <sup>2</sup>	bit		12
readout noise	$e^-$ rms	range / typical	11 .. 14 / 12
imaging frequency, frame rate	fps	@ full frame / @ binning 2x ver / @ binning 4x ver	50 / 95 / 177
pixel scan rate	MHz		20
A/D conversion factor	$e^-$ / count		6.5
spectral range	nm		290 .. 1100
exposure time	s		5 $\mu\text{s}$ .. 65 s
anti-blooming factor		@ 100 ms exposure time	> 1000
smear	%		0.005
binning horizontal	pixel		1, 2
binning vertical	pixel		1, 2, 4

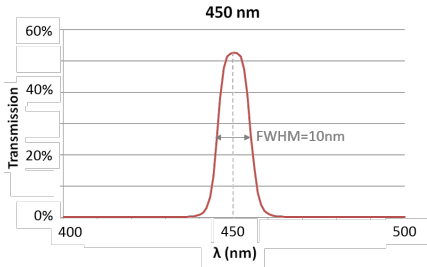
Figure A.2: *PixelFly* CCD specifications [PixelFly, 2015].Figure A.3: Quantum efficiency curves measured by *PCO*. Consider only the *VGA* CCD sensor used in this work (blue line) [PixelFly, 2015].

## A.2.2 JETI Spectrometer

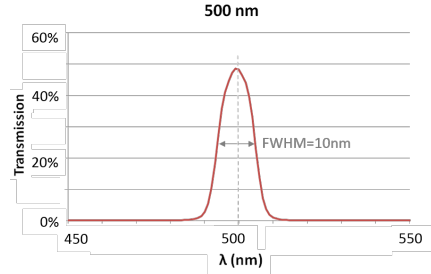
<b>Specifications</b>	
<b>Optical Parameters</b>	
Spectral range	specbos 1211 : 350 nm - 1000 nm specbos 1211UV : 230 nm - 1000 nm
Optical resolution (FWHM)	4.5 nm
Calculated wavelength step	1 nm
Digital electronic resolution	16 Bit ADC (15 Bit used)
Viewing angle	1.8° (Luminance mode)
Measuring distance / diameter	20 cm - Ø 6 mm; 100 cm - Ø 31 mm (luminance mode)
Measuring values	Spectral radiance Total luminance/ total radiance Total illuminance/ total irradiance Chromaticity coordinates x , y ; u' , v' Correlated Color Temperature, color purity Color Rendering Index, RGB Circadian metrics, Photosynthetically Active Radiation
<b>Measuring ranges and accuracies</b>	
Measuring range luminance	0.1 - 2500 cd/m <sup>2</sup> (higher values with optional filter)
Measuring range illuminance	2 - 10 000 lx
Luminance accuracy	± 2 % @ 100 cd/m <sup>2</sup> and illuminant A
Luminance reproducibility	± 1 %
Chromaticity accuracy	± 0.001 x , y @ illuminant A
Color reproducibility	± 0.0005 x , y
CCT reproducibility	± 20 K @ illuminant A
Wavelength accuracy	± 0.5 nm
<b>Other technical data</b>	
Dispersive element	Imaging grating (flat field)
Light receiving element	CCD array 2048 pixel
Power supply	USB powered
PC interface	USB 2.0 fullspeed
Dimensions (drawing)	180 mm * 82 mm * 53 mm
Weight	450 g
Operating conditions	Temperature 10 - 40 °C Humidity < 85 % relative humidity at 35 °C
<b>Miscellaneous</b>	
All inclusive accessories packet	Cosine corrector head-piece Tripod Transport box PC software JETI LiVal JETI SDK LabVIEW VI's ( Virtual Instruments ) Operating instructions and firmware commands (digital) USB cable Trigger connector
Calibration	NIST traceable
Recommended recalibration interval	1 year

Figure A.4: *Specbos 1201 JETI* Spectroradiometer specifications [JETI, 2015].

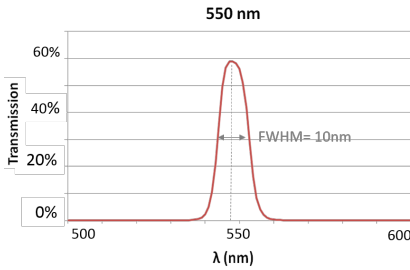
### A.3 Transmission of Filters



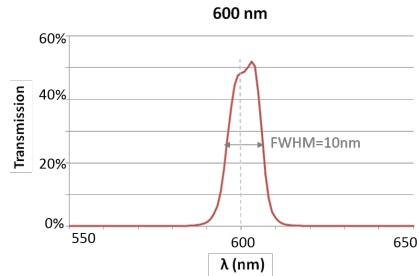
(a) Transmission of 450 nm filter.



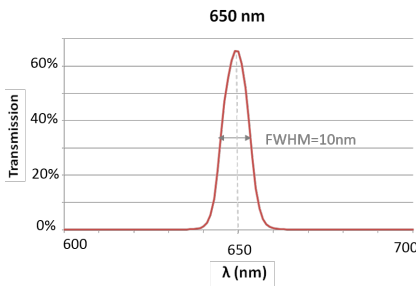
(b) Transmission of 500 nm filter.



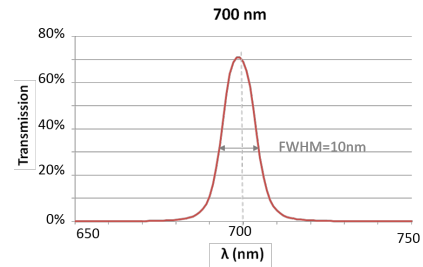
(c) Transmission of 550 nm filter.



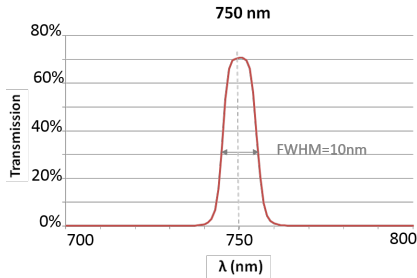
(d) Transmission of 600 nm filter.



(e) Transmission of 650 nm filter.



(f) Transmission of 700 nm filter.



(g) Transmission of 750 nm filter.

Figure A.5: Filters Transmission.



The whole setup is covered with a black cloth and measurements are taken in ambient obscurity to avoid pollution from ambient lightning.

Diffuse reflection measurements on *X-rite* color samples placed at the object plane are taken with both techniques under filtered light and compared.

### A.4.2 Measurement procedure

The lamp source is fixed to 3000K for maximal spectral distribution of the spectrometer working range between 380-780 nm.

Four *X-rite* color samples are chosen with the intention of covering different ranges of the working spectrum with different reflection intensities. The selected color samples are blue, green, red and white colors to cover the primary colors of the visible spectrum (see crosses of Figure A.7).

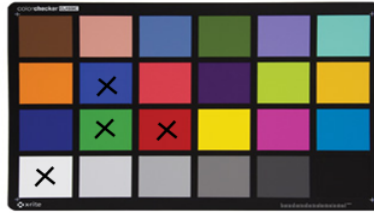


Figure A.7: *X-rite* color samples used are marked with a cross: white, blue, green and red.

Filters ranging from 400 to 750 nm are used and optimized to the selected *X – rite* color samples as summarized in Table A.1.

Table A.1: Filters used (x) for the various *X-rite* color samples (blue, green, red, white) are marked with a cross.

Filter	Blue	Green	Red	White
450 nm	x			x
500 nm	x	x		x
550 nm	x	x	x	x
600 nm	x	x	x	x
650 nm	x	x	x	
700 nm	x	x	x	x
750 nm		x	x	x

Diffuse reflection images are taken with an exposure time  $t$  that is adapted to the *X – rite* color sample, the filter used, and the fixed illumination intensity. To correct from the inhomogeneous illumination, the curved focal plane of the objective lens and the positioning of the filter, the flat field is measured. This is done for each filter position by placing a white Teflon board at the object plane under the same illumination conditions. Since there is no pollution from varying ambient lightning, background light is considered stable and measured only once at the various integration times used. These

images are representative of the CCD's offset (thermal effect and readout noise) which is subtracted from the images. To reduce photon noise, the diffuse reflection, flat field and offset are measured through the average of three images.

Point Spectroscopy measurements are taken just after the image measurement without changing the filter or sample position to ensure the same illumination conditions on the same sample area. To do so, the CCD detector and objective lens are removed and the JETI spectrometer is placed in the same image plane as shown in Figure A.6. Since the spectrometer automatically adapts its integration time  $t$ , no manual adjustment of the dynamic range is needed. The spectrometer's offset is measured under the same dark conditions.

### A.4.3 Signal Processing

Diffuse Reflection  $S$  and flat field  $S_{flat}$  images are corrected from the background  $S_{offset}$  at the same integration time. Reflection images  $S$  are then corrected from the flat field through the correction factor  $FF$  and exposure time  $t$  as described in Equations A.1 and A.2. A region of interest in the corrected image  $S_c$  is chosen and the average intensity grey value  $S_{av}$  is used for further comparison with point spectroscopy.

$$FF = \frac{S_{flat} - S_{offset}}{\max(S_{flat} - S_{offset})} \quad (\text{A.1})$$

$$S_c = \frac{S - S_{offset}}{FF \cdot t} \quad (\text{A.2})$$

Point Spectroscopy radiance measurements provided by the spectrometer are already corrected from the exposure time  $t$ . Therefore only the instrumental offset correction is considered (subtracted).

### A.4.4 Optical analysis for unit agreement

Spectroscopy measurements are calibrated from the detector response and therefore considered to be the reference to which imaging measurements are compared. For comparison, reflection measurements taken with both modalities have to be converted to the same units. The average intensity  $I_{av}$  from Spectral Imaging in  $gv$  and Radiance from Spectroscopy in  $\frac{W}{sr \cdot m^2}$ , are converted to Photon Flux  $E_{PF}$  in  $\frac{N_p}{s \cdot m^2}$ , ( $N_p$  being number of photons). To facilitate the comprehension of the unit conversion, Figure A.8 depicts the optical decomposition of both modalities in the combined setup shown in Figure A.6.

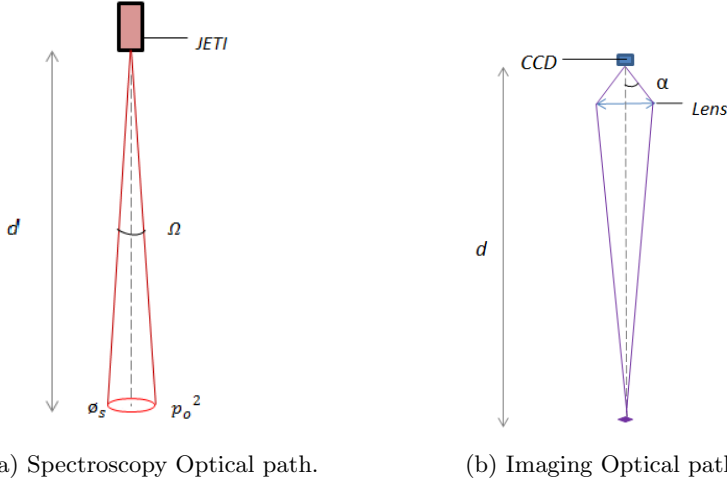


Figure A.8: Optical decomposition of punctual spectroscopy and spectral imaging setups of Figure A.6

### A.4.5 Spectroscopy: Radiance conversion

The number of photons  $N_p$  can be derived from the ratio of the total radiation energy  $E_{total}$  and the quantum energy of a single photon  $E_{photon}$  according to Equation A.3.

$$N_p = \frac{E_{total}}{E_{photon}} \quad (\text{A.3})$$

$E_{photon}$  is calculated according to the Planck hypothesis expressed in Equation A.4.

$$E_{photon} = \frac{hc}{\lambda} \quad (\text{A.4})$$

where  $h$  is the Planck constant in  $\frac{J}{s}$ ,  $c$  is the speed of light in  $\frac{m}{s}$ , and  $\lambda$  is the wavelength in  $m$ .

Spectroscopy measurements are given as Radiance  $R_m$  in  $\frac{W}{sr \cdot m^2}$  by the setup shown in Figure A.8a. This is converted to Photon Flux  $E_{PF}$  in  $\frac{N_p}{s \cdot m^2}$  for comparison with Imaging measurements through Equation A.5.

$$E_{PF} = R_m \cdot \Omega \cdot \frac{1}{E_{photon}} \quad (\text{A.5})$$

where  $\Omega$  is the solid angle in  $sr$ , calculated with Equation A.6.

$$\Omega = \frac{\pi \cdot (\frac{1}{2} \cdot \phi_s)^2}{d^2} \quad (\text{A.6})$$

### A.4.6 Imaging: Intensity conversion

The imaging setup is analysed for one object pixel as shown in Figure A.8b. The Intensity  $I_{av}$  in *grey value (gv)* for an integration time  $t$  is converted to Photon Flux  $E_{PF}$  in  $\frac{N_p}{s \cdot m^2}$  with the use of Eq. A.7.

$$E_{PF} = \frac{gv \cdot q}{t \cdot QE \cdot \sin^2(\alpha) \cdot p_o^2} \cdot T_{lens, \lambda_i} \quad (\text{A.7})$$

where  $q$  is the quantization step in number of electrons  $N_e$  per grey value  $\frac{N_e}{gv}$ ,  $QE$  is the quantum efficiency or photon-to-converted electron ratio of the CCD in  $N_e/N_p$  (refer to Figure A.3),  $\sin(\alpha)$  is the image numerical aperture calculated for an  $f\# = 12$  (see Equation A.8),  $p_o$  is the size of an object pixel in  $m$  (see Equation A.9),  $T_{lens, \lambda_i}$  is the lens transmission for a distinct wavelength  $\lambda_i$ .

$$\sin(\alpha) = \frac{1}{2 \cdot f\#} \quad (\text{A.8})$$

$$p_o = \frac{p_i}{G} \quad (\text{A.9})$$

where  $p_i$  is the size of an image pixel in  $m$  and  $G$  is the magnification.

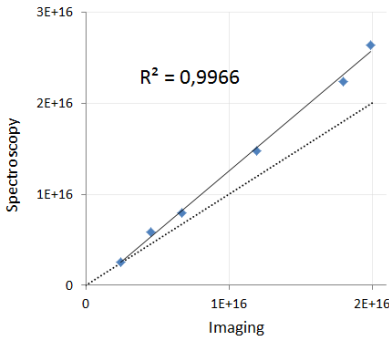
$G$  is calculated by imaging a ruler at the object plane (at a distance  $d$  from the CCD). For an image size of 1392 x 1024 pixels and pixel size  $p_i = 6.45 \mu m$ ,  $G$  is 0.124. Thus, the object pixel has a size  $p_o$  of  $52.25 \mu m$  according to Equation A.9.

### A.4.7 Results and Discussion

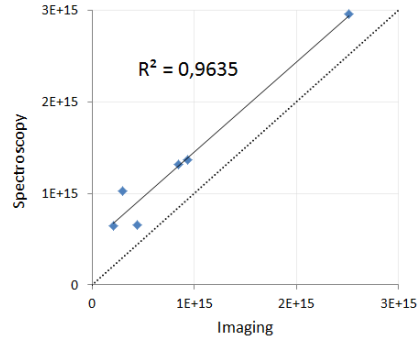
Diffuse reflection measurements of the four *X-rite* color samples with Point Spectroscopy and Imaging are compared and analysed in this Section. Figure A.9 shows the linear correlation between reflection measurements in  $E_{PF}$  under all filtered light.

The overall linearity between Punctual Spectroscopy and Spectral Imaging is clearly confirmed. It is noticed that the higher the signal-to-noise ratio, the higher the correlation  $R^2$  between both measurement modalities is (i.e. the white sample, with the highest intensity signal, has the best  $R^2$ ). From these results, a linear function can be derived to convert imaging measurements into the reference spectroscopy measurements. This function deviates from the 1:1 ratio between modalities (dotted black lines of Figure A.9) and therefore absolute analogy between modalities is not possible because of the various simplifications that were made in the measurement and conversion procedures:

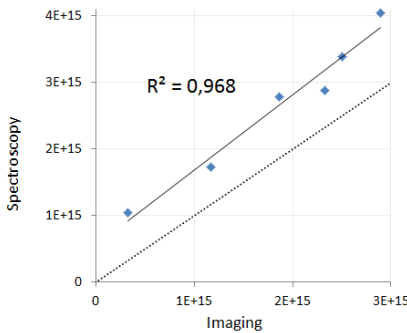
- There exists an uncertainty in the measurement of the distance  $d$  between the sample and the JETI detector since the distance from the case to the detector is unknown. This affects the value of  $\Omega$ .
- The  $E_{photon}$  is calculated for the central filter wavelength only. This simplification disregards the filter's wavelength width having a *FWHM* of  $10 \text{ nm}$  (see Appendix A.3).



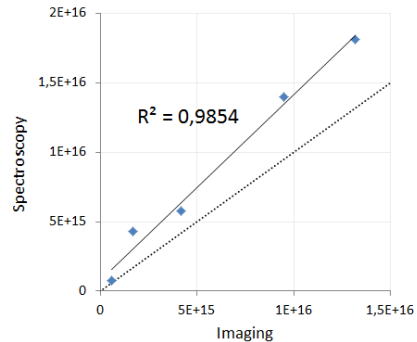
(a) White sample



(b) Blue sample



(c) Green sample



(d) Red sample

Figure A.9: Correlation of  $E_{PF}$  in  $\frac{N_p}{s \cdot m^2}$  of Imaging and Spectroscopy measurements.

### A.4.8 Conclusion

The linear spectral correlation of Spectral Imaging and Point Spectroscopy has been validated through a simple experimental setup and an extensive unit conversion process. With the same experimental and processing procedure, it is possible to apply the derived linear function to convert imaging measurements into reference spectroscopy measurements.

## A.5 Improved CCD-based Non-Contact DRSSr setup

As seen in Section 3.4.2, the use of the beamsplitter provokes a non-negligible parasite halo around the projection of the illumination beam. To remove it, we propose to include a diaphragm between the doublets of the illumination path as shown in Figure A.10.

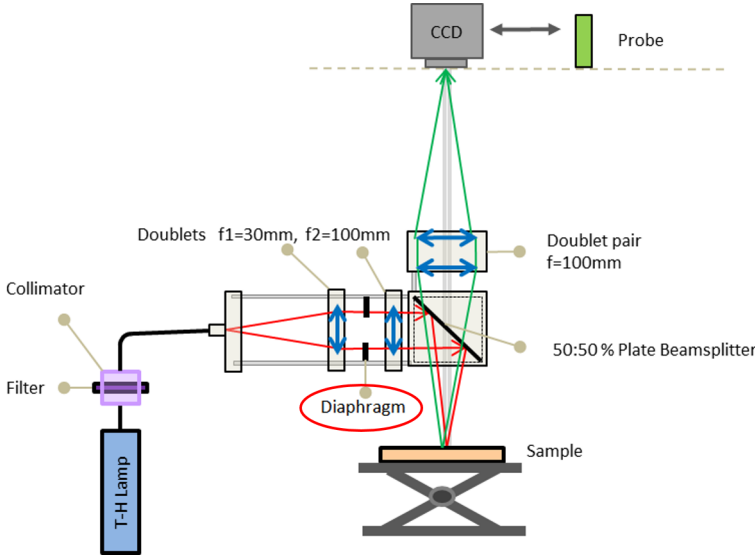


Figure A.10: Non-Contact CCD-based DRSSr setup with an additional diaphragm between the doublets of the illumination path.

To show the effect of the diaphragm and filters on the illumination profile, the resulting normalized profiles with and without diaphragm and various filters are plotted in Figure A.11 together with that of the *folded* and *initial Non-Contact DRSSr* setups (see Figures 3.35 and 3.23). Comparing the profiles, it is seen that the different filters do not provoke different effects. What is more, it is clear that the diaphragm cuts down the illumination intensity protrusion between  $D_6$  and  $D_5$  caused by the beamsplitter's parasite halo and reduces further extension. Therefore, the use of the diaphragm should be considered in an advanced version of the CCD-based DRSSr setup.

Overall, it is seen that the illumination beam profile of the Non-Contact probe-based and CCD-based with different filters are comparable, and that the use of a diaphragm improves the profile at closer distances.

This profile enhancement will most probably improve optical properties estimations with the *ACA-Pro* calibration algorithm explained in Chapter 4.

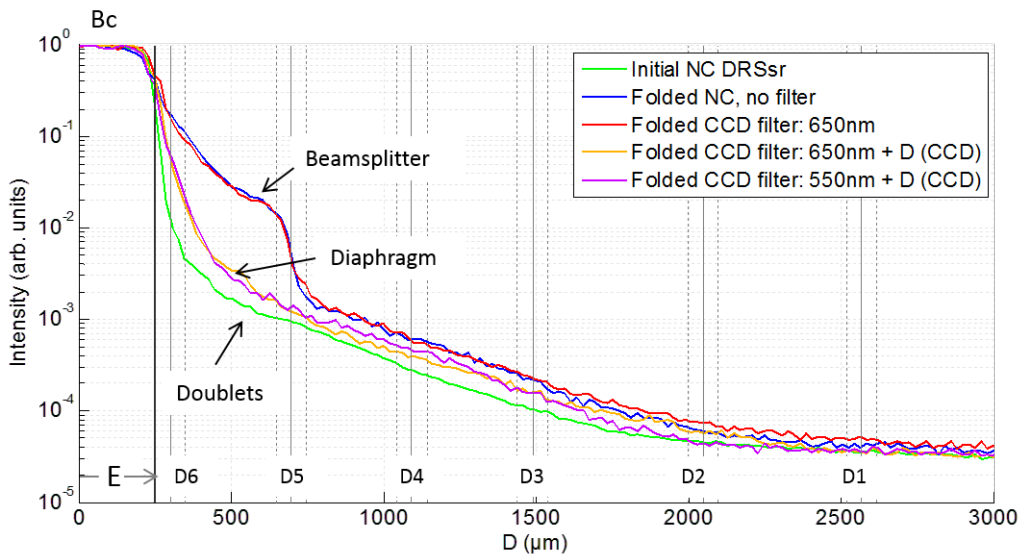
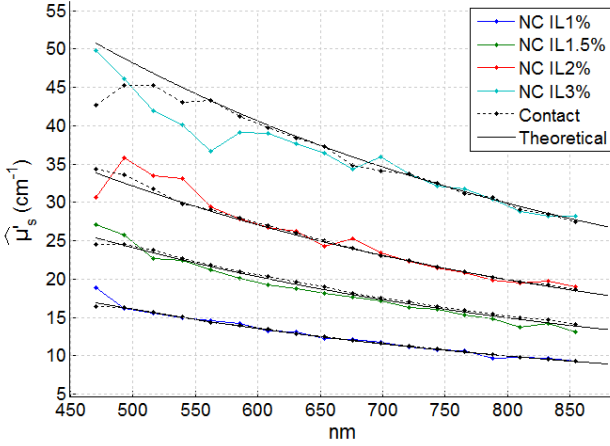


Figure A.11: Illumination beam profiles of *folded Non-Contact DRSSr* setups with and without filters and/or diaphragm: ND=No Diaphragm, D=Diaphragm.

## A.6 Validation of ACA-Pro with folded Non-Contact DRSSr measurements

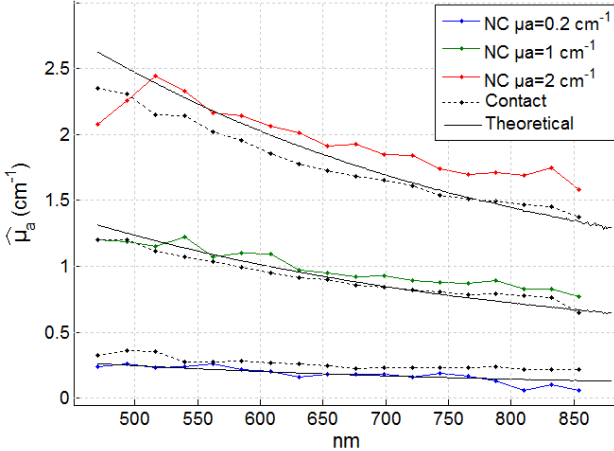
Figure A.12 shows the optical property estimation of phantoms having different  $\mu'_{s,theo}$  and  $\mu_{a,theo}$  with the Adaptive Calibration Algorithm *ACA-Pro*, described in Chapter 4. For a more detailed explanation refer to [Dehghani et al., 2015].

Phantoms with different %IL and same estimated  $\mu_a = 0.4 \pm 0.04 \text{ cm}^{-1}$  at 600 nm



(a)

Phantoms with different  $\mu_a$  and same estimated  $\mu'_s = 20 \pm 0.2 \text{ cm}^{-1}$  at 600 nm



(b)

Figure A.12: (a)  $\widehat{\mu'_s}$  estimation (b)  $\widehat{\mu_a}$  estimation with measurements obtained with *folded Non-Contact DRSSr* measurements and *ACA-Pro* calibration.

# B

---

## Scientific Communications

To date, the present work has established various communications covering patents, proceedings for oral and poster presentations, and journal articles.

### B.1 Patents

#### Submitted

*Procédé de traitement d'un signal de rétrodiffusion* (2015).

#### Submitted

*Multimodal Quantitative Multispectral Imaging* (2016).

### B.2 Communications

1. Poster: '*Large Field quantification of optical properties*'. BIOMED (2016).
2. Oral: '*Non-Contact Quantitative Diffuse Reflectance spectroscopy*'. European Conferences of Biomedical Optics (ECBO). International Society for Optics and Photonics (2015) [Dehghani et al., 2015].
3. Poster: '*Diffuse Reflectance Spectral Imaging for the quantification of absorption and diffusion properties in homogeneous turbid media*'. GRETSI (2015).
4. Poster: '*New Multispectral Imaging Technique*'. European Society for Photobiology (2014).

### B.3 Journal Articles

#### Published

*'ACA-Pro: Calibration Protocol for quantitative diffuse reflectance spectroscopy. Validation of Contact and Non-Contact probe- and CCD- based systems*'. JBO (2016) [Sorgato et al., 2016].

#### In progress

*'Wide-Field quantification of optical properties in biological ex-vivo and in-vivo skin models with Dual-Step Multispectral Imaging Technique*'.



# Bibliography

- [Arridge et al., 1998] Arridge, S. R., and Lionheart, W. R. (1998). Nonuniqueness in diffusion-based optical tomography. *Optics Letters*, 23(11):882–884.
- [Bashkatov et al., 2005] Bashkatov, A., Genina, E., Kochubey, V., and Tuchin, V. (2005). Optical properties of human skin, subcutaneous and mucous tissues in the wavelength range from 400 to 2000 nm. *Journal of Physics D: Applied Physics*, 38(15):2543.
- [Basiri et al., 2010] Basiri, A., Nabili, M., Mathews, S., Libin, A., Groah, S., Noordmans, H. J., and Ramella-Roman, J. C. (2010). Use of a multi-spectral camera in the characterization of skin wounds. *Optics express*, 18(4):3244–3257.
- [Bays et al., 1996] Bays, R., Wagnieres, G., Robert, D., Braichotte, D., Savary, J.-F., Monnier, P., van den Bergh, H., et al. (1996). Clinical determination of tissue optical properties by endoscopic spatially resolved reflectometry. *Applied optics*, 35(10):1756–1766.
- [Bedard et al., 2013] Bedard, N., Schwarz, R. A., Hu, A., Bhattar, V., Howe, J., Williams, M. D., Gillenwater, A. M., Richards-Kortum, R., and Tkaczyk, T. S. (2013). Multimodal snapshot spectral imaging for oral cancer diagnostics: a pilot study. *Biomedical optics express*, 4(6):938–949.
- [Bevilacqua, 1998] Bevilacqua, F. (1998). *Local optical characterization of biological tissues in vitro and in vivo*. PhD thesis, EPFL.
- [Bish et al., 2014] Bish, S. F., Sharma, M., Wang, Y., Triesault, N. J., Reichenberg, J. S., Zhang, J. X., and Tunnell, J. W. (2014). Handheld diffuse reflectance spectral imaging (drsi) for in-vivo characterization of skin. *Biomedical optics express*, 5(2):573–586.
- [Bjorgan et al., 2014] Bjorgan, A., Milanic, M., and Randeberg, L. L. (2014). Estimation of skin optical parameters for real-time hyperspectral imaging applications. *Journal of biomedical optics*, 19(6):066003–066003.
- [Bolt et al., 1993] Bolt, R., and Ten Bosch, J. (1993). Method for measuring position-dependent volume reflection. *Applied optics*, 32(24):4641–4645.
- [Bourg-Heckly et al., 2013] Bourg-Heckly, G., and Mordon, S. (2013). *Optics in Instruments: Applications in Biology and Medicine. Chapter 4: Therapeutic applications of lasers*.

- [Bouslimani et al., 2015] Bouslimani, A., Porto, C., Rath, C. M., Wang, M., Guo, Y., Gonzalez, A., Berg-Lyon, D., Ackermann, G., Christensen, G. J. M., Nakatsuji, T., et al. (2015). Molecular cartography of the human skin surface in 3d. *Proceedings of the National Academy of Sciences*, 112(17):E2120–E2129.
- [Burmeister et al., 2015] Burmeister, D. M., Ponticorvo, A., Yang, B., Becerra, S. C., Choi, B., Durkin, A. J., and Christy, R. J. (2015). Utility of spatial frequency domain imaging (sfdi) and laser speckle imaging (lsi) to non-invasively diagnose burn depth in a porcine model. *Burns*, 41(6):1242–1252.
- [Cary-300, 2015] Cary-300, V. (2015). Varian cary-300. <http://www.labwrench.com/equipment.view/equipmentNo/4795/Varian/Cary-300/>. Last visited:22/08/2015.
- [Cen et al., 2009] Cen, H., and Lu, R. (2009). Quantification of the optical properties of two-layer turbid materials using a hyperspectral imaging-based spatially-resolved technique. *Applied optics*, 48(29):5612–5623.
- [Cuccia et al., 2009] Cuccia, D. J., Bevilacqua, F., Durkin, A. J., Ayers, F. R., and Tromberg, B. J. (2009). Quantitation and mapping of tissue optical properties using modulated imaging. *Journal of biomedical optics*, 14(2):024012–024012.
- [Dehghani et al., 2015] Dehghani, H., and Taroni, P. (2015). Diffuse optical imaging v. In *Proc. of SPIE Vol*, volume 9538, pages 953801–1.
- [Diks et al., 2001] Diks, S. H., van Deventer, S. J., and Peppelenbosch, M. P. (2001). Invited review: Lipopolysaccharide recognition, internalisation, signalling and other cellular effects. *Journal of endotoxin research*, 7(5):335–348.
- [Ding et al., 2006] Ding, H., Lu, J. Q., Wooden, W. A., Kragel, P. J., and Hu, X.-H. (2006). Refractive indices of human skin tissues at eight wavelengths and estimated dispersion relations between 300 and 1600 nm. *Physics in medicine and biology*, 51(6):1479.
- [Doornbos et al., 1999] Doornbos, R., Lang, R., Aalders, M., Cross, F., and Sterenborg, H. (1999). The determination of in vivo human tissue optical properties and absolute chromophore concentrations using spatially resolved steady-state diffuse reflectance spectroscopy. *Physics in medicine and biology*, 44(4):967.
- [East et al., 2008] East, J. E., Suzuki, N., Stavrinidis, M., Guenther, T., Thomas, H. J., and Saunders, B. P. (2008). Narrow band imaging for colonoscopic surveillance in hereditary non-polyposis colorectal cancer. *Gut*, 57(1):65–70.
- [Foschum et al., 2015] Foschum, F., Bodenschatz, N., Krauter, P., Nothelfer, S., Liemert, A., Simon, E., Kröner, S., and Kienle, A. (2015). Surface layering effect of diluted intralipid. In *European Conferences on Biomedical Optics*, pages 95381A–95381A. International Society for Optics and Photonics.
- [Foschum et al., 2011] Foschum, F., Jäger, M., and Kienle, A. (2011). Fully automated spatially resolved reflectance spectrometer for the determination of the absorption and scattering in turbid media. *Review of Scientific Instruments*, 82(10):103104.

- [Gioux et al., 2011] Gioux, S., Mazhar, A., Lee, B. T., Lin, S. J., Tobias, A. M., Cuccia, D. J., Stockdale, A., Oketokoun, R., Ashitate, Y., Kelly, E., et al. (2011). First-in-human pilot study of a spatial frequency domain oxygenation imaging system. *Journal of biomedical optics*, 16(8):086015–086015.
- [Gono et al., 2004] Gono, K., Obi, T., Yamaguchi, M., Ohyama, N., Machida, H., Sano, Y., Yoshida, S., Hamamoto, Y., and Endo, T. (2004). Appearance of enhanced tissue features in narrow-band endoscopic imaging. *Journal of biomedical optics*, 9(3):568–577.
- [Gono et al., 2003] Gono, K., Yamazaki, K., Doguchi, N., Nonami, T., Obi, T., Yamaguchi, M., Ohyama, N., Machida, H., Sano, Y., Yoshida, S., et al. (2003). Endoscopic observation of tissue by narrowband illumination. *Optical Review*, 10(4):211–215.
- [Gussakovskiy et al., 2010] Gussakovskiy, E., Yang, Y., Rendell, J., Jilkina, O., and Kupriyanov, V. (2010). Mapping the myoglobin concentration, oxygenation, and optical pathlength in heart ex vivo using near-infrared imaging. *Analytical biochemistry*, 407(1):120–127.
- [Herr et al., 2011] Herr, H. W., and Donat, S. M. (2011). Reduced bladder tumour recurrence rate associated with narrow-band imaging surveillance cystoscopy. *BJU international*, 107(3):396–398.
- [Hulst et al., 1957] Hulst, H. C., and Van De Hulst, H. (1957). *Light scattering by small particles*. Courier Corporation.
- [Igarashi et al., 2007] Igarashi, T., Nishino, K., and Nayar, S. K. (2007). The appearance of human skin: A survey. *Foundations and Trends® in Computer Graphics and Vision*, 3(1):1–95.
- [Jacques, 1998] Jacques, S. L. (1998). Skin optics. <http://omlc.org/news/jan98/skinoptics.html>. [ECE532 Biomedical Optics, Oregon Graduate Institute].
- [Jacques, 2013] Jacques, S. L. (2013). Optical properties of biological tissues: a review. *Physics in medicine and biology*, 58(11):R37.
- [Jacques et al., 1993] Jacques, S. L., Gutsche, A., Schwartz, J., Wang, L., and Tittel, F. (1993). Video reflectometry to extract optical properties of tissue in vivo. *Medical optical tomography: functional imaging and monitoring*, 11:211–226.
- [Jacques et al., 1998] Jacques, S. L., and Prahl, S. A. (1998). Reduced scattering coefficient. <http://omlc.org/classroom/ece532/class3/musp.html>. [ECE532 Biomedical Optics, Oregon Graduate Institute].
- [Jacques et al., 2010] Jacques, S. L., Samatham, R., and Choudhury, N. (2010). Rapid spectral analysis for spectral imaging. *Biomedical optics express*, 1(1):157–164.
- [JETI, 2015] JETI (2015). Vis spectroradiometer. <http://www.jeti.com/cms/index.php/instruments-55/radiometer/specbos/specbos-1201>. Last visited: 11/10/2015.

- [Kan, 2012] Kan, L. (2012). *Multimodal Optical Spectroscopy and Imaging for improving Cancer Detection in the Head and Neck at Endoscopy*. PhD thesis.
- [Kersten et al., 1982] Kersten, R. T., and Le-Hiep, T. (1982). Wavelength dependence of the numerical aperture of optical fibers. *Optics Communications*, 41(2):99–101.
- [Kienle et al., 1998] Kienle, A., Patterson, M. S., Dögnitz, N., Bays, R., Wagnieres, G., van Den Bergh, H., et al. (1998). Noninvasive determination of the optical properties of two-layered turbid media. *Applied optics*, 37(4):779–791.
- [Kim et al., 2010] Kim, A., Roy, M., Dadani, F., and Wilson, B. C. (2010). A fiberoptic reflectance probe with multiple source-collector separations to increase the dynamic range of derived tissue optical absorption and scattering coefficients. *Optics express*, 18(6):5580–5594.
- [Kim et al., 2015] Kim, B., Lee, S. H., Yoon, C. J., Ghoo, Y. S., Ahn, G.-O., and Kim, K. H. (2015). In vivo visualization of skin inflammation by optical coherence tomography and two-photon microscopy. *Biomedical optics express*, 6(7):2512–2521.
- [Kim et al., 2012] Kim, O., McMurdy, J., Lines, C., Duffy, S., Crawford, G., and Alber, M. (2012). Reflectance spectrometry of normal and bruised human skins: experiments and modeling. *Physiological measurement*, 33(2):159.
- [Koenig et al., 2013] Koenig, A., Grande, S., Dahel, K., Planat-Chrétien, A., Poher, V., Goujon, C., and Dinten, J.-M. (2013). Diffuse reflectance spectroscopy: a clinical study of tuberculin skin tests reading. In *SPIE BiOS*, pages 85920S–85920S. International Society for Optics and Photonics.
- [Koenig et al., 2015] Koenig, A., Roig, B., Le Digabel, J., Josse, G., and Dinten, J.-M. (2015). Accessing deep optical properties of skin using diffuse reflectance spectroscopy. In *European Conferences on Biomedical Optics*, pages 95370E–95370E. International Society for Optics and Photonics.
- [Labsphere, 2016] Labsphere (2016). Spectralon diffuse reflectance material. <https://www.labsphere.com/labsphere-products-solutions/materials-coatings-2/coatings-materials/spectralon/>. Last visited: 30/05/2016.
- [Laughney et al., 2013] Laughney, A. M., Krishnaswamy, V., Rice, T. B., Cuccia, D. J., Barth, R. J., Tromberg, B. J., Paulsen, K. D., Pogue, B. W., and Wells, W. A. (2013). System analysis of spatial frequency domain imaging for quantitative mapping of surgically resected breast tissues. *Journal of biomedical optics*, 18(3):036012–036012.
- [Li et al., 2013] Li, Q., He, X., Wang, Y., Liu, H., Xu, D., and Guo, F. (2013). Review of spectral imaging technology in biomedical engineering: achievements and challenges. *Journal of biomedical optics*, 18(10):100901–100901.
- [Meglinski et al., 2002] Meglinski, I. V., and Matcher, S. J. (2002). Quantitative assessment of skin layers absorption and skin reflectance spectra simulation in the visible and near-infrared spectral regions. *Physiological measurement*, 23(4):741.

- [Mourant et al., 1997] Mourant, J. R., Fuselier, T., Boyer, J., Johnson, T. M., and Bigio, I. J. (1997). Predictions and measurements of scattering and absorption over broad wavelength ranges in tissue phantoms. *Applied Optics*, 36(4):949–957.
- [Nave, 2012] Nave, R. (2012). Rayleigh and mie scattering. hyperphysics. <http://hyperphysics.phy-astr.gsu.edu/hbase/atmos/blusky.html>. [Georgia State University].
- [Nichols et al., 2015] Nichols, B. S., Schindler, C. E., Brown, J. Q., Wilke, L. G., Mulvey, C. S., Krieger, M. S., Gallagher, J., Geradts, J., Greenup, R. A., Von Windheim, J. A., et al. (2015). A quantitative diffuse reflectance imaging (qdri) system for comprehensive surveillance of the morphological landscape in breast tumor margins. *PLoS one*, 10(6):e0127525.
- [Optics, 2015] Optics, A. (2015). Introduction to beam splitters for optical research applications. <http://www.azooptics.com/Article.aspx?ArticleID=871>. Last visited: 15/09/2015.
- [Palmer et al., 2006] Palmer, G. M., and Ramanujam, N. (2006). Monte carlo-based inverse model for calculating tissue optical properties. part i: Theory and validation on synthetic phantoms. *Applied optics*, 45(5):1062–1071.
- [Pham et al., 2000] Pham, T. H., Bevilacqua, F., Spott, T., Dam, J. S., Tromberg, B. J., and Andersson-Engels, S. (2000). Quantifying the absorption and reduced scattering coefficients of tissuelike turbid media over a broad spectral range with noncontact fourier-transform hyperspectral imaging. *Applied optics*, 39(34):6487–6497.
- [PixelFly, 2015] PixelFly (2015). High performance digital 12 bit ccd camera system. [http://www.pco.de/fileadmin/user\\_upload/db/products/datasheet/pixelfly\\_20090505\\_02.pdf](http://www.pco.de/fileadmin/user_upload/db/products/datasheet/pixelfly_20090505_02.pdf). Last visited: 11/10/2015.
- [Planat-Chrétien et al., 2016] Planat-Chrétien, A., Berger, M., Guichard, N., Breugnot, J., Vyumvuhore, R., Le Guillou, M., and Dinten, J.-M. (2016). Stop: a spectroscopic tip optical probe for skin complexion characterization. In *Clinical and Translational Biophotonics*, pages JM3A–28. Optical Society of America.
- [Qin et al., 2006] Qin, J., and Lu, R. (2006). Hyperspectral diffuse reflectance imaging for rapid, noncontact measurement of the optical properties of turbid materials. *Applied optics*, 45(32):8366–8373.
- [Rajaram et al., 2008] Rajaram, N., Nguyen, T. H., and Tunnell, J. W. (2008). Lookup table-based inverse model for determining optical properties of turbid media. *Journal of biomedical optics*, 13(5):050501–050501.
- [Rakotomanga et al., 2015] Rakotomanga, P., and Planat-Chrétien, A. (2015). Modélisation bicouche de la peau. Université de Montpellier and LISA laboratory, LETI, CEA.
- [Randeberg et al., 2005] Randeberg, L. L., Winnem, A., Haaverstad, R., and Svaasand, L. O. (2005). Performance of diffusion theory vs monte carlo methods. In *European Conference on Biomedical Optics*, page ThB3. Optical Society of America.

- [Reif et al., 2007] Reif, R., A’Amar, O., and Bigio, I. J. (2007). Analytical model of light reflectance for extraction of the optical properties in small volumes of turbid media. *Applied optics*, 46(29):7317–7328.
- [Roig et al., 2013] Roig, B., Guilbert, M., Koenig, A., Piot, O., Perraut, F., Manfait, M., and Dinten, J.-M. (2013). Can diffuse reflectance spectroscopy emphasize skin-collagen alterations due to ageing? In *ISBS/SICC*.
- [Ross et al., 2003] Ross, M. H., Kaye, G. I., and Pawlina, W. (2003). *Histology: a text and atlas: with cell and molecular biology*. Lippincott Williams & Wilkins.
- [Saager et al., 2011] Saager, R. B., Truong, A., Cuccia, D. J., and Durkin, A. J. (2011). Method for depth-resolved quantitation of optical properties in layered media using spatially modulated quantitative spectroscopy. *Journal of biomedical optics*, 16(7):077002–077002.
- [Schatz, 2012] Schatz, P. (2012). *Human Anatomy and Physiology*. OpenStax College.
- [Scholkmann et al., 2013] Scholkmann, F., and Wolf, M. (2013). General equation for the differential pathlength factor of the frontal human head depending on wavelength and age. *Journal of biomedical optics*, 18(10):105004–105004.
- [Schwarz et al., 2008a] Schwarz, R. A., Gao, W., Daye, D., Williams, M. D., Richards-Kortum, R., and Gillenwater, A. M. (2008a). Autofluorescence and diffuse reflectance spectroscopy of oral epithelial tissue using a depth-sensitive fiber-optic probe. *Applied optics*, 47(6):825–834.
- [Schwarz et al., 2008b] Schwarz, R. A., Gao, W., Daye, D., Williams, M. D., Richards-Kortum, R., and Gillenwater, A. M. (2008b). Autofluorescence and diffuse reflectance spectroscopy of oral epithelial tissue using a depth-sensitive fiber-optic probe. *Applied optics*, 47(6):825–834.
- [Scott, 1998] Scott, P. (1998). Molar extinction coefficients of oxy and deoxyhemoglobin. <http://omlc.ogi.edu/spectra/hemoglobin/>. Oregon Medical Laser Center.
- [Soloplast, 2015] Soloplast (2015). Résine gts pro. <http://www.soloplast-vosshemie.fr/resine-gts-pro.htm>. Last visited: 11/10/2015.
- [Sorgato et al., 2016] Sorgato, V., Berger, M., Emain, C., Vever-Bizet, C., Dinten, J.-M., Bourg-Heckly, G., and Planat-Chrétien, A. (2016). Aca-pro: calibration protocol for quantitative diffuse reflectance spectroscopy. validation on contact and noncontact probe-and ccd-based systems. *Journal of Biomedical Optics*, 21(6):065003–065003.
- [Svaasand et al., 1995] Svaasand, L., Norvang, L., Fiskerstrand, E., Stopps, E., Berns, M., and Nelson, J. (1995). Tissue parameters determining the visual appearance of normal skin and port-wine stains. *Lasers in Medical Science*, 10(1):55–65.
- [Thueller et al., 2003] Thueller, P., Charvet, I., Bevilacqua, F., Ghislain, M. S., Ory, G., Marquet, P., Meda, P., Vermeulen, B., and Depeursinge, C. (2003). In vivo endoscopic tissue diagnostics based on spectroscopic absorption, scattering, and phase function properties. *Journal of biomedical optics*, 8(3):495–503.

- [Tuan, 2003] Tuan, V.-D. (2003). *Biomedical Photonics handbook*.
- [Van Staveren et al., 1991] Van Staveren, H. J., Moes, C. J., van Marie, J., Prahl, S. A., and Van Gemert, M. J. (1991). Light scattering in Intralipid-10% in the wavelength range of 400–1100 nm. *Applied optics*, 30(31):4507–4514.
- [Venugopalan et al., 1998] Venugopalan, V., You, J., and Tromberg, B. (1998). Radiative transport in the diffusion approximation: an extension for highly absorbing media and small source-detector separations. *Physical Review E*, 58(2):2395.
- [Vogel et al., 2007] Vogel, A., Chernomordik, V. V., Riley, J. D., Hassan, M., Amyot, F., Dasegeb, B., Demos, S. G., Pursley, R., Little, R. F., Yarchoan, R., et al. (2007). Using noninvasive multispectral imaging to quantitatively assess tissue vasculature. *Journal of biomedical optics*, 12(5):051604–051604.
- [Vogel et al., 2003] Vogel, A., and Venugopalan, V. (2003). Mechanisms of pulsed laser ablation of biological tissues (chem. rev. 2003, 103, 577-644. published on the web 02/12/03.). *Chemical Reviews*, 103(5):2079–2079.
- [Wang et al., 2016] Wang, A., Lu, R., and Xie, L. (2016). A sequential method for measuring the optical properties of two-layer media with spatially-resolved diffuse reflectance: simulation study. In *SPIE Commercial+ Scientific Sensing and Imaging*, pages 98640Q–98640Q. International Society for Optics and Photonics.
- [Wang et al., 2012] Wang, L. V., and Wu, H.-i. (2012). *Biomedical optics: principles and imaging*. John Wiley & Sons.
- [Whateley et al., 1984] Whateley, T., Steele, G., Urwin, J., and Smail, G. (1984). Particle size stability of intralipid and mixed total parenteral nutrition mixtures. *Journal of Clinical Pharmacy and Therapeutics*, 9(2):113–126.
- [Yang et al., 2015] Yang, S.-W., Lee, Y.-S., Chang, L.-C., Hwang, C.-C., Luo, C.-M., and Chen, T.-A. (2015). Clinical characteristics of narrow-band imaging of oral erythroplakia and its correlation with pathology. *BMC cancer*, 15(1):1–8.
- [Yaroshevsky et al., 2011] Yaroshevsky, A., Glasser, Z., Granot, E., and Sternklar, S. (2011). Transition from the ballistic to the diffusive regime in a turbid medium. *Optics letters*, 36(8):1395–1397.
- [Yoshida et al., 2004] Yoshida, T., Inoue, H., Usui, S., Satodate, H., Fukami, N., and Kudo, S.-e. (2004). Narrow-band imaging system with magnifying endoscopy for superficial esophageal lesions. *Gastrointestinal endoscopy*, 59(2):288–295.
- [Yu et al., 2014] Yu, B., Shah, A., Nagarajan, V. K., and Ferris, D. G. (2014). Diffuse reflectance spectroscopy of epithelial tissue with a smart fiber-optic probe. *Biomedical optics express*, 5(3):675–689.
- [Yu et al., 2008] Yu, C.-C., Lau, C., O’Donoghue, G., Mirkovic, J., McGee, S., Galindo, L., Elackattu, A., Stier, E., Grillone, G., Badizadegan, K., et al. (2008). Quantitative spectroscopic imaging for non-invasive early cancer detection. *Optics express*, 16(20):16227–16239.

- [Zeng et al., 2008] Zeng, H., Fawzy, Y. S., Short, M., Tercelj, M., McWilliams, A., Petek, M., Palcic, B., Zhao, J., Lui, H., Lam, S., et al. (2008). Combining field imaging endoscopy with point analysis spectroscopy for improving early lung cancer detection. In *Engineering in Medicine and Biology Society, 2008. EMBS 2008. 30th Annual International Conference of the IEEE*, pages 1849–1850. IEEE.
- [Zhong et al., 2014] Zhong, X., Wen, X., and Zhu, D. (2014). Lookup-table-based inverse model for human skin reflectance spectroscopy: two-layered monte carlo simulations and experiments. *Optics express*, 22(2):1852–1864.
- [Zhu et al., 2011] Zhu, C., and Liu, Q. (2011). Validity of the semi-infinite tumor model in diffuse reflectance spectroscopy for epithelial cancer diagnosis: a monte carlo study. *Optics express*, 19(18):17799–17812.
- [Zonios et al., 2006] Zonios, G., and Dimou, A. (2006). Modeling diffuse reflectance from semi-infinite turbid media: application to the study of skin optical properties. *Optics express*, 14(19):8661–8674.
- [Zonios et al., 2011] Zonios, G., and Dimou, A. (2011). Modeling diffuse reflectance from homogeneous semi-infinite turbid media for biological tissue applications: a monte carlo study. *Biomedical optics express*, 2(12):3284–3294.
- [Zuzak et al., 2002] Zuzak, K. J., Schaeberle, M. D., Lewis, E. N., and Levin, I. W. (2002). Visible reflectance hyperspectral imaging: characterization of a noninvasive, in vivo system for determining tissue perfusion. *Analytical Chemistry*, 74(9):2021–2028.







# Abstract

The Novel *Dual-Step* Multispectral Imaging Technique that has been developed intends to contribute to the clinical diagnosis of superficial lesions by providing non-invasively quantitative spatial wide field maps of absorption and scattering endogenous optical properties. The approach relies on the combination of a Non-Contact Spatially-resolved Diffuse Reflectance Spectroscopy (DRSsr) technique with a Multispectral Imaging (MSI) technique. Absolute quantification is based on the scattering estimation with Non-Contact DRSsr which is subsequently used by MSI to estimate wide field absorption. The instrumental setups of each technique are built and thoroughly characterized in this work. The optimal quantification of optical properties relies on a newly established calibration algorithm (*ACA-Pro*) that achieves minimal estimation errors inferior to 3.3% for scattering and 5.5% for absorption. The developed *Dual-Step* technique has been validated not only with an extensive intralipid phantom study but also with *ex-vivo* biological human skin samples and *in-vivo* inflammation skin models on rats. The results show the potential of the *Dual-Step* technique as a valid quantitative, wide-field, and non-invasive clinical diagnosis approach.

# Résumé

La nouvelle technique '*Dual-Step*' d'Imagerie Multispectrale qui a été développée a comme objectif de contribuer au diagnostic clinique des lésions superficielles, en procurant des cartes grand champ quantitatives des propriétés optiques endogènes telles que l'absorption et la diffusion. L'approche repose sur la combinaison d'une technique sans-contact de Spectroscopie de Réflectance Diffuse spatialement résolue (DRSsr) pour estimer la diffusion utilisée ensuite par une autre technique d'Imagerie Multispectrale (MSI) pour estimer l'absorption. Les bancs d'essai de chaque technique ont été construits et caractérisés dans le cadre de ce travail. La quantification optimale des propriétés optiques s'appuie sur un nouvel algorithme de calibration (*ACA-Pro*) qui atteint des erreurs d'estimation minimales et inférieures à 3.3% pour la diffusion et 5.5% pour l'absorption. La technique '*Dual-Step*' a été validée sur des fantômes d'intralipide mais aussi sur des échantillons *ex-vivo* de peau humaine et des modèles *in-vivo* d'inflammation de peau de rats. Les résultats montrent la faisabilité de la technique '*Dual-Step*' et son potentiel en diagnostic clinique grâce à son approche quantitative, grand champ et non-invasive.